An adaptive three-dimensional mutiresolution algorithm for the resolution of parabolic PDEs. Application to thermodiffusive flame instabilities.

Olivier Roussel

UNIVERSITE DE LA MEDITERRANEE
Ecole Supérieure de Mécanique de Marseille

THESE

pour obtenir le grade de

DOCTORAT DE L'UNIVERSITE DE LA MEDITERRANEE
AIX-MARSEILLE II
Discipline: Mécanique, physique et modélisation
Option: Mécanique des fluides

présentée et soutenue publiquement par

Olivier ROUSSEL

le 24 mars 2003

DEVELOPPEMENT D'UN ALGORITHME MULTIRESOLUTION ADAPTATIF TRIDIMENSIONNEL POUR LA RESOLUTION DES EQUATIONS AUX DERIVEES PARTIELLES PARABOLIQUES.
APPLICATION AUX INSTABILITES THERMODIFFUSIVES DE FLAMME.

Directeur de thèse: *Kai SCHNEIDER*, Professeur, Université de Provence

RAPPORTEURS :
Henning BOCKHORN, Professeur, Université de Karlsruhe, Allemagne
Rosa DONAT BENEITO, Professeur, Université de Valence, Espagne

JURY :
Henning BOCKHORN, Professeur, Université de Karlsruhe, Allemagne
Rosa DONAT BENEITO, Professeur, Université de Valence, Espagne
Pierre HALDENWANG, Professeur, Université de Provence
Jacques LIANDRAT, Professeur, Université de la Méditerranée
Siegfried MÜLLER, Docteur habilité, Université d'Aix-la-Chapelle, Allemagne
Kai SCHNEIDER, Professeur, Université de Provence

La condition du progrès, sans doute est-ce un équilibre raisonnable entre le travail omniprésent de l'homme et les autres sources énergétiques de remplacement. C'est un profit illusoire que l'homme les concurrence outre mesure (...) En vérité, pas de progrès sans une certaine valorisation de l'homme. Qu'il soit une source d'énergie d'un certain prix de revient, et il faudra songer à l'aider, ou mieux à le remplacer.

Fernand Braudel.

Remerciements

Je tiens tout d'abord à remercier Jacques Liandrat pour les nombreux conseils qu'il m'a prodigués sur les méthodes multiresolution. C'est un honneur pour moi qu'il ait accepté de présider ce jury.

J'adresse ensuite tous mes remerciements à Rosa Donat et Henning Bockhorn, qui ont accepté la lourde tâche de rapporteur. Leur expertise complémentaire, la première pour la partie numérique, le second pour la partie combustion, a grandement contribué à la qualité du manuscrit. Je remercie également Henning Bockhorn pour m'avoir accueilli dans son laboratoire - dans le cadre du programme européen d'échange TMR - et d'avoir pu y travailler dans les meilleures conditions.

Je souhaite également remercier Pierre Haldenwang et Siegfried Müller d'avoir accepté de faire partie de ce jury. Je les remercie en outre pour les nombreux conseils qu'ils m'ont donnés tout au long de cette thèse.

Mais ce travail n'aurait sans doute pas existé sans Kai Schneider, qui a accepté d'être mon directeur de thèse. Je le remercie pour la confiance qu'il m'a toujours accordée. Ses conseils judicieux, sa rigueur scientifique et l'expertise qu'il possède à la fois en méthodes numériques et en combustion ont été déterminants dans le bon déroulement de cette thèse.

Je remercie aussi les autres membres du réseau européen TMR "Wavelets in numerical simulation" pour leur collaboration, en particulier Francesc Arandiga, Sylvia Bertoluzza, Guillaume Chiavassa, Albert Cohen, Wolfgang Dahmen, Sidi-Mahmoud Kaber et Marie Postel.

Tous mes remerciements vont également à l'équipe du L3M de Marseille, à son directeur Patrick Bontoux qui m'a accueilli dans son laboratoire, aux membres permanents, aux doctorants et post-doctorants: Marc Forrestier, Magalie Garde, Umberto d'Ortonna, Dominique Fougère, Giulio Pellegrino, Bernard Roux, Eric Serre et Sylvain Suard.

Lors de mon séjour à Karlsruhe, j'ai travaillé au sein du groupe "Numerik" de l'ICT. Je remercie vivement toute l'équipe pour leur accueil et leur sympathie: Jochen Fröhlich, Wolfgang Gerlinger, Leo Rutz, Astrid Schön, Nadia Sebbar, Thomas Stoll et Jörg Ziuber, sans oublier la secrétaire Hildegard Huck pour son efficacité et sa disponibilité. Merci également aux stagiaires qui ont collaboré avec moi et dont le travail a été d'une grande utilité: Eve-Marie Duclairoir, Alexandre Fornel et Bastien Pellicioli. Enfin, un remerciement particulier pour Alexei Tsigulin, de l'Université de Novossibirsk, avec qui j'ai co-écrit le code CARMEN.

Pour terminer, je souhaiterais remercier ma famille et mes amis qui ont toujours été à

mes côtés et qui constituent un "môle", un soutien indéfectible dans toutes les situations. Au premier rang, il y a bien entendu mes parents et Carmen, celle qui partage ma vie, et à qui je dédie cette thèse.

Résumé

Le but de cette thèse est le développement d'un algorithme adaptatif pour la résolution des équations aux dérivées partielles paraboliques en géométrie cartésienne pour des problèmes en dimension un, deux et trois et l'application aux instabilités de flamme dans l'approximation thermodiffusive. Partant d'un schéma de discrétisation de type volumes finis explicite, nous appliquons une décomposition adaptative multi-résolution pour représenter la solution sur un maillage localement raffiné. Les flux numériques sont calculés directement sur la grille adaptative. Afin de suivre l'évolution de la solution au cours du temps, nous utilisons une stratégie d'adaptation dynamique basée sur la représentation des données en multi-résolution. Cette dernière consiste à représenter la solution à l'aide des valeurs sur une grille grossière, plus l'ensemble des différences de prédiction entre les valeurs d'une grille donnée et celles d'une grille plus fine, l'ensemble consistuant une hiérarchie de grilles emboîtées. La compression des données s'obtient en supprimant les différences inférieures à une certaine tolérance fixée.

Nous validons cette méthode par la résolution numérique d'équations de référence, comme l'équation de convection-diffusion ou l'équation de Burgers diffusive, afin de montrer la précision de la méthode et son efficacité par rapport au même schéma volumes finis sur grille fine. En particulier, pour l'équation linéaire de convection-diffusion, nous donnons une relation entre la tolérance et le nombre d'échelles qui permet de réduire le temps de calcul et la place mémoire nécessaires tout en maintenant l'ordre de précision du schéma volumes finis. Ce résultat est confirmé par le calcul numérique.

Nous utilisons ensuite la méthode adaptative pour étudier les instabilités de flammes prémélangées dans l'approximation thermodiffusive. En particulier, pour les flammes planes, nous déterminons la limite d'apparition des flammes pulsantes, limite que nous comparons aux données de la littérature, tant numériques que théoriques. Nos calculs confirment la théorie pour les grandes valeurs de l'énergie d'activation. Nous montrons également numériquement l'existence de flames planes non-pulsantes lorsque la conduction de la chaleur est très supérieure à la diffusion des réactants. Nous étudions également les ballons de flamme et montrons que, lorsqu'ils interagissent avec une paroi adiabatique, leur comportement présente une analogie avec la capillarité en mécanique des fluides. Le dernier résultat concerne l'interaction d'un ballon de flamme avec un tourbillon. Il ouvre des perspectives sur la simulation adaptative des ballons de flamme dans un fluide en mouvement.

Mots-clés. flamme pulsante, ballon de flamme, multi-résolution, adaptativité, ondelette, volume fini, équation aux dérivées partielles parabolique.

Abstract

This thesis is concerned with the development of an adaptive numerical algorithm for solving parabolic PDEs in Cartesian geometry in one, two and three space dimensions and the application to thermodiffusive flame instabilities. Applying a finite volume discretization with explicit time integration, both of second order, we employ an adaptive multiresolution scheme to represent the solution on locally refined nested grids. The fluxes are evaluated on the adaptive grid. A dynamical adaption strategy to advance the grid in time and to follow the time evolution of the solution directly exploits the multiresolution representation. The latter aims at representing the solution as values on a coarse grid plus a series of differences in predicting the values of the next finer grid in the hierarchy of nested dyadic grids. Data compression is obtained by removing differences that are smaller than a prescribed tolerance.

We validate this method by solving several test problems in one, two and three space dimensions, like convection-diffusion and viscous Burgers equations, in order to show its accuracy and its efficiency. For the linear convection-diffusion equation, we find a theoretical relation between the prescribed tolerance and the number of grid levels which enables us to maintain the accuracy order of the finite volume scheme, while reducing CPU time and memory requirements. This result is confirmed by numerical computations.

We then apply the adaptive method to study the stability behavior of premixed flames in the thermo-diffusive approximation. We determine the limit between stable and pulsating planar flames and compare it to previous work on the subject, both theoretical and numerical. The numerical computations confirm the theoretical results for large values of the activation energy. We also show that non-pulsating planar flames can exist when heat conduction largely exceeds the diffusion of chemical reactants. We also perform numerical simulations of flame balls and show that their interaction with adiabatic walls creates a phenomenon which presents an analogy with capillarity for fluid droplets. The last result concerns the interaction of a flame ball with a vortex, which opens perspectives for the adaptive numerical simulation of flame balls in a moving fluid.

Keywords. pulsating flame, flame ball, multiresolution, adaptivity, wavelet, finite volume, parabolic partial differential equation

Zusammenfassung

Gegenstand dieser Arbeit ist die Entwicklung eines adaptiven numerischen Algorithmus zur Lösung parabolischer partieller Differentialgleichungen in ein-, zwei- und dreidimensionaler kartesischer Geometrie, sowie die Anwendung zur Untersuchung der Flammeninstabilitäten in der thermo-diffusiven Approximation. Die entwickelte Methode basiert auf einer Finite-Volumen-Approximation im Ort mit expliziter Zeitdiskretisierung. Wir benutzen eine Multiresolutionsanalyse, um die Lösung auf einem hierarchischen Gitter abzubilden. Die Flüsse werden auf diesem adaptiven Gitter berechnet. Die Strategie, die das hierarchische Gitter während der Lösung automatisch adaptiert, basiert auf eine Multiresolutionanalyse. Diese Stategie zielt darauf ab, Daten auf einem feinen Gitter als Daten auf einem groben Gitter und Unterschiede in der Vorhersage der nächsten Ebene des hierarchsichen Gitter darzustellen. Die Unterschiede, die kleiner als eine gegebene Toleranz sind, werden aus dem Speicher gelöscht, um die Datenmenge erheblich zu reduzieren.

Die numerische Methode wird zuerst anhand Testprobleme validiert, wie z.B. Konvektions-Diffusions- und diffusive Burgers-Gleichungen, um den Wirkungsgrad und die Genauigkeit des Algorithmus zu bestimmen. Für lineare Konvektions-Diffusions-Gleichungen finden wir eine theoretische Beziehung zwischen der Toleranz und der Gitterfeinheit. Mit dieser Beziehung wird die Rechenzeit und der Speicherbedarf reduziert, ohne die Ordnung der Genauigkeit des Finite-Volumen-Schemas zu beeinträchtigen. Diese Beziehung wird durch die Rechnungen bestätigt.

Anschließend wird die Methode zur numerischen Simulation von Flammeninstabilitäten in der thermo-diffusiven Approximation angewandt. Insbesonderes bestimmen wir die Grenze zwischen stabilen und pulsierenden planaren Flammen. Die Ergebnisse werden mit früheren theoretischen und numerischen Arbeiten verglichen. Wir bestätigen hier das theoretische Ergebnis für große Aktivierungsenergien. Ebenso zeigen wir, daß nichtpulsierenden planare Flammen existieren, wenn der Transport durch die Warmeleitung viel größer als der der Diffusion ist. Wir führen auch Simulationen sphärischer Flammenstrukturen durch und zeigen, daß ihre Wechselwirkung mit einem adiabatischen Rand Ähnlichkleiten zu Kapillaritätseffekten aufweist. Das letzte Ergebnis befaßt sich mit der Wechselwirkung sphärischer Flammenstrukturen mit einem Wirbel. Dieses öffnet weitere Perspektiven auf adaptive Simulationen reagierender Strömungen.

Schlüsselwörter. pulsierende Flamme, flame ball, Multiresolution, Adaptivität, Wavelet, finite Volumen, parabolische partielle Differentialgleichung

Resumen

El objetivo de esta tesis es el desarrollo de un algoritmo adaptativo para resolver ecuaciones en derivadas parciales parabólicas expresadas en geométria cartesiana en una, dos y trés dimensiones y la aplicación a las inestabilidades de llamas en aproximación termodifusiva. Partiendo de un esquema de discretización de tipo volumen finito explícito, aplicamos una descomposición adaptativa multiresolución para representar la solución sobre una malla refinada localmente. Los flujos numéricos son calculados directamente sobre la grilla adaptativa.

Con el fin de seguir la evolución de la solución respecto al tiempo, utilizamos un método de adaptación dinámica basado en la representación de los datos por multiresolución. Éste método consiste en representar la solución utilizando una grilla con poca definición más el conjunto de errores en la predicción de los valores entre una grilla dada y otra con mayor resolución creando así una jerarquía de grillas anidadas. La compresión de los datos se obtiene suprimiendo los errores que son inferiores a una cierta tolerancia prefijada.

Este método ha sido validado gracias a la resolución de ecuaciones de referencia como la ecuación de convección-difusión y la ecuación difusiva de Burgers con el fin de demostrar la precision del cálculo y su eficacia respecto al mismo esquema de volumen finito sobre una grilla fina. En particular, para el caso de la ecuación linear de convección-difusión, se ha encontrado una relación teórica entre la tolerancia y el número de escalas que permiten reducir el tiempo de cálculo y el espacio de memoria necesarios manteniendo al mismo tiempo el orden de precisión alcanzado con un esquema de volumen finito. Esta relación ha sido verificada por el cálculo.

A continuación el método adaptativo es utilizado para estudiar las inestabilidades de llamas pre-mezcladas en aproximación termodifusiva. En particular, para las llamas planas, determinamos el límite de aparición de llamas pulsadas, límite que comparamos a los datos, tanto numéricos como teóricos, que podemos encontrar en la literatura. Nuestros cálculos confirman la teoría para los grandes valores de la energía de activación. Se muestra igualmente, de forma numérica, la existencia de llamas planas quien no pulsan cuando la conducción del calor es muy superior a la difusión de los reactantes químicos. Asimismo se han realizado simulaciones numéricas sobre balones de llamas donde aparece que, cuando estos interaccionan con una pared adiabática, su comportamiento presenta una analogiá con la capilaridad en mecánica de fluidos. El último resultado concierne la interacción de un balón de llamas con un torbellino. Éste abre la perspectiva para próximos trabajos sobre la simulación adaptativa de los balones de llamas dentro de un fluido en movimiento.

Palabras calve. Llama pulsada, balon de llamas, multiresolución, adaptatividad, wavelet, volumen finito, ecuación en derivadas parciales parabólica.

Version abrégée en français

Depuis le début de la révolution industrielle et de nos jours encore, la combustion couvre la grande majorité de nos besoins énergétiques. Cependant, les réserves de combustible ne sont pas infinies. Elles ont même tendance à diminuer de plus en plus vite, étant donné que la consommation d'énergie à l'échelle planétaire ne cesse de croître. En outre, depuis les années 1970, l'opinion publique a pris conscience de la dégradation de l'environnement, en grande partie due à la combustion. Ces facteurs ont conduit les industriels à concevoir des moteurs à combustion plus efficaces et moins pollutants pour les automobiles, les avions, les fusées, etc., ce qui nécessite de comprendre en détail la combustion des mélanges pauvres en carburant. Malheureusement, les mécanismes physico-chimiques qui interviennent dans de tels mélanges ne sont pas complètement compris. Les flammes pauvres constituent encore aujourd'hui un sujet de recherche très important, tant du point de vue théorique qu'expérimental.

Depuis les années 1980, un nouvel outil est venu compléter les recherches théoriques et expérimentales: la simulation numérique par ordinateur. Le principal avantage de cet outil est qu'il permet de "réaliser" des expériences en série en changeant simplement les paramètres. De plus, il permet d'avoir accès partout à toutes les quantités physico-chimiques (pression, température, proportion des gaz frais, etc.) et même à des quantités qu'on ne peut mesurer expérimentalement. Le principal inconvénient par rapport à l'expérience est que le calcul résout les équations d'un modèle théorique. La solution obtenue n'est donc valable que dans le cadre des hypothèses du modèle choisi. De plus, plus le modèle est proche de la réalité, plus il est complexe, et plus le calcul est coûteux en terme de temps de calcul et de place mémoire. Parmi les diverses méthodes de simulation numérique, l'une des plus courantes utilise la démarche suivante: d'abord, on modélise le phénomène physico-chimique par un système d'équations aux dérivées partielles (EDP); ensuite, on résout ces équations de façon approchée sur un ensemble de points - le maillage - qui constitue une représentation discrète du domaine physique.

Cependant, du point de vue numérique, le problème de la combustion est "raide". Cela signifie qu'il fait intervenir un grand nombre d'échelles temporelles et spatiales. En particulier, la réaction chimique a lieu dans une zone extrêmement fine. Il est donc nécessaire d'utiliser un maillage très fin, ce qui, en trois dimensions, rend le temps de calcul et la place mémoire nécessaires prohibitifs. Or, dans le reste du domaine physique, un maillage nettement plus grossier est largement suffisant. Il apparaît donc clairement qu'un maillage adapté permettrait de maintenir la précision du calcul tout en réduisant significativement

son coût en termes de temps de calcul et de place mémoire. Par ailleurs, sachant que la zone de réaction chimique se déplace au cours du temps, il apparaît nécessaire d'utiliser un maillage qui s'adapte automatiquement à la solution au cours du temps.

Depuis les années 1970-80, de nombreuses méthodes adaptatives ont été développées, en général pour des problèmes de capture de chocs dans des écoulements de fluide compressible. Parmi celles-ci, les méthodes multi-échelles ont fait appel à un ensemble de grilles superposées les unes sur les autres, telles les méthodes MLAT (*Multi-Level Adaptive Techniques*) (Brandt [17]) ou AMR (*Adaptive Mesh Refinement*) (Berger *et al* [9, 8], Quirk [74], Bell *et al* [7]). Le principe consiste à calculer d'abord la solution sur la grille grossière, puis à faire appel à des niveaux de grille plus raffinés dans les régions de fort gradients ou, lorsque le calcul commençe sur deux grilles, dans les zones ou l'erreur de troncature entre les solutions sur les deux grilles était élevée. Toutefois, le taux de compression des données est élevé dans les régions où la solution est quasiment constante, mais pas dans celles où la solution est régulière.

Plus récemment, des méthodes adaptatives en ondelettes ont été développeés pour résoudre les EDP. Pour une description générale et une classification de ces méthodes, nous invitons le lecteur à consulter Dahmen [32], Cohen [27], Fröhlich et Schneider [45]. L'interêt d'utiliser de telles méthodes est double. D'abord, on peut représenter de façon approchée à l'aide de peu de coefficients d'ondelettes les fonctions localement irrégulières, c'est-à-dire les fonctions dont la régularité au sens de Besov est supérieure à la régularité au sens de Sobolev (DeVore [40], Dahmen [32]). Ensuite, un grand nombre d'opérateurs intégro-différentiels ont une représentation creuse dans des bases d'ondelettes (Beylkin [10]). Ils peuvent être facilement préconditionnés (Jaffard [59], Dahmen [34]). Pour des problèmes d'évolution, les schémas en ondelettes permettent d'adapter automatiquement la base à la solution, en activant ou désactivant les coefficients d'ondelettes au voisinage des points actifs. Ces propriétés ont conduit au développement de nombreux schémas adaptatifs en ondelettes pour divers types d'EDP: équation de Burgers diffusive (Liandrat et Tchamitchian [64], Maday *et al* [65, 66]), équations thermo-diffusives (Fröhlich et Schneider [43, 45]), équations de Stokes 2D (Urban [91]), équations de Navier-Stokes 2D (Charton et Perrier [20], Fröhlich et Schneider [44], Schneider *et al* [88], Schneider et Farge [87]). Dans ces travaux, les schémas numériques sont de type Pétrov-Galerkine avec des ondelettes comme base de fonctions-tests.

L'approche choisie dans cette thèse diffère des précédentes et s'apparente plutôt à la multi-résolution de Harten [54, 55]. Elle repose sur un schéma d'évolution temporelle de type volumes finis, auquel on adjoint une analyse multi-résolution. Dans les régions régulières, on remplace les calculs de flux par de simples interpolations à partir des valeurs des grilles plus grossières, ce qui permet de réduire le temps de calcul. Cette méthode a montré son efficacité et a été étendue à de nombreux problèmes: initialement, les EDP hyperboliques en 1D (Harten [54]), puis en 2D (Bihari et Harten [12]), ensuite les EDP en 1D avec un terme de diffusion (Bihari [11]), les équations d'Euler compressible en 2D (Chiavassa et Donat [21]), les EDP hyperboliques en 2D avec des maillages structurés curvilignes (Dahmen *et al* [33]) et non-structurés (Abgrall et Harten [2], Cohen *et al* [30]). Toujours dans le contexte des équations hyperboliques, une version multi-résolution adap-

tative a été développée afin de réduire également la place mémoire (Gottschlich-Müller et Müller [48], Cohen *et al* [31]). Ces travaux ont été étendus aux équations de Navier-Stokes 2D compressibles pour des problèmes où la convection domine, ce qui conduit à un problème quasi-hyperbolique (Bramkamp *et al* [16]). Dans la méthode adaptative, la solution est représentée et calculée sur un ensemble de grilles qui s'adaptent automatiquement à la solution. Plusieurs stratégies ont été proposées pour évaluer les flux sans qu'il soit nécessaire d'avoir toutes les valeurs de la grille la plus fine. Pour plus de détails sur les techniques multi-résolution adaptatives dans le cas de lois de conservations hyperboliques, nous invitons le lecteur à consulter le livre de Müller [70]. Les différences entre approches AMR et multirésolution sont décrites dans Cohen [28].

Ici, notre but est de simuler numériquement à un coût réduit les flammes prémélangées dans l'approximation de masse volumique constante. Dans ce cas, les équations de conservation de l'énergie et des espèces chimiques sont découplées de celles de la dynamique du mélange gazeux. On obtient alors le *modèle thermo-diffusif*, qui se réduit à un système de deux EDP non-linéaires paraboliques. Dans le cadre de cette hypothèse, une des applications concerne l'étude des flammes prémélangées pour lesquelles la conduction de la chaleur excède la diffusion des espèces chimiques. L'analyse de stabilité linéaire montre que, pour des grandes valeurs de l'énergie d'activation de la réaction chimique et pour certaines valeurs d'autres paramètres, des flammes planes pulsantes peuvent apparaître (Joulin et Clavin [60], Clavin [25]). Des flammes pulsantes ont été observées expérimentalement, mais aussi simulées numériquement (Booty *et al* [15], Bayliss *et al* [6]). La limite entre flammes stables et pulsantes a été déterminée numériquement (Rogg [77]). Cependant, étant donné que des échelles de plus en plus fines sont nécessaires lorsque l'énergie d'activation augmente, le temps de calcul devient prohibitif pour les très grandes valeurs de l'énergie d'activation, ce qui explique que des régions du diagramme de bifurcation demeurent numériquement inexplorées.

Une autre application concerne les ballons de flamme. Ces structures apparaissent à l'intérieur des chambres de combustion pour des gaz prémélangés pauvres en carburant. Pour étudier ces phénomènes en l'absence de poussée d'Archimède - celle-ci génère de la convection qui perturbe la réaction - les ballons de flamme sont étudiés expérimentalement en micro-gravité. Parmi les travaux sur le sujet, citons ceux de Ronney [78] qui s'est plus particulièrment intéressé aux mélanges pauvres hydrogène-air. Les ballons de flamme ont été simulés numériquement loin des parois de la chambre de combustion à l'aide de méthodes pseudo-spectrales (Bockhorn *et al* [13], Gerlinger *et al* [47, 46]). Des calculs adaptatifs ont également été effectués à l'aide d'algorithmes de type ondelette-vaguelette (Bockhorn *et al* [14], Schneider [85]). Cependant, ces méthodes sont restreintes à des conditions aux limites périodiques. Elles ne peuvent donc pas être utilisées pour la simulation de phénomènes comme l'interaction des ballons de flamme avec les parois de la chambre de combustion. Ceci nous incite donc à utiliser des méthodes multi-résolution adaptatives basées sur les volumes finis pour simuler à moindre coût de tels phénomènes.

Dans cette thèse, nous présentons donc un schéma multi-résolution adaptatif pour résoudre les EDP paraboliques en dimension un, deux et trois avec différentes sortes de conditions aux limites. Nous étendons les travaux précendents sur les équations hyper-

boliques en dimension un et deux aux équations paraboliques et au cas 3D. Nous présentons également une analyse d'erreur spécifique au cas parabolique. En outre, comme nous souhaitons garantir la conservativité dans le calculs des flux aux interfaces - conservativité qui n'est pas nécéssairement assurée aux interfaces de cellules de différents niveaux - nous proposons une formulation du calcul des flux qui garantit une stricte conservativité. Nous présentons en outre un algorithme récursif original qui permet de réduire véritablement à la fois le temps de calcul et la place mémoire nécessaires. Enfin, nous appliquons la méthode précédente à la simulation numérique des problèmes d'instabilité thermo-diffusive dans les flammes prémélangées. En particulier, nous étendons le diagramme de stabilité des flammes planes pulsantes aux très grandes valeurs de l'énergie d'activation et aux grandes valeurs du nombre de Lewis. Nous déterminons également les différents comportements des ballons de flamme lorsqu'ils interagissent avec une paroi adiabatique. Enfin, nous présentons des premiers calculs adaptatifs de l'interaction d'un ballon de flamme avec un tourbillon, ce dernier point étant le début de futurs travaux sur la simulation adaptative de ballons de flamme dans des fluides en mouvement.

*
* *

Le Chapitre 1 présente le système d'équations qui permet de modéliser la propagation des flammes prémélangées. Ce système est en fait constituté des équations de bilan sur les quantités conservatives en jeu: masse totale, quantité de mouvement, énergie, espèces chimiques. Dans le cadre de cette étude, nous nous restreignons au cas d'une réaction chimique simple, mettant en jeu deux réactants et un produit, le premier réactant et le produit étant considérés comme très dilués dans le second reactant, ce qui est la cas par exemple pour la combustion de l'hydrogène dans l'air. Ensuite, nous considérons que la cinétique chimique est à un pas et qu'elle vérifie la loi d'Arrhénius. Nous modélisons par ailleurs les pertes de chaleur dues au rayonnement par la loi de Stefan-Boltzmann, qui correspond au rayonnement des corps noirs. Enfin, comme nous nous restreignons à la propagation des flammes, c'est-à-dire à des *déflagrations*, nous considérons que la vitesse des gaz est fortement subsonique, ce qui nous permet de négliger les variations de pression dans le bilan d'énergie. On obtient alors le systèmes d'équations des *flammes isobares* (Eq. 1.1, p. 10). Deux autres hypothèses permettent de simplifier ce système: l'hypothèse des coefficients de transport constants et l'approximation de masse volumique constante. Ces dernières sont valables pour des flammes qui se propagent lentement. Avec ces hypothèses, la réaction chimique n'a plus d'influence sur la dynamique des gaz. On peut donc se contenter de résoudre les seules équations de bilan d'énergie et d'une espèce chimique - celle du premier réactant par exemple - et considérer la vitesse du mélange donnée par les équations de Navier-Stokes incompressible. On aboutit alors au *modèle thermo-diffusif* (Eq. 1.5, p. 11). Celui-ci est consitué de deux EDP non-linéaires paraboliques de type convection-diffusion-réaction, qui se réduisent au type diffusion-réaction lorsque le mélange gazeux est au repos.

Nous présentons ensuite la forme adimensionnée des équations thermo-diffusives, puis l'analyse de Zeldovich et Frank-Kamenetskii [94, 93] pour les grandes valeurs de l'énergie d'activation. Dans cette hypothèse, le terme d'Arrhenius du taux de réaction devient nul partout sauf dans une zone extrêmement mince: la zone de réaction chimique. On définit alors le nombre de Zeldovich Ze comme l'énergie d'activation adimensionnée. Dans la section suivante, nous présentons les flammes planes stationnaires. Leur existence a été démontrée expérimentalement, lorsqu'une flamme se propage dans un tube infiniment long et que le mélange gazeux est advecté à une vitesse égale à l'opposé de la vitesse de propagation de la flamme. De plus, dans l'hypothése où Ze tend vers l'infini, on peut déterminer une solution analytique des équations thermo-diffusives planes et stationnaires. Nous décrivons ensuite la structure de la flamme plane stationnaire. Celle-ci peut se découper schématiquement en quatre zones: la zone des gaz frais, la zone de pré-chauffage, la zone de réaction, la zone des gaz brûlés. La propagation de la flamme plane peut être décrite de la façon suivante: considérons une "tranche de gaz" frais au repos proche de la zone de réaction; lorsque la flamme avance, cette tranche reçoit par conduction thermique de la chaleur produite par la réaction chimique. La température de cette tranche s'élève alors jusqu'à ce que la réaction puisse se produire. Lorsque la tranche s'enflamme, la réaction dégage de la chaleur qui chauffe la tranche suivante, et ainsi de suite ... Lorsque tout le gaz frais est brûlé, la réaction s'arrête dans la tranche.

La dernière partie du chapitre est consacrée aux instabilités thermo-diffusives, dont l'analyse de stabilité linéaire a été établie par Sivashinsky [89] pour le cas adiabatique et Joulin et Clavin [60] pour le cas non-adiabatique, dans l'hypothèse où Ze tend vers l'infini. Cette étude a été vérifiée pour des valeurs de Ze finies par des calculs numériques (Denet et Haldenwang [38]). L'instabilité thermo-diffusive apparaît lorsque le front de flamme n'est plus plan. Dans la direction perpendiculaire au plan, la flamme est caractérisée par des profils de température et de concentration proches de ceux décrits pour la flamme plane. Par contre, des flux de chaleur et de masse existent dans la direction tangentielle au front. Les flux de masse ont tendance à augmenter les perturbations, tandis que ceux de chaleur les réduisent. Les flux de masse ont donc un effet *déstabilisant*, la chaleur ayant au contraire un effet *stabilisant*. Le nombre de Lewis Le, rapport entre les diffusivités de chaleur et de masse, est donc un paramètre essentiel pour déterminer la stabilité des flammes dans l'hypothèse thermo-diffusive. Pour établir la stabilité linéaire, nous écrivons l'équation des flammes pour des faibles perturbations harmoniques. En soustrayant la solution de base non-perturbée et en linéarisant, on obtient un système d'équations différentielles ordinaires (Eq. 1.27, p. 21). On peut obtenir alors une relation de dispersion dans l'hypothèse des grandes valeurs de l'énergie d'activation, à l'aide d'un développement asymptotique en puissance de Ze^{-1}. Pour des petites valeurs du nombre d'onde de la perturbation, on obtient la relation (Eq. 1.29, p. 22). Le domaine de stabilité correspond donc à

$$l = Ze\,(Le-1) > -2\,.$$

Dans la zone où $l < -2$, on observe la formation de *flammes cellulaires*. A l'inverse, pour les grandes valeurs de l, en particulier pour $l > 16$, on observe des *flammes pulsantes*. Ce mécanisme d'instabilité apparaît même lorsqu'il n'y a pas de perturbation, ce

qui signifie qu'il existe des *flammes planes pulsantes*. Celles-ci ont d'ailleurs été observées expérimentalement et simulées numériquement (voir par exemple Clavin [25], Williams [92]). Dans [77], Rogg donne l'explication suivante de ce phénomène: considérant un mélange gazeux dont le nombre de Lewis est supérieur à l'unité, le flux de chaleur sortant de la zone de réaction excède le flux de réactant qui y entre. La conséquence est que l'enthalpie décroît dans la zone de réaction, ce qui a pour effet de diminuer la température dans la zone de réaction, et donc aussi la vitesse de flamme. A l'inverse, l'enthalpie croît dans la zone de pré-chauffage, ce qui a pour effet d'*accélérer* l'allumage des réactants à l'interface entre la zone de réaction et la zone de pré-chauffage. Cet effet augmente donc la vitesse de flamme. Ainsi, c'est l'équilibre entre ces deux effets qui est à l'origine des pulsations. En effet, lorsque l'énergie d'activation est faible, l'effet d'accélération est faible et les pulsations sont amorties (Fig. 1.7, côté gauche, p. 24). Inversement, pour une énergie d'activation supérieure à un certain seuil, la vitesse de flamme diminue du fait de la chute d'enthalpie dans la zone de réaction, puis augmente du fait de l'augmentation d'enthalpie dans la zone de pré-chauffage, et ainsi de suite (Fig. 1.7, côté droit, p. 24).

La limite de pulsation en fonction des nombres de Lewis et Zeldovich a été établie dans [77]. Elle est cependant limitée à des nombres de Zeldovich modérés. En effet, plus le nombre de Zeldovich est grand, plus la zone de réaction est fine et plus le taux de réaction y est élevé. Ainsi, pour des valeurs de nombre de Zeldovich élevées (typiquement $Ze > 40$), un pas d'espace très fin est requis et, avec lui, un pas de temps également très petit. Etant donné que seule la zone de réaction nécessite des petites échelles, une méthode adaptative semble une bonne solution pour atteindre la précision nécessaire aux grands Ze avec un coût de calcul raisonnable. Dans cette thèse, c'est une méthode multi-résolution adaptative qui est préconisée. Elle est décrite au chapitre suivant.

*
* *

Le chapitre 2 est consacré à la description de la méthode multi-résolution adaptative. Basée sur une évolution temporelle en volumes finis, elle fait appel à une analyse multi-résolution pour adapter automatiquement la structure des données à la solution. Nous décrivons d'abord la méthode volumes finis utilisée. Celle-ci repose sur une formulation intégrale des équations aux dérivées partielles - ici paraboliques - et une discrétisation des flux dans l'espace direct. Le domaine de calcul est partitionné en cellules (ou mailles). La formulation volumes finis se ramène donc à un bilan sur chaque cellule: la variation d'une quantité intégrale donnée (masse, quantité de mouvement, énergie, espèce chimique) est la somme de la production interne de cette quantité et des flux qui traversent la cellule. Dans chaque cellule, la quantité stockée est la *moyenne de maille* de la quantité en question.

L'intégration temporelle repose sur une formulation explicite de type Runge-Kutta d'ordre deux (Eq. 2.5, p. 30) ou trois (Eq. 2.6, p. 30). La discrétisation spatiale des flux fait appel à un schéma centré d'ordre deux pour les flux diffusifs, décentré d'ordre

deux de type ENO (*Essentally Non-Oscillatory*) pour les flux convectifs. La formulation mono-dimensionnelle du schéma global est donnée par (Eq. 2.10, p. 31).

La multi-résolution consiste à représenter l'ensemble des données exprimées sur un maillage fin régulier comme les données sur un maillage grossier et l'ensemble des erreurs de prédiction entre un niveau de maillage et le niveau directement plus fin. En particulier, dans les zones où la solution est régulière, ces erreurs sont faibles. Lorsqu'elles sont inférieures à une certaine tolérance, elles sont considérées comme nulles et supprimées de la mémoire. Toutefois, les données nécessitent d'être organisées d'une façon particulière pour qu'on puisse y accéder facilement. Pour ce genre de problème, on fait appel en général à une structure de données en *arbre gradué* (Fig. 2.1, p. 33). Dans la terminologie des ondelettes, cette structure correspond à l'*approximation adaptative*. Cela signifie qu'aucun "trou" n'est admis à l'intérieur de la structure d'arbre, même si l'erreur de prédiction dans cette cellule est inférieure à la tolérance. Pour passer des données du niveau l au niveau $l-1$, on utilise l'opérateur de *projection* (ou restriction) (Fig. 2.2, p. 35). Cet opérateur est exact et unique. Dans l'autre direction, on fait appel à un opérateur de *prédiction* (ou prolongation) (Fig. 2.3, p. 36), qui estime de façon approchée la valeur du niveau $l+1$ à partir des valeurs du niveau l. Il existe une infinité d'opérateurs de prédiction. Cependant, cet opérateur doit être *consistant* avec la projection. De plus, pour qu'il soit utilisable dans une structure d'arbre gradué, il doit être *local*, c'est-à-dire qu'il doit faire appel à la cellule-parent et, au plus, ses n premiers voisins dans toutes les directions. Dans notre cas, chaque cellule contient une *moyenne de maille*. L'opérateur de projection considère donc que la moyenne de maille de la cellule-parent est simplement la moyenne des moyennes de maille des cellules-enfants. L'opérateur de prédiction, de son côté, fait une interpolation polynômiale à partir des valeurs moyennes du parent et de ses premiers voisins, comme il est proposé dans la multi-résolution de Harten [54]. Afin de ne pas perdre de l'information ou en créer artificiellement, on calcule le *détail*, différence entre la valeur exacte et la valeur prédite. Ce détail est en fait l'erreur de prédiction définie précedemment. Comme la somme de tous les détails est nulle par définition, ceux-ci sont redondants. Ainsi, pour un parent ayant n enfants, la connaissance des moyennes de maille des n enfants est équivalente à la connaissance de la moyenne de maille du parent et $n-1$ détails. L'opération transformant les valeurs des n enfants en la valeur du parent et les $n-1$ détails, répetée du niveau le plus bas au niveau le plus haut, est appelée la *transformée multi-résolution* [54]. Cette transformation est en fait une *transformation en ondelettes* [27].

La méthode numérique globale consiste donc à créer un arbre gradué correspondant à la condition initiale, puis y ajouter une zone de sécurité d'un niveau supplémentaire pour prévoir l'évolution future de la solution. Ensuite, à chaque pas de temps, on calcule l'évolution temporelle de la solution par le schéma volumes finis ; puis, on fait une transformée multi-résolution pour calculer les détails; ensuite, on élimine les cellules dont les détails sont inférieurs à la tolérance, en respectant la structure d'arbre gradué; enfin, on ajoute une zone de sécurité pour prévoir l'évolution future de la solution. Afin de s'assurer que le calcul des flux numériques est bien conservatif, c'est-à-dire que les flux sortants d'une cellule sont égaux aux flux rentrants dans ses voisines, ce qui n'est pas garanti quand deux cellules voisines sont de niveau différent, on calcule toujours les flux sur le niveau supérieur

(Fig. 2.5, p. 39). Le flux rentrant dans la cellule de niveau inférieur est fixé comme la somme des flux sortants du niveau supérieur. Un autre problème concerne l'estimation de l'erreur. Pour que la méthode soit précise, il faut que l'erreur due à la multi-résolution, appelée *erreur de perturbation* soit du même ordre de grandeur que l'*erreur de discrétisation* du schéma volumes finis. En s'inspirant du résultat obtenu pour le cas hyperbolique [31], on trouve pour l'équation linéaire de convection-diffusion la tolérance qu'il faut fixer en fonction du nombre d'échelles pour garantir que les deux erreurs précitées soient du même ordre (Eq. 2.33, p. 41). Ce résultat sera validé par le calcul dans le chapitre suivant. Enfin, la dernière section du chapitre présente l'algorithme original que nous avons utilisé pour le calcul. Le diagramme de cet algorithme est présenté dans la figure 2.6 (p. 42). La complexité de l'algorithme est au plus $O(N \log N)$, N désignant le nombre de degrés de liberté, mais il évite d'utiliser des tables de hachage, qui peuvent prendre beaucoup de place mémoire, en particulier pour des calculs à petite échelle en trois dimensions.

*
* *

Le chapitre 3 concerne la validation numérique. Nous résolvons numériquement à l'aide de la méthode multi-résolution adaptative des équations aux dérivées partielles paraboliques de référence - convection-diffusion, Burgers diffusif - pour lesquelles on connaît une solution analytique. Nous comparons les performances en termes de temps de calcul (ou temps CPU) et de place mémoire à celles obtenues avec le même schéma volumes finis sur la grille régulière la plus fine. Nous comparons également les erreurs $\mathcal{L}^1$ et $\mathcal{L}^\infty$ par rapport à la solution analytique à celles obtenues par la méthode volumes finis.

Nous nous intéressons d'abord à l'equation linéaire de convection-diffusion en dimension un, dans sa forme adimensionnée (Eq. 3.2, p. 50). Le principal paramètre de contrôle est le nombre de Péclet Pe. La solution initiale est discontinue et les conditions aux limites sont de type Dirichlet. Nous effectuons des calculs pour $Pe = 1000$ avec différentes valeurs du nombre maximal de niveaux L et de la tolérance ϵ. Nous obtenons que, pour $L > 7$, la méthode adaptative est plus rentable à la fois en temps CPU et en mémoire que la méthode volumes finis sur grille fine. Cependant, pour des grandes valeurs de la tolérance et pour des grandes échelles, le calcul perd en précision par rapport à la méthode non-adaptative. Ceci est dû à l'accumulation d'erreurs de perturbation, comme il a été explique au chapitre précédent. Nous effectuons ensuite le même calcul avec la relation théorique (2.33), présentée au chapitre précédent, qui définit la tolérance en fonction du nombre d'échelles. Cette fois-ci, nous montrons que le calcul est également plus efficace par la méthode adaptative, mais qu'en plus *l'ordre de précision* de l'erreur est préservé. Toutefois, l'erreur est plus grande que celle du calcul volumes finis sur grille fine, mais ceci s'observe également lorsque l'on travaille avec un maillage irrégulier [41]. Nous effectuons ensuite les mêmes calculs à $Pe = 10000$ pour vérifier que la relation théorique (2.33), qui dépend de Pe, est aussi valable pour d'autres valeurs du nombre de Peclet. Nous montrons que l'ordre de précision de l'erreur est également préservé, tandis que les performances

relatives sont accrues. Ceci est dû au fait que la diffusivité est moins grande que pour $Pe = 1000$. En effet, dans ce cas, la discontinuité initiale est moins étalée au cours du calcul. Il faut donc moins de points à petite échelle que pour $Pe = 1000$. Enfin, nous vérifions que la complexité de l'algorithme utilisé est bien $O(N \log N)$.

Nous vérifions également la performance et la précision de l'algorithme pour l'équation non-linéaire de Burgers diffusif en dimension un. En particulier, nous montrons que la relation théorique (2.33) avec le nombre de Reynolds Re comme paramètre de contrôle permet également d'accroître la performance par rapport au calcul volumes finis tout en maintenant l'ordre de précision de l'erreur. Nous terminons le chapitre par une validation en dimensions deux et trois pour l'équation de convection-diffusion. La condition initiale est une gaussienne et les conditions aux limites sont de type Neuman. La gaussienne reste suffisament loin des parois pour que l'on puisse comparer avec la solution analytique dans un domaine infini. On montre également que la performance est supérieure à celle du schéma volumes finis, tout en garantissant une erreur du même ordre.

*
* *

Le chapitre 4 concerne l'application de la méthode aux instabilités thermo-diffusives de flamme. Dans un premier temps, nous simulons des flammes planes stationnaires, d'abord sans rayonnement, puis avec rayonnement. Nous comparons les résultats avec ceux obtenus par la méthode volumes finis sur grille fine. Etant donné qu'il n'existe pas de solution analytique, nous comparons la vitesse de flamme obtenue pour les deux méthodes. Nous montrons, à une échelle fixée, que plus la tolérance est petite, plus le calcul est précis, et moins il est performant. Cependant, pour des valeurs de la tolérance de l'ordre de 10^{-2}, nous pouvons considérer le calcul comme suffisament précis. Nous comparons ensuite la solution obtenue pour differentes valeurs de Le et Ze à une solution asymptotique. Nous testons enfin la propagation d'une flamme plane, pour vérifier que la structure de données suit bien la solution, comme c'était le cas pour les équations de convection- diffusion et Burgers diffusif dans le chapitre précédent.

Nous nous intéressons ensuite aux flammes planes pulsantes. Dans un premier temps, nous décrivons le comportement d'une flamme plane pulsante pour $Le = 2$ et $Ze = 17.5$ et montrons l'évolution temporelle des profils de température et de taux de réaction. Nous observons que le taux de réaction croît jusqu'à ce que la temperature dans la zone de réaction dépasse la température des gaz brûlés. Ensuite, du fait que la conduction de chaleur soit dirigée de la zone de réaction vers les deux zones de pré-chauffage et des gaz brûlés, la température diminue dans la zone de réaction et, avec elle, le taux de réaction décroît, jusqu'à atteindre un minimum. Puis, lorsque la température dans la zone de réaction est inférieure à celle des gaz brûlés, le taux de réaction repart à la hausse. L'effet de pulsation est donc dû aux fortes variations du taux de réaction, très sensible lui-même aux variations de température. La vitesse de flamme étant proportionnelle à l'intégrale du taux de réaction, celle-ci varie avec lui, à la même fréquence. Nous nous intéressons ensuite

aux divers comportements de la vitesse de flamme en fonction des nombres de Lewis et Zeldovich. Nous distinguons clairement cinq états: d'abord, le cas *stable* (Fig. 4.8, côté gauche, p. 81), lorsque les pulsations s'amortissent au cours du temps; ensuite, le cas *périodique* (Fig. 4.8, côté droit, p. 81), lorsque la fréquence et l'amplitude des pulsations est constante, en général après une période de transition; ensuite, le cas *périodique où plusieurs fréquences existent* (Fig. 4.9, côté gauche, p. 81); ensuite, le cas *apériodique* (Fig. 4.9, côté droit, p. 81); enfin, le cas *instable*, lorsque la vitesse de flamme semble tendre vers l'infini. Ce dernier cas est très difficile à estimer du point de vue numérique, car il conduit toujours à une instabilité numérique, quel que soit le pas de temps utilisé. On ne peut donc qu'estimer que, lorsque la vitesse de flamme croît de façon monotone et qu'elle atteint des grandes valeurs, alors elle tend vers l'infini.

Nous traçons ensuite sur un diagramme $Le - Ze$ la limite entre les états stable et pulsant. Ce résultat est comparé au résultat théorique de Joulin-Clavin pour $Ze >> 1$ [60] et aux calculs numériques de Rogg par une méthode non-adaptative [77] (Fig. 4.12, p. 84). Nous montrons que nos calculs sont conformes au résultat théorique pour les grandes valeurs de Ze, ce qui n'était pas le cas dans [77]. En effet, plus Ze est grand, plus un maillage fin est nécessaire. De plus, lorsque l'on utilise un schéma explicite, plus le maillage est fin, plus le pas de temps doit être petit. Pour $Ze > 40$, un calcul non-adaptatif devient soit inexact, soit trop coûteux. La méthode multi-résolution adaptative apparaît donc comme une bonne solution pour calcul ce genre de problème à un coût raisonnable. Nous avons également étendu le diagramme aux grandes valeurs de Le, ce qui n'avait pas été fait auparavant. Pour $10 \leq Ze < 15$, on remarque que, aux grandes valeurs de Le, la flamme redevient stable. Ceci est du au fait que, dans cette zone de grands Le et de Ze modérés, les pertes de chaleur dans la zone de réaction compensent la production de chaleur due à la réaction chimique. Nous étudions enfin l'amplitude des pulsations dans la zone $10 \leq Ze \leq 15$. On remarque que, lorsque Le augmente, l'amplitude augmente, atteint un maximum, puis redescend. Le maximum de cette amplitude augmente avec Ze. Nous proposons l'interprétation suivante à ce phénomène: lorsque Le est petit, la chute d'enthalpie dans la zone de réaction et son augmentation dans la zone de pré-chauffage sont trop faibles pour engendrer des pulsations régulières. On obtient donc un amortissement des pulsations. Ensuite, pour des nombres de Lewis plus élevés, on observe des pulsations, car les pertes de chaleur dus à la conduction dans la zone de réaction ne compensent pas la production de chaleur due à la réaction. Enfin, pour les grandes valeurs de Le, la conduction de chaleur compense la production, et la flamme redevient stable.

La partie suivante concerne les ballons de flamme. Cette fois-ci, le front de flamme n'est plus plan, mais circulaire en 2D et sphérique en 3D. A l'intérieur du ballon, les gaz brûlés sont majoritaires. Le front correspond à la zone de réaction, puis suit une bande circulaire correspondant à la zone de préchauffage. Le reste du domaine est rempli de gaz frais (Fig. 4.15, p. 88). Les premiers calculs concernent la simulation numérique de ballons de flamme en dimensions deux et trois, lorsque le ballon est suffisament loin des parois pour négliger leur influence. Ces cas-tests ont été initialement effectués à l'aide de méthodes pseudo-spectrales Fourier ou adaptatives de type ondelette-vaguelette, avec des conditions aux limites périodiques [14, 47]. On obtient des résultats analogues à ceux

obtenus par les autres méthodes numériques. En particulier, pour différentes valeurs de Le et du coefficient de radiation γ, on observe bien les différent scénarios d'évolution d'un ballon de flamme initialement étiré: croissance sphérique (amortissement de l'étirement) pour $Le = 1$ et $\gamma = 0$, éclatement du ballon en plusieurs morceaux pour $Le = 0.3$ et γ modéré, extinction du ballon de flamme pour $Le = 0.3$ lorsque la radiation est trop forte.

Nous nous interessons ensuite à l'interaction d'une flamme avec une paroi adiabatique. En effet, les chambres de combustion sont de taille finie et, lorsqu'un ballon de flamme croît, il finit par toucher la paroi. Pour cette étude, nous commençons par considérer un front de flamme plan, ce qui nous ramène à un problème monodimensionnel. A l'instant initial, le front est décentré et se propage vers la droite. Nous remarquons différents comportements lorsque le front de flamme atteint la paroi adiabatique. Lorsque $Le < 1$, le taux de réaction baisse progressivement lorsque le front s'approche de la paroi, jusqu'à l'extinction. Pour $Le = 1$, le taux de réaction est à peu près constant, puis s'éteint lorsque le front touche la paroi. En revanche, pour $Le > 1$, le taux de réaction augmente, puis devient nul au contact de la paroi (Fig. 4.24, p. 101). L'interprétation suivante peut être avancée: lorsque $Le < 1$, la diffusion des réactants excède la conduction de la chaleur. Or, plus on s'approche de la paroi, moins il y a de réactants disponibles. Le taux de réaction décroît donc et la vitesse de flamme ralentit. En revanche, pour $Le > 1$, le phénomène d'allumage accéléré décrit dans la section concernant les flammes pulsantes favorise la croissance du taux de réaction et, avec lui, de la vitesse de flamme. Le taux de réaction augmente donc, jusqu'à ce que le front touche la paroi. Comme il ne reste plus alors de gaz frais, la réaction s'arrête brutalement. Le cas bi-dimensionnel pour des ballons de flamme confirme les résultats du cas monodimensionnel lorsque l'on fait une coupe dans la direction perpendiculaire à la paroi qui interagit avec le ballon de flamme. De plus, on observe un phénomène analogue à la *capillarité* lorsqu'une goutte de fluide interagit avec une paroi. Suivant la valeur de Le, le ballon de flamme se reserre ou s'étale lorsqu'il touche la paroi, à la manière d'une goutte de fluide lorsqu'elle touche une paroi solide (Figs. 4.26-4.28, pp. 104-106). L'explication suivante peut être avancée: pour $Le < 1$, le flux de réctants au contact du front de flamme est élevé, sauf précisément près de la paroi, où il est en déficit. Ainsi, près de la paroi, le taux de réaction décroît et la progression du front ralentit. A l'inverse, pour $Le > 1$, l'allumage de la flamme est accéléré dans la région proche de la paroi, comme il a été vu dans le cas mono-dimensionnel. Ensuite, quand le ballon a touché la paroi, cette accélération de l'allumage est visible à l'intersection entre la paroi et le front, ce qui explique que la partie du front près de la paroi avance plus rapidement. Le ballon de flamme s'étale donc au contact de la paroi lorsque $Le < 1$, alors qu'il se rétracte pour $Le < 1$. Des calculs similaires ont été effectués en trois dimensions, mais cet effet est plus difficile à visualiser.

La dernière partie concerne l'interaction d'un ballon de flamme avec un tourbillon. Ceci est un premier calcul et se présente plutôt comme une introduction à une future étude sur les ballons de flamme dans un fluide en mouvement. Ici, le tourbillon est une solution analytique des équations de Navier-Stokes incompressible. On peut donc encore utiliser le modèle thermo-diffusif, mais il se ramène cette fois-ci à un système de deux équations de convection-diffusion-réaction. Le tourbillon est au centre du domaine de calcul et le ballon de flamme est décentré. On observe la déformation du ballon de flamme due au tourbillon.

De plus, comme le nombre de Lewis à été choisi inférieur à l'unité, cette perturbation est amplifiée. Au contact de la paroi, le ballon se ressère, comme il a été expliqué dans la section précedente (Fig. 4.35, p. 115). Lorsqu'on compare les intégrales du taux de réaction avec et sans tourbillon, on remarque que, dans un premier temps, le tourbillon favorise la réaction chimique, mais après un temps suffisamment long, il la pénalise.

*
* *

Ainsi, dans cette thèse, nous avons développé un nouvel algorithme multi-résolution adaptatif en espace pour accélérer la résolution en volumes finis des équations aux dérivées partielles paraboliques non-linéaires en géométrie cartésienne et en dimension un, deux et trois. Nous avons démontré son efficacité et sa précision par rapport à la méthode volumes finis sur grille fine régulière par plusieurs cas-tests d'EDP paraboliques linéaires et non-linéaires de référence.

Le principe de la méthode repose sur une discrétisation spatiale de type volumes finis sur un maillage cartésien, une intégration temporelle explicite, toutes deux d'ordre au moins deux. Une analyse multi-résolution discrète permet de réduire le nombre de points de calculs en supprimant de la mémoire des cellules non-significatives tout en maintenant la précision d'ordre deux du schéma. Nous avons également présenté une stratégie d'adaptation basée sur la représentation en multi-résolution en ajoutant ou en supprimant des cellules voisines aux cellules existantes, afin de prévoir l'évolution future de la solution. L'évaluation des flux aux interfaces de cellules de niveaux différents est faite de façon conservative, sans pour autant augmenter significativement le coût du calcul. Une rélation théorique entre la tolérance et le nombre maximal d'échelles disponible permet, pour l'équation linéaire de convection-diffusion, de maintenir l'ordre de précision du schéma volumes finis tout en réduisant significativement le coût du calcul. Ce résultat est vérifié numériquement. Nous avons présenté un algorithme récursif original basé sur une structure des données en arbre gradué. L'accès à un élément de l'arbre se fait à l'aide d'un algorithme récursif. Bien que ce concept soit un peu plus complexe, c'est-à-dire une complexité $O(N \log N)$ au lieu de $O(N)$, N étant le nombre de degrés de liberté, ce choix nous permet d'éviter d'utiliser des tables de hachage, qui requièrent beaucoup de mémoire, en particulier pour des calculs tri-dimensionnels.

La précision de l'algorithme à été validée par la résolution des équations paraboliques de convection-diffusion et de Burgers diffusif. Nous avons comparé la solution obtenue avec la solution exacte et étudié l'erreur en fonction du nombre maximal d'échelles et de la tolérance. La relation théorique entre le nombre maximal d'échelles et la tolérance permettant de garantir la précision d'ordre deux du schéma numérique a été confirmée par nos calculs.

Pour démontrer l'efficacité de l'algorithme, nous avons comparé la performance en termes de temps CPU et de place mémoire à celle de la méthode volumes finis sur la grille régulière de l'échelle la plus fine avec une structure de données statique. Nous avons

montré que la performance relative augmente avec le nombre d'échelles et tend vers un minimum qui dépend du cas-test. De plus, le gain augmente significativement avec la dimension du problème.

Finalement, nous avons présenté plusieurs applications à des problèmes de combustion dans l'approximation thermo-diffusive. En particulier, nous avons amélioré le diagramme de stabilité des flammes planes pulsantes. Pour les grandes valeurs de l'énergie d'activation, nos résultats confirment le résultat théorique obtenu par un développement asymptotique [60]. Nous avons également montré que des flammes planes stables existent aux grands nombres de Lewis. Concernant les ballons de flamme, nous avons ensuite montré qu'un ballon qui intéragit avec une paroi adiabatique présente des analogies avec la capillarité en mécanique des fluides. Enfin, nous avons présenté un premier calcul en multirésolution adaptative d'un ballon de flamme dans un fluide en mouvement.

Actuellement, nous préparons la parallélisation de l'algorithme multi-résolution adaptatif sur un *cluster* de PC afin de réaliser des calculs tridimensionnels avec plus d'échelles. Pour ce faire, la structure de données est organisée en "forêt", c'est-à-dire en un ensemble d'arbres, chacun travaillant sur un processeur. Une étude future concerne l'extension de ces schémas au système des équations de Navier-Stokes réactives, afin de prendre en compte les effets hydrodynamiques dans les problèmes de combustion. Nous souhaitons aussi utiliser l'approche de la simulation des tourbillons cohérents (CVS ou *Coherent Vortex Simulation*) [42] pour modéliser les écoulements de fluide turbulents et réactifs sur des maillages adaptatifs. Ensuite, pour effectuer des simulations dans des géométries industrielles, l'extension de cette méthode aux géometries complexes s'impose. Celle-ci a été effectuée en deux dimensions avec des maillages structurés [16] et non-structurés triangulaires [31], mais uniquement pour des problèmes hyperboliques. Enfin, une approche pourrait être utilisée pour réduire le temps de calcul: l'adaptativité en temps. L'utilisation d'un pas de temps par échelle spatiale a été testée avec succès dans les méthodes adaptatives de type AMR [74]. Ici, nous souhaiterions utiliser un pas de temps qui évolue avec l'échelle et également au cours du temps.

Contents

Introduction

Since the beginning of the industrial revolution, energy conversion by way of combustion has been playing a major role. Nowadays, it still covers the large majority of our energetic needs. However, the reservoirs of oil and natural gas on Earth are finite and strongly decreasing, since people consume more and more energy. Moreover, since the 1970s, the public opinion has become aware of environmental damages due to combustion. These phenomena led the industry to conceive low-pollution and efficient combustion engines for automobiles, airplanes, spacecrafts, etc., which all require a profound understanding of lean flames. Up to now, the physical and chemical mechanisms involved in the combustion of lean mixtures are not yet completely understood. It still constitutes a subject of active research, theoretically and experimentally.

Since the 1980s, another tool completes theoretical and experimental investigations: numerical simulation. The main advantage of this tool is to be able to perform a large number of "numerical experiments" with different parameter values. It also enables to have access to all quantities everywhere, even to those which cannot be measured experimentally. The main drawback of numerical simulation is that is relies on a mathematical modelling of the problem. Therefore the solution is only valid in the frame of the chosen hypotheses. Moreover, for a model closer to reality, we have to solve a more complex system of equations, which usually requires more CPU time and memory. When the problem exhibits too many degrees of freedom, it is necessary to model again the equations. Among all the methods developed for numerical simulation, a commonly used approach consists in computing an approximate solution of the equations modelling the physical-chemical problem on an ensemble of grid points representing a discrete partition of the space domain. In our case, the system of equations modelling the propagation of premixed flames is a set of parabolic partial differential equations (PDEs).

From the numerical point of view, this system of PDEs constitutes a stiff problem, since it involves a large number of spatial and temporal scales. Moreover, as small scales in space are only needed locally, i.e. in the thin chemical reaction zone, the solution may be over-resolved in large subsets of the computational domain when using equidistant fine grids. Given that computations become more expensive when using finer grids, three-dimensional simulations on very fine grids still remain unaffordable, even with supercomputers. This motivates the introduction of some kind of adaptivity.

A suitable tool to define adaptive discretization schemes are multiresolution techniques which allow an efficient data representation with an accurate estimation of the local ap-

proximation error, together with a dynamic grid adaption strategy for evolution problems. In the past different adaptive methods have been introduced to improve the computational efficiency and to reduce the memory requirement of the algorithms for solving large scale problems. Historically, adaptive grid methods like Multi-Level Adaptive Techniques (MLAT) (Brandt [17]) or Adaptive Mesh Refinement (AMR) methods (Berger *et al* [9, 8], Quirk [74], Bell *et al* [7]) were the first to achieve this goal, using a set of locally refined grids where steep gradients or high truncation errors are found. Adaptive mesh refinement methods were also applied to combustion front tracking (see e.g. Haldenwang and Pignol [51]). However, the data compression rate is high where the solution is almost constant, but remains low where the solution is smooth.

More recently, adaptive wavelet methods to solve PDEs have been developed. For an overview and a classification of the different methods we refer e.g. to Dahmen [32], Cohen [27], Fröhlich and Schneider [45]. The motivation to use wavelet methods to construct numerical schemes is twofold. First, the scale-space representation of functions exhibiting e.g. steep gradients or boundary layers, i.e. functions whose Besov regularity is larger than its Sobolev regularity, is efficient using nonlinear approximation, i.e. by thresholding the wavelet coefficients (DeVore [40], Dahmen [32]). The result is that only few coefficients are necessary to represent a function for a given accuracy. Second, a large class of differential and integral operators have a sparse representation in a wavelet basis (Beylkin *et al* [10]) and can be preconditioned by simple rescaling (Jaffard [59], Dahmen and Kunoth [34]). For evolutionary problems, wavelet schemes offer the possibility to adapt the basis automatically in time by simply switching on wavelet coefficients in the neighborhood of the active ones. These properties led to the development of several adaptive wavelet schemes, e.g. for 1D viscous Burgers equations (Liandrat and Tchamitchian [64], Maday *et al* [65, 66]), for thermo-diffusive flame computations (Fröhlich and Schneider [43, 45], Bockhorn *et al* [14]), for 2D Stokes equations (Urban [91]) and 2D Navier-Stokes equations (Charton and Perrier [20], Fröhlich and Schneider [44], Schneider *et al* [88], Schneider and Farge [87]). The above schemes mainly use wavelets as trial and/or test functions in Petrov-Galerkin schemes.

The current approach is somehow different and can be seen in the spirit of Harten's pioneering work [54, 55]. Starting point is a finite volume scheme for hyperbolic conservation laws on a regular grid. Subsequently, a discrete multiresolution analysis is used to avoid expensive flux computations in smooth regions, first without reducing memory requirements, e.g for 1D hyperbolic conservation laws (Harten [54]), 1D conservation laws with viscosity (Bihari [11]), 2D hyperbolic conservations laws (Bihari and Harten [12]), 2D compressible Euler equations (Chiavassa and Donat [21]), 2D hyperbolic conservation laws with curvilinear patches (Dahmen *et al* [33]) and unstructured meshes (Abgrall and Harten [2], Cohen *et al* [30]). A fully adaptive version, still in the context of hyperbolic conservation laws, has been developed to reduce also memory requirements (Gottschlich-Müller and Müller [48], Cohen *et al* [31]). The previous work was extended to compressible Navier-Stokes equations for convection-dominated problems, which leads to a quasi-hyperbolic problem (Bramkamp *et al* [16]). Therewith the solution is represented and computed on a dynamically evolving automatically adapted grid. Different strategies have been proposed

to evaluate the flux without requiring a full knowledge of fine grid cell-average values. For an overview on adaptive multiresolution techniques for hyperbolic conservation laws, we refer to Müller [70]. For more details on similarities and differences between adaptive mesh refinement and multiresolution approaches, we refer the reader to Cohen [28].

In this thesis, we develop a new adaptive multiresolution algorithm for solving parabolic PDEs in one, two and three space dimensions with different types of boundary conditions. With respect to previous work, we extend the algorithms developed for hyperbolic equations [31] to the case of parabolic ones, together with the corresponding error analysis. As we are concerned with problems arising from physical-chemical context, conservation of physical quantities - e.g. global mass - in flux computations is of special interest. In the case of adaptive flux evaluation, ingoing and outgoing fluxes, both approximated at interfaces from cell-average values of different levels, are not necessarily balanced. Therefore we devise a new formulation for adaptive flux computation at the interfaces between two different levels being strictly conservative.

The practical application concerns the simulation of premixed flames in the thermodiffusive approximation. This simplifying hypothesis is valid for flames having small gas expansion. As one of the applications we study the behavior of premixed flames for which heat conduction exceeds the diffusion of chemical reactants. A linear stability analysis for large values of the energy activation shows that, depending on some physical parameters, spinning and pulsating flames can appear (Joulin and Clavin [60], Clavin [25]). Pulsating planar flames have been experimentally observed and numerically simulated (Booty *et al* [15], Bayliss *et al* [6]). The limit between stable and pulsating flames has also been determined using numerical simulations (Rogg [77]). However, given that the computational cost becomes prohibitive for large values of the activation energy, this investigation is limited to restricted parameter ranges. The understanding and control of such behaviors is of great interest for industry, e.g. for combustion of fuel-rich mixtures or solids (see e.g. Buckmaster and Ludford [18]).

Another application deals with the numerical simulation of flame balls. Such structures appear in combustion chambers containing a quiescent, premixed lean gas mixture. In order to avoid the effects of buoyancy, which on Earth generates convection, strongly influencing the reaction, flame balls have been experimentally studied in micro-gravity (μg) conditions, in drop towers, aircrafts and even in the space shuttle [78]. Important experimental work on flame balls has been done by Ronney, who investigated flame balls in lean H_2-air mixtures [78]. Numerical simulations of flame balls far from the walls of the combustion chamber have been done using pseudo-spectral methods (Bockhorn *et al* [13], Gerlinger *et al* [47, 46]). These investigations show the existence of stable, i.e. non-growing, flame balls when radiation effects are taken into account. Adaptive computations using wavelet-vaguelette algorithms have also been performed to reduce CPU time and memory requirements (Bockhorn *et al* [14], Schneider [85]). As these methods require the use of periodic boundary conditions, interactions of flame balls with the walls of the combustion chamber cannot be simulated therewith. This motivates the use of adaptive multiresolution methods based on finite volumes for such problems.

In the present work, we apply the developed adaptive multiresolution algorithm to

study thermodiffusive flame instabilities. In particular, we extend the stability diagram of pulsating planar flames to large values of the activation energy and to the case where heat conduction largely exceeds the diffusion of reactants. Then we perform numerical simulations of flame balls far from the boundaries and compare our results to previous work [85, 14, 47, 46]. We also determine the different behaviors of a flame ball interacting with adiabatic walls. Finally, we present an adaptive computation of a flame ball in a moving fluid interacting with a vortex and show that the adaption strategy also works well in the presence of convective terms.

The document is organized as follows: in chapter 1, the governing equations used to model flame propagation in the thermodiffusive approximation are presented. This results in a system of non-linear parabolic partial differential equations. In chapter 2, the adaptive multiresolution method is described, including the finite volume schemes used, the multiresolution representation of data, and the 3D algorithm developed in the frame of this thesis. Chapter 3 is devoted to its numerical validation. The algorithm is tested for prototype linear and non-linear parabolic equations for which analytical solutions are known. Application to thermodiffusive flame instabilities is the subject of Chapter 4. Then, we conclude and present some perspectives for future work. Finally, in appendix A, we present some features of the wavelet theory that are useful to understand the adaptive multiresolution method, and, in appendix B, we give the coefficients of Harten's prediction operator in one, two and three space dimensions.

Chapter 1

Governing equations for thermodiffusive flames

Abstract. *This chapter presents the system of equations used to model flame propagation in the thermodiffusive approximation. Starting from the isobaric flame model and assuming the global density to be constant, hydrodynamics is decoupled from chemical reaction. This results in the thermodiffusive equations, which are a system of non-linear parabolic partial differential equations. Then we express this system in dimensionless form and discuss the large activation energy approximation. In the frame of this hypothesis, we describe the structure of steady planar flames and explain the flame propagation mechanism. An analytical solution is also given for the activation energy tending towards infinity. Then, when the flame structure is no more planar, different instabilities may appear. Here, we discuss the thermodiffusive instability and give the dispersion relation in the large activation energy approximation. Finally, we briefly describe two unstable states: cellular flames and pulsating flames.*

1.1 Introduction

Modelling combustion requires to take into account different phenomena, which are furthermore strongly interacting: the fluid flow, the mixing of the different species and the chemical reaction. In general, this results in a system of partial differential equations (PDE) which express the conservation of the main physical quantities: global mass, momentum, total energy and chemical species.

For a complete description of combustion models, we refer to textbooks and review articles [18, 62, 92, 93]. Here, we restrict ourselves to the combustion of a premixed gas in a laminar flow. The mixture is assumed to be a perfect gas and contains only two reactants and one product, the first reactant and the product being highly diluted in the second reactant. We also consider that the chemical reaction follows a one-step finite rate Arrhenius kinetics. Finally, gravity effects are neglected, in order to avoid perturbations due to buoyant convection.

The chapter is organized as follows: in section 1.2, the model of isobaric flames is pre-

sented. In the hypothesis of constant density, we deduce in section 1.3 the thermodiffusive equations. Section 1.4 presents its dimensionless form, and section 1.5 the expression of the reaction rate in the large activation energy approximation. Then, section 1.6 is devoted to the description of steady planar flames. The chapter ends with the presentation of the thermodiffusive instability, including the description of cellular and pulsating flames.

1.2 Isobaric flame equations

In the present work, we restrict ourselves to the study of *deflagrations*, i.e. *flames*. They are characterized by a *strongly subsonic* fluid flow. Therefore the pressure variations can be ignored in the energy conservation equation. Moreover, kinetic energy and its conversion to thermal energy by way of viscous dissipation are assumed to be negligible. Following [92], the system of conservation equations which models the propagation of a flame writes

$$\begin{aligned}
\frac{\partial \rho}{\partial t} + \vec{\nabla} \cdot (\rho \vec{v}) &= 0 \\
\rho \frac{\partial v_i}{\partial t} + \rho \vec{v} \cdot \vec{\nabla} v_i &= -\frac{\partial p}{\partial x_i} + \sum_{j=1}^{3} \frac{\partial \tau_{i,j}}{\partial x_j}, \quad i = 1, 2, 3 \\
\rho C_p \frac{\partial T}{\partial t} + \rho C_p \, \vec{v} \cdot \vec{\nabla} T &= \vec{\nabla} \cdot \left(\lambda \vec{\nabla} T \right) + Q\omega - s \\
\rho \frac{\partial Y}{\partial t} + \rho \vec{v} \cdot \vec{\nabla} Y &= \vec{\nabla} \cdot \left(\rho D \vec{\nabla} Y \right) - \omega
\end{aligned} \tag{1.1}$$

where

- t denotes the time ;
- $\vec{x} = (x_1, x_2, x_3)$ the position in space ;
- $\vec{v} = (v_1, v_2, v_3)$ the velocity of the mixture ;
- T the temperature ;
- Y the partial mass of the limiting reactant ;
- $(\tau_{i,j}),\ i, j \in \{1, 2, 3\}$ the viscous strain tensor ;
- λ the thermal conductivity of the mixture ;
- D the mass diffusivity of the mixture ;
- Q the heat release due to chemical reaction ;
- s the heat loss due to radiation.

Following the Arrhenius law, the reaction rate ω verifies [92]

$$\omega = \rho Y B(T) \exp\left(-\frac{E}{RT}\right). \tag{1.2}$$

where $B(T)$ is an algebraic function of temperature and E denotes the *activation energy* of the reaction. Additionally, the global mixture is supposed to behave like a Newtonian fluid with the Stokes hypothesis, i.e.

$$\tau_{i,j} = -\frac{2}{3}\mu\left(\vec{\nabla}\cdot\vec{v}\right)\delta_{i,j} + \mu\left(\frac{\partial v_i}{\partial x_j} + \frac{\partial v_j}{\partial x_i}\right),$$

where μ denotes the dynamic viscosity of the mixture. Finally, the radiation is assumed to verify the black-body hypothesis and the corresponding heat loss follows the Stefan-Boltzmann law [92]

$$s = \frac{4\,\sigma_{SB}}{l_P}\left(T^4 - T_{ref}^4\right) \tag{1.3}$$

where σ_{SB} denotes the Stefan-Boltzmann constant, l_P the Planck length, and T_{ref} a reference temperature, further expressed (see Section 1.4). This hypothesis is valid for optically thin media, which is the case for gas-phase combustion [92].

Two simplifications can be introduced: the *transport coefficients* and the *density* are assumed to be *constant*. This hypothesis is valid for slowly propagating flames [14], which will always be the case in the present work. In the frame of this approximation, (1.1) becomes

$$\begin{aligned}
\vec{\nabla}\cdot\vec{v} &= 0 \\
\rho\frac{\partial v_i}{\partial t} + \rho\vec{v}\cdot\vec{\nabla}v_i &= -\frac{\partial p}{\partial x_i} + \mu\nabla^2 v_i\,, \quad i = 1,2,3 \\
\rho C_p\frac{\partial T}{\partial t} + \rho C_p\,\vec{v}\cdot\vec{\nabla}T &= \lambda\nabla^2 T + Q\omega - s \\
\rho\frac{\partial Y}{\partial t} + \rho\vec{v}\cdot\vec{\nabla}Y &= \rho D\nabla^2 Y - \omega
\end{aligned} \tag{1.4}$$

where ρ is a constant and ω verifies (1.2).

Thanks to this additional hypothesis, the chemical reaction has no more influence on the fluid flow. The interest of such an approximation is to enable to describe the flame structure, i.e. $T(\vec{x},t)$ and $Y(\vec{x},t)$, with the energy and species conservation equations only. The velocity field of the mixture $\vec{v}(\vec{x},t)$ is considered as given, and satisfies the Navier-Stokes equations for an incompressible flow. Moreover, when the fluid is initially at rest, we have $\vec{v}(\vec{x},t) = \vec{0}$.

1.3 The thermodiffusive model

Considering the velocity field of the mixture $\vec{v}(\vec{x},t)$ as given, the system (1.4) is [92]

$$\frac{\partial T}{\partial t} + \vec{v}\cdot\vec{\nabla}T = \kappa\nabla^2 T + \frac{Q}{\rho C_p}\omega - \frac{1}{\rho C_p}s \tag{1.5}$$

$$\frac{\partial Y}{\partial t} + \vec{v} \cdot \vec{\nabla} Y = D\nabla^2 Y - \frac{1}{\rho}\omega$$

where

$$\kappa = \frac{\lambda}{\rho C_p}.$$

Denoting $\mathbf{U} = (T, Y)^T$, the previous system can be written in the following form

$$\frac{\partial \mathbf{U}}{\partial t} + (\vec{v} \cdot \vec{\nabla})\, \mathbf{U} = \mathcal{M}\nabla^2 \mathbf{U} + S(\mathbf{U}), \tag{1.6}$$

where $\mathcal{M}$ is a 2×2 diagonal matrix and $S(\mathbf{U})$ is a non-linear function of $\mathbf{U}$. The following system of *thermodiffusive equations* is a system of *convection-diffusion-reaction* equations.

Finally, when the fluid is initially at rest, i.e. $\vec{v} = \vec{0}$, we have

$$\begin{aligned} \frac{\partial T}{\partial t} &= \kappa\nabla^2 T + \frac{Q}{\rho C_p}\omega - \frac{1}{\rho C_p}s \\ \frac{\partial Y}{\partial t} &= D\nabla^2 Y - \frac{1}{\rho}\omega \end{aligned} \tag{1.7}$$

The thermodiffusive equations now reduce to a system of *reaction-diffusion* equations, completed with suitable initial and boundary conditions. From a mathematical point of view, we have to deal with a system of *non-linear parabolic* partial differential equations, the non-linearity being in the source term.

1.4 Dimensionless equations

In order to show similarities between states having different parameter ranges, we write (1.5) and (1.7) in dimensionless form. Following [92], we introduce the temperature and partial mass of the fresh **u**nburnt mixture, respectively T_u and Y_u, and the ones of the **b**urnt mixture T_b and Y_b. The heat release due to chemical reaction can be expressed by

$$QY_u = C_p\,(T_b - T_u)$$

Since the limiting reactant and the burnt gas are assumed to be highly diluted in the second reactant, we have $Y_u = 1$ and $Y_b = 0$. Denoting by L a characteristic length scale (e.g. the size of the domain), we define the following characteristic scales

$$l_\star = L\ ,\quad t_\star = \frac{L^2}{\kappa}\ ,\quad v_\star = \frac{\kappa}{L}$$

The corresponding dimensionless variables are

$$\vec{v}_+ = \frac{\vec{v}}{v_\star}\ ,\quad \vec{x}_+ = \frac{\vec{x}}{l_\star}\ ,\quad t_+ = \frac{t}{t_\star}.$$

The dimensionless temperature T_+ is defined by

$$T_+ = \frac{T - T_u}{T_b - T_u}$$

Following the previous notations, the system of thermodiffusive equations (1.5) becomes [92]

$$\begin{aligned} \frac{\partial T_+}{\partial t_+} + \vec{v}_+ \cdot \vec{\nabla}_+ T_+ &= \nabla_+^2 T_+ + \frac{L^2}{\rho\kappa}\omega - \frac{L^2}{\rho Q \kappa} s \\ \frac{\partial Y}{\partial t_+} + \vec{v}_+ \cdot \vec{\nabla}_+ Y &= \frac{D}{\kappa}\nabla_+^2 Y - \frac{L^2}{\rho\kappa}\omega \end{aligned} \tag{1.8}$$

Introducing the *Lewis* number

$$Le = \frac{\kappa}{D}$$

and the dimensionless variables

$$\omega_+ = \frac{\omega}{\omega_\star} = \frac{L^2}{\rho\kappa}\omega\,, \quad s_+ = \frac{s}{s_\star} = \frac{L^2}{\rho Q \kappa} s$$

we get the following system

$$\begin{aligned} \frac{\partial T_+}{\partial t_+} + \vec{v}_+ \cdot \vec{\nabla}_+ T_+ &= \nabla_+^2 T_+ + \omega_+ - s_+ \\ \frac{\partial Y}{\partial t_+} + \vec{v}_+ \cdot \vec{\nabla}_+ Y &= \frac{1}{Le}\nabla_+^2 Y - \omega_+ \end{aligned} \tag{1.9}$$

The same way, (1.7) becomes

$$\begin{aligned} \frac{\partial T_+}{\partial t_+} &= \nabla_+^2 T_+ + \omega_+ - s_+ \\ \frac{\partial Y}{\partial t_+} &= \frac{1}{Le}\nabla_+^2 Y - \omega_+ \end{aligned} \tag{1.10}$$

According to (1.3), the heat loss due to radiation s now verifies

$$s = \frac{4\,\sigma_{SB}}{l_P}\left(T^4 - T_u^4\right).$$

Its dimensionless form s_+ can therefore be written in function of the dimensionless temperature T_+, following

$$s_+ = \gamma\left[\left(T_+ + \frac{1}{\alpha} - 1\right)^4 - \left(\frac{1}{\alpha} - 1\right)^4\right] \tag{1.11}$$

where

$$\gamma = \frac{4\ \sigma_{SB}\ L^2}{l_P\ Q\ \rho\ \kappa}(T_b - T_u)^4$$

The dimensionless reaction rate ω_+ can be written in a simple form in the hypothesis of the large activation energy. This will be the subject of the next section.

One more simplification occurs in the particular case where radiative effects are assumed to be negligible and where heat and mass diffusivities are equal, i.e $Le = 1$. In this case, we have $T_+ + Y = 1$ and the previous system can be reduced to a single reaction-diffusion equation. Omitting the subscript $+$, one gets

$$\frac{\partial u}{\partial t} = \nabla^2 u + \omega(u) \tag{1.12}$$

where $T = u$, $Y = 1-u$, and $\omega(u)$ is a non-linear function of u. This is the most elementary PDE used to describe a combustion phenomenon.

1.5 Large activation energy approximation

This hypothesis was initially proposed by Zeldovich and Frank-Kamenetskii in their pioneering work [94, 93]. Using the fact that the Arrhenius term strongly depends on the temperature, the reaction rate tends to a δ-peak in the limit of large values of the activation energy.

Let us denote by α the temperature ratio

$$\alpha = \frac{T_b - T_u}{T_b}\ ,\ 0 < \alpha < 1\ .$$

The dimensionless activation energy, also called *Zeldovich number*, is defined by

$$Ze = \alpha\frac{E}{R\,T_b} = \frac{E}{R\,T_b}\frac{T_b - T_u}{T_b}$$

Thus, the Arrhenius term in its dimensionless form becomes

$$\frac{\exp\left(-\frac{E}{RT}\right)}{\exp\left(-\frac{E}{RT_b}\right)} = \exp\left[-\frac{Ze(1-T_+)}{1-\alpha(1-T_+)}\right]\ . \tag{1.13}$$

In the limit $Ze \to \infty$, Eq. (1.13) shows that the dimensionless Arrhenius term, and with it the dimensionless reaction rate ω_+, is extremely small, i.e. $O(e^{-Ze})$, and thus negligible everywhere except very close to the temperature of the burnt gas T_b, where $Ze(1-T_+) = O(1)$, i.e. $1 - T_+ = O(Ze^{-1})$ (Fig. 1.1). Thus, the chemical reaction is localized in a zone which is thin compared to the flame thickness, the flame being understood as the region where the partial masses of the chemical species strongly vary.

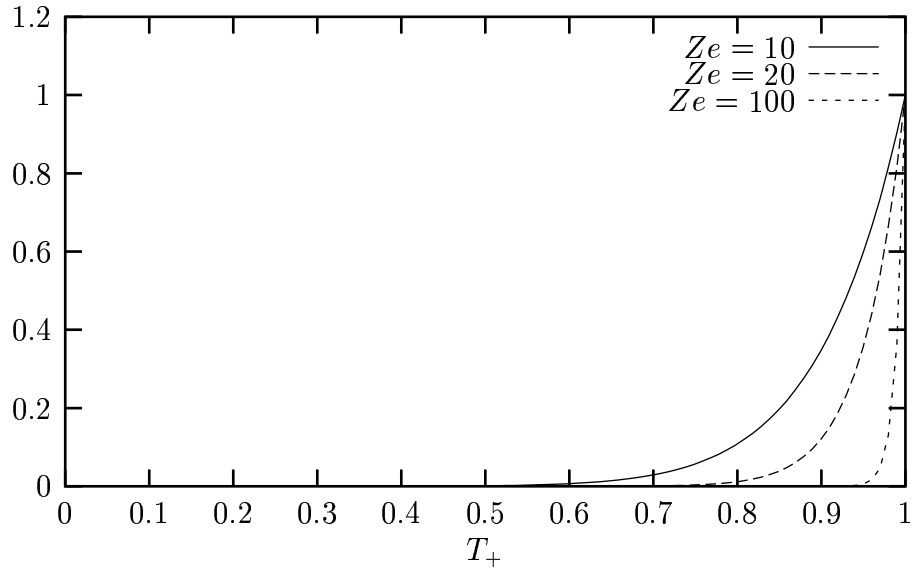

Figure 1.1: Dimensionless Arrhenius term in function of T_+ for different Ze and for $\alpha = 0.5$. Here this term is extremely small everywhere, except in the region which approximately corresponds to $1 - 5Ze^{-1} \leq T_+ \leq 1$.

Moreover, the dimensionless reaction rate ω_+ can be written in the following form

$$\omega_+ = \frac{L^2}{\kappa}\, Y\, B(T)\, \exp\left(-\frac{E}{RT}\right) = \mathcal{A}\, Ze^2\, Y\, \exp\left[-\frac{Ze(1-T_+)}{1-\alpha(1-T_+)}\right],$$

where

$$\mathcal{A} = \frac{L^2}{\kappa\, Ze^2} B(T)\, \exp\left(-\frac{E}{RT_b}\right).$$

Following [19], $\mathcal{A}$ can be developed asymptotically in powers of (Ze^{-1}). For $Ze >> 1$, one gets

$$\mathcal{A} = \frac{1}{2\, Le} + O(Ze^{-1}).$$

Therefore, in the large activation energy approximation, the dimensionless reaction rate ω_+ becomes

$$\omega_+ = \frac{Ze^2}{2\, Le}\, Y\, \exp\left[-\frac{Ze(1-T_+)}{1-\alpha(1-T_+)}\right]. \tag{1.14}$$

1.6 Steady planar flames

Let us consider an experiment in which a flame propagates at velocity $\vec{v}$ in a premixed gas contained in an infinitely long cylindrical tube. When the fresh mixture is advected at velocity $-\vec{v}$, we can observe a *steady planar flame* [25, 62]. This phenomenon will be

treated in this section. It enables us to understand the mechanism of flame propagation. For reasons of simplicity, we first neglect the radiation effects.

To get the *steady planar solution* of (1.9), we consider that the variables only depend on the coordinate x. The continuity equation gives

$$\frac{dv_x}{dx} = 0, \text{ i.e. } v_x = v_f$$

where v_f is a constant. We choose as characteristic length scale

$$L = \frac{\kappa}{v_f} ,$$

so that $v_* = v_f$ and $v_+ = 1$, and we omit the subscript + everywhere. The steady planar form of Eq. (1.9) now reduces to the following one-dimensional system of ODEs

$$\begin{aligned} \frac{dT}{dx} &= \frac{d^2T}{dx^2} + \omega \\ \frac{dY}{dx} &= \frac{1}{Le}\frac{d^2Y}{dx^2} - \omega \end{aligned} \tag{1.15}$$

with the following boundary conditions

$$T(-\infty) = 0 , \;\; T(+\infty) = 1 , \;\; Y(-\infty) = 1 , \;\; Y(+\infty) = 0 . \tag{1.16}$$

Considering the large activation energy approximation, the analysis of Zeldovich and Frank-Kamenetskii [94, 93] allows us to get an asymptotical solution of (1.15). Let us denote by $[x_1, x_2]$ the thin chemical reaction zone where $Ze(1 - T) = O(1)$. Away from this region, the reaction rate is negligible, and (1.15) reduces to

$$\begin{aligned} -\frac{d^2T}{dx^2} + \frac{dT}{dx} &= 0 \\ -\frac{1}{Le}\frac{d^2Y}{dx^2} + \frac{dY}{dx} &= 0 \end{aligned} \tag{1.17}$$

Using the boundary conditions (1.16), one gets the following solution

$$T = \begin{cases} T(x_1)\, e^x & \text{if} \quad x \le x_1 \\ 1 & \text{if} \quad x \ge x_2 \end{cases}$$

$$Y = \begin{cases} 1 + [Y(x_1) - 1]\, e^{Le\, x} & \text{if} \quad x \le x_1 \\ 0 & \text{if} \quad x \ge x_2 \end{cases}$$

where $T(x_1)$ and $Y(x_1)$ are unknown values. Inside $[x_1, x_2]$, the solution is not yet determined.

In the limit $Ze \to \infty$, the thin chemical reaction zone reduces to a δ-peak, and x_1 and x_2 coincide. As the solution is steady, we can consider that the front is localized at the

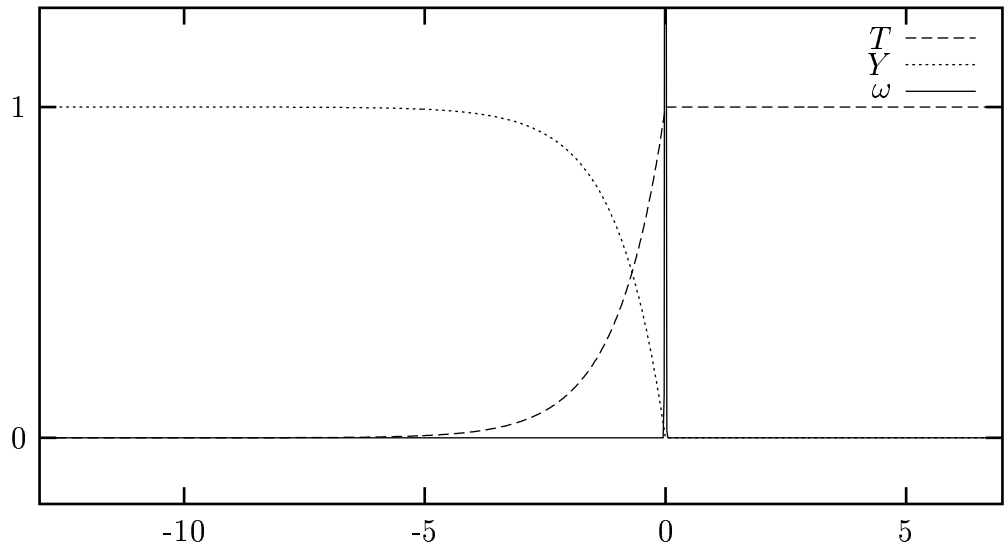

Figure 1.2: Asymptotic solution $Ze \to \infty$ for the steady planar flame equations with $Le = 1$.

origin, i.e. $x_1 = x_2 = 0$. The continuity conditions on temperature and concentration at the front yield $T(0) = T(x_1) = T(x_2) = 1$ and $Y(0) = Y(x_1) = Y(x_2) = 0$. Thus, the asymptotic solution for $Ze \to \infty$ is

$$T = \begin{cases} e^x & \text{if} \quad x \leq 0 \\ 1 & \text{if} \quad x \geq 0 \end{cases} \tag{1.18}$$

$$Y = \begin{cases} 1 - e^{Le\, x} & \text{if} \quad x \leq 0 \\ 0 & \text{if} \quad x \geq 0 \end{cases} \tag{1.19}$$

The solution for $Le = 1$ is plotted in Fig. 1.2. This result allows us to explain in detail the mechanism of flame propagation, which is mainly governed by two phenomena: on one hand, the heat release due to the chemical reaction ; on the other hand, the diffusive transport of energy towards the fresh mixture.

A steady planar flame structure with finite Ze is presented in Fig. 1.3. One can split it into four regions:

- the *fresh mixture zone* (AB), where $T \approx 0$ and $Y \approx 1$;
- the *preheat zone* (BC), where the dominant mechanism is the heat conduction, and where the temperature profile grows exponentially;
- the *reaction zone* (CD), whose thickness is of $O(Ze^{-1})$;
- the *burnt mixture zone* (DE), where $T \approx 1$ and $Y \approx 0$.

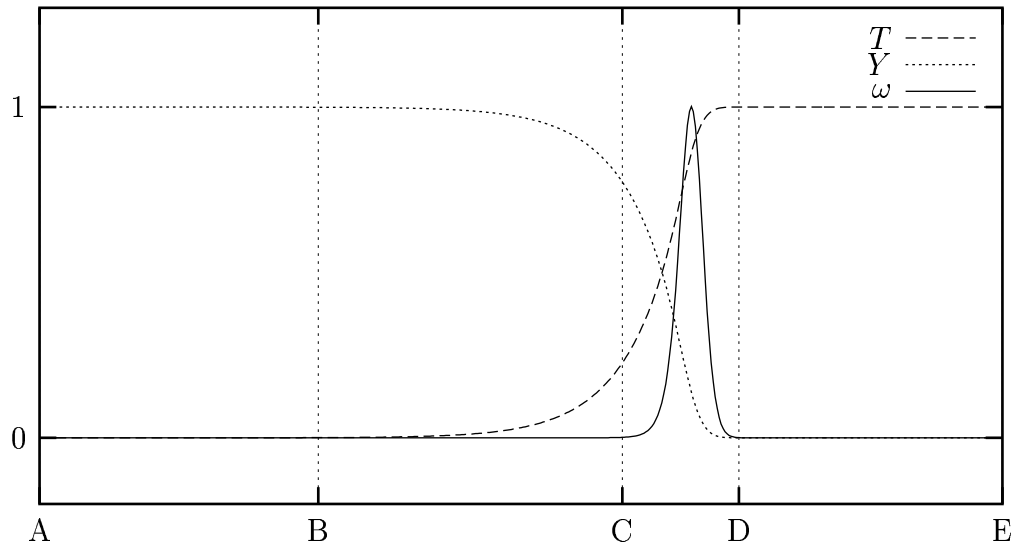

Figure 1.3: Steady planar flame structure for $Le = 1$, $Ze = 10$.

Let us follow the movement of a small slice of gas mixture; coming from the fresh mixture with a velocity v_f, it reaches the preheat zone. In this region, the reaction rate is very weak. Therefore the temperature increase is not due to chemical reaction, but to heat conduction coming from the reaction zone; then, heated by thermal conduction, the control volume reaches the reaction zone with a temperature sufficiently high for the chemical reaction to occur; finally, when all the deficient reactant is burnt, the chemical reaction almost stops and the control volume leaves the reaction zone.

When considering the gas mixture at rest and the flame moving at the velocity v_f, the same mechanism is involved: a chemical reaction occurs in a control volume of gas mixture; the reaction being exothermic, the heat release reaches the neighboring control volume by thermal conduction; the temperature in this neighboring control volume increases until it is sufficient for the chemical reaction to occur; this reaction induces a heat release, which also reaches the next control volume by thermal conduction.

The influence due to radiation is illustrated in Fig. 1.4. We observe that, in the burnt mixture zone, temperature is reduced. Far from the reaction zone, the gas receives little heat by thermal conduction. Due to radiative loss, the temperature decreases. A second effect can be seen on the reaction rate, highly dependent on temperature in the reaction zone. When the temperature in the reaction zone decreases, it also affects the intensity of the chemical reaction.

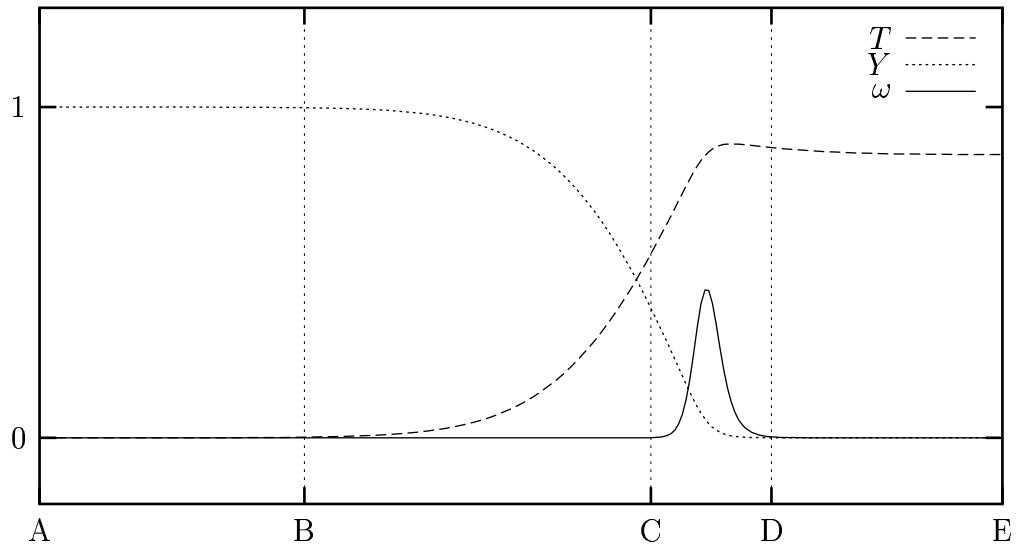

Figure 1.4: Steady planar flame structure with radiation for $Le = 1$, $Ze = 10$, and $\gamma = 0.01$.

1.7 Thermodiffusive instability

The linear analysis of the thermodiffusive instability for $Ze >> 1$ has been established by Sivashinsky [89] for the adiabatic case and by Joulin and Clavin [60] for the non-adiabatic one. Denet and Haldenwang [38] studied the instability behavior for finite Ze and without radiation using numerical simulations.

We only recall here the adiabatic case and therefore neglect the radiation effects. When the geometry of the front is no longer one dimensional, i.e. when the flame front is no more planar, we have to take into account the development of diffusive fluxes in the direction tangential to the flame front. In the direction perpendicular to the flame front, the flame structure is characterized by temperature and concentration profiles close to those corresponding to the planar flame. When the front is perturbated, these profiles are shifted by the front displacement. This induces temperature and concentration gradients in the tangential directions and thus produces diffusive fluxes of heat and mass in the same direction (Fig. 1.5).

Another process is the deflection of streamlines through the perturbated front due to gas expansion. Convective fluxes are developed inside the flame in directions tangential to the flame front. This mechanism is the base of the *hydrodynamic instability*, also called *Darrieus-Landau instability* [36, 61]. In the present work, since the gas expansion is assumed to be small, this effect is negligible.

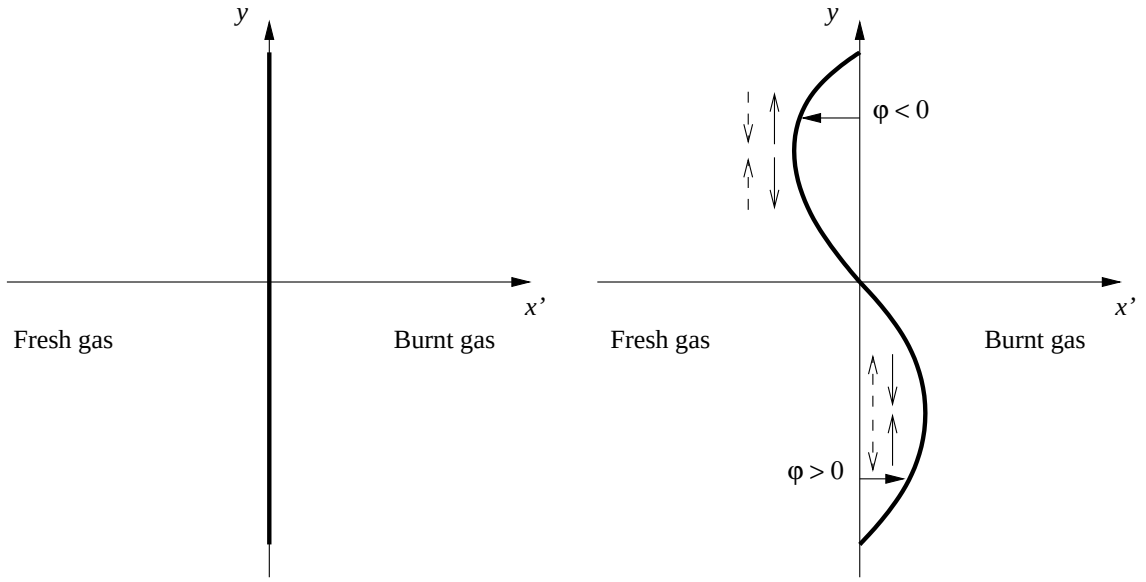

Figure 1.5: Planar (*left*) and perturbated (*right*) flame fronts. Plain arrows represent the tangential heat fluxes, dashed arrows the tangential species fluxes. Flame fronts are represented in the moving plan (x', y), where $x' = x + v_f t$.

1.7.1 Governing equations for a perturbated flame front

The following is inspired by [89, 60]. Assuming the premixed gas to be at rest, we consider the dimensionless thermodiffusive equations in the large activation energy approximation and, as in the previous section, we choose the characteristic length scale L such that $v_* = v_f$. The planar flame front is located at $x = -v_f t$ i.e., under dimensionless form, $x_+ = -t_+$. Therefore, in dimensionless variables, the perturbated front is located at the position

$$x_+ = -t_+ + \varphi(y_+, t_+).$$

where φ is the non-dimensional perturbation of the flame front.

In the following, the subscript $+$ is omitted everywhere. For the sequel it is convenient to introduce the following dimensionless curvilinear coordinates attached to the perturbated flame front

$$\xi = x + t - \varphi \ , \quad \eta = y \ , \quad \tau = t \ .$$

In the new dimensionless variables, the system (1.10) writes

$$\begin{aligned} \frac{\partial T}{\partial \tau} + \left(1 - \frac{\partial \varphi}{\partial \tau}\right) \frac{\partial T}{\partial \xi} &= \tilde{\nabla}^2 T + \omega \\ \frac{\partial Y}{\partial \tau} + \left(1 - \frac{\partial \varphi}{\partial \tau}\right) \frac{\partial Y}{\partial \xi} &= \frac{1}{Le} \tilde{\nabla}^2 Y - \omega \end{aligned} \tag{1.20}$$

where $\tilde{\nabla}^2$ denotes the Laplacian operator

$$\tilde{\nabla}^2 = \left[1 + \left(\frac{\partial\varphi}{\partial\eta}\right)^2\right] \frac{\partial^2}{\partial\xi^2} - 2\,\frac{\partial\varphi}{\partial\eta}\,\frac{\partial^2}{\partial\xi\,\partial\eta} - \frac{\partial^2\varphi}{\partial\eta^2}\,\frac{\partial}{\partial\xi} + \frac{\partial^2}{\partial\eta^2}.$$

We complete this system with boundary conditions

$$T(-\infty) = 0\ ,\ \ T(+\infty) = 1\ ,\ \ Y(-\infty) = 1\ ,\ \ Y(+\infty) = 0. \tag{1.21}$$

At the flame front itself, we have the following continuity conditions

$$\begin{aligned} T(-0,\eta,\tau) &= T(+0,\eta,\tau)\ , \\ Y(-0,\eta,\tau) &= Y(+0,\eta,\tau)\ . \end{aligned} \tag{1.22}$$

To investigate the linear stability of the flame front, we use the classical method of *small harmonic perturbations* [89]. Each physical quantity is expressed as an unperturbated solution plus a small harmonic perturbation. The perturbated solution has the form

$$\begin{aligned} \varphi(\eta,\tau) &= \Phi\ \exp(ik\eta + \sigma\tau) \\ T(\xi,\eta,\tau) &= \mathcal{T}_0(\xi) + \mathcal{T}(\xi)\ \Phi\ \exp(ik\eta + \sigma\tau) \\ Y(\xi,\eta,\tau) &= \mathcal{Y}_0(\xi) + \mathcal{Y}(\xi)\ \Phi\ \exp(ik\eta + \sigma\tau) \end{aligned} \tag{1.23}$$

where the unperturbated steady solution $(\mathcal{T}_0, \mathcal{Y}_0)$ verifies

$$\begin{aligned} \frac{d\mathcal{T}_0}{d\xi} &= \frac{d^2\mathcal{T}_0}{d\xi^2} + \omega(\mathcal{T}_0, \mathcal{Y}_0) \\ \frac{d\mathcal{Y}_0}{d\xi} &= \frac{1}{Le}\frac{d^2\mathcal{Y}_0}{d\xi^2} - \omega(\mathcal{T}_0, \mathcal{Y}_0) \end{aligned} \tag{1.24}$$

in the approximation $Ze \to \infty$. Therefore, according to (1.18- 1.19), we have

$$\mathcal{T}_0(\xi) = \begin{cases} e^{\xi} & \text{if} \quad \xi \le 0 \\ 1 & \text{if} \quad \xi \ge 0 \end{cases} \tag{1.25}$$

$$\mathcal{Y}_0(\xi) = \begin{cases} 1 - e^{Le\,\xi} & \text{if} \quad \xi \le 0 \\ 0 & \text{if} \quad \xi \ge 0 \end{cases} \tag{1.26}$$

Subtracting (1.24) from (1.20) and linearizing by removing non-linear terms, the resulting system is a set of linear ordinary differential equations for $\mathcal{T}$ and $\mathcal{Y}$

$$\begin{aligned} \sigma\mathcal{T} + \frac{d\mathcal{T}}{d\xi} - \sigma\frac{d\mathcal{T}_0}{d\xi} &= \frac{d^2\mathcal{T}}{d\xi^2} - k^2\mathcal{T} + k^2\frac{d^2\mathcal{T}_0}{d\xi^2} \\ \sigma\mathcal{Y} + \frac{d\mathcal{Y}}{d\xi} - \sigma\frac{d\mathcal{Y}_0}{d\xi} &= \frac{1}{Le}\left(\frac{d^2\mathcal{Y}}{d\xi^2} - k^2\mathcal{Y} + k^2\frac{d^2\mathcal{Y}_0}{d\xi^2}\right) \end{aligned} \tag{1.27}$$

1.7.2 Dispersion relation

The dispersion relation $\sigma(k)$ can be obtained in the large activation energy approximation, i.e. when $Ze >> 1$. Following [89, 60], using an asymptotic expansion in powers of Ze^{-1} for the system (1.27) and applying it to the boundary conditions, one gets the following relation characterizing the growth rate of sinusoidal perturbations of wavelength k

$$(1-\Gamma)\,\Gamma^2 = -\frac{Ze\,(Le-1)}{2}(1-\Gamma+2\sigma)\,, \tag{1.28}$$

where

$$\Gamma = \sqrt{1+4(\sigma+k^2)}\,.$$

For small values of k, this result can be expanded in powers of k. One gets

$$\sigma(k) = -\left[1+\frac{1}{2}Ze\,(Le-1)\right]k^2 - 4k^4 \tag{1.29}$$

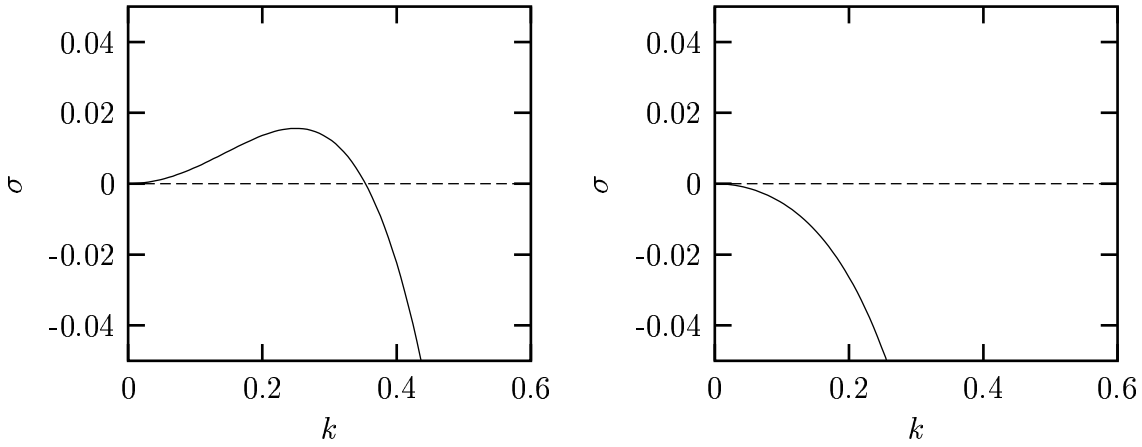

Figure 1.6: Theoretical growth rate *vs.* wave vector for $Ze\ (Le-1) = -3$ (*left*) and $Ze\ (Le-1) = -1$ (*right*). On the left side, the most amplified wavelength is $k \approx 0.25$.

In the adiabatic case, i.e. when no heat loss exists, the only control parameter is $Ze\ (Le-1)$. The stability domain ($Re(\sigma) < 0$) is found to be defined by

$$Ze\ (Le-1) > -2.$$

Denet and Haldenwang [38] solved numerically this problem and compared it to the linear theory in the adiabatic case. They showed a good agreement with theory in the high Ze limit. However, for finite Ze, the correction scales like Ze^{-1}. Therefore, the difference between theory and numerical results can be large for moderate Ze values.

1.7.3 Cellular flames

In the domain corresponding to $Ze\ (Le-1) < -2$, we observe the formation of *cellular flame structures* [89]. The mechanism of the instability can be described this way: let us consider a perturbated flame, as represented on the right side of Fig. 1.5. In the part of the flame pointing at the fresh mixture, the tangential reactant fluxes tend to increase the concentration of fresh gases, and with it the reaction. Therefore the flame is propagating faster in this region, and its shape becomes more and more curved. This effect is balanced by the heat flux, which tends to extract energy in the same region. Therefore it reduces the reaction and with it the flame propagation, which also reduces the curvature of the flame. Thus, the tangential reactant flux has a destabilizing effect for the flame front, whereas the tangential heat flux has a stabilizing effect. This shows the influence of the Lewis Le number in the formation of cellular flames.

1.7.4 Pulsating flames

For $Ze\ (Le-1) > -2$, no formation of cellular flame is observed. However, other instabilities can appear. Following [60], for

$$Ze\ (Le-1) > 16\ , \tag{1.30}$$

an instability mechanism appears at $k = 0$, leading to possible *pulsations* of planar flames. Radiative heat loss is also found to lower the critical Lewis number to values which correspond to more realistic gas mixtures. One-dimensional *pulsating flames* have been observed experimentally in ammonia-oxygen flames standing on a cooled porous plug burner. It has also been simulated numerically (see e.g. [92, 25]).

For these pulsating planar flames, the thermodiffusive model is appropriate, because convection terms can be canceled using a moving reference frame. This is no longer the case for perturbated flames, since the transport of mass and energy produced in tangential directions by convection is of the same order of magnitude as transport by the diffusion process [25].

In [77], the mechanism of pulsation is explained this way: let us consider a mixture whose Lewis number is larger that unity. As was pointed out in [63], the rate of heat conduction from the burnt gases into the preheat zone exceeds the rate of diffusion at which the reactants are transported out of it, leading to an excess enthalpy in the preheat zone. As a consequence, the enthalpy is decreased in the thin chemical reaction zone. This implies a decrease in temperature and, due to its strong sensitivity to the temperature, the flame velocity is decreased.

On the other side, the increase of enthalpy and temperature in the preheat zone involves an accelerated ignition of the reactant at the interphase between preheat and reaction zones. This is a *velocity increasing effect*, which counteracts the velocity decreasing in the reaction zone. Therefore, the flame velocity reaches a minimum and increases again.

If the activation energy lies far from the lower oscillation limit, the velocity increasing effect is rather weak. Thus, in this case, the flame velocity tends to its steady state value.

Two typical time evolutions of the flame velocity v_f are plotted in Fig. 1.7: a damped and a steady pulsating flame.

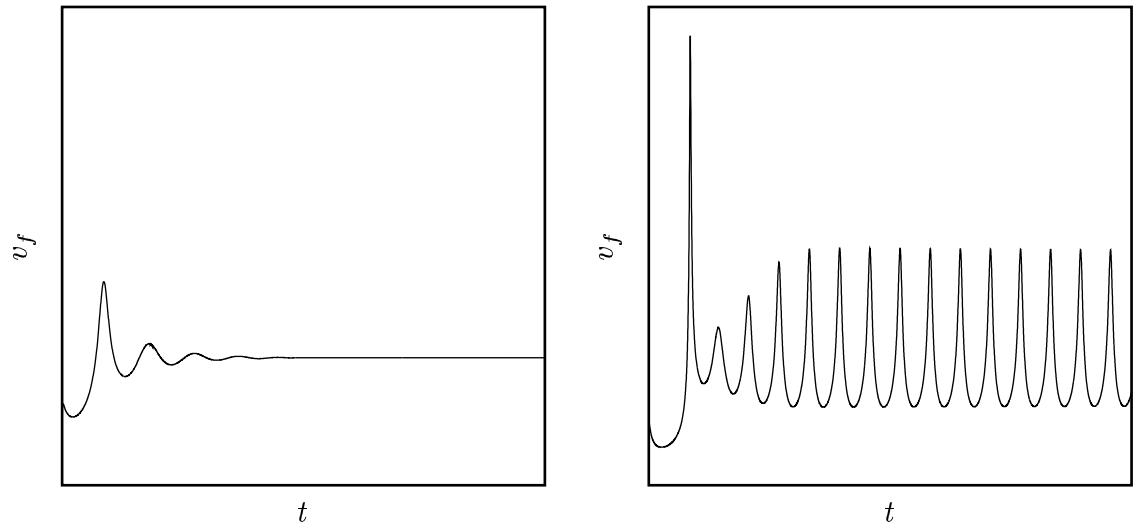

Figure 1.7: Evolution of the flame velocity v_f: damped oscillations (*left*) and pulsating flame (*right*).

Numerical simulations have been performed to determine the regions of the $Le - Ze$ diagram where pulsating flames are observed [77]. However, this result is limited to moderate values of Ze, the computations requiring too much CPU time and memory for larger values of the activation energy when using an equidistant fine grid. In chapter 4, a more complete bifurcation diagram in the $Le - Ze$ plan is established using the adaptive multiresolution method. The stability curve is compared with the theoretical result for $Ze >> 1$ [60] and to the numerical result obtained in [77].

1.8 Conclusion

In this chapter, we have presented the system of equations governing the propagation of a flame in the thermodiffusive approximation. Starting from the isobaric flame model, we have deduced the thermodiffusive equations and given their dimensionless form in the large activation energy approximation. This results in a system of non-linear parabolic partial differential equations, which are either convection-diffusion-reaction or diffusion-reaction equations. Using the thermodiffusive model, we have described the structure of a steady planar flame. Using a linear stability analysis, we have also explained the different instabilities than can appear in the frame of this approximation.

To investigate numerically the behavior of flames in the fully non-linear regime, it is clear from section 1.6 that very fine scales are required, but only in the thin chemical reaction zone, whose thickness is proportional to Ze^{-1}. This property motivates the intro-

duction of some *adaptive discretization*, as the solution may be overresolved in large subsets of the computational domain when using equidistant grids. The numerical method developed in this thesis, an adaptive multiresolution method based on a finite volume scheme, is described in the next chapter.

Chapter 2

Adaptive multiresolution method for parabolic PDEs

Abstract. *The present chapter is devoted to the presentation of the numerical method used for the simulation of thermodiffusive flames. The principle relies on a time evolution performed through an explicit finite volume scheme. Then a multiresolution analysis is used to threshold data and keep only the most significant coefficients. In this goal, the data structure is organized as a graded tree. The main advantage of the adaptive multiresolution method is that the error due to the thresholding operation, called perturbation error, can be estimated. If one knows the discretization error due to the finite volume scheme, one can estimate the global error between exact and computed solution. For the linear convection-diffusion equation, we derive a prescribed tolerance to be set if one wants the perturbation error to be of the same order of magnitude as the discretization error. This result will be tested for convection-diffusion and viscous Burgers equations in the next chapter. We conclude with an overview of the algorithm implemented in the computational code named CARMEN.*

2.1 Introduction

In the previous chapter, the system of PDEs used to model combustion in the thermodiffusive approximation has been presented. The resulting model is stiff in space. Since very fine scales in space are required, but only locally, some kind of adaptivity is useful to reduce CPU time and memory requirements.

In the recent past, thermodiffusive flame computations have been performed using an adaptive wavelet-vaguelette algorithm [43, 44, 45, 14]. Its ability to reduce the number of degrees of freedom while following the evolution of the flame has been shown. However, due to the choice of the wavelet-vaguelette decomposition, this method is limited to periodic boundary conditions. Therefore, it can not be used to simulate problems like the interaction between flames and adiabatic walls. A solution to this problem could be the use of a penalization technique (see e.g. [87]).

The method chosen here relies on the multiresolution algorithm developed for 1D and

2D hyperbolic equations in [52, 53, 54, 55], and extended to the fully adaptive case in [48, 27, 70, 69], in order to reduce both CPU time and memory requirements. The principle relies on a time evolution performed with a finite volume scheme, which enables to use several kinds of boundary conditions, and a multiresolution analysis, which aims at thresholding data to keep only the most significant details [84]. Here, with respect to previous work, we extend the method to the parabolic case and to three-dimensional Cartesian geometries. We also present the corresponding error analysis in the linear case.

The first section of the chapter is devoted to the presentation of the general finite volume method, including the description of time integration and space discretization schemes used. Then, the adaptive multiresolution scheme is described, including a way to ensure conservative flux computations and a theoretical relation between the tolerance and the level if one wants to maintain the accuracy order of the finite volume scheme. The last section presents the algorithm developed to perform the numerical simulations. Details concerning the algorithm, the data structure and the practical implementation are also given.

2.2 Finite volume method

The principle of the finite volume method is to express the PDEs in their integral form on a set of cells which constitutes a partition of the computational domain. Inside each cell, the variation in time of a given integral physical quantity is the sum of the fluxes going through the cell and the internal production of this quantity.

2.2.1 Parabolic conservation laws

In this thesis we are concerned with the initial value problem for parabolic conservation laws of the form

$$\begin{aligned} \frac{\partial u}{\partial t} + \nabla \cdot F(u, \nabla u) &= S(u) \\ u(x,0) &= u_0(x) \end{aligned} \tag{2.1}$$

where $u \in \mathbb{R}^m$, $(x,t) \in \Omega \times [0, +\infty)$, $\Omega \subset \mathbb{R}^d$. We complete the system with appropriate boundary conditions. In the present work, we restrict ourselves to the case where the diffusive flux of the quantity u is proportional to $-\nabla u$, assuming constant diffusivity $\nu > 0$, i.e.

$$F(u, \nabla u) = f(u) - \nu \nabla u.$$

For ease of notation, we denote by $\mathcal{D}(u, \nabla u) = -\nabla \cdot F(u, \nabla u) + S(u)$ the *divergence and source term*. Thus, (2.1) can be written in the form

$$\frac{\partial u}{\partial t} = \mathcal{D}(u, \nabla u). \tag{2.2}$$

2.2.2 Discretized equations

Let us consider the computational domain Ω in dimension d with an arbitrary shape, and let us partition it into cells $(\Omega_i)_{i\in\Lambda}$, $\Lambda = \{1, \ldots, i_{max}\}$. We then denote by $\bar{q}_i(t)$ the cell-average value of a given quantity q on Ω_i at the instant t,

$$\bar{q}_i(t) = \frac{1}{|\Omega_i|}\int_{\Omega_i} q(x,t)\,dx$$

where $|\Omega_i| = \int_{\Omega_i} dx$ is the volume of the cell. Integrating (2.2) on Ω_i yields

$$\int_{\Omega_i} \frac{\partial u}{\partial t}(x,t)dx = \int_{\Omega_i} \mathcal{D}\left(u(x,t),\, \nabla u(x,t)\right)\, dx$$

i.e.

$$\frac{\partial \bar{u}_i}{\partial t}(t) = \bar{\mathcal{D}}_i(t) \tag{2.3}$$

Applying the divergence theorem, we get

$$\bar{\mathcal{D}}_i(t) = -\frac{1}{|\Omega_i|}\int_{\partial\Omega_i} F\left[u(x,t), \nabla u(x,t)\right]\cdot\sigma_i(x)\,dx + \bar{S}_i(t) \tag{2.4}$$

where $\sigma_i(x)$ denotes the outer normal vector to Ω_i.

Conservativity in the flux computation is ensured if and only if, for two adjacent cells Ω_{i_1} and Ω_{i_2}, the outgoing flux from Ω_{i_1} to Ω_{i_2} balances with the one from Ω_{i_2} to Ω_{i_1}. In the next subsections, we will describe the time integration and space discretization schemes applied to (2.3).

2.2.3 Runge-Kutta time integration

Runge-Kutta schemes are a family of explicit, non-linear and high-order accurate schemes which offer the possibility to use only two time levels for each step. They can achieve high accuracy by involving multiple steps [57]. The principle is the following one: considering the operator $\mathcal{D}$ be linear, i.e. $\mathcal{D}(u, \nabla u) = Au$, A being a $m \times m$ diagonal matrix, and omitting the subscript i everywhere, (2.3) becomes

$$\frac{\partial \bar{u}}{\partial t}(t) = A\bar{u}\ .$$

Let us denote by Δt the time step, and by $t^n = n\Delta t$. Considering $\bar{u}^n = \bar{u}(t^n)$, the expression of $\bar{u}^{n+1}$ in function of $\bar{u}^n$ is

$$\bar{u}^{n+1} = \bar{u}^n e^{A\,\Delta t}\ ,$$

The explicit Runge-Kutta time integration consists in approximating the exponential by its development in a series in terms of $A\,\Delta t$, i.e.

$$\bar{u}^{n+1} = \bar{u}^n\left[1 + A\,\Delta t + \frac{(A\,\Delta t)^2}{2} + \ldots\right].$$

High accuracy orders are obtained by computing different intermediary states between t^n and t^{n+1}, using only two states to compute a new one. For example, the first-order Runge-Kutta scheme is the explicit Euler method, i.e.

$$\bar{u}^{n+1} = \bar{u}^n + \Delta t \, (A\bar{u}^n)$$

and a second-order Runge-Kutta scheme can be e.g.

$$\begin{aligned} \bar{u}^* &= \bar{u}^n + \frac{\Delta t}{2}(A\bar{u}^n) \\ \bar{u}^{n+1} &= \bar{u}^n + \Delta t \, (A\bar{u}^*) \end{aligned}$$

In the present computations, we use second-order (RK2) and third-order (RK3) Runge-Kutta schemes. The RK2 scheme used in the computations is defined by

$$\begin{aligned} \bar{u}^* &= \bar{u}^n + \Delta t \, \bar{\mathcal{D}}^n \\ \bar{u}^{n+1} &= \frac{1}{2}\left[\bar{u}^n + \bar{u}^* + \Delta t \, \bar{\mathcal{D}}^*\right] \end{aligned} \tag{2.5}$$

and the RK3 scheme by

$$\begin{aligned} \bar{u}^* &= \bar{u}^n + \Delta t \, \bar{\mathcal{D}}^n \\ \bar{u}^{**} &= \left(3\bar{u}^n + \bar{u}^* + \Delta t \, \bar{\mathcal{D}}^*\right)/4 \\ \bar{u}^{n+1} &= \left(\bar{u}^n + 2\bar{u}^{**} + 2\Delta t \, \bar{\mathcal{D}}^{**}\right)/3 \end{aligned} \tag{2.6}$$

The general discrete time evolution operator is denoted by $\bar{\mathbf{E}}(\Delta t)$ and verifies

$$\bar{u}^{n+1} = \bar{\mathbf{E}}(\Delta t) \cdot \bar{u}^n \tag{2.7}$$

For the RK2 method described above, $\bar{\mathbf{E}}(\Delta t)$ is defined as

$$\bar{\mathbf{E}}(\Delta t) = \mathbf{I} + \frac{\Delta t}{2}\bar{\mathcal{D}} + \frac{\Delta t}{2}\bar{\mathcal{D}}\left(\mathbf{I} + \Delta t\bar{\mathcal{D}}\right) \ , \tag{2.8}$$

where $\mathbf{I}$ denotes the identity operator. The discretization of the operator $\bar{\mathcal{D}}$ is described in the following subsection, the stability conditions being treated in Subsection 2.2.5.

2.2.4 Numerical flux

We now consider a fixed instant t^n and, in the following, the superscript n is omitted everywhere. For the 1D case, Ω_i is a segment $[x_{i-\frac{1}{2}}, x_{i+\frac{1}{2}}]$ with step size $\Delta x_i = x_{i+\frac{1}{2}} - x_{i-\frac{1}{2}}$. Eq. (2.4) becomes

$$\bar{\mathcal{D}}_i = -\frac{1}{\Delta x_i}\left(\bar{F}_{i+\frac{1}{2}} - \bar{F}_{i-\frac{1}{2}}\right) + \bar{S}_i \tag{2.9}$$

Advective and diffusive terms are approximated differently. For the advective part, we use Roe's scheme [76] with a second-order ENO interpolation [56, 11], whereas, for the diffusive part, we choose a second-order accurate centered scheme. Bihari [11] showed that the resulting global scheme, which is non-linear, is second-order accurate in space.

$$\bar{F}_{i+\frac{1}{2}} = f^R\left(\bar{u}^-_{i+\frac{1}{2}}, \bar{u}^+_{i+\frac{1}{2}}\right) - \nu\frac{\bar{u}_{i+1} - \bar{u}_i}{\Delta x_{i+\frac{1}{2}}} \tag{2.10}$$

where $\Delta x_{i+\frac{1}{2}} = \frac{1}{2}(\Delta x_i + \Delta x_{i+1})$

The term f^R denotes, for the advective part, Roe's approximate solution to the Riemann problem given the left (-) and right (+) values of u. Its scalar version is given by

$$f^R(u^-, u^+) = \frac{1}{2}\left[f(u^-) + f(u^+) - |a(u^-, u^+)|(u^+ - u^-)\right] \tag{2.11}$$

where

$$a(u^-, u^+) = \begin{cases} \dfrac{f(u^+) - f(u^-)}{u^+ - u^-} & \text{if} \quad u^- \neq u^+ \\ \\ f'(u^-) & \text{if} \quad u^- = u^+ \end{cases}$$

The left and right terms, $\bar{u}^-_{i+\frac{1}{2}}$ and $\bar{u}^+_{i+\frac{1}{2}}$ respectively, are computed using a second-order ENO interpolation [11]

$$\begin{array}{rcl} \bar{u}^-_{i+\frac{1}{2}} & = & \bar{u}_i + \frac{1}{2}M\left(\bar{u}_{i+1} - \bar{u}_i, \bar{u}_i - \bar{u}_{i-1}\right) \\ \bar{u}^+_{i+\frac{1}{2}} & = & \bar{u}_{i+1} + \frac{1}{2}M\left(\bar{u}_{i+2} - \bar{u}_{i+1}, \bar{u}_{i+1} - \bar{u}_i\right) \end{array} \tag{2.12}$$

where M is the *Min-Mod* limiter, which chooses the minimal slope between the left and right sides, i.e.

$$M(a, b) = \begin{cases} a \text{ if } |a| \leq |b| \\ b \text{ if } |a| > |b| \end{cases}$$

The source term is approximated by $\bar{S}_i \approx S(\bar{u}_i)$. For a general non-linear source term, this choice yields a second-order accuracy.

Extension to higher dimension in Cartesian geometries is performed through a tensor product approach. For the 2D case, $\Omega_{i,j}$ is a rectangle with volume of size $|\Omega_{i,j}| = \Delta x_i\, \Delta y_j$. Eq. (2.3) can be written as

$$\frac{\partial \bar{u}_{i,j}}{\partial t}(t) = \bar{\mathcal{D}}_{i,j}(t) \tag{2.13}$$

where

$$\bar{\mathcal{D}}_{i,j} = -\frac{1}{\Delta x_i}\left(\bar{F}_{i+\frac{1}{2},j} - \bar{F}_{i-\frac{1}{2},j}\right) - \frac{1}{\Delta y_j}\left(\bar{F}_{i,j+\frac{1}{2}} - \bar{F}_{i,j-\frac{1}{2}}\right) + \bar{S}_{i,j}.$$

The same numerical flux as in the 1D case is applied in each direction.

$$\begin{array}{rcl} \bar{F}_{i+\frac{1}{2},j} & = & f^R\left(\bar{u}^-_{i+\frac{1}{2},j}, \bar{u}^+_{i+\frac{1}{2},j}\right) - \nu\dfrac{\bar{u}_{i+1,j} - \bar{u}_{i,j}}{\Delta x_{i+\frac{1}{2}}} \\ \bar{F}_{i,j+\frac{1}{2}} & = & f^R\left(\bar{u}^-_{i,j+\frac{1}{2}}, \bar{u}^+_{i,j+\frac{1}{2}}\right) - \nu\dfrac{\bar{u}_{i,j+1} - \bar{u}_{i,j}}{\Delta y_{j+\frac{1}{2}}} \end{array} \tag{2.14}$$

where $\Delta x_{i+\frac{1}{2}} = \frac{1}{2}(\Delta x_i + \Delta x_{i+1})$ and $\Delta y_{j+\frac{1}{2}} = \frac{1}{2}(\Delta y_j + \Delta y_{j+1})$.

Analogously, for the 3D case, $\Omega_{i,j,k}$ is a rectangle parallelepiped with volume of size $|\Omega_{i,j,k}| = \Delta x_i \, \Delta y_j \, \Delta z_k$. Hence we get

$$\frac{\partial \bar{u}_{i,j,k}}{\partial t}(t) = \bar{\mathcal{D}}_{i,j,k}(t) \tag{2.15}$$

where

$$\begin{aligned} \bar{\mathcal{D}}_{i,j,k} &= -\frac{1}{\Delta x_i}\left(\bar{F}_{i+\frac{1}{2},j,k} - \bar{F}_{i-\frac{1}{2},j,k}\right) - \frac{1}{\Delta y_j}\left(\bar{F}_{i,j+\frac{1}{2},k} - \bar{F}_{i,j-\frac{1}{2},k}\right) \\ &\quad -\frac{1}{\Delta z_k}\left(\bar{F}_{i,j,k+\frac{1}{2}} - \bar{F}_{i,j,k-\frac{1}{2}}\right) + \bar{S}_{i,j,k}. \end{aligned}$$

The fluxes are in this case

$$\begin{aligned} \bar{F}_{i+\frac{1}{2},j,k} &= f^R\left(\bar{u}^-_{i+\frac{1}{2},j,k},\, \bar{u}^+_{i+\frac{1}{2},j,k}\right) - \nu \frac{\bar{u}_{i+1,j,k} - \bar{u}_{i,j,k}}{\Delta x_{i+\frac{1}{2}}} \\ \bar{F}_{i,j+\frac{1}{2},k} &= f^R\left(\bar{u}^-_{i,j+\frac{1}{2},k},\, \bar{u}^+_{i,j+\frac{1}{2},k}\right) - \nu \frac{\bar{u}_{i,j+1,k} - \bar{u}_{i,j,k}}{\Delta y_{j+\frac{1}{2}}} \\ \bar{F}_{i,j,k+\frac{1}{2}} &= f^R\left(\bar{u}^-_{i,j,k+\frac{1}{2}},\, \bar{u}^+_{i,j,k+\frac{1}{2}}\right) - \nu \frac{\bar{u}_{i,j,k+1} - \bar{u}_{i,j,k}}{\Delta z_{k+\frac{1}{2}}} \end{aligned} \tag{2.16}$$

where $\Delta x_{i+\frac{1}{2}} = \frac{1}{2}(\Delta x_i + \Delta x_{i+1})$, $\Delta y_{j+\frac{1}{2}} = \frac{1}{2}(\Delta y_j + \Delta y_{j+1})$, and $\Delta z_{k+\frac{1}{2}} = \frac{1}{2}(\Delta z_k + \Delta z_{k+1})$.

2.2.5 Numerical stability

In the multiresolution computations, the time step is the same for all scales. Hence, the stability condition is the one of the same finite volume scheme on the finest grid. A sufficient condition of numerical stability can be obtained in the linear case. Let us consider the linear convection-diffusion equation

$$\frac{\partial u}{\partial t} + c\frac{\partial u}{\partial x} = \nu \frac{\partial^2 u}{\partial x^2}\,.$$

Denoting by c the velocity and by Δx the smallest step size, the CFL number σ is given by

$$\sigma = \frac{c\Delta t}{\Delta x}$$

and the mesh Reynolds number R by

$$R = \frac{c\Delta x}{\nu}$$

Bihari [11] showed that a sufficient stability condition for the above finite volume scheme is

$$\sigma \leq \min\left(\frac{R}{2}, \frac{6}{R}\right) \tag{2.17}$$

Moreover, a sufficient condition, so that this scheme is Total Variation Diminishing (TVD), is

$$\sigma \leq \frac{R}{R+4} \tag{2.18}$$

The main advantage of an explicit treatment for the diffusive term is that no linear system needs to be solved. However, it usually implies that $\Delta t = O(\Delta x^2)$. Only when $R >> 1$, we have $\Delta t = O(\Delta x)$.

2.3 Adaptive multiresolution scheme

The concept of multiresolution analysis (MRA) was firstly introduced by Mallat [67]. Its extension to cell-average data representation was done by Harten [52, 54]. For more details on MRA, we refer to textbooks [37, 68, 27].

The principle of multiresolution analysis is to represent a set of data given on a fine grid as values on a coarser grid plus a series of differences at different levels of nested dyadic grids. These differences contain the information of the solution when going from a coarse to a finer grid. In particular, these coefficients are small in regions where the solution is smooth. The data structure needs to be organized as a dynamic *graded tree* if one wants to compress data, while still being able to navigate through it.

2.3.1 Dynamic graded tree

In the wavelet terminology, a graded tree structure corresponds to an *adaptive approximation*. Its difference with the classical *non-linear approximation* is that the connectivity in the tree structure is always ensured. In other words, no hole is admitted inside the tree. DeVore [40] showed that the difference between both approximations is negligible in terms of required nodes.

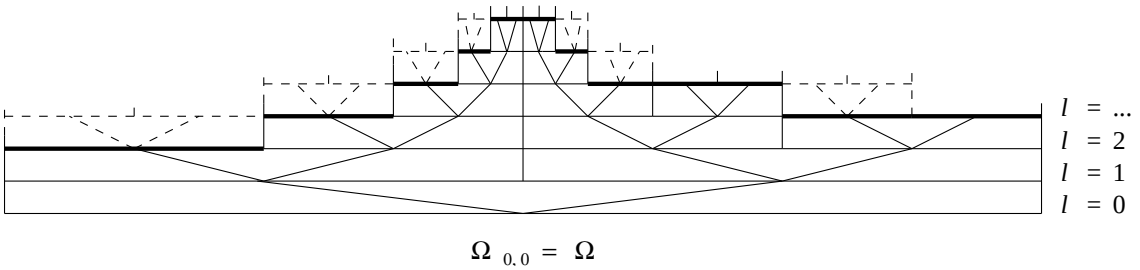

Figure 2.1: Example of graded tree data structure in 1D for $s = 1$, $s' = 2$.

Following [31], we first introduce a terminology to define the tree structure.

- The *root* is the basis of the tree;
- A *node* is an element of the tree. Here, every cell, when existing, can be considered as a node;
- A *parent* node has 2^d *children* nodes, d being the space dimension of the problem;
- The children nodes of the same parent are called *brothers*;
- A given node has nearest neighbors in each direction, called the *nearest cousins*. The brothers can also be considered as nearest cousins;
- Given a child node, the nearest cousins of the parent node are called the *nearest uncles*;
- A node is called a *leaf* when it has no children;
- In order to compute the ingoing and outgoing fluxes of a given leaf, we need its nearest cousins. When one of them is not existing, it is created as *virtual leaf*. A virtual leaf is not considered as an existing node and is only used for flux computations. As a consequence, no time evolution is made on it.

Fig. 2.1 illustrates the graded tree structure in the 1D case. The standard nodes are represented by a *thin* line, the leaves by a *bold* line, the virtual leaves by a *dotted* line.

A *dynamic tree* is a tree which changes in time. When needed, some nodes can be added or removed. To remain *graded*, it must respect the following conditions :

- When a child is created, all its brothers are also created in the same time;
- A given node has always its s nearest uncles in each direction, diagonal included. When not existing, create them as nodes;
- A given node has always its s' nearest cousins in each direction. When not existing, create them as virtual leaves;

As a consequence, a node can be removed only if all its brothers can also be removed, and if it is not the nearest uncle of an existing node. The number of nearest cousins s' depends on the accuracy of the space discretization. For a second-order TVD accurate scheme, as the one described in the previous section, a five-point space scheme is applied for each dimension. Therefore we have $s' = 2$. In addition, the number of nearest uncles s depends on the multiresolution accuracy and will be explained in the next subsection.

2.3.2 Multiresolution representation

Starting point is the cell-average multiresolution representation introduced in [52, 53, 54]. The nodes are cell-average values and two operators are defined to navigate through the tree. In the following, a complete description of the 1D multiresolution representation is given, together with the extension to higher dimensions in Cartesian geometry using a tensor product approach.

We denote by Λ the ensemble of the indices of the existing nodes, by $\mathcal{L}(\Lambda)$ the restriction of Λ to the leaves, and by Λ_l the restriction of Λ to a level l, $0 \leq l < L$.

For the 1D case, we denote by $\Omega = \Omega_{0,0}$ the root cell, $\Omega_{l,i}$, $0 \leq l < L$, $i \in \Lambda_l$ the different node cells, $\bar{q}_{l,i}$ the cell-average value of the quantity q on the cell $\Omega_{l,i}$, and $\bar{Q}_l = (\bar{q}_{l,i})_{i \in \Lambda_l}$ the ensemble of the existing cell-average values at the level l.

To estimate the cell-averages of a level l from the ones of the level $l+1$, we use the **projection** (or restriction) operator $P_{l+1 \to l}$.

$$P_{l+1 \to l} : \bar{U}_{l+1} \mapsto \bar{U}_l \tag{2.19}$$

This operator is *exact* and *unique*, given that the parent cell-average is nothing but the weighted average of the children cell-averages. For a regular grid structure in 1D, it is simply defined by the mean value

$$\bar{u}_{l,i} = (P_{l+1 \to l} \bar{U}_{l+1})_i = \frac{1}{2}(\bar{u}_{l+1,2i} + \bar{u}_{l+1,2i+1}) \tag{2.20}$$

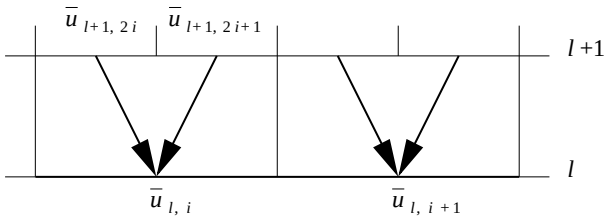

Figure 2.2: Projection operator $P_{l+1 \to l}$ in 1D.

To estimate the cell-averages of a level $l+1$ from the ones of the level l, we use the **prediction** (or prolongation) operator $P_{l \to l+1}$.

$$P_{l \to l+1} : \bar{U}_l \mapsto \hat{U}_{l+1} \tag{2.21}$$

This operator gives an *approximation* of $\bar{U}_l$ at the level $l+1$ by interpolation. It is *not unique*, nevertheless, in order to be applicable in the dynamic graded tree structure as defined above, this operator must satisfy two properties:

- It has to be *local*, i.e. the interpolation for a child is made from the cell-averages of its parent and its s nearest uncles in each direction ;

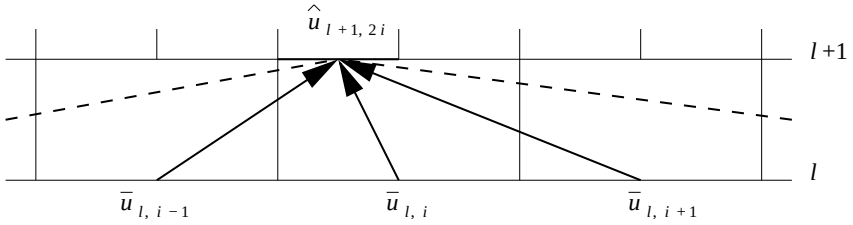

Figure 2.3: Prediction operator $P_{l\to l+1}$ in 1D.

- It has to be *consistent with projection*, i.e. $P_{l+1\to l} \circ P_{l\to l+1} = \mathrm{Id}$.

For a regular grid structure in 1D, we use as prediction operator a polynomial interpolation on the cell-average values, like the one proposed by Harten [54]:

$$\begin{aligned} \hat{u}_{l+1,2i} &= I(\bar{U}_l; l+1, 2i) = \bar{u}_{l,i} + \sum_{m=1}^{s} \gamma_m (\bar{u}_{l,i+m} - \bar{u}_{l,i-m}) \\ \hat{u}_{l+1,2i+1} &= I(\bar{U}_l; l+1, 2i+1) = \bar{u}_{l,i} - \sum_{m=1}^{s} \gamma_m (\bar{u}_{l,i+m} - \bar{u}_{l,i-m}) \end{aligned} \tag{2.22}$$

The accuracy order of the multiresolution method is denoted by r. A r-th order accuracy corresponds to a polynomial interpolation of degree $(r-1)$. The degree r is therefore related to the number of required nearest uncles s by the relation $r = 2s+1$. The corresponding coefficients used in the computations are

$$\begin{cases} r = 3 \;\Rightarrow\; \gamma_1 = -\dfrac{1}{8} \\ \\ r = 5 \;\Rightarrow\; \gamma_1 = -\dfrac{22}{128},\ \gamma_2 = \dfrac{3}{128} \end{cases} \tag{2.23}$$

The *detail* is the difference between the exact and the predicted value. In the 1D case, it is defined as

$$\bar{d}_{l,i} = \bar{u}_{l,i} - \hat{u}_{l,i} \tag{2.24}$$

These coefficients are redundant, the sum of the details for all the brothers of a parent cell being equal to zero by definition (Harten [54]). Given that a parent has 2^d children, only $2^d - 1$ details are independent. Thus, the knowledge of the cell-average value on the 2^d children is equivalent to the knowledge of the cell-average value of the parent and these $2^d - 1$ independent details. This can be expressed by

$$(\bar{u}_{l+1,2i}, \bar{u}_{l+1,2i+1}) \longleftrightarrow (\bar{d}_{l+1,2i}, \bar{u}_{l,i})$$

For more details on this equivalence, we refer to [54]. For a given level l, it can be summarized by

$$\bar{U}_l \longleftrightarrow (\bar{D}_l, \bar{U}_{l-1})$$

Repeating this operation recursively on L levels, one gets the so-called *multiresolution transform* on the cell-average values [54].

$$\bar{\mathbf{M}} : \bar{U}_L \longmapsto (\bar{D}_L, \bar{D}_{L-1}, \ldots, \bar{D}_1, \bar{U}_0) \tag{2.25}$$

In the case $r = 1$, we can remark that, as shown in [81], the details $d_{l+1,2i}$ and $d_{l+1,2i+1}$ are related to the gradient of u in $x_{l,i}$ by

$$d_{l+1,2i} = -d_{l+1,2i+1} = \frac{\Delta x_{l+1}}{2} \left(\frac{\partial u}{\partial x} \right)_{l,i} + O(\Delta x_{l+1}^2). \tag{2.26}$$

For the 2D case, we denote by $\Omega = \Omega_{0,0,0}$ the root cell, $\Omega_{l,i,j}$, $0 \leq l < L$, $(i,j) \in \Lambda_l$ the different node cells, by $\bar{q}_{l,i,j}$ the cell-average value of the quantity q on the cell $\Omega_{l,i,j}$. For ease of notation, we denote by $\bar{Q}_l = (\bar{q}_{l,i,j})_{(i,j)\in\Lambda_l}$ the ensemble of the existing cell-average values at the level l.

The projection operator for a regular Cartesian grid is then defined by

$$\bar{u}_{l,i,j} = (P_{l+1\to l}\, \bar{U}_{l+1})_{i,j} = \frac{1}{4} \sum_{n=0}^{1} \sum_{p=0}^{1} \bar{u}_{l+1,2i+n,2j+p}$$

and the prediction operator based on a linear polynomial interpolation is defined by, for $n, p \in \{0, 1\}$,

$$\hat{u}_{l+1,2i+n,2j+p} = I(\bar{U}_l; l+1, 2i+n, 2j+p)$$

The four values $I(\bar{U}_l; l+1, 2i, 2j)$, $I(\bar{U}_l; l+1, 2i+1, 2j)$, $I(\bar{U}_l; l+1, 2i, 2j+1)$, and $I(\bar{U}_l; l+1, 2i+1, 2j+1)$ are given in appendix B.2.
As in the 1D case, the details are defined by $\bar{d}_{l,i,j} = \bar{u}_{l,i,j} - \hat{u}_{l,i,j}$ and the knowledge of the cell-average values on the 4 children is equivalent to the knowledge of the cell-average value of the parent and 3 independent details.

Analogously to the 2D case, for the 3D case we denote by $\Omega = \Omega_{0,0,0,0}$ the root cell, $\Omega_{l,i,j,k}$, $0 \leq l < L$, $(i,j,k) \in \Lambda_l$ the different node cells, $\bar{q}_{l,i,j,k}$ the cell-average value of the quantity q on the cell $\Omega_{l,i,j,k}$, and $\bar{Q}_l = (\bar{q}_{l,i,j,k})_{(i,j,k)\in\Lambda_l}$ the ensemble of the existing cell-average values at the level l.

The projection operator for a regular Cartesian grid becomes

$$\bar{u}_{l,i,j,k} = (P_{l+1\to l}\, \bar{U}_{l+1})_{i,j,k} = \frac{1}{8} \sum_{n=0}^{1} \sum_{p=0}^{1} \sum_{q=0}^{1} \bar{u}_{l+1,2i+n,2j+p,2k+q}$$

and the prediction operator based on a linear polynomial interpolation is defined by, for $n, p, q \in \{0, 1\}$,

$$\hat{u}_{l+1,2i+n,2j+p,2k+q} = I(\bar{U}_l; l+1, 2i+n, 2j+p, 2k+q).$$

For the eight values $I(\bar{U}_l; l+1, 2i+n, 2j+p, 2k+q)$, $n,p,q \in \{0,1\}$, we refer to the appendix B.3.
As in the 1D and 2D cases, the details are $\bar{d}_{l,i,j,k} = \bar{u}_{l,i,j,k} - \hat{u}_{l,i,j,k}$ and the knowledge of the cell-average values on the 8 children is equivalent to the knowledge of the cell-average value of the parent and 7 independent details.

In conclusion, the knowledge of the cell-average values of all the leaves is equivalent to the knowledge of the cell-average value of the root and the details of all the other nodes of the tree structure.

2.3.3 Adaptive multiresolution and finite volumes

The principle of the *adaptive multiresolution* is to transform the cell-averages contained in the leaves into the cell-average of the root cell and a series of details in the nodes of the graded tree, as explained in previous subsection. The *thresholding* operation then consists in removing the cells whose detail is smaller than a prescribed tolerance, i.e.

$$|\bar{d}_{l,i}| < \epsilon_l \ . \tag{2.27}$$

where ϵ_l is the prescribed tolerance at the level l. This way, the global error due to the adaptive multiresolution scheme can be estimated. It will be the subject of section 2.3.5.

The general principle is the following: given the initial condition, one can build an *initial* graded tree data structure. On the tree, we add one more level as *security zone* [64, 65], in order to forecast the tree structure needed after one time evolution step. As we choose a multiresolution on the cell-average values, each node contains a cell-average. These values are used for the *finite volume* time evolution. For the flux computations, we use the cell-averages in the adjacent cells and, when not existing, in the adjacent virtual cells. However, it is no use computing the time evolution on all the nodes. We only compute the time evolution on the leaves, and then we can get the new cell-averages on all the nodes by a recursive projection from leaves to root. This procedure is called a *tree refreshing*.

After the time evolution, a multiresolution transform is performed to compute the details. When a cell has a detail smaller than a prescribed tolerance and when its deletion does not affect the graded tree data structure, the cell is removed from memory. Then, one more level is added everywhere as security zone.

This can be summarized by the following relation

$$\begin{aligned}
(\bar{u}^n_{l,i})_{(l,i)\in\mathcal{L}(\Lambda^n)} &\xrightarrow{\bar{\mathbf{E}}(\Delta t)} (\bar{u}^{n+1}_{l,i})_{(l,i)\in\mathcal{L}(\Lambda^n)} \\
(\bar{u}^{n+1}_{l,i})_{(l,i)\in\mathcal{L}(\Lambda^n)} &\xrightarrow{\bar{\mathbf{M}}} (\bar{u}^{n+1}_{0,0}, \bar{d}^{n+1}_{l,i})_{(l,i)\in\Lambda^n} \\
(\bar{u}^{n+1}_{0,0}, \bar{d}^{n+1}_{l,i})_{(l,i)\in\Lambda^n} &\xrightarrow{\bar{\mathbf{T}}(\epsilon_l)} (\bar{u}^{n+1}_{0,0}, \bar{d}^{n+1}_{l,i})_{(l,i)\in\tilde{\Lambda}^{n+1}} \\
(\bar{u}^{n+1}_{0,0}, \bar{d}^{n+1}_{l,i})_{(l,i)\in\tilde{\Lambda}^{n+1}} &\xrightarrow{\mathbf{A}} (\bar{u}^{n+1}_{0,0}, \bar{d}^{n+1}_{l,i})_{(l,i)\in\Lambda^{n+1}} \\
(\bar{u}^{n+1}_{0,0}, \bar{d}^{n+1}_{l,i})_{(l,i)\in\Lambda^{n+1}} &\xrightarrow{\bar{\mathbf{M}}^{-1}} (\bar{u}^{n+1}_{l,i})_{(l,i)\in\mathcal{L}(\Lambda^{n+1})}
\end{aligned} \tag{2.28}$$

where $\bar{\mathbf{M}}$ is the *multiresolution transform* operator, $\bar{\mathbf{M}}^{-1}$ its inverse operator, $\bar{\mathbf{T}}(\epsilon_l)$ the *thresholding* operator with the prescribed tolerance ϵ_l, $\mathbf{A}$ the *add security zone* operator, and $\bar{\mathbf{E}}$ the discrete *time evolution* operator, as defined in (2.7). In the following, for ease of notations, we denote by $\mathbf{T} = \bar{\mathbf{T}} \circ \mathbf{A}$.

2.3.4 Conservative flux computation

To illustrate the conservative flux computation, we first consider a 1D leaf $\Omega_{l+1,2i+1}$ whose cousins in the right direction $\Omega_{l+1,2i+2}$ and $\Omega_{l+1,2i+3}$ are virtual. Therefore their father $\Omega_{l,i+1}$ is a leaf.

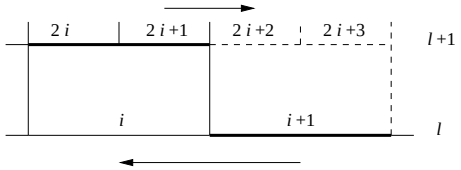

Figure 2.4: Ingoing and outgoing flux computation in 1D for two different levels.

As shown in Fig. 2.4, the outgoing flux from $\Omega_{l+1,2i+1}$ in the right direction $F_{l+1,2i+1 \to l+1,2i+2}$ is not balanced with the outgoing flux from $\Omega_{l,i+1}$ in the left direction $F_{l,i+1 \to l,i}$. Of course, we could directly compute the outgoing fluxes from $\Omega_{l+1,2i+1}$ to $\Omega_{l,i+1}$ in 1D, but such a computation cannot be extended to higher dimensions, as we can see in Fig. 2.5.

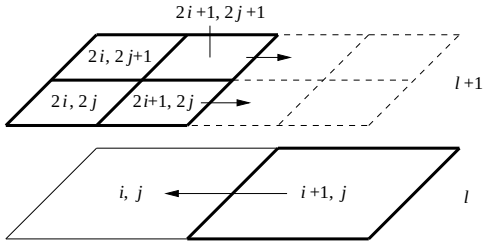

Figure 2.5: Ingoing and outgoing flux computation in 2D for two different levels.

So we decided to compute only the ones at the level $l+1$ and to set the ingoing flux on the leaf of level l equal to the sum of the outgoing fluxes on the leaves of level $l+1$, i.e.

$$F_{l,i,j \to l,i+1,j} = F_{l+1,2i+1,2j \to l+1,2i+2,2j} + F_{l+1,2i+1,2j+1 \to l+1,2i+2,2j+1} \cdot$$

This choice ensures a strict conservativity in the flux computation between cells of different levels, without increasing significantly the number of costly flux evaluations.

2.3.5 Error analysis

The global error between the cell-average values of the exact solution at the level L, denoted by $\bar{u}^L_{ex}$, and those of the multiresolution computation with a maximum level L, denoted by $\bar{u}^L_{MR}$, can be decomposed into two errors

$$||\bar{u}^L_{ex} - \bar{u}^L_{MR}|| \leq ||\bar{u}^L_{ex} - \bar{u}^L_{FV}|| + ||\bar{u}^L_{FV} - \bar{u}^L_{MR}|| \tag{2.29}$$

where $||\cdot||$ denotes e.g. the $\mathcal{L}^1$, $\mathcal{L}^2$, or $\mathcal{L}^\infty$ norms. The first error on the right-hand side, called *discretization error* is the one of the finite volume scheme on the finest grid of level L. It can be bounded by

$$||\bar{u}^L_{ex} - \bar{u}^L_{FV}|| \leq C\, 2^{-\alpha L} \ , \ C > 0 \tag{2.30}$$

where α is the convergence order of the finite volume scheme. In the present case, as we use second-order accurate schemes in time and space, we have $\alpha \leq 2$ and the best we can expect is $\alpha = 2$.

For the second error, called *perturbation error*, Cohen *et al* [31] showed in the hyperbolic case and under certain assumption, i.e. that, if the details on a level l are deleted when smaller than a prescribed tolerance ϵ_l, if the discrete time evolution operator $\bar{\mathbf{E}}$ is contractive for the chosen norm and if the tolerance ϵ_l at the level l is set to

$$\epsilon_l = 2^{d(l-L)}\, \epsilon$$

where d is the space dimension, that then the difference between finite volume solution on fine grid and solution obtained by multiresolution accumulates in time and verifies

$$||\bar{u}^L_{FV} - \bar{u}^L_{MR}|| \leq C\, n\epsilon \ , \ C > 0 \tag{2.31}$$

where n denotes the number of time steps and $||\cdot||$ denotes here the $\mathcal{L}^1$-norm. At a fixed time $T = n\,\Delta t$, this leads to

$$||\bar{u}^L_{FV} - \bar{u}^L_{MR}|| \leq C\, \frac{T}{\Delta t}\epsilon \ , \ C > 0.$$

For the linear convection-diffusion equation with the numerical scheme defined above, the time step Δt, following (2.18), must verify

$$\Delta t \leq \frac{\Delta x^2}{4\nu + c\Delta x}$$

Denoting X the size of the domain and Δx the smallest space step, we have $\Delta x = X\, 2^{-L}$, from which we deduce that

$$\Delta t = C\frac{\Delta x^2}{4\nu + c\Delta x} = C\frac{X\, 2^{-2L}}{4\nu + cX\, 2^{-L}} \ , \ 0 < C < 1.$$

If we want the perturbation error to be of the same order as the discretization error, we need that

$$\frac{\epsilon}{\Delta t} \propto 2^{-\alpha L}$$

i.e.

$$\epsilon\, 2^{2L}\, \left(4\nu + cX\, 2^{-L}\right) \propto 2^{-\alpha L}$$

Defining the Peclet number $Pe = cX\nu^{-1}$, the previous condition can be rewritten as

$$\epsilon \propto \frac{2^{-(\alpha+1)L}}{Pe + 2^{L+2}} \tag{2.32}$$

For the inviscid case (i.e. $\nu = 0$ or $Pe \to +\infty$), (2.32) is equivalent to the result obtained in [31], i.e. $\epsilon \propto 2^{-(\alpha+1)L}$. In the numerical computations in the next chapter, the so-called *reference tolerance* will be set to

$$\epsilon_R = C\frac{2^{-(\alpha+1)L}}{Pe + 2^{L+2}} \tag{2.33}$$

To choose an acceptable value for the factor C, a series of computations with different tolerances will be necessary, as shown in the next chapter.

2.4 Algorithm

In the following, the principle of the algorithm is presented. First, depending on the initial condition, an *initial graded tree* is created. Then, given the graded tree structure, a *time evolution* is made on the *leaves*. Then details are computed by *multiresolution transform*, in order to *remesh* the tree. To be able to navigate inside the tree structure, we propose to use a *recursive* algorithm. The chosen data structure can handle 1D, 2D and 3D Cartesian geometries.

2.4.1 Description

A flow chart of the algorithm is given in Fig. 2.6. A more detailed description is given below.

Step 1 INITIALIZE

- **Initialize parameters**
  e.g. number of Runge-Kutta (RK) steps, number of time steps, maximum level, domain size
- **Create the initial graded tree structure**
  - Create first cell (root) and compute its cell-average value with the initial condition
  - Split cell and compute the cell-average values in the children cells with the initial condition
  - Compute details in the children cells by *multiresolution transform*

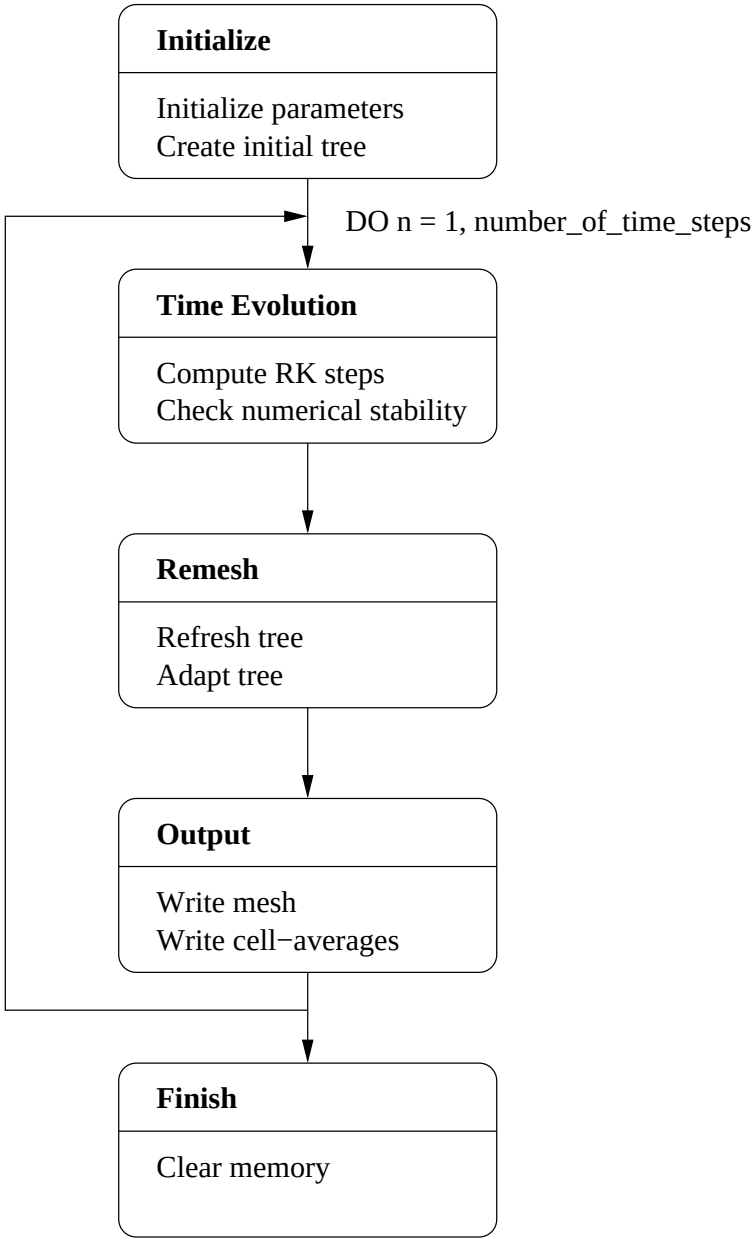

Figure 2.6: Flow chart of the algorithm.

- IF the detail in a child cell is larger than the prescribed tolerance, THEN split this child
- Former child becomes a parent. Repeat the same procedure until all the children cells have low details or the maximum level is reached.

DO n=1, number_of_time_steps

Step 2 TIME EVOLUTION

- **Compute Runge-Kutta steps**
  DO m=0, number_of_RK_steps-1
  - Compute divergence operator for all the leaves
    Compute $(\bar{\mathcal{D}}_{l,i}^{n,m})_{(l,i)\in\mathcal{L}(\Lambda)}$
  - Compute Runge-Kutta step for all the leaves
    e.g. for number_of_RK_steps=2,
    $m=0$: $\bar{u}_{l,i}^{n,1} = \bar{u}_{l,i}^{n,0} + \Delta t \bar{\mathcal{D}}_{l,i}^{n,0},\ 0 \le l < L,\ i \in \mathcal{L}(\Lambda_l)$
    $m=1$: $\bar{u}_{l,i}^{n+1,0} = \frac{1}{2}\left[\bar{u}_{l,i}^{n,0} + \bar{u}_{l,i}^{n,1} + \Delta t \bar{\mathcal{D}}_{l,i}^{n,1}\right],\ 0 \le l < L,\ i \in \mathcal{L}(\Lambda_l)$

  END DO m
- **Check numerical stability**
  IF one value is overflow THEN the computation is considered as numerically unstable
- Compute integral values
  e.g. $\int_\Omega |u|\, dx$

Step 3 REMESH

- **Refresh Tree**
  Recalculate values in nodes and virtual leaves by projection from leaves
- **Adapt the graded tree structure**
  - For the whole tree from leaves to root $(0 \le l < L, i \in \Lambda_l)$
    - Compute detail in node $d_{l,i}$ by *multiresolution transform*
    - IF the details in this node and in its brothers are smaller than the prescribed tolerance
      THEN the cell and its brothers are *deletable*
  - For the whole tree from leaves to root $(0 \le l < L, i \in \Lambda_l)$
    - IF this node and all its children nodes are deletable
      AND the children nodes are simple leaves (i.e. they are leaves without virtual children)
      THEN delete children
      (It means that we keep one more level)
    - IF this node has no children
      AND it is not deletable
      AND it is not at the maximum level

THEN create children for this node
(It means that we add one more level for each undeletable leaf)

Step 4 OUTPUT
Write mesh and cell-average values into a file.

END DO n

Step 5 FINISH
Deallocate tables

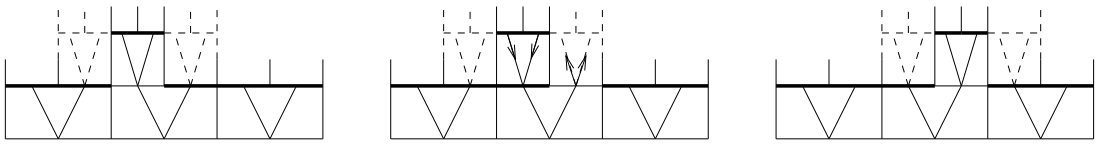

Figure 2.7: Sketch of a time evolution of tree structure at time step t^n (*left*), at time step t^{n+1} before remeshing (*middle*), and at time step t^{n+1} after remeshing (*right*). Deletable cells are represented by a *bold* line, undeletable cells by a *thin* line, and virtual leaves by a *dotted* line.

Thus, the algorithm can schematically be summarized by

$$\bar{u}^{n+1} = \bar{\mathbf{M}}^{-1} \cdot \mathbf{T}(\epsilon) \cdot \bar{\mathbf{M}} \cdot \bar{\mathbf{E}}(\Delta t) \cdot \bar{u}^n \tag{2.34}$$

where $\bar{\mathbf{M}}$ is the *multiresolution transform* operator, $\bar{\mathbf{M}}^{-1}$ its inverse operator, $\mathbf{T}(\epsilon)$ the *thresholding* operator with the prescribed tolerance ϵ, including the security zone, and $\bar{\mathbf{E}}$ the discrete *time evolution* operator, as defined in (2.7).

2.4.2 Dynamical data structure

In the implementation of the algorithm, we use a dynamic graded tree structure to represent data in the computer memory. The adaptive grid corresponds to a set of nested dyadic grids generated by refining recursively a given cell depending on the local regularity of the solution.

In the program, the tree is represented by a set of nodes with links between them. The main element of the tree structure is the *node*, which consists of a set of *geometric and physical quantities*, and *pointers to the children*, which are in the next finer subgrid. The *root* is the first cell of the tree structure.

Each node can be addressed by its level number l and its coordinate in this level i (i, j in 2D, and i, j, k in 3D respectively). The procedure *GetNode* achieves this goal: starting from the root element, it finds the path to the cell, level by level, by opting for the child which is an ancestor of the target cell.

Thus, any node can be found by a maximum of L steps, L being the maximal level number. Denoting by $N_{\max}$ the maximal number of cells, we have $N_{\max} = 2^{dL}$, i.e. $L = \frac{1}{d}\log_2 N_{\max}$, d being the dimension. Therefore, in the worst case, the global algorithm is of $O(N \log N)$ complexity. Nevertheless, for a highly compressed solution, the L steps are required only in small regions and the number of cells is usually much smaller that N_{max}.

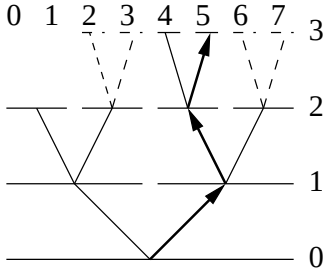

Figure 2.8: Path used by *GetNode* to reach the node $l = 3$, $i = 5$.

Another possibility to avoid a *GetNode* procedure would be the use of a hash-table [70]. In this case, the algorithm is at least of $O(N)$ complexity. The trade off is that this table can be large and requires much memory, especially for large scale 3D computations. That is why we decided here to opt for a solution which optimizes the memory requirements, with a slightly more complex algorithm.

2.4.3 Implementation

The conservative fully adaptive multiresolution algorithm has been implemented in our experimental code named CARMEN. Its version 1.0 solves PDEs for 1D, 2D and 3D geometries. In order to provide good portability, the language C++ was chosen for the code implementation. The results reported here were obtained by running the code on a x86 PC and AMD Cluster.

There are two files which determine the parameters of the computation.

- `carmen.ini` contains the description of the initial condition (Fig. 2.9);
- `carmen.par` is the complete list of parameters for the computations (Fig. 2.10).

The result of the running program is a set of files `.dat` in ASCII format for selected time steps.

2.5 Conclusion

In this chapter, we have presented the adaptive multiresolution method for solving parabolic PDEs in one, two and three space dimensions for Cartesian geometries. Applying a finite volume discretization with an explicit time integration, both of second order, we employ an

```
// --- Additionnal variables ----------------------------------------

float r;
float pi = 3.141593;
float a  = -pi/6;
float R = 1.;

float x2, y2;

// --- Define initial condition Q[i] in function of (x,y,z) ---------

x2 = .25*( x*cos(a) + y*sin(a) );
y2 =     - x*sin(a) + y*cos(a)  ;

r = sqrt( x2*x2 + y2*y2 );

if (r < R)
{
        Q[1] = 1.;
        Q[2] = 0.;
}
else
{
        Q[1] = exp(1-r/R);
        Q[2] = 1-exp(Le*(1-r/R));
}
```

Figure 2.9: Example of file `carmen.ini`.

adaptive multiresolution scheme to represent the solution on locally refined nested grids. The fluxes are evaluated on the adaptive grid in a conservative way. A dynamical adaptation strategy to advance the grid in time and to follow the time evolution of the solution exploits the multiresolution representation. Finally, the algorithm used for the numerical simulations of the next chapters has been presented.

The originality of the method relies on the extension of the adaptive multiresolution scheme initially developed for hyperbolic equations in 1D and 2D to the parabolic case and to three space dimensions in Cartesian geometry. Furthermore, we extend the theoretical relation for the level dependent tolerance to maintain the second-order accuracy, previously given for the hyperbolic case, to the parabolic case for linear convection-diffusion equations. Moreover, an original recursive 3D algorithm has been developed in the frame of this thesis.

In the next chapter, the algorithm is numerically validated by solving different parabolic PDEs where analytical solutions are known. In particular, computations are performed on different levels for convection-diffusion and viscous Burgers equations in order to validate

the theoretical relation (2.33) and determine a choice for an optimal threshold.

```
// 1) Time integration -----------------------------------------

RungeKuttaStepNb=2;
PhysicalTime=30.;
//IterationNb = 1;
CFL=.4;
// TimeStep=1.E-4;
Refresh = 100;

// 2) Solved equations -----------------------------------------

EquationType = 4;  // Reaction-diffusion equation

// 3) Geometry -------------------------------------------------

Dimension=2;

XMin[1]=-50.;
XMax[1]=50.;
XMin[2]=-50.;
XMax[2]=50.;

CMin[1]=2;  // 2 = Neuman boundary condition
CMax[1]=2;
CMin[2]=2;
CMax[2]=2;

// 4) Multiresolution ------------------------------------------

Multiresolution = true;
ScaleNb   = 8;
Tolerance = 5.E-02;

// 5) Physics --------------------------------------------------

//Re = 1.;

// 6) Chemistry ------------------------------------------------

Le = 0.3;
Ze = 10.;
Alpha = 0.8;
Radiation = 0.01;
```

Figure 2.10: Example of file `carmen.par`.

Chapter 3

Numerical validation

Abstract. *In this chapter, we validate the adaptive multiresolution method by solving numerically different prototype parabolic PDEs - convection-diffusion, viscous Burgers - where analytical solutions are known. For the linear case, one-, two- and three-dimensional convection-diffusion equations are solved. For the non-linear case, we solve the one-dimensional viscous Burgers equation. The CPU and memory performances, as well as the error to the analytical solution, are compared to the ones obtained by the same numerical schemes using a finite volume method on the finest grid. For both equations, we perform computations with different values of tolerance for the thresholding. We find an accurate value for the constant required for the optimal threshold, devised in Eq. 2.33. Then, performing the computations following this law, we show that CPU and memory performances can be improved using the adaptive multiresolution method, while the accuracy order of the finite volume method is preserved. Finally, we verify that the complexity of the algorithm is well $O(N\ logN)$, N denoting the number of modes, as predicted by the theory.*

3.1 Introduction

In the previous chapter, the adaptive multiresolution method and the algorithm implemented in the computational code have been presented in some detail. Before using it for combustion problems, we first need to verify that the numerical results given by the code are valid, i.e. that both numerical schemes and algorithm give accurate results. In this goal, we solve prototype parabolic PDEs containing the essential features of the "real world" equations, and for which analytical solutions are known. Here, convection-diffusion and viscous Burgers equations have been chosen. Moreover, we need to show that the method is not only accurate, but also more efficient than a non-adaptive one. Therefore we compare the performances and the computational error to the ones obtained by the same finite volume scheme without adaptivity. A classical finite volume algorithm using the same schemes has also been implemented in the code, and CPU time and memory requirements are always expressed as a percent of the ones required by the finite volume algorithm on the regular finest grid. Finally, we need to verify numerically the theoretical relations presented in the previous chapter, i.e. the complexity of the algorithm and

the dependency of the tolerance on the maximal level to maintain the accuracy order of the computation. This kind of adaptive method is efficient only if the accuracy order is preserved, while CPU and/or memory requirements significantly decrease.

The chapter is organized as follows: in Section 3.2, we solve 1D linear convection-diffusion equation for an initial discontinuity using both finite volume and adaptive multiresolution algorithms. In particular, we show the influence of tolerance and maximal level on the four control elements: CPU compression, memory compression, $\mathcal{L}^1$ error, and $\mathcal{L}^\infty$ error, and verify that the reference tolerance, i.e. the tolerance which verifies (2.33), is well adapted to maintain the accuracy order of the finite volume scheme. To show that (2.33) is valid for different Peclet numbers, computations are performed for $Pe = 1000$ and $Pe = 10000$. Then, the dependency of the CPU time per iteration on the number of modes is computed to verify the complexity of the algorithm. Section 3.3 presents the extension to the non-linear case. In that part, the viscous Burgers equation is solved the same way as the convection-diffusion equation, but for only one value of the Reynolds number. Then, Sections 3.4 and 3.5 extend the results of Section 3.2 to two- and three-dimensional Cartesian geometries. Finally, we discuss the numerical result and draw a conclusion.

3.2 One-dimensional convection-diffusion equation

We consider the equation

$$\frac{\partial u}{\partial t} + c\frac{\partial u}{\partial x} = \nu\frac{\partial^2 u}{\partial x^2} \tag{3.1}$$

for $(x,t) \in [-1,1] \times [0,+\infty)$, $c > 0$, $\nu > 0$. Considering as characteristic length scale the size of the domain X and as characteristic time scale $T = \frac{c}{X}$, this equation can be written in the following dimensionless form

$$\frac{\partial u}{\partial t} + \frac{\partial u}{\partial x} = \frac{1}{Pe}\frac{\partial^2 u}{\partial x^2} \tag{3.2}$$

where Pe denotes the Peclet number $Pe = \frac{cX}{\nu}$. We choose as initial condition

$$u_0(x) = \begin{cases} 1 & \text{if} \quad x \leq 0 \\ 0 & \text{if} \quad x > 0 \end{cases}$$

and Dirichlet conditions at the left and right boundaries, i.e.

$$\begin{aligned} u(0,t) &= 1 \\ u(1,t) &= 0 \end{aligned}$$

The analytical solution in an infinite domain is given in Hirsch [58]

$$u_{ex}(x,t) = \frac{1}{2}\,\mathrm{erfc}\left(\frac{x-t}{2}\sqrt{\frac{Pe}{t}}\right) \tag{3.3}$$

In the computations, the boundaries are sufficiently far to consider their influence as negligible.

3.2.1 Numerical results for a given scale and a given tolerance at Pe=1000

The numerical solution of (3.2) at $t = 0.5$ is given in Fig. 3.1 for $Pe = 1000$, $\epsilon = 10^{-3}$, and $L = 11$ scales, which corresponds to a maximum of $2^{11} = 2048$ cells. In the right part of Fig. 3.1, only the leaves of the mesh are represented. The phenomenon observed here is a linear propagation of a contact discontinuity in the right direction, the diffusivity changing the initial discontinuity into a sharp, but continuous, slope. The Peclet number is the control parameter.

First, we can notice that, for the chosen tolerance $\epsilon = 10^{-3}$, the last level $L = 11$ is never required. Then, the highest level is reached around the steep gradient region, which proves that the multiresolution method automatically detects the region where small scales are necessary and tracks the propagation phenomenon. In Fig. 3.2, the time evolution of $\mathcal{L}^\infty$- and $\mathcal{L}^1$-errors are plotted for both finite volume and multiresolution computations. We clearly see that the $\mathcal{L}^\infty$-error decreases with time for the finite volume computation, whereas it slightly increases for the multiresolution computation. The difference between both curves also increases for the $\mathcal{L}^1$-error, although it is not so visible. As a consequence, the *perturbation error* accumulates in time, which confirms the theoretical result in (2.31) for the $\mathcal{L}^1$-error. This result is also satisfied numerically for the $\mathcal{L}^\infty$-error in this case.

3.2.2 Influence of maximal level and tolerance on CPU time, memory, and errors at Pe=1000

In this part, CPU time, memory requirements, $\mathcal{L}^\infty$- and $\mathcal{L}^1$-errors are given for different maximal levels and tolerances. CPU time and memory requirements are compared to the ones obtained by the finite volume method with the same numerical schemes and on the finest regular grid. They are expressed in percentage (Fig. 3.3). The corresponding errors are given in Fig 3.4.

We first notice that, for such a configuration and for $L > 7$, the multiresolution computation is always cheaper in CPU time and memory requirements than the finite volume method on the finest grid. However, the advantage is only significant for a large L, whatever the tolerance. Fig. 3.4 shows that, as expected, a computation cannot be second-order accurate for small scales and big tolerances. As shown in section 2.3.5, the accumulated *perturbation error* is responsible for this loss of accuracy.

3.2.3 Dependency of CPU time, memory, and error on maximal level with the reference tolerance at Pe=1000

In this part, we verify that multiresolution computations with the reference tolerance defined in (2.33)

$$\epsilon_R = C \frac{2^{-(\alpha+1)L}}{Pe + 2^{L+2}} \tag{3.4}$$

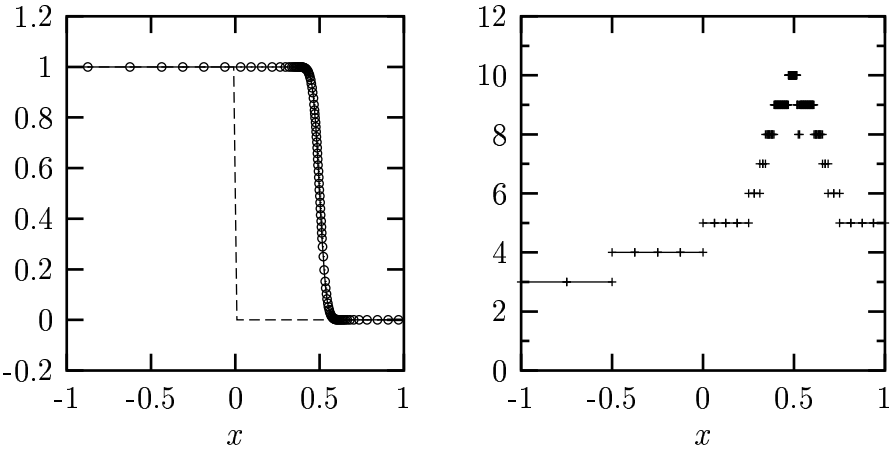

Figure 3.1: Left: Initial solution (*dashed*), analytical solution (*plain*), and computed points by multiresolution (*circles*) at $t = 0.5$ for the convection-diffusion equation $Pe = 1000$, $L = 11$, $\epsilon = 10^{-3}$. Right: corresponding tree structure at $t = 0.5$.

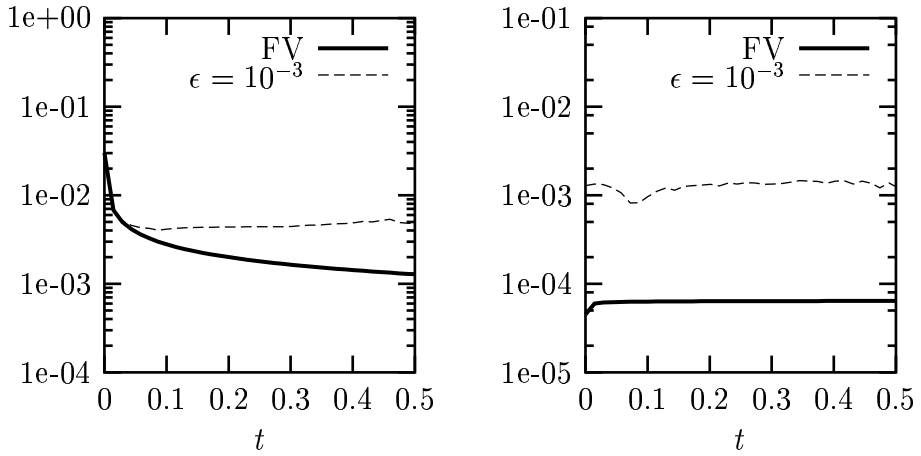

Figure 3.2: Errors $||\bar{u} - \bar{u}_{ex}||_\infty$ (*left*) and $||\bar{u} - \bar{u}_{ex}||_1$ (*right*) from $t = 0$ to $t = 0.5$ for the convection-diffusion equation $Pe = 1000$, $L = 11$, $\epsilon = 10^{-3}$.

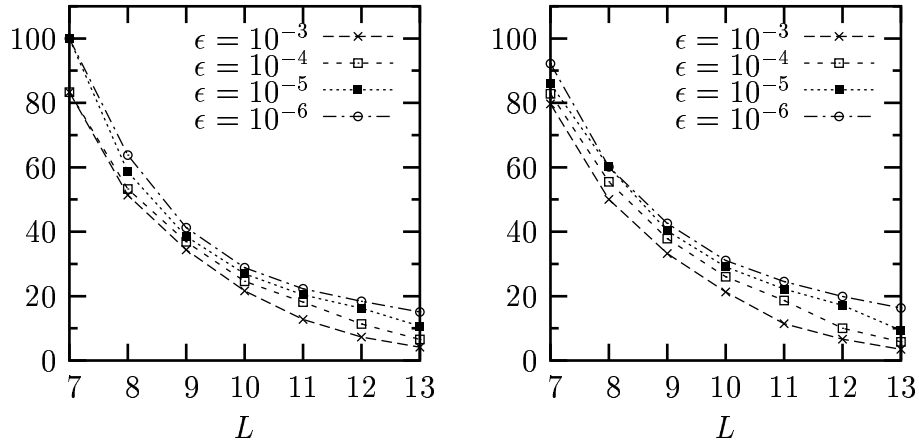

Figure 3.3: % CPU compression (*left*) and % memory compression (*right*) for different scales L and for different tolerances ϵ at $t = 0.2$ for the convection-diffusion equation, $Pe = 1000$.

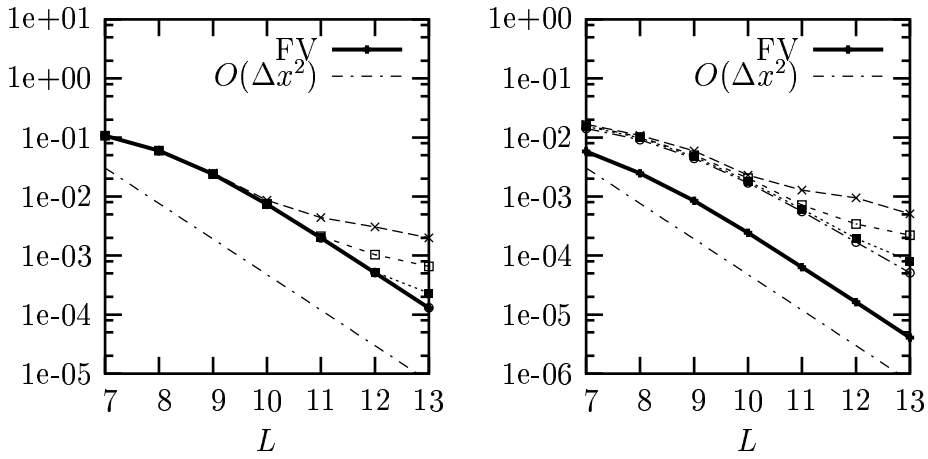

Figure 3.4: Errors $||\bar{u}-\bar{u}_{ex}||_\infty$ (*left*) and $||\bar{u}-\bar{u}_{ex}||_1$ (*right*) for different scales L and different tolerances ϵ at $t = 0.2$ for the convection-diffusion equation, $Pe = 1000$. Same line style as in Fig. 3.3.

enables us to maintain the same second-order accuracy as for the finite volume method on the finest regular grid, while reducing CPU time and memory requirements. To determine the constant C, we refer to the results obtained in the previous part for different tolerances (Fig. 3.4). Reading both curves, we consider as sufficiently accurate the computation performed with $Pe = 1000$, $L = 10$, and $\epsilon = 10^{-4}$. Thus we find a factor $C = 5.10^8$. We observe the second-order accuracy of the multiresolution computation (Fig. 3.6), while CPU time and memory requirements decrease with L and reach a minimum around 20% for high levels (Fig. 3.5).

We also observe no visible difference between finite volume and multiresolution computations in the $\mathcal{L}^\infty$-error curve of Fig. 3.6. This is due to the fact that the maximum of the error is in the region of the steep gradient, where the discretization error is dominating and the perturbation error is negligible, given that all available scales are used there.

3.2.4 Dependency of CPU time, memory, and error on maximal level with the reference tolerance at Pe=10000

To evaluate the influence of the Peclet number in the estimation of ϵ_R, we now perform computations with $Pe = 10000$. The diffusion phenomenon is less important than in the previous case, and therefore the gradient will be steeper. As before, we observe the second-order accuracy of multiresolution computations (Fig. 3.8), while CPU time and memory compressions decrease with L and seem to reach a minimum around 10% for large levels (Fig. 3.7). Due to the fact that there is less diffusion, both CPU time and memory performances are better than for $Pe = 1000$.

As in 3.2.3 and for the same reason, there is no visible difference between finite volume and multiresolution computations in the $\mathcal{L}^\infty$-error curve of Fig. 3.8.

3.2.5 Complexity of the algorithm

In this part, the dependency of the CPU time per iteration against the number of modes N is plotted in Fig. 3.9 for both finite volume and adaptive multiresolution algorithms. The number of modes is here the number of cells used in the computation. For the finite volume method in 1D, the number of modes is constant in the computation. This is not the case when using the adaptive method. Thus we choose to work with the average number of modes in the computation. Denoting by M the average memory compression over time, it is defined by

$$\bar{N} = 2^L \, M \, .$$

As expected, the finite volume algorithm is of order $O(N)$. On the other hand, we verify that the adaptive multiresolution algorithm presented in the previous chapter is well of order $O(\bar{N} \log \bar{N})$. However, $\bar{N}$ is usually much smaller than $N = 2^L$.

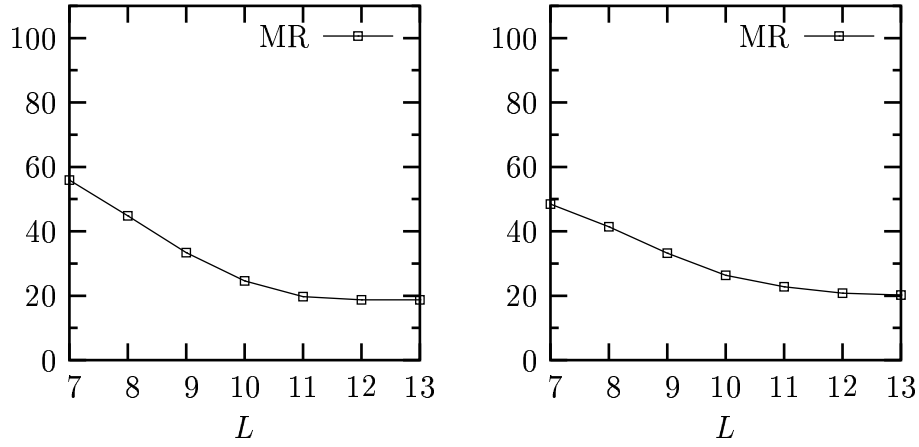

Figure 3.5: % CPU compression (*left*) and % memory compression (*right*) for different scales L and for the reference tolerance ϵ_R at $t = 0.2$ for the convection-diffusion equation, $Pe = 1000$.

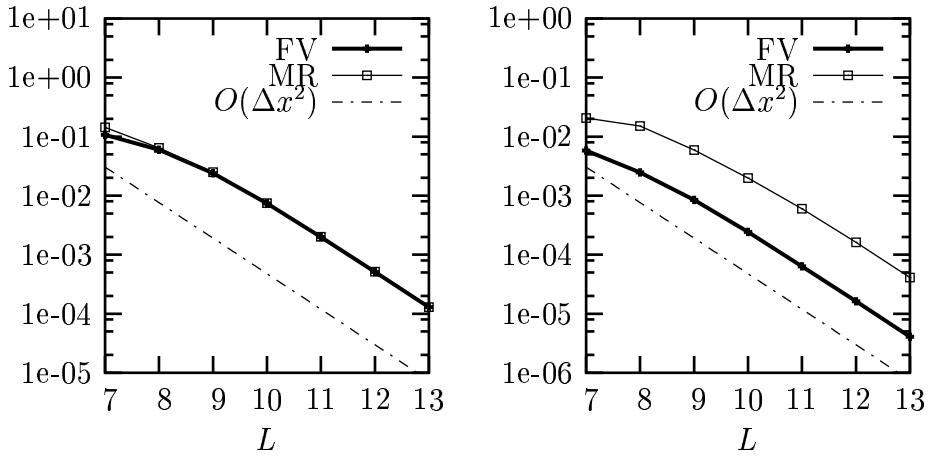

Figure 3.6: Errors $||\bar{u} - \bar{u}_{ex}||_\infty$ (*left*) and $||\bar{u} - \bar{u}_{ex}||_1$ (*right*) for different scales L and the reference tolerance ϵ_R at $t = 0.2$ for the convection-diffusion equation, $Pe = 1000$.

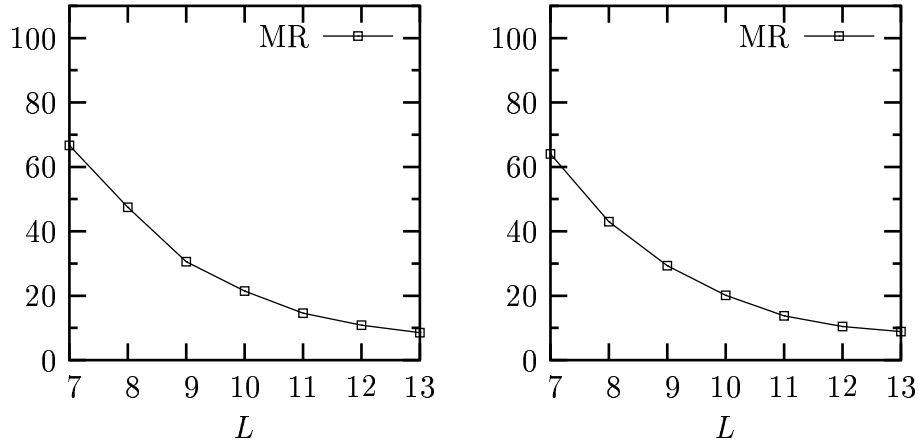

Figure 3.7: % CPU compression (*left*) and % memory compression (*right*) for different scales L and the reference tolerance ϵ_R at $t = 0.2$ for the convection-diffusion equation, $Pe = 10000$.

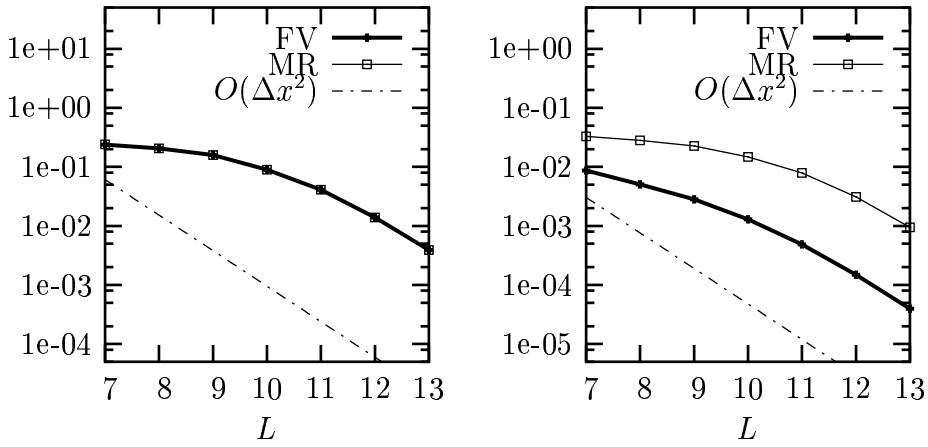

Figure 3.8: Errors $||\bar{u} - \bar{u}_{ex}||_\infty$ (*left*) and $||\bar{u} - \bar{u}_{ex}||_1$ (*right*) for different scales L and the reference tolerance ϵ_R at $t = 0.2$ for the convection-diffusion equation, $Pe = 10000$.

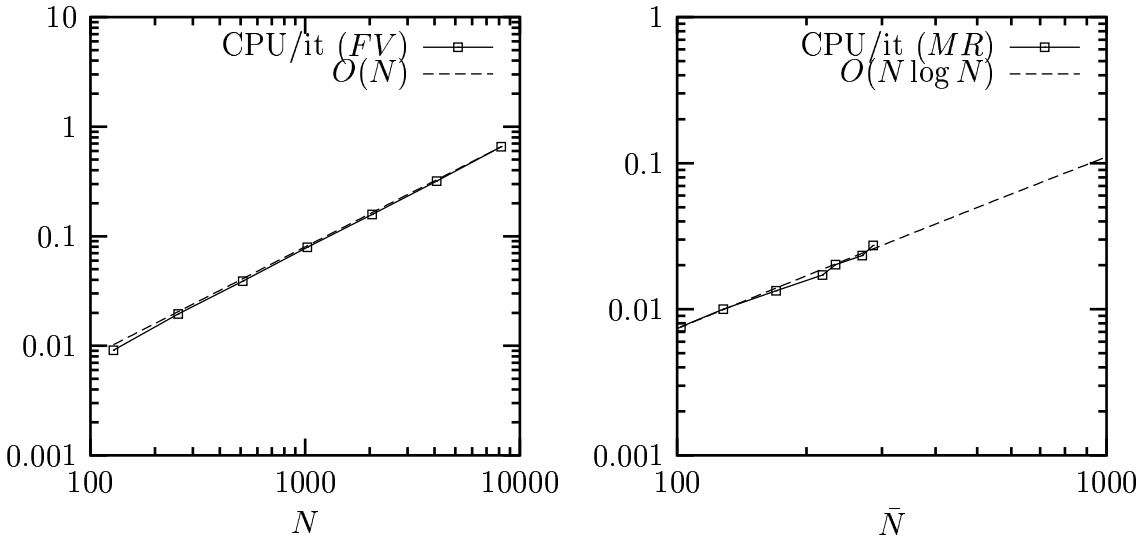

Figure 3.9: CPU time per iteration *vs* number of modes (N for FV, $\bar{N}$ for MR) in log-log scale for finite volume (*left*) and adaptive multiresolution (*right*) algorithms. The convection-diffusion equation is solved with $Pe = 1000$. For the adaptive multiresolution, the tolerance is set to $\epsilon = \epsilon_R$.

3.3 One-dimensional viscous Burgers equation

We now perform multiresolution computations for the viscous Burgers equation, which contains a non-linear convective term, and for which analytical solutions are known. For $(x,t) \in [-1,1] \times [0,+\infty)$, it can be written in the dimensionless form

$$\frac{\partial u}{\partial t} + \frac{\partial}{\partial x}\left(\frac{u^2}{2}\right) = \frac{1}{Re}\frac{\partial^2 u}{\partial x^2} \tag{3.5}$$

where Re is the Reynolds number, with the initial condition

$$u_0(x) = \begin{cases} 1 & \text{if} \quad x \leq 0 \\ 0 & \text{if} \quad x > 0 \end{cases}$$

and Dirichlet conditions at the right and left boundaries, i.e.

$$\begin{aligned} u(0,t) &= 1 \\ u(1,t) &= 0 \end{aligned}$$

The analytical solution in an infinite domain is given in [58]

$$u_{ex}(x,t) = \frac{1}{2}\left[1 - \tanh\left(\left(x - \frac{t}{2}\right)\frac{Re}{4}\right)\right] \tag{3.6}$$

As in the previous section, the boundaries are sufficiently far so that their influence is negligible.

3.3.1 Numerical results for a given scale and a given tolerance at Re=1000

The numerical solution of (3.5) at $t = 0.5$ is given in Fig. 3.10 for $Re = 1000$, $\epsilon = 10^{-3}$, and $L = 11$ scales, which corresponds to a maximum of $2^{11} = 2048$ cells. As for the convection-diffusion computation, only the leaves of the mesh are represented on the right figure. We observe here a non-linear propagation of a "shock" in the right direction, the diffusivity having the same effect on the discontinuity as in the linear case.

We notice that, this time, all available scales are used, given that the gradient is steeper than in the linear case. The time evolution of the errors between computed and analytical solutions are given in Fig. 3.11. This time, one gets the same $\mathcal{L}^\infty$-error as with the finite volume method on the finest grid. Therefore the choice for ϵ is well adapted.

3.3.2 Dependency of CPU time, memory, and error on maximal level and tolerance at Re=1000

As in the linear case, CPU time, memory requirements, $\mathcal{L}^\infty$- and $\mathcal{L}^1$-errors are given for different maximal levels and tolerances. CPU time and memory requirements are compared to the ones obtained by the finite volume method on the finest grid and expressed in percent (Fig. 3.12). The corresponding errors with the analytical solution are given in Fig 3.13.

The main difference with the linear case is a larger discretization error, that we can notice in both finite volume and multiresolution computations. Given that the discretization error is more important than in the linear case, one can choose a larger tolerance than the reference tolerance ϵ_R. Here, the computation is always second-order accurate, except for $\epsilon = 10^{-3}$ and $L = 13$ where the perturbation error is too large. Since the shock is sharper than in the linear case, both CPU time and memory compressions are further increased.

3.3.3 Dependency of CPU time, memory, and error on maximal level with the reference tolerance at Re=1000

In the chosen test-case, we know that $0 \leq u \leq 1$ along the computation. Therefore, the TVD condition defined for the linear case in (2.18) remains valid with

$$\sigma = \frac{u_{\max}\,\Delta t}{\Delta x}, \text{ where } u_{\max} = 1$$

We repeat the computations performed for the convection-diffusion equation with the same reference tolerance ϵ_R, which is this time

$$\epsilon_R = C\frac{2^{-(\alpha+1)L}}{Re + 2^{L+2}} \tag{3.7}$$

where

$$Re = \frac{u_{\max}\,L}{\nu}\,.$$

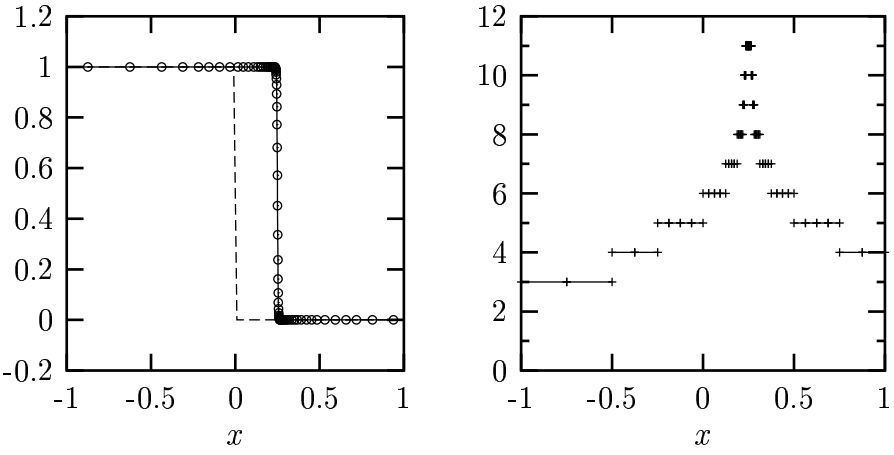

Figure 3.10: Left: Initial solution (*dotted*), analytical solution (*plain*), and computed points by multiresolution (*circles*) at $t = 0.5$ for the viscous Burgers equation $Re = 1000$, $L = 11$, $\epsilon = 10^{-3}$. Right: corresponding tree structure at $t = 0.5$.

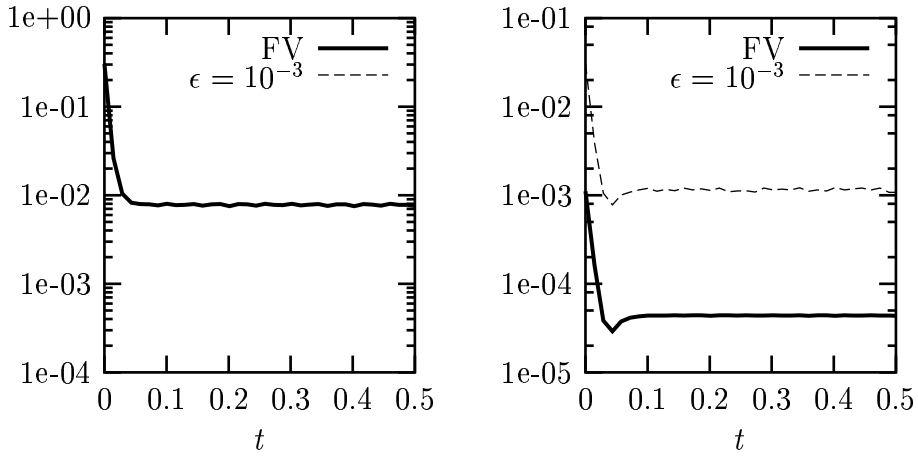

Figure 3.11: Errors $||\bar{u}-\bar{u}_{ex}||_\infty$ (*left*) and $||\bar{u}-\bar{u}_{ex}||_1$ (*right*) for the viscous Burgers equation $Re = 1000$, $t = 0.5$, $L = 11$, $\epsilon = 10^{-3}$.

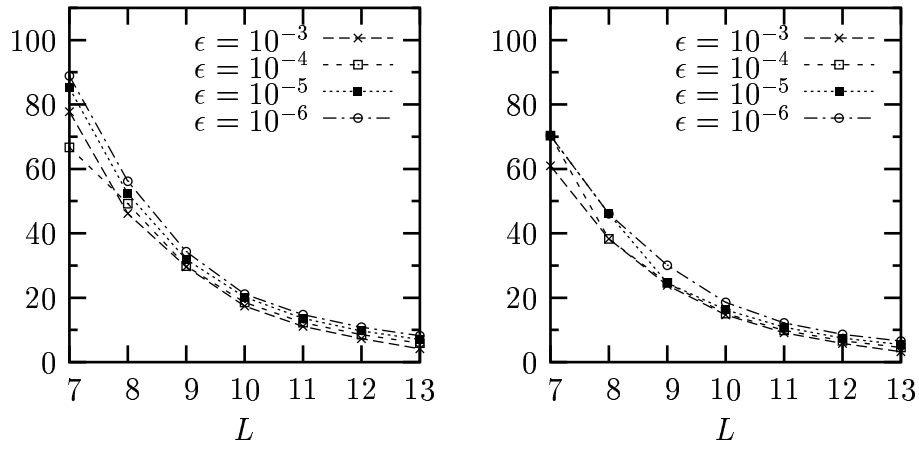

Figure 3.12: % CPU compression (*left*) and % memory compression (*right*) for different scales L and different tolerances ϵ for the viscous Burgers equation at $t = 0.2$, $Re = 1000$.

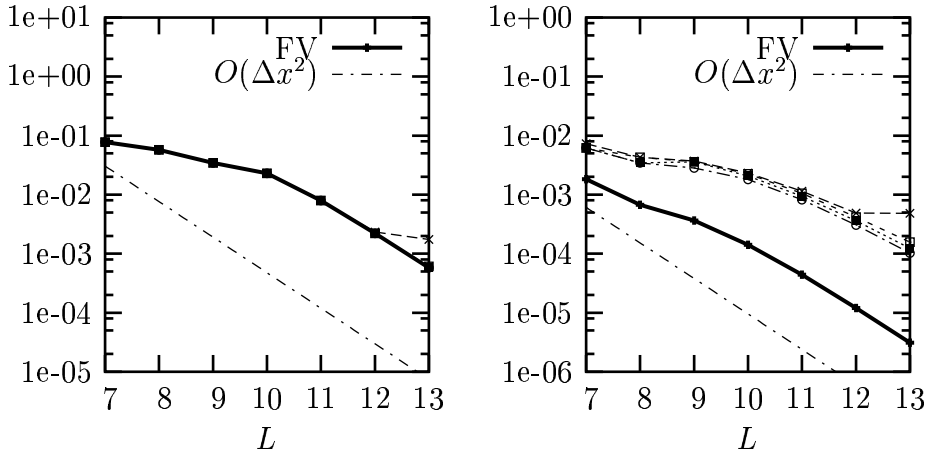

Figure 3.13: Errors $||\bar{u} - \bar{u}_{ex}||_\infty$ (*left*) and $||\bar{u} - \bar{u}_{ex}||_1$ (*right*) for different scales L and different tolerances ϵ for the viscous Burgers equation at $t = 0.2$, $Re = 1000$.

The same value for the factor C is used as in the linear case. We notice the second-order accuracy of the computation ($\mathcal{L}^\infty$ and $\mathcal{L}^1$ errors in Fig. 3.15), the CPU time and memory compression decreasing with L and reaching a minimum around 10% for the highest levels (Fig. 3.14).

We finally remark that the chosen finite volume scheme conserves both momentum and energy. Due to the choice made for flux computations, this is also the case for the adaptive multiresolution scheme. Nevertheless, in the adaptive case, the difference between exact and computed momentum and energy shows small oscillations of amplitude lower than 10^{-5}. This is due to the remeshing of the grid at each time step.

3.4 Two-dimensional convection-diffusion equation

In this part, we study the performances and check the second-order accuracy of the multiresolution scheme with the reference tolerance defined in (2.33) in the 2D case. Therefore we consider the dimensionless equation for $(x, y, t) \in [-5, 5]^2 \times [0, +\infty)$

$$\frac{\partial u}{\partial t} + \mathbf{V} \cdot \nabla u = \frac{1}{Pe} \nabla^2 u \tag{3.8}$$

with the initial condition $u(x, y, 0) = u_0(x, y)$. Here we consider a convection in the x-direction, i.e. $\mathbf{V} = (1, 0)^T$. For the initial condition $u_0(x, y) = \delta(x)\,\delta(y)$, where δ denotes the Dirac distribution, we have the analytical solution in an infinite domain

$$u(x, y, t) = \frac{Pe}{4\,\pi\,t}\, e^{-Pe\,\frac{(x-t)^2+y^2}{4t}} \tag{3.9}$$

To get a Gaussian initial condition, we can change variables ($x \leftarrow x - \tau$, $t \leftarrow t - \tau$, where $\tau > 0$). Thus, given the initial condition

$$u_0(x, y) = \frac{Pe}{4\,\pi\,\tau}\, e^{-Pe\,\frac{x^2+y^2}{4\tau}}$$

we get the analytical solution

$$u(x, y, t) = \frac{Pe}{4\,\pi\,(t+\tau)}\, e^{-Pe\,\frac{(x-t)^2+y^2}{4\,(t+\tau)}} \tag{3.10}$$

For the numerical computations, as in the 1D case, the boundaries are taken sufficiently far from the Gaussian bump, so that their influence can be considered as negligible.

3.4.1 Numerical results for a given scale and a given tolerance at Pe=1000

The numerical solution of (3.8) for an initial Gaussian bump is represented in Fig. 3.16 for $Pe = 1000$, $\epsilon = \epsilon_R$, and $L = 8$ scales, which represents a maximum of $(2^8)^2 = 256^2$

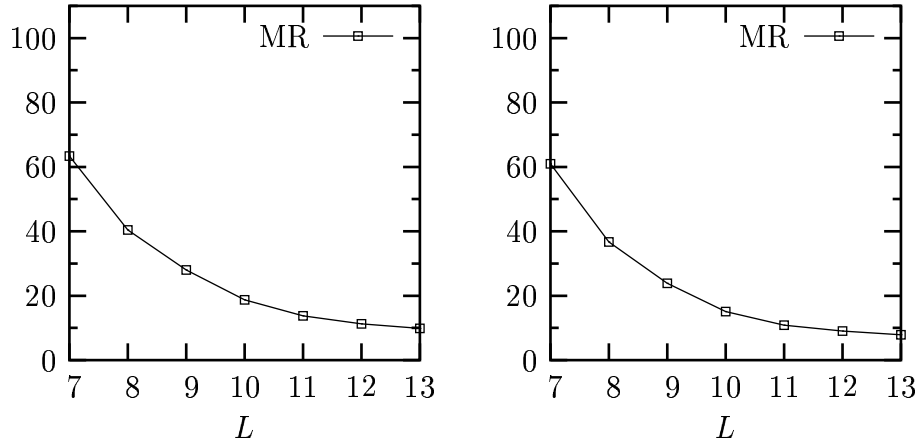

Figure 3.14: % CPU compression (*left*) and % memory compression (*right*) for different scales L and for the reference tolerance ϵ_R for the viscous Burgers equation $Re = 1000$, $t = 0.2$.

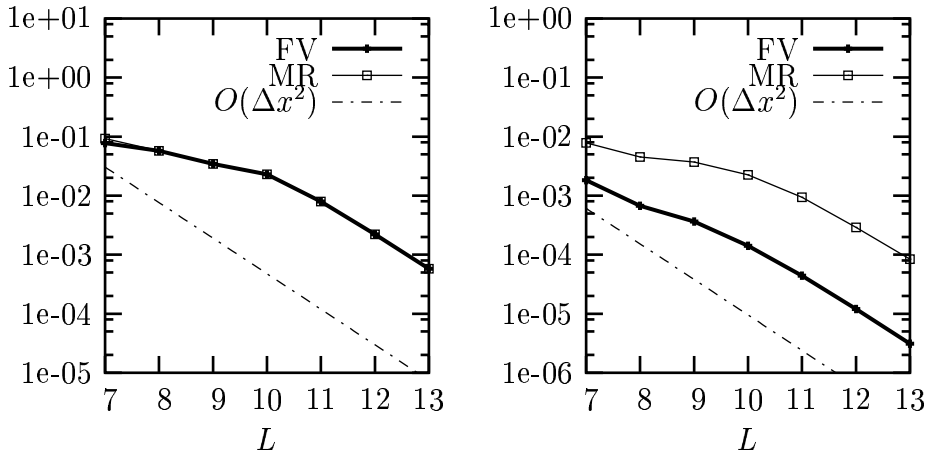

Figure 3.15: Errors $||\bar{u} - \bar{u}_{ex}||_\infty$ (*left*) and $||\bar{u} - \bar{u}_{ex}||_1$ (*right*) for different scales L and for the reference tolerance ϵ_R for the viscous Burgers equation $Re = 1000$, $t = 0.2$.

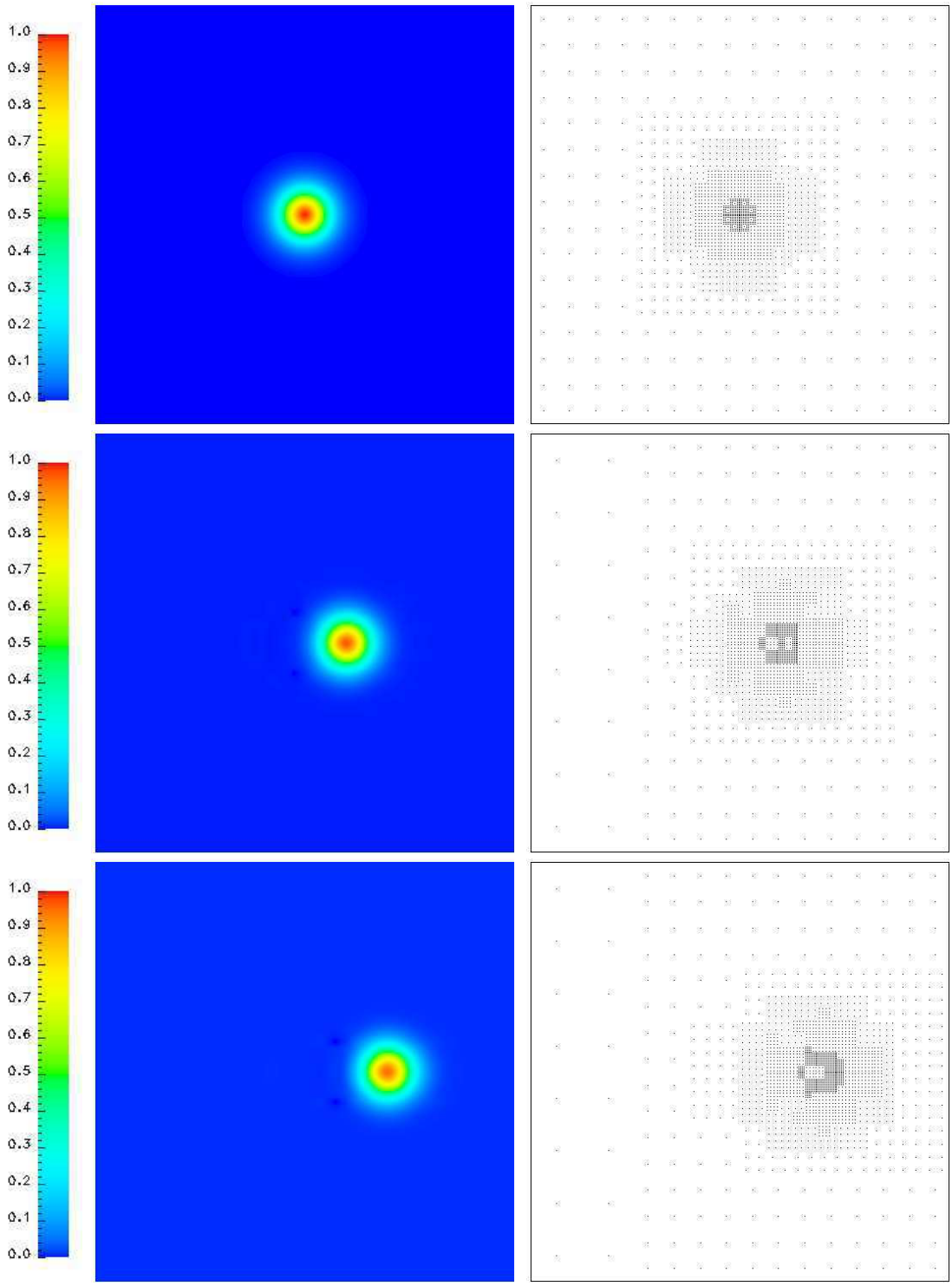

Figure 3.16: Solution u (*left*) and corresponding mesh(*right*) for the 2D convection-diffusion equation at $t = 0$ (*top*), $t = 1$ (*middle*), and $t = 2$ (*bottom*).

cells. In the figures where the corresponding meshes are plotted, each point represents a leaf. For the initial condition, we set $\tau = 0.1$.

We observe the phenomenon of linear propagation of the 2D Gaussian bump in the x-direction. The effect of diffusion is difficult to detect, but we can see that the radius of the smallest circle slightly decreases with time. We also remark that the adaptive mesh follows well the propagation. Nevertheless, although the mesh is well symmetric at the initial condition, we have a mirror symmetry on the horizontal line only, not on the vertical line. This is due to the fact that the advection takes place in the x-direction.

3.4.2 Dependency of CPU time, memory, and error on maximal level with the reference tolerance at Pe=1000

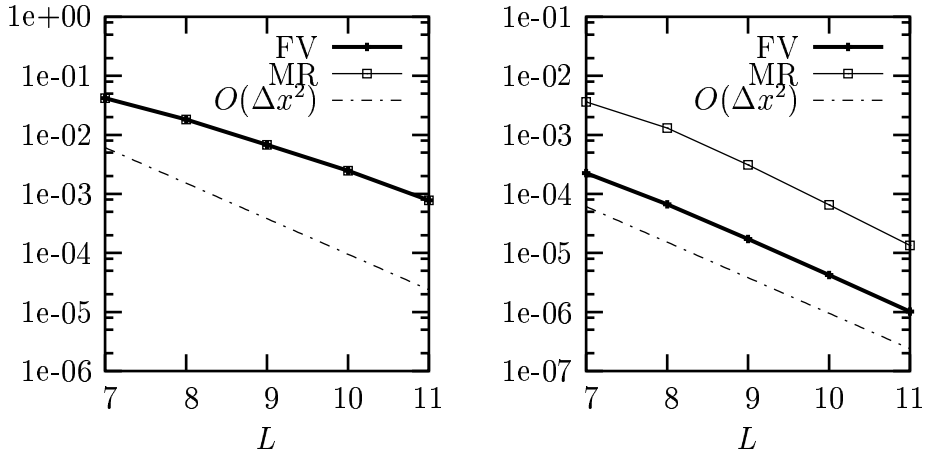

Figure 3.17: Errors $||\bar{u} - \bar{u}_{ex}||_\infty$ (*left*) and $||\bar{u} - \bar{u}_{ex}||_1$ (*right*) for different scales L and the reference tolerance ϵ_R for the 2D convection-diffusion equation $Pe = 1000$, $t = 0.5$.

The definition of the reference tolerance being the same in 1D, 2D or 3D, we use the same one as in the 1D case. We remark here that both CPU and memory compressions are low and stable with L (around 15 % for the CPU compression, 10 % for the memory compression), the errors showing that the computation is well second-order accurate (Fig. 3.17). However, for the $\mathcal{L}^\infty$-norm, it seems that more than 11 scales are necessary to show the second-order accuracy. This time, as no discontinuity exists in the initial condition and as the equation is linear, no steep gradient exists, which explains that the same percentage of leaves is used whatever L, although more levels are used around the Gaussian bump.

3.5 Three-dimensional convection-diffusion equation

Finally, we solve the previous equation in three dimensions. Analogously, an analytical solution can be found for an initial Gaussian bump. Considering the dimensionless equation

CPU compression	2.16 %
Memory compression	1.27 %
$\mathcal{L}^\infty$-error	$6.65.10^{-2}$
$\mathcal{L}^1$-error	$8.41.10^{-3}$

Table 3.1: Adaptive multiresolution method for the 3D advection-diffusion equation: CPU and memory compression compared to the finite volume method on the regular finest grid, errors to the analytical solution.

for $(x, y, z, t) \in [-5, 5]^3 \times [0, +\infty)$

$$\frac{\partial u}{\partial t} + \mathbf{V} \cdot \nabla u = \frac{1}{Pe} \nabla^2 u \tag{3.11}$$

with a convection in the x-direction, i.e. $\mathbf{V} = (1, 0, 0)^T$ and the initial condition

$$u_0(x, y, z) = \frac{Pe}{4\,\pi\,\tau}\, e^{-Pe\,\frac{x^2+y^2+z^2}{4\tau}} ,$$

the analytical solution in an infinite domain is

$$u(x, y, z, t) = \frac{Pe}{4\,\pi\,(t+\tau)}\, e^{-Pe\,\frac{(x-t)^2+y^2+z^2}{4\,(t+\tau)}} \tag{3.12}$$

As in the 2D case, since the boundaries are far from the Gaussian bump, their influence is negligible. The numerical solution of (3.11) is represented in Fig. 3.18 for $L = 7$ scales. The other parameters are the same as in the 2D case.

As before, the Gaussian bump is advected in the x-direction. We observe that, due to diffusion, the region between the isosurfaces $u = 0.5$ and $u = 0.2$ is growing. Here, the computation has been performed only with $L = 7$. CPU and memory compressions, as well as $\mathcal{L}^1$- and $\mathcal{L}^\infty$-errors to the analytical solution are given in Table 3.1. We remark that the compression rate, both for CPU time and memory, is much smaller than in the 2D case, while the errors are comparable to the ones obtained in 2D. The method is therefore more efficient in 3D than in 2D.

3.6 Discussion of the results

In the 1D case, when a "shock" or a contact discontinuity is advected, the adaptive multiresolution method is very efficient, both in terms of CPU time and memory requirements, when compared to the finite volume method using the same numerical schemes on the finest grid. The relative CPU time and memory requirements decrease with the number of levels and reach a minimum which depends on the test-case. Moreover, when the tolerance is set using the thresholding law defined in the previous chapter, the accuracy order of

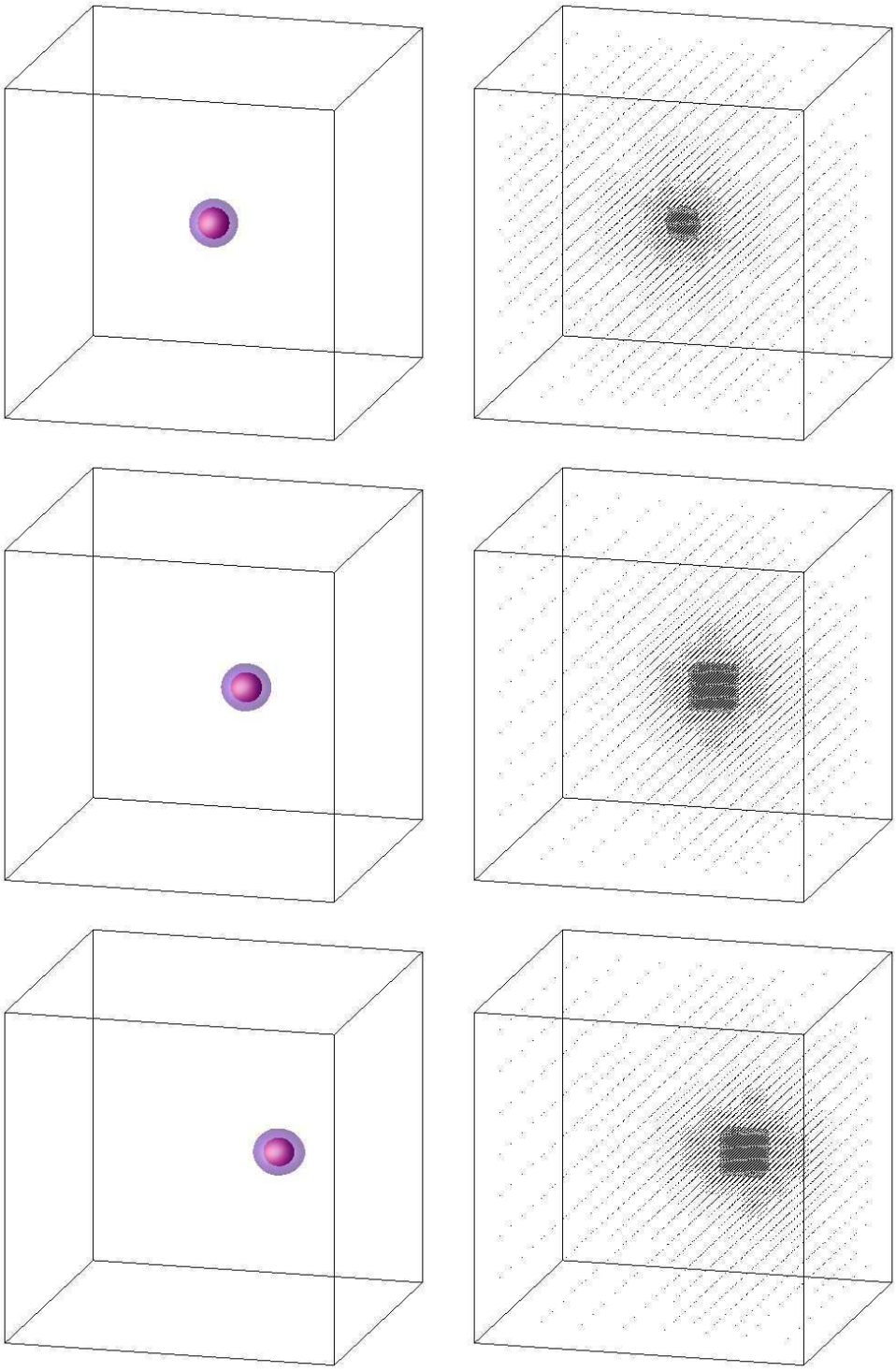

Figure 3.18: Left: Isosurfaces $u = 0.5$ (*red*) and 0.2 (*purple*) for the 3D convection-diffusion equation at $t = 0$ (*top*), $t = 1$ (*middle*), and $t = 2$ (*bottom*). Right: Corresponding meshes.

the numerical schemes can be preserved, while CPU time and memory requirements are reduced.

However, the $\mathcal{L}^1$-errors curves show that only the *slope* of the error is preserved, which means that only the *accuracy order* is preserved, the error remaining larger. Nevertheless, the same effect can also be observed when computing on a distorted mesh instead of a regular Cartesian mesh [41]. The more distorted the mesh is, the larger the error is, even if the accuracy order is preserved.

In the 2D case, when a Gaussian bump is advected instead of a discontinuity, the computation is already efficient for few scales, and thus the gain compared to the finite volume method remains almost constant. This shows that the gain is not inherent to the method, but that it is highly dependent on the chosen configuration. Finally, comparisons of CPU and memory performances for the 2D and 3D cases show that the performance significantly increases with the dimension of the problem.

3.7 Conclusion

In this chapter, we have validated numerically the multidimensional adaptive multiresolution algorithm described in the previous chapter by solving prototype parabolic linear and non-linear parabolic PDEs. We solved the linear convection-diffusion equation for an initial discontinuity in 1D, and for an initial Gaussian bump in 2D and 3D. The non-linear viscous Burgers equation was also solved for an initial discontinuity in 1D. We have verified that the complexity of the algorithm with the chosen data structure is well $O(N \log N)$, N being the number of active modes, as expected in the previous chapter. We have also shown that, when the tolerance is set following the relation (2.33), the accuracy order of the finite volume scheme is preserved, while CPU time and memory requirements significantly decrease. This result has been verified for both linear and non-linear cases in 1D and for the linear case in 2D and 3D.

The theoretical relation (2.33) for choosing the threshold is not general and cannot be applied to other non-linear parabolic PDEs like convection-diffusion-reaction or diffusion-reaction equations. In this case, several computations have to be performed to find an accurate value for the tolerance. Now that the validation of the algorithm has been done, we can use it to simulate flame propagation in the thermodiffusive approximation. This is the objective of the next chapter.

Chapter 4

Application to thermodiffusive flame instabilities

Abstract. *In the two previous chapters, we have described the adaptive multiresolution method and validated it with different test problems. This method enables us to study stiff problems, like e.g. premixed flames for large values of the activation energy. In this chapter, we investigate thermodiffusive flame instabilities for values of the activation energy that are prohibitive in terms of CPU time and memory requirements for computations on an equidistant fine grid. First, we extend the instability diagram of pulsating planar flames to* $Ze > 40$ *and* $Le > 5$. *The new result is compatible with the asymptotic theory for a Zeldovich number sufficiently large. Then, we study instabilities of circular and spherical flame structures - the so-called flame balls - in the fully nonlinear regime and far from the wall. For a flame ball initially stretched, the scenarios of evolution - spherical growth, splitting, extinction - are in agreement with experiments and previous numerical computations using other numerical methods. Then, the study of flame balls interacting with adiabatic walls shows behaviors similar to capillarity for fluid droplets. As perspective for future work, an adaptive computation concerning a flame ball interacting with a vortex is presented.*

4.1 Introduction

The present chapter aims at understanding the instability of premixed flames in the thermodiffusive approximation for large values of the activation energy. The first problem concerns pulsating planar flames, which appear for Lewis numbers greater than unity. When the activation energy is large, e.g. when $Ze > 40$, it becomes a spatially very stiff problem. Pulsating flames have been observed experimentally for both rich, light hydrocarbon/air and lean, heavy hydrocarbon/air mixtures (see e.g. [71, 72, 79]). An important application concerns the combustion of lean mixtures of heavy hydrocarbons such as octane in air ($Le \approx 3$), which is relevant to lean-burning automotive engines. In [60], the theoretical limit between stable and pulsating behaviors has been determined using asymptotic methods and considering $Ze >> 1$. In [77], this limit has been determined numerically in

function of Le and Ze. However, for $Ze > 40$, computations using non-adaptive methods become prohibitive in terms of CPU time, even in 1D, because extremely fine space scales are required to resolve the reaction zone. Consequently, for explicit methods, also very small time steps are required. A fully implicit treatment is possible, but it involves a partial linearization of the source term. An implicit treatment of the diffusive terms only may be disadvantageous, since the source term imposes to use a time step which can sometimes be smaller than the one required by the same discretized equations without source. Thus, the time integration used here is always explicit. Moreover, to the best of our knowledge, the study of large values of Le, i.e. $Le > 5$, has not yet been done. Here we complete the $Le - Ze$ diagram for both large Ze and large Le and compare with the previous theoretical [60] and numerical results [77].

A different problem is the interaction of a flame ball with adiabatic walls. This situation occurs in combustion chambers due to their finite size. The evolution of flame balls far from walls has been studied experimentally in micro-gravity [78, 79] and numerically using non-adaptive Fourier pseudo-spectral methods [13, 47] and adaptive wavelet-vaguelette methods [14]. In these papers, the authors found different scenarios for the evolution of flame balls initially perturbated: extinction, spherical growth, and splitting. These scenarios have been observed experimentally. They also show the existence of steady flame balls in 2D and 3D. In both numerical methods, periodic approximation with sufficiently large period has been chosen, since the interest is the behavior far from the wall. For the problem of a flame ball interacting with adiabatic walls, however, Neuman boundary conditions are required. One solution consists in adding a penalization technique to the previous methods, as proposed in [87]. Another solution, the one chosen here, is the use of an adaptive multiresolution method based on finite volume schemes. The choice of such methods enables to use non-periodic boundary conditions, while reducing significantly CPU time and memory requirements for stiff problems. In the present work, we study the evolution of flame balls initially stretched and far from the wall. The results are compared to the ones obtained with the periodic approximation. Then, we study the case of a planar flame interacting with an adiabatic wall, which leads to a 1D problem. We also study the case of flame balls interacting with adiabatic walls in 2D and 3D configurations. The aim is to show the different scenarios of evolution after the interaction. The last problem studied here concerns flame balls in a moving fluid. As example, we consider a flame ball interacting with a vortex.

The present chapter is organized as follows: in Section 4.2, we present adaptive simulation of steady and propagating planar flames. The numerical results are compared to theoretical ones, obtained with an asymptotic development in the large values of the activation energy. Section 4.3 deals with pulsating planar flames. In particular, the description of this phenomenon, the bifurcation diagram $Le - Ze$, and the amplitude of pulsations for moderate Ze are given. Then, Section 4.4 is concerned with multidimensional simulations of flame balls initially stretched, to check if they undergo instabilities. The results are compared to the ones obtained by classical Fourier pseudo-spectral and adaptive wavelet-vaguelette methods. Section 4.5 is devoted to the interaction of a flame with an adiabatic wall, first in a planar flame, which corresponds to a 1D case, then for a flame ball in 2D and

in 3D. The next section presents a flame ball interacting with a vortex, a first computation performed with a moving fluid using this method. Finally, we discuss the numerical results and conclude.

4.2 Adaptive simulation of planar flames

Planar flames in the thermodiffusive approximation have been presented in Section 1.6, and the structure of *steady planar flames* has been explained in some detail. In this section, we perform adaptive computations of steady and propagating planar flames in order to check the accuracy of the adaptive computations and show the efficiency of the adaptive multiresolution method for such problems. In the whole section, the computational domain, denoted by Ω, is one-dimensional. We use the notation $\Omega = [x_0,\ x_M]$. The maximal number of scales is denoted by L.

4.2.1 Steady planar flame

As explained in Section 1.6, to observe a steady planar flame, we can consider either the gaseous mixture at rest in a moving reference frame, or a stationary flame in a gaseous mixture advected at the velocity $-v_f$, v_f being the flame velocity. In the thermodiffusive approximation, the system of dimensionless equations modelling the unsteady physical problem is, for $(x,t) \in \Omega \times [0,+\infty)$,

$$\begin{aligned}
\frac{\partial T}{\partial t} + v_f \frac{\partial T}{\partial x} &= \frac{\partial^2 T}{\partial x^2} + \omega - s \\
\frac{\partial Y}{\partial t} + v_f \frac{\partial Y}{\partial x} &= \frac{1}{Le}\frac{\partial^2 Y}{\partial x^2} - \omega \\
\omega(T,Y) &= \frac{Ze^2}{2\,Le}\, Y\, \exp\left[-\frac{Ze(1-T)}{1-\alpha(1-T)}\right] \\
s(T) &= \gamma\left[\left(T+\frac{1}{\alpha}-1\right)^4 - \left(\frac{1}{\alpha}-1\right)^4\right]
\end{aligned} \tag{4.1}$$

where the variables are the ones defined in Chapter 1, with the subscript + omitted everywhere. The resulting system is a set of two one-dimensional convection-diffusion-reaction equations. In order to compare with the asymptotic results of [73], we use the same parameters, initial and boundary conditions. Thus we choose as initial condition the asymptotic solution for $Ze \to \infty$ given in (1.18), i.e.

$$T(x,0) = \begin{cases} e^x & \text{if} \quad x \le 0 \\ 1 & \text{if} \quad x \ge 0 \end{cases} \tag{4.2}$$

$$Y(x,0) = \begin{cases} 1 - e^{Le\,x} & \text{if} \quad x \le 0 \\ 0 & \text{if} \quad x \ge 0 \end{cases} \tag{4.3}$$

and Dirichlet and Neuman boundary conditions at the two extremities

$$\begin{aligned} T(x_0,t) &= 0 \\ Y(x_0,t) &= 1 \\ \frac{\partial T}{\partial x}(x_M,t) &= 0 \\ \frac{\partial Y}{\partial x}(x_M,t) &= 0 \end{aligned} \tag{4.4}$$

Following [43], the flame velocity v_f in 1D is defined as

$$v_f = \int_\Omega \omega \; dx.$$

For $Ze \to \infty$, and $Le = 1$, we have $v_f = 1$. The steady state is assumed to be reached when the flame velocity becomes constant. For all the numerical simulations in this section, the temperature ratio is $\alpha = 0.8$, and radiations effects are yet neglected. The computational domain is $\Omega = [-20, 20]$, a maximum of $L = 9$ scales being available.

First, we focus on the case $Le = 1$ and $Ze = 10$. For these parameters, we study the influence of the tolerance ϵ on v_f. The temperature profile and the corresponding adaptive mesh for a given tolerance $\epsilon = 1.5 \cdot 10^{-2}$ are plotted in Fig. 4.1. The profile of ω and the time evolution of v_f for the same tolerance are given in Fig. 4.2.

We observe that the computation performed with the adaptive multiresolution method gives the same result as the one obtained by the finite volume method on the finest grid. We also remark small oscillations for the time evolution of the flame velocity. This is due to the adaption strategy. In fact, small changes in the tree structure slightly modify the integral values, such as v_f.

To estimate the accuracy and the efficiency of the method, several computations have been done for different values of the tolerance (Table 4.1). This time, as no analytical solution exists, we measure the difference between the flame velocity of the steady state obtained by finite volume and multiresolution methods. The absolute and relative errors measured here are in fact *perturbation errors* (see Chapter 2). As expected, the computation is more accurate, but also more costly, when the tolerance is smaller. The asymptotic value of v_f, whose definition is given in [73], is also given for comparison.

Now we study the flame velocity for different values of Le and Ze. In Table 4.2, we compare the flame velocity obtained by the multiresolution method with the asymptotic value [73] for different Le and Ze. We find a good agreement between both values.

Now we perform computations with radiation to verify that their influence corresponds to the one described in the first chapter, i.e the reaction rate is decreased in the reaction zone and the temperature is decreased in the burnt mixture zone far from the flame front. Following the experiments [78], the radiative heat loss can be modified by adding CF_3Br to the mixture. This component does not modify the main chemical reaction, but increases the radiative heat loss due to soot production. In this computation, the radiation coefficient is $\gamma = 0.002$, and the tolerance is $\epsilon = 1.5.10^{-2}$. The other control parameters are the same

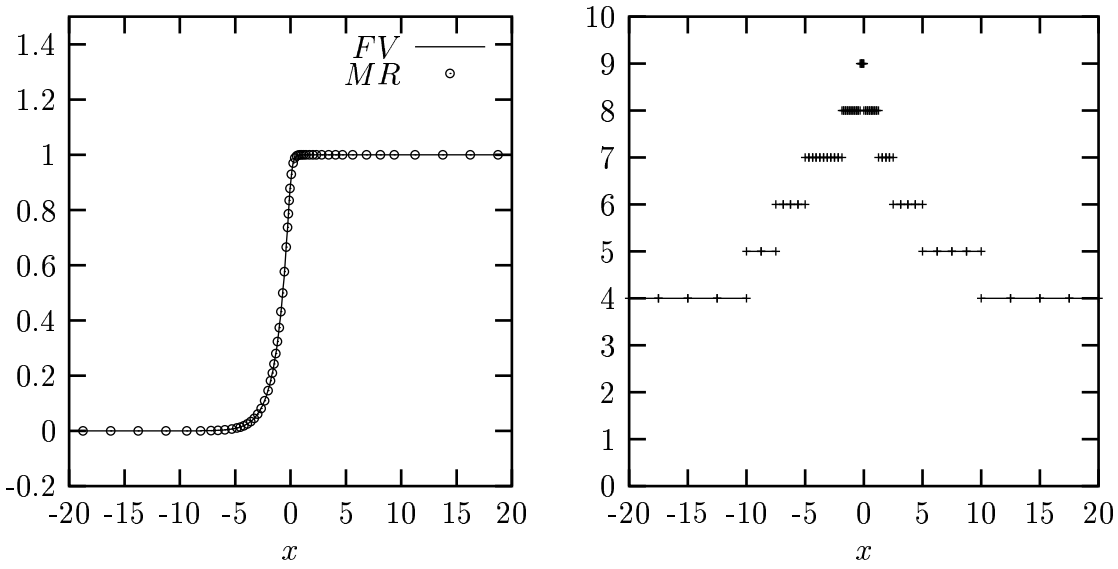

Figure 4.1: Left: Profile of T for the steady planar flame at $t = 5$ for $\gamma = 0$, $L = 9$, $\epsilon = 1.5.10^{-2}$. Right: corresponding adaptive mesh.

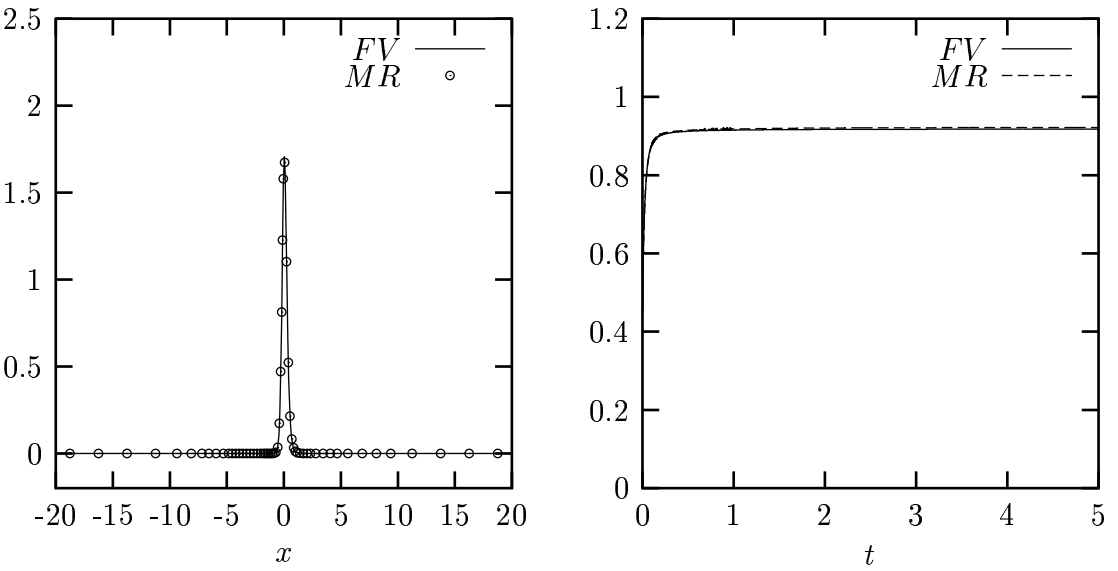

Figure 4.2: Left: Profile of ω for the steady planar flame at $t = 5$ for $\gamma = 0$, $L = 9$, $\epsilon = 1.5.10^{-2}$. Right: Time evolution of the flame velocity v_f.

Method	% CPU	% Mem	v_f	$\lvert v_f - v_f(FV)\rvert$	% Err
FV	100.0 %	100.0 %	0.9177744	0	0 %
MR $\epsilon = 1.5.10^{-2}$	29.7 %	26.5 %	0.9220062	$4.232.10^{-3}$	0.461 %
MR $\epsilon = 10^{-2}$	29.9 %	28.9 %	0.9206184	$2.844.10^{-3}$	0.310 %
MR $\epsilon = 10^{-3}$	40.6 %	38.3 %	0.9178404	$6.600.10^{-5}$	0.011 %
MR $\epsilon = 10^{-4}$	59.8 %	51.6 %	0.9178003	$2.591.10^{-5}$	0.0072 %
MR $\epsilon = 10^{-5}$	70.2 %	64.9 %	0.9177821	$7.700.10^{-6}$	0.0008 %
MR $\epsilon = 10^{-6}$	88.7 %	78.3 %	0.9177734	$1.000.10^{-6}$	0.0001 %
Asymptotic [73]			0.9080		

Table 4.1: CPU and memory compression, flame velocity at the steady state, absolute and relative errors on v_f for finite volume and multiresolution methods, $Le = 1$, $Ze = 10$.

Ze	10	10	20	20
Le	0.5	2	0.5	1
v_f (asymptotic)	0.9486	0.8417	0.9733	0.9510
v_f (MR)	0.9616	0.8498	0.9890	0.9575

Table 4.2: Asymptotic and computed values of the flame velocity v_f for different values of Le and Ze. For the cases $Ze = 10$, we chose $L = 9$ and $\epsilon = 10^{-3}$. For the cases $Ze = 20$, we have $L = 10$ and $\epsilon = 5 \cdot 10^{-4}$.

as before. Adaptive mesh, profiles of temperature and reaction rate and time evolution of the flame velocity are plotted in Figs. 4.3-4.4. We first remark that the effects of radiation - temperature decrease in the burnt gas region, reaction rate lower in the chemical reaction zone - can be well observed in the present computations. Moreover, more time is necessary to reach the steady state, i.e. to get a constant flame velocity. Then, from the numerical point of view, we observe as before that the adaptive multiresolution computation agrees again well with the one obtained with the finite volume method on the finest grid. This time, CPU time and memory compression are respectively 28.5% and 27.4%. However, the error between the values of the steady flame velocity compared to the reference finite volume computation is $6.14.10^{-3}$, which yields a relative error of 0.72%. This error is larger than in the non-radiative case, and can be easily observed on the right side of Fig. 4.4, whereas CPU time and memory compression are comparable. This is due to the accumulation of perturbation error, since more time iterations have to be performed to reach a steady state.

4.2.2 Propagating planar flame

In this part, we simulate the propagation of a planar flame to verify that the dynamic grid follows well the flame propagation. This time, we do not use a moving reference frame. The system of thermodiffusive equations is a set of reaction-diffusion equations.

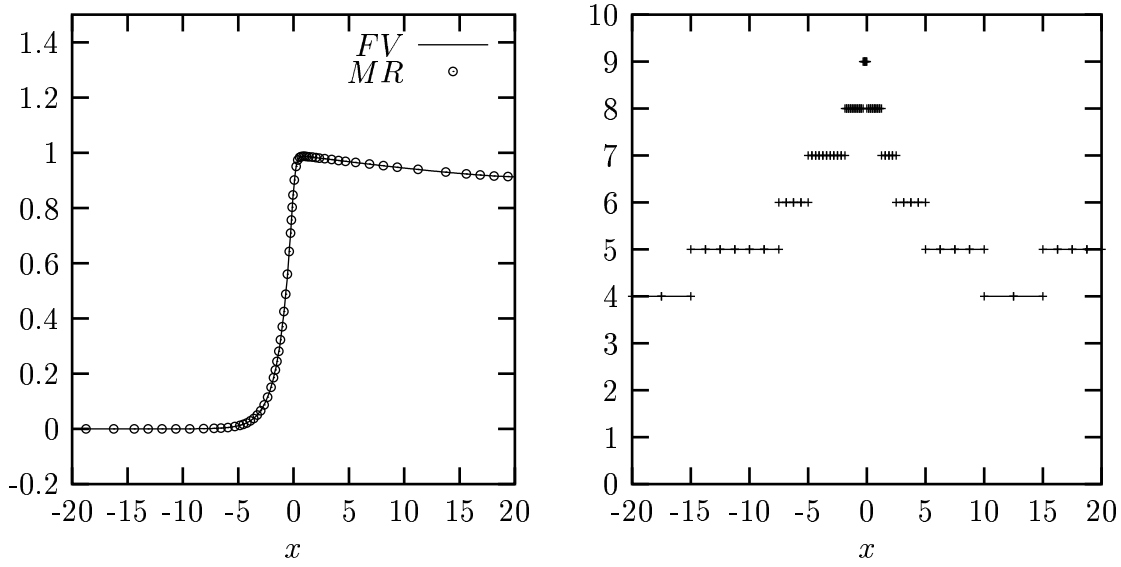

Figure 4.3: Left: Profile of T for the steady planar flame at $t = 25$ for $\gamma = 0.002$, $L = 9$, $\epsilon = 1.5.10^{-2}$. Right: corresponding adaptive mesh.

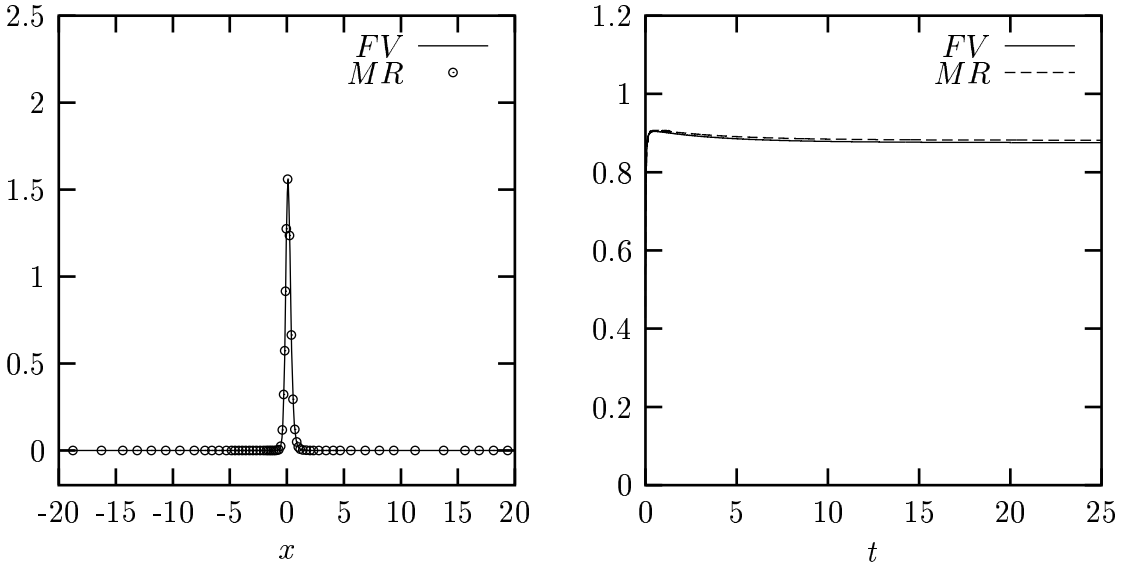

Figure 4.4: Left: Profile of ω for the steady planar flame at $t = 25$ for $\gamma = 0.002$, $L = 9$ scales and $\epsilon = 1.5.10^{-2}$. Right: Time evolution of the flame velocity v_f.

For $(x,t) \in \Omega \times [0,+\infty)$, it is written in the following form

$$\begin{aligned} \frac{\partial T}{\partial t} &= \frac{\partial^2 T}{\partial x^2} + \omega - s \\ \frac{\partial Y}{\partial t} &= \frac{1}{Le}\frac{\partial^2 Y}{\partial x^2} - \omega \end{aligned} \tag{4.5}$$

where $\Omega = [x_0, x_M] = [0, 40]$, and ω and s are the same as in (4.1).

We choose as initial condition

$$T(x,0) = \begin{cases} 1 & \text{if} \quad x \leq 1; \\ \exp(1-x) & \text{if} \quad x > 1. \end{cases} \tag{4.6}$$

$$Y(x,0) = \begin{cases} 0 & \text{if} \quad x \leq 1; \\ 1 - \exp[Le(1-x)] & \text{if} \quad x > 1. \end{cases} \tag{4.7}$$

The boundaries are considered as sufficiently far from the flame, so that their influence is negligible. For the numerical simulations, we use the same boundary conditions as previously. Radiative effects are neglected. The other control parameters are the same as in the previous subsection, i.e. $Le = 1$, $Ze = 10$, and $\alpha = 0.8$. Computations are performed on a maximum of $L = 9$ scales, and with a tolerance $\epsilon = 10^{-2}$.

In Fig. 4.5, we observe the *flame propagation* in the x-direction. The highest level is reached in the reaction zone. As for convection-diffusion and viscous Burgers equations, the adaptive mesh follows well the propagation of the flame front. The CPU time and memory compressions are respectively 27.5% and 26.0%. They are comparable with the ones measured for the steady state. The flame velocity tends to a steady state. At $t = 20$, we have $v_f = 0.918$. This results agrees well with the one computed at the steady state (Subsection 4.2.1).

4.3 Pulsating planar flames

In the previous section, planar flames have been simulated numerically for equal heat and mass diffusivities, i.e. with a Lewis number equal to unity. In this case, planar flames are always stable. For Lewis number greater than unity, pulsating planar flames can be observed, as explained in the first chapter (Subsection 1.7.4). In this section, we perform adaptive computations of planar flames for Lewis numbers greater than unity, in order to show the different pulsating states of flames, and to determine for which parameter ranges such phenomena happen.

Let us consider a planar flame propagating at the velocity v_f in the x-direction, with fresh mixture advected at the velocity $-v_f$ in order to maintain the flame at the origin. As in Subsection 4.2.1, the system of equations modelling this physical problem is given by (4.1). We complete this system with the same initial and boundary conditions. We now choose a gas mixture whose Lewis number is greater that unity. This is the case for e.g. a lean 2.65% C_2H_6-air mixture, whose Lewis number is $Le = 1.40$ [79], or a lean mixture of butane and oxygen highly diluted with helium ($Le \approx 3$) [71, 72]. The control parameters are the Lewis number Le and the Zeldovich number Ze. Radiative effects are neglected.

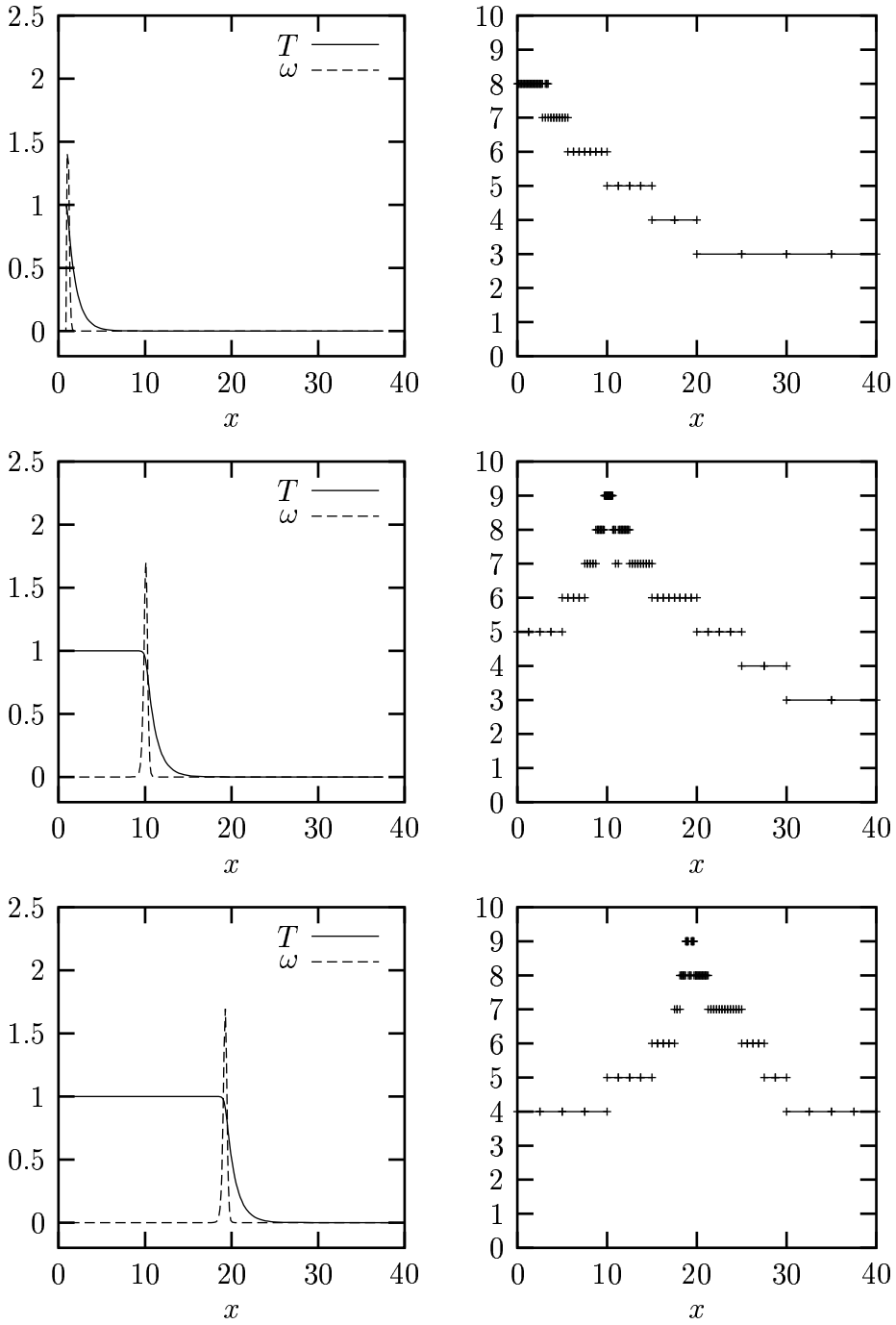

Figure 4.5: Left: Profile of T (*plain*) and ω (*dashed*) at $t = 0$ (*top*), $t = 10$ (*middle*), and $t = 20$ (*bottom*) for the propagating planar flame front, $L = 9$, $\epsilon = 10^{-2}$. Right: corresponding adaptive mesh.

4.3.1 Description of a pulsating flame

In Fig. 4.6, temperature, concentration and reaction rate are plotted from $t = 3$ to $t = 8$ for $Le = 2$ and $Ze = 17.5$. This represents one period of pulsation. The corresponding time evolution of the flame velocity v_f is plotted in Fig. 4.7. From $t = 3$ to $t = 5$, we observe ω increasing inside the reaction zone. This is due to a large heat flux going from the reaction zone to the pre-heat zone - a phenomenon of accelerated ignition. As the temperature in the reaction zone is greater than in the burnt mixture zone, we also observe a heat flux going from the reaction zone to the burnt mixture zone. Due to this heat loss, the reaction rate decreases from $t = 6$ to $t = 8$ whereas, in the same time, the temperature in the reaction zone decreases.

Thus, the Lewis number is the main control parameter. It determines the intensity of heat loss compared to mass diffusivity. On the other side, the Zeldovich number determines the size of the reaction zone - its thickness is $O(Ze^{-1})$ - and the maximum of the reaction rate. The larger the Zeldovich number is, the thinner the reaction zone is, and the larger the maximum of ω is in this zone. Therefore large values of Ze make the problem stiffer and increase the effects due to large Le numbers.

4.3.2 Flame velocity of stable and pulsating flames

Fig. 4.8 (*left*) shows the situation for a value of Ze close below the oscillation limit. As already observed in [77], the flame velocity overshoots its steady state value. The oscillations are damped in time, because both, heat loss due to conduction and heat production due to reaction, balance, even if the flame velocity increases. This results in a stabilization effect on the temperature and concentration profiles and on the flame velocity.

For Ze above this limit, the rate of heat loss cannot compensate the rate of heat production due to reaction. Therefore the temperature in the reaction zone increases exponentially, causing the reaction rate to do likewise, and a thermal explosion results. Thus, the flame velocity increases sharply until the reactant is consumed in a large region ahead of the flame. Then, heat production quickly slows down and the temperature in the reaction zone decreases due to heat losses. This results in a rapidly decreasing flame velocity. With time, more reactant becomes available, and so the reaction is gradually accelerated, although the flame velocity is still decreasing. Furthermore, depending on the control parameters, we observe pulsations with a single frequency (Fig. 4.8, right side), with several frequencies (Fig.4.9, left side), or without any periodicity (Fig. 4.9, right side). These pulsating flames and their transition to chaos have already been observed in previous numerical simulations [77, 6].

To check the periodicity of v_f, we plot in Fig. 4.10 the energy spectrum of the flame velocity

$$E(\xi) = \frac{1}{2}|\hat{v}_f(\xi)|^2$$

computed by Fast Fourier Transform (FFT) on the $2^{15} = 32768$ last points of the time evolution of v_f, in order to get the spectrum of the pulsating part only. The axis of the

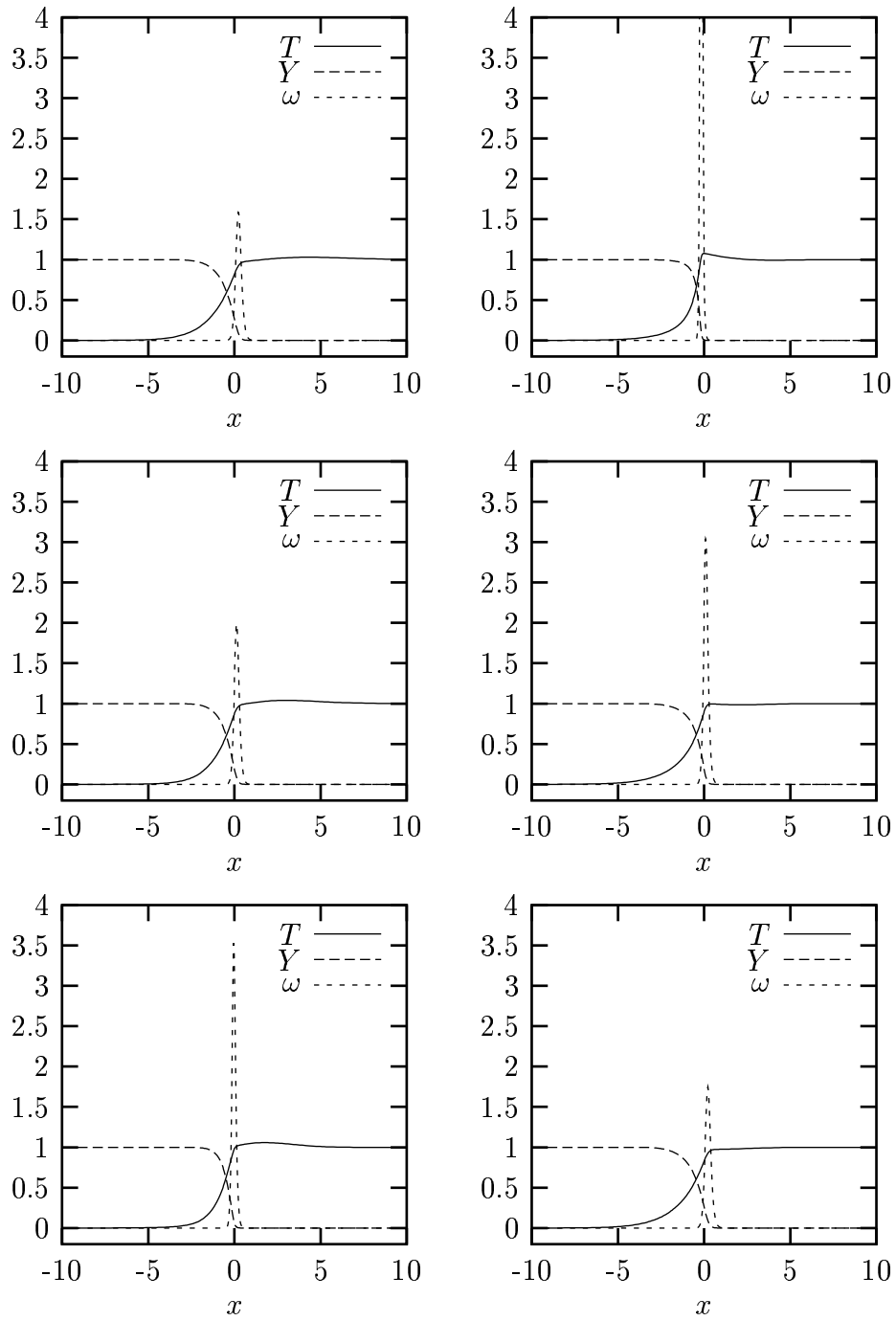

Figure 4.6: Left: Profiles of T, Y and ω at $t = 3$ (*top left*), $t = 4$ (*middle left*), $t = 5$ (*bottom left*), $t = 6$ (*top right*), $t = 7$ (*middle right*), and $t = 8$ (*bottom right*), for a pulsating planar flame, $Ze = 17.5$, $Le = 2$, $L = 11$, $\epsilon = 5.10^{-4}$.

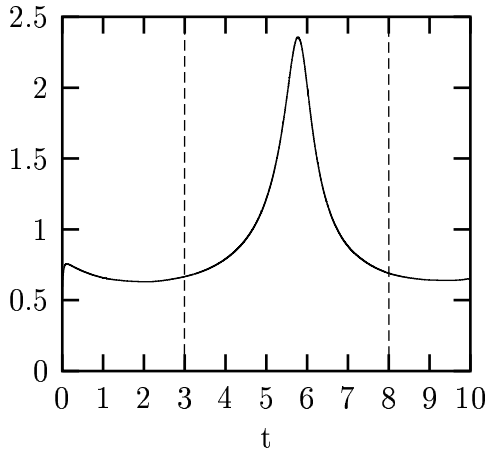

Figure 4.7: Time evolution of the flame velocity v_f for the pulsating planar flame, $Ze = 17.5$, $Le = 2$, $L = 11$, $\epsilon = 5.10^{-4}$. The zone between the two dashed lines corresponds to the profiles plotted in Fig. 4.6.

frequencies ξ was calibrated by computing the FFT for $f_k(t) = \sin 2k\pi t$, $k \in \mathbb{Z}$. The corresponding continuous Fourier transform of $v_f(t)$ is

$$\widehat{v_f}(\xi) = \int_{-\infty}^{+\infty} v(t) e^{-2\pi i \xi t}\, dt\ . \tag{4.8}$$

In Fig.4.10 (*left side*), we only plot the part corresponding to the 10% highest peaks and, on the right side, we focus on the lowest frequencies that give these highest peaks. They correspond to the main frequencies of the signal. We find that the case $Ze = 10$, $Le = 4$, is well periodic, with a frequency approximately equal to 0.1, which corresponds to a period $T \approx 10$. This period can be observed on the left side of Fig. 4.8. We also confirm that several frequencies exist for $Ze = 20$, $Le = 3$ and for $Ze = 15$, $Le = 4$. Finally the case $Ze = 20$, $Le = 3$ seems to become chaotic, since its spectrum shows an increasing number of frequencies.

4.3.3 Bifurcation diagram

In this part, we perform a parametric study with large number of computations to determine the limit between stable and pulsating planar flames. As explained in Chapter 1, the flame thickness is of $O(Ze^{-1})$. Thus, for very large values of the Zeldovich number, the reaction zone becomes very thin. Consequently, a very fine mesh is required in this region. To determine how many scales are necessary for a given Zeldovich number, several computations of stable cases have been performed with $Le = 1.25$. Considering that we need a minimum of 15 points to have a correct estimation of ω inside the reaction zone, we use the following maximal scales in the computations (Table 4.3).

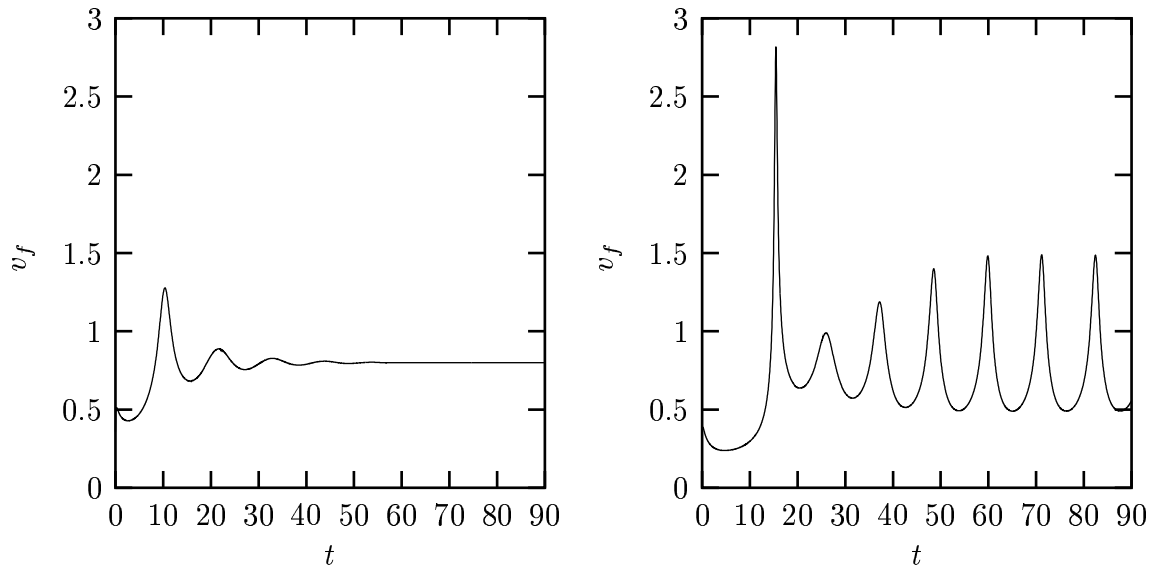

Figure 4.8: Flame velocity v_f: damped pulsations, $Ze = 10$, $Le = 3$ (*left*), and steady pulsations, $Ze = 10$, $Le = 4$, (*right*).

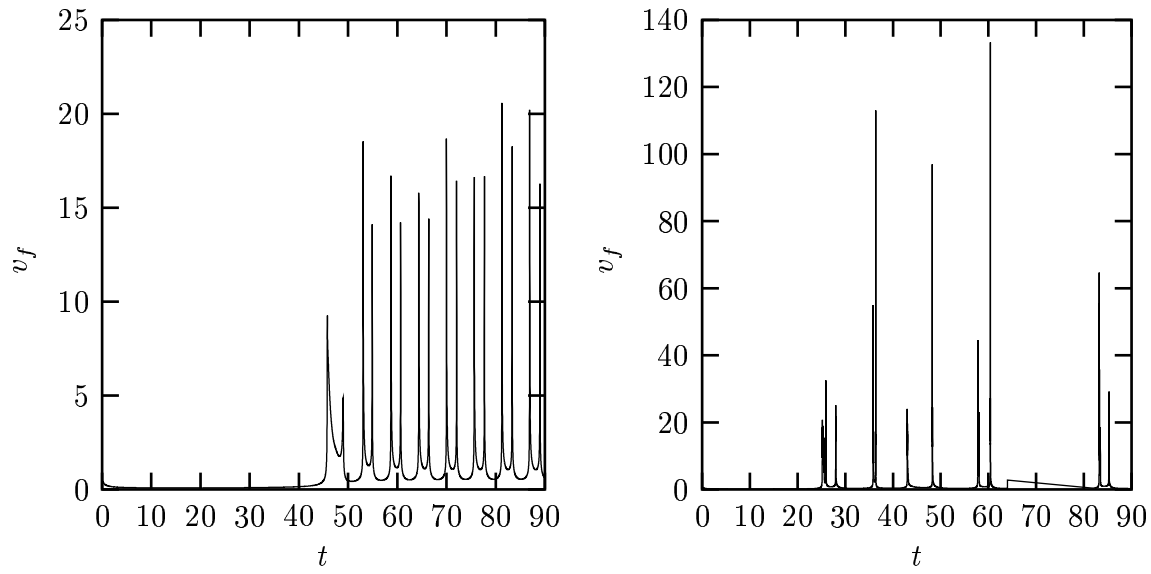

Figure 4.9: Flame velocity v_f: pulsations with several frequencies, $Ze = 15$, $Le = 4$ (*left*), and without periodicity, $Ze = 20$, $Le = 3$ (*right*).

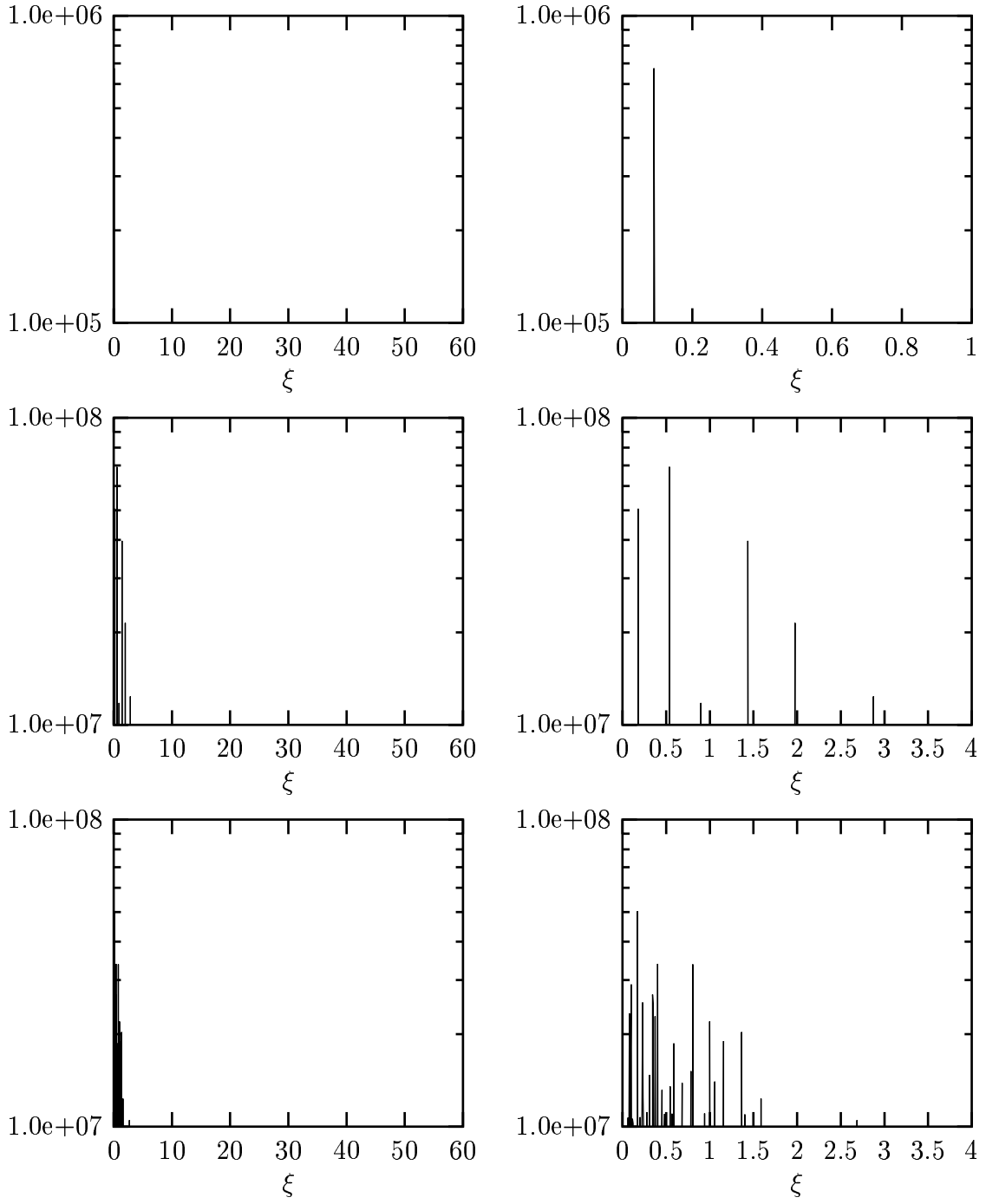

Figure 4.10: Left: Energy spectrum as function of the frequency ξ for $Ze = 10$, $Le = 4$ (*top*), $Ze = 15$, $Le = 4$ (*middle*), and $Ze = 20$, $Le = 3$ (*bottom*). Right: Zoom on the lowest visible frequencies.

Ze	L	Max. resolution	Points
10	9	512	20
15	10	1024	31
20	10	1024	24
25	10	1024	22
30	11	2048	28
35	11	2048	25
40	11	2048	22
45	11	2048	20
50	12	4096	18
55	12	4096	17

Table 4.3: Number of required scales L and maximal resolution for a given Ze. The number of points in the reaction zone are measured at the steady state for $Le = 1.25$.

The result of the numerical computations is plotted in Fig. 4.11. Four different behaviors have been observed: stable flame velocities, periodic pulsations, transition, aperiodic pulsations. The latter one, called *unstable*, is characterized by a flame velocity which seems to tend towards infinity. This results in a numerical instability, even for very small time steps. From a theoretical point of view, this last behavior exists [92], but it cannot be simulated numerically using an explicit method.

The $Le - Ze$ bifurcation diagram is plotted in Fig. 4.12 together with the asymptotic result from [60] which shows that, for $Ze >> 1$ and without radiation, the limit of the pulsating flames corresponds to $Ze\ (Le - 1) = 16$ (see Eq. 1.30). It is also compared with other numerical simulations performed using a method of lines [77], which is a finite element method based on B-splines.

We first remark that, for $15 < Ze < 40$, the results obtained here are comparable with both non-adaptive simulation and theoretical results. However, for $Ze > 40$, the non-adaptive computation differs significantly from the asymptotic result, which becomes theoretically more and more accurate when $Ze \to \infty$. For large Ze, only the adaptive computation is compatible with theory. This is due to the fact that, for large Ze, a very large number of points is required. Moreover, the flame velocity increasing with Ze, smaller and smaller time steps are required to maintain the numerical stability. Therefore, when using a regular grid, the computation becomes either too expensive, or inaccurate.

For $Ze < 15$, both adaptive and non-adaptive computations show that the asymptotic result is no more accurate. In this part, we observe a good agreement between the adaptive computation and the non-adaptive one. We also perform computations for larger values of Le. We observe that the curve is increased again for $Le > 7$. This phenomenon was not observed in [77] and was not predicted by the asymptotic theory in [60]. We can give the following interpretation to this phenomenon: as explained in [77], the pulsations are a consequence of the fact that heat loss due to conduction cannot compensate heat production due to reaction. However, for large values of the Lewis number, the heat

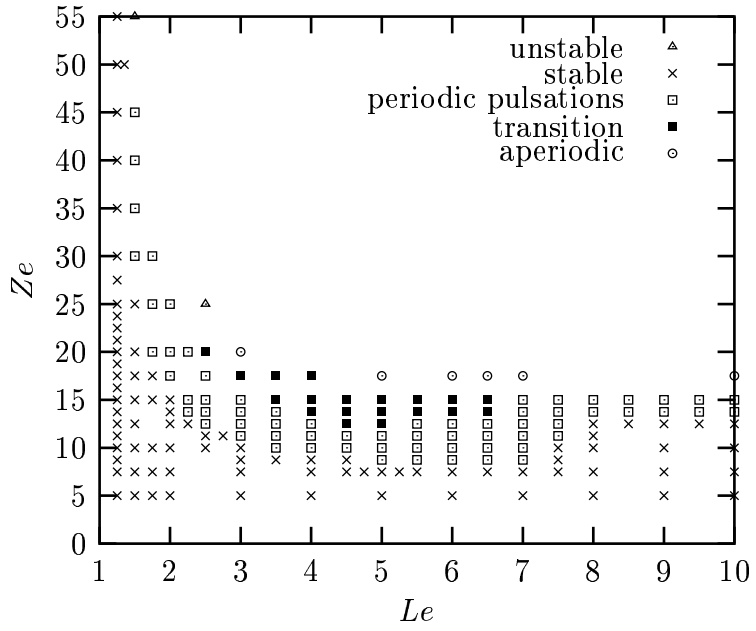

Figure 4.11: Bifurcation diagram $Le - Ze$ for the pulsating planar flames: computed points with the adaptive multiresolution method.

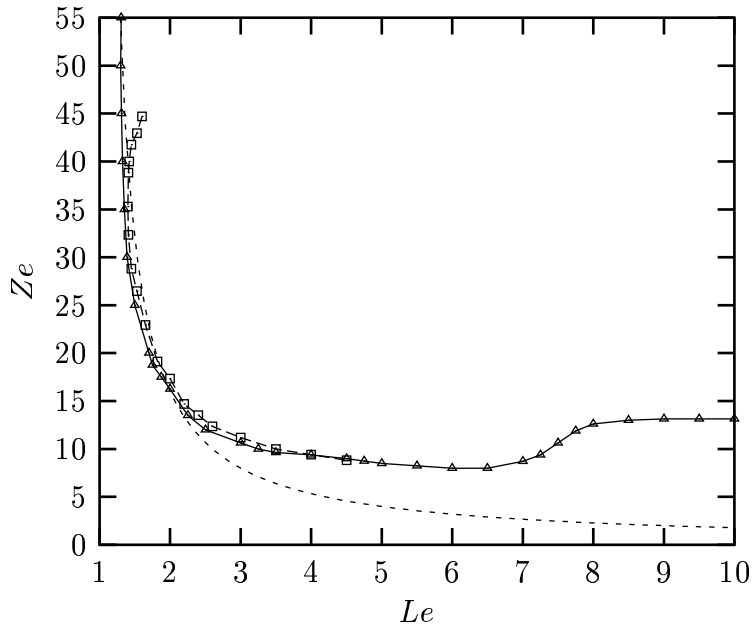

Figure 4.12: Bifurcation diagram $Le - Ze$ for the pulsating planar flames: computed values with the adaptive multiresolution method (*triangles, plain line*), computed values of [77] (*squares*), and theoretical asymptotic value for $Ze >> 1$ (Eq. 1.30) (*dashed line*).

conduction is stronger and both effects can balance when the heat production remains moderate, i.e. when Ze is not too large.

4.3.4 Amplitude of pulsations

This part aims at understanding the pulsating behavior of flames for moderate Zeldovich numbers. In this goal, the extrema of the flame velocity are plotted in Fig. 4.13 in function of the Lewis number. Four values of the Zeldovich number have been chosen : $Ze = 7.5$, where no pulsations have been observed ; $Ze = 10$, where pulsations are periodic and disappear for large values of the Lewis number ; $Ze = 12.5$, where transitional states exist ; $Ze = 15$, where pulsations do not disappear for high Le.

For $Ze = 7.5$, we remark that the flame velocity decreases with Le, reaches a minimum for $Le = 6$ and increases again. However, the variations are moderate and, as already shown in Fig. 4.12, no pulsations are observed. For $Ze = 10$ and $Ze = 12.5$, the flame velocity first decreases, then pulsations are observed. The amplitude of the pulsations increases, reaches a maximum for $Le \approx 5$, then decreases. Finally, the pulsations disappear for $Le \approx 8$, and the flame velocity increases again. The difference between these two cases is that, for $Ze = 10$, the amplitude is smaller than for $Ze = 12.5$.

The main difference is observed for $Ze = 15$. When Le is small, as before, no pulsations are observed. Then, when flames are pulsating, the amplitude increases, decreases, increases again, and almost tends to zero for $Le = 7$. For $Le > 7$, another pulsating state appears, with pulsations of weak amplitude (Fig. 4.14, *bottom right*).

We give the following interpretation to this phenomenon: when Le is small, the heat flux from the reaction zone to the pre-heat zone is not strong enough to accelerate the ignition. Moreover, the flame velocity does not initially decrease, because the conductive heat loss in the reaction zone remains low. Consequently the flame is stable (Fig. 4.14, *left*). Then, for moderate values of Le, due to accelerated ignition, the flame velocity overshoots its steady state value, but both effects of accelerated ignition and velocity decrease due to heat loss are not strong enough to maintain the pulsations. Then, when Le is sufficiently large that steady pulsations occur, both amplitude and frequency increase with Le. However, the amplitude reaches a maximum and then decreases because, the heat production remaining moderate, the heat loss reduces the energy in the reaction zone. Finally, for large values of Le, when the heat production remains moderate, i.e. when $Ze < 15$, the flame velocity decreases and increases again, but the heat loss in the reaction zone compensates the heat production due to reaction and, as a consequence, after a strong increase of the flame velocity, this one remains high, but becomes stable (Fig 4.14, *right, top and middle*).

For $Ze > 15$, we observe that, even for large Le, the heat production due to reaction is too important to be compensated by conductive heat loss. The limit is reached around $Ze = 15$, where pulsations of weak amplitude and low frequency appear for $Le > 7$ (Fig. 4.14, *bottom right*) whereas pulsations of larger amplitude and higher frequency have been observed for smaller values of the Lewis number (Fig. 4.14, *bottom center*). In Fig. 4.14 (*bottom center*), the black zone actually corresponds to pulsations of very high frequency.

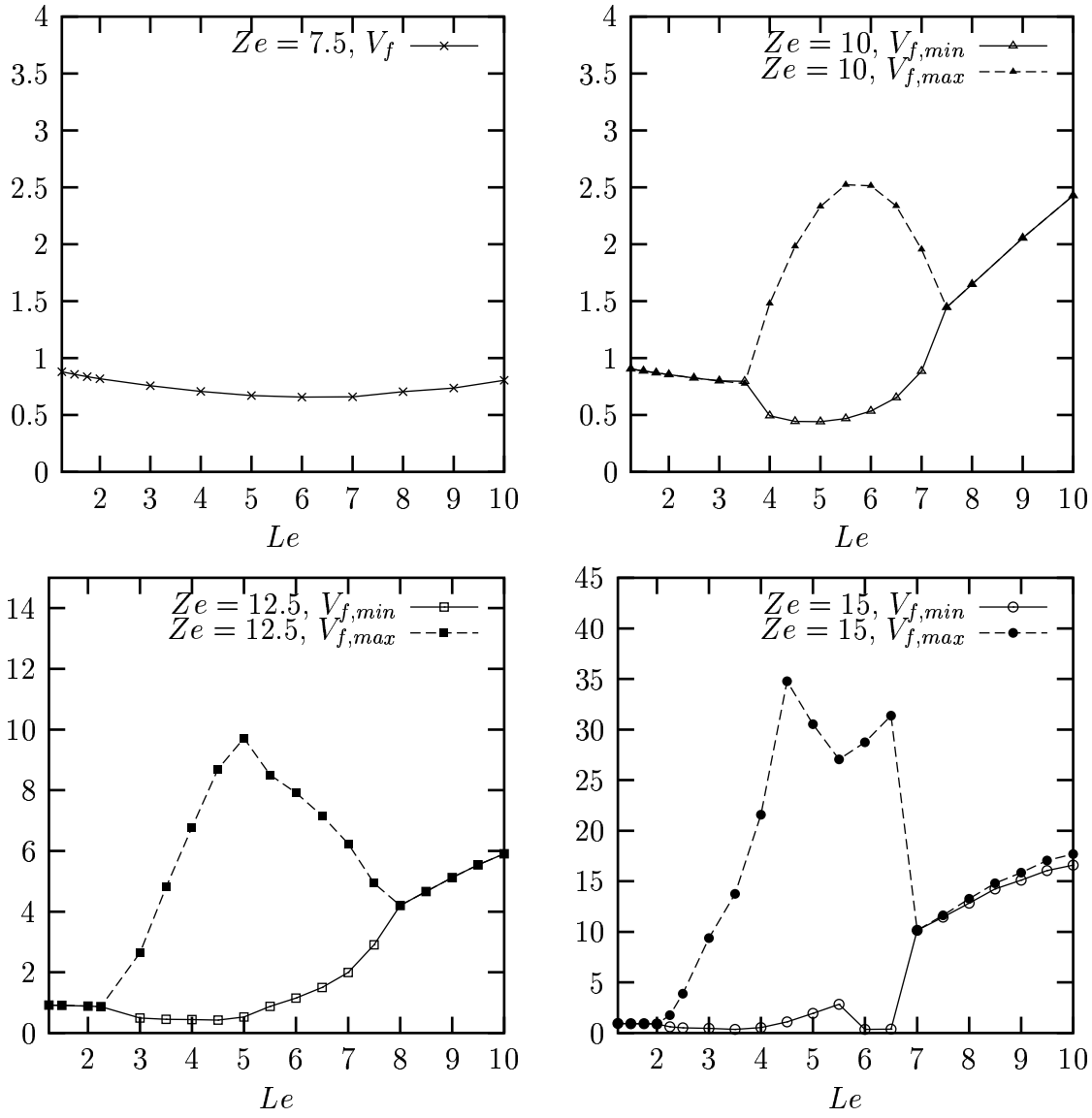

Figure 4.13: Extrema of the flame velocity v_f as function of Le for different values of Ze.

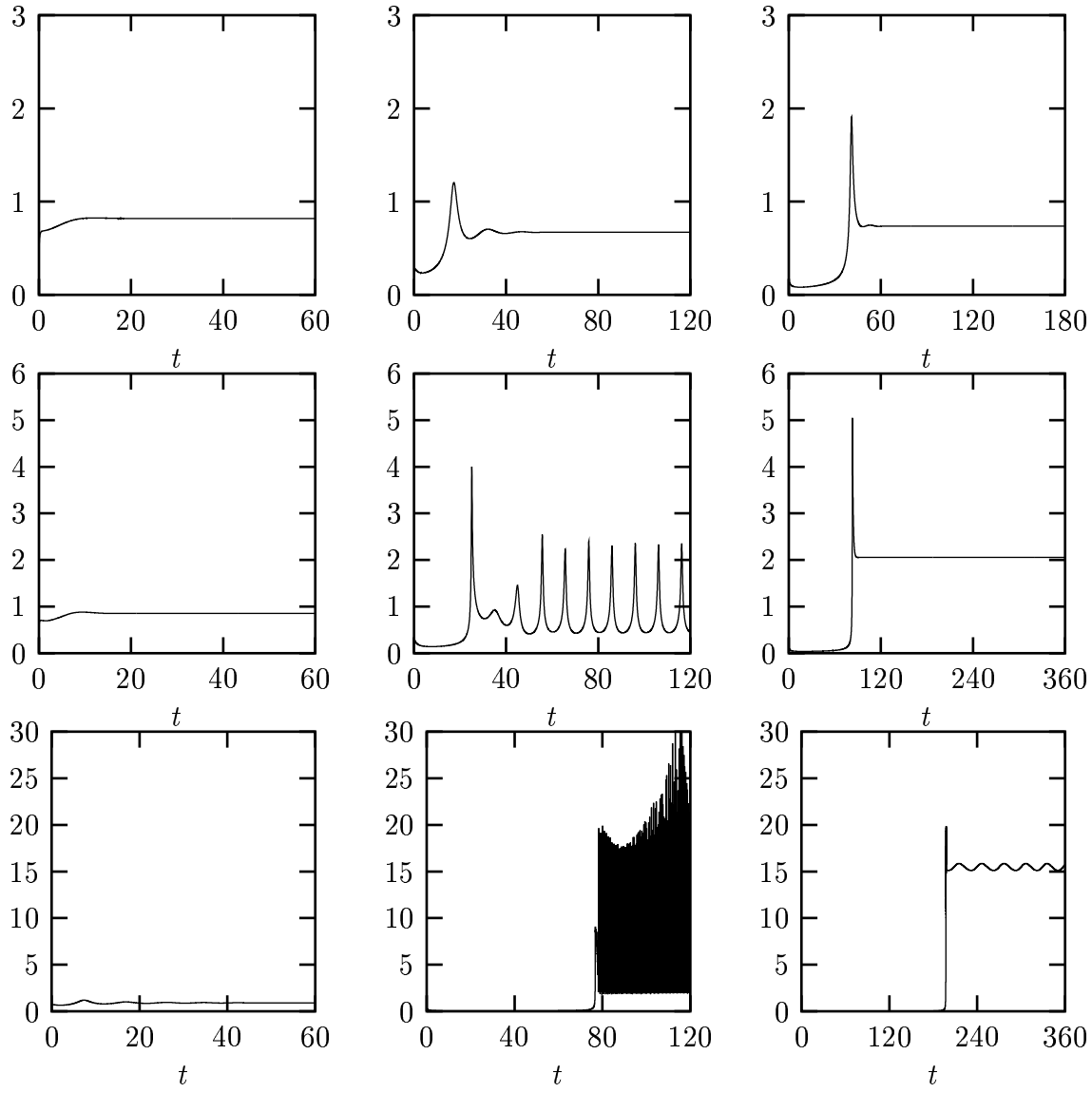

Figure 4.14: Flame velocity v_f for $Le = 2$ (*left*), $Le = 5$ (*center*), $Le = 9$ (*right*) and for $Ze = 7.5$ (*top*), $Ze = 10$ (*middle*), $Ze = 15$ (*bottom*).

4.4 Adaptive simulation of flame balls

A flame ball is a stationary or slowly propagating spherical flame structure in a premixed gaseous mixture. Such flames have been experimentally observed for low Lewis numbers under micro-gravity conditions. Otherwise, buoyant convection destroys the structure [78]. The study of such configurations for lean mixtures is of great interest, because it allows the determination of flammability limits in an "absolute" way, i.e. in function of the reaction mechanism only, independently of the setup [85].

In Fig. 4.15, a flame ball is represented schematically together with the physical mechanisms involved. The chemical reaction occurs in the circular zone delimiting the ball. Inside this ball, the gas is burnt. The rest of the domain is filled by fresh premixed gas. The pre-heat zone is not represented in this figure.

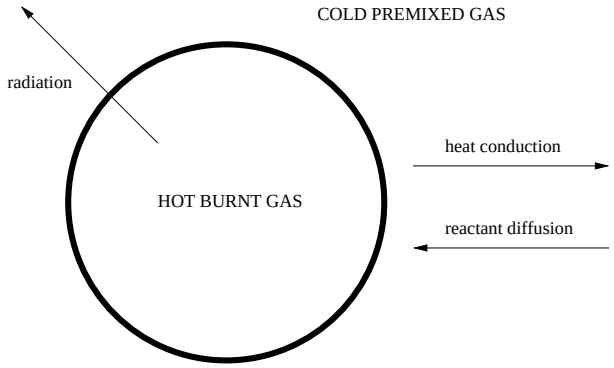

Figure 4.15: Schematic view of a flame ball and the involved mechanisms.

The thermodiffusive approximation is well adapted for the computation of flame ball, because the flame velocity is very small. Considering also constant density and one-step chemical kinetics approximations, the system of equations modelling such a flame structure is a set of two diffusion-reaction equations of the form

$$\frac{\partial T}{\partial t} = \nabla^2 T + \omega - s \tag{4.9}$$

$$\frac{\partial Y}{\partial t} = \frac{1}{Le}\nabla^2 Y - \omega \tag{4.10}$$

where ω and s are defined in (4.1). The chosen initial condition is the circular version of the one used for the planar flame. Denoting by r_0 the radius of the flame ball at $t = 0$, it has the following form

$$T(r,0) = \begin{cases} 1 & \text{if} \quad r \leq r_0; \\ \exp\left(1 - \frac{r}{r_0}\right) & \text{if} \quad r > r_0. \end{cases} \tag{4.11}$$

$$Y(r,0) = \begin{cases} 0 & \text{if} \quad r \leq r_0; \\ 1 - \exp\left[Le\left(1 - \frac{r}{r_0}\right)\right] & \text{if} \quad r > r_0. \end{cases} \tag{4.12}$$

where $r = \sqrt{x^2 + y^2}$ in 2D and $r = \sqrt{x^2 + y^2 + z^2}$ in 3D respectively. To study the stability of such structures, we consider that the walls are sufficiently far from the flame ball so that their influence is negligible. Therefore we use periodic boundary conditions in all directions. This enables us to compare the numerical results with previous one obtained by other methods, i.e.. Fourier pseudo-spectral or adaptive wavelet-vaguelette methods [46, 14].

4.4.1 Two-dimensional flame ball

In this subsection, we perform numerical simulations of flame balls in two dimensions. The aim is to show the influence of the Lewis number and the radiation on a flame ball initially perturbated. The results are compared to the ones obtained with an adaptive wavelet-vaguelette algorithm [14].

In a first step, we focus on the influence of the Lewis number. Thus we neglect radiation effects. The computational domain is $\Omega = [-50, 50]^2$. The circular initial condition is perturbated by stretching the circle in one direction. We also apply a rotation, so that the symmetry axes of the problem are not lined up with the grid.

$$r = \sqrt{\frac{X^2}{a^2} + \frac{Y^2}{b^2}}$$

where

$$\begin{cases} X &= x\cos\theta + y\sin\theta \\ Y &= -x\sin\theta + y\cos\theta \end{cases}$$

The parameters are the Zeldovich number $Ze = 10$, and the temperature ratio $\alpha = 0.64$. The aspect ratio of the ellipse is given by $a = 2$, $b = 1$, the rotation angle is $\theta = -\frac{\pi}{6}$, and the initial radius is $r_0 = 1$. The elapsed time is $t = 30$. We compute the evolution of the flame ball for three different values of Le: $Le = 0.3$, $Le = 1$, and $Le = 1.4$. The case $Le = 0.3$ corresponds to a 6.5% H_2-air mixture, the case $Le = 1$ to a 0.5% $CH_4 - O_2 - N_2$ mixture with a CH_4:O_2 mole ratio of 83.6%, and the case $Le = 1.4$ to a 2.65% C_2H_6-air mixture [79].

We initially made all the computations with a maximum of 8 scales. However, for $Le = 0.3$, since the symmetry of the problem was not respected, we set the maximal number of scales to 9, which involves a smaller time step and consequently more iterations to reach the same elapsed time. In fact, for $Le = 0.3$, all the perturbations are amplified, including those due to the mesh.

For $Le = 1$ (Fig. 4.16), we observe the relaxation of the elliptic flame towards a circularly symmetric structure which is then growing in space. For $Le = 0.3$ (Fig. 4.17), we observe the elliptical flame structure splitting and growing in space. These results are in agreement with the previous computations [14, 85]. As explained in section 1.7, at

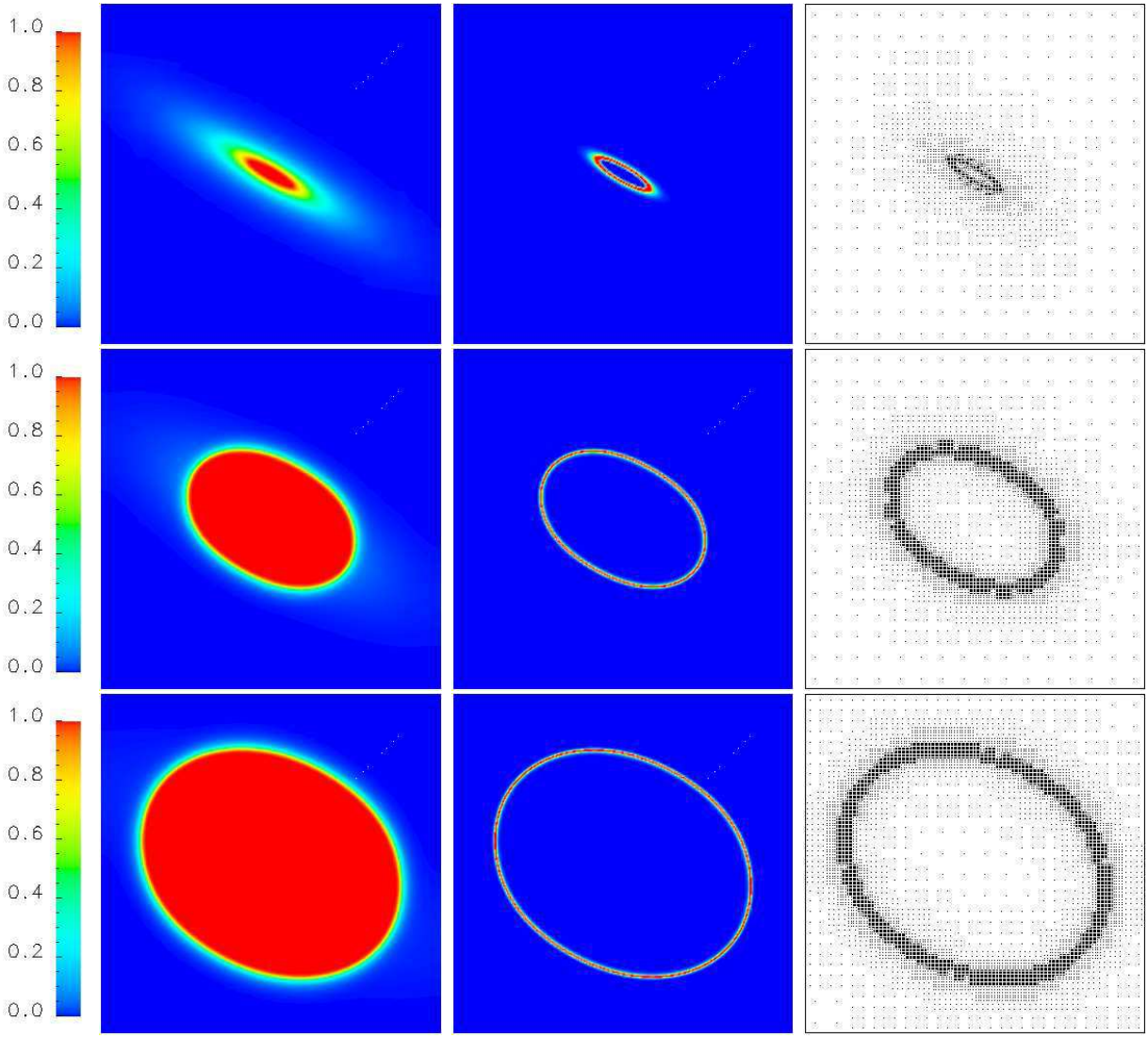

Figure 4.16: Temperature (*left*), reaction rate (*center*) and corresponding mesh (*right*) at $t = 0$ (*top*), $t = 15$ (*middle*), and $t = 30$ (*bottom*) for a 2D flame ball, $r_0 = 1$, $Le = 1$, $Ze = 10$, $\alpha = 0.64$, $\gamma = 0$.

the two extremities of the long axis of the ellipse, the tangential reactant flux tends to increase the concentration of fresh gases, and with it the reaction. Therefore the flame is propagating faster in the direction of the long axis of the ellipse. As a consequence, the flame is splitting at the two extremities of the short axis of the ellipse. We observe at $t = 30$ a local extinction of the reaction at these extremities (Fig. 4.17, bottom).

To estimate the influence of the Lewis number on the chemical reaction, we study the time evolution of the integral of the reaction rate

$$\mathcal{R} = \int_{\Omega} \omega \, dx \, dy \tag{4.13}$$

for three different values of the Lewis number (Fig. 4.20, left side). We observe that the growth of the global reaction rate is more important for Lewis numbers lower than unity. The explanation is the following one: when $Le < 1$, more heat remains inside the flame ball than when $Le > 1$. Therefore, even if the flame ball splits, the flame front grows faster for $Le < 1$ than for $Le \geq 1$. However, when radiative losses are no more negligible, we get a significantly different solution.

To check this, we perform numerical simulations of flame balls for $Le = 0.3$ taking into account radiation effects. We know from Section 4.2 that the radiation coefficient can be modified by adding e.g. CF_3Br in the fresh mixture. In the following computations, we perform simulations with the following values of the radiation coefficient: $\gamma = 2.10^{-3}$, $\gamma = 0.01$, $\gamma = 0.05$, and $\gamma = 0.1$. The other parameters are the same as before. The temperature T, the reaction rate ω, and the corresponding adaptive mesh are plotted in Fig. 4.18 for $\gamma = 0.01$ and in Fig. 4.19 for $\gamma = 0.05$. The time evolution of $\mathcal{R}$ for the different values of γ is plotted in Fig. 4.20 (right side).

We observe that, for $\gamma = 0.01$, the flame front approximately behaves like when $\gamma = 0$. However, its growth is slower and the temperature is decreasing inside the flame ball. Then, for $\gamma = 0.05$, the flame front splits into four parts at $t = 15$, eight parts at $t = 30$. For $\gamma = 0.1$, the flame ball extinguishes at $t \approx 2.5$. The evolution of $\mathcal{R}$ for the different values of γ agrees well with the results obtained using the adaptive wavelet-vaguelette method [14]. Moreover, when comparing the two sides of Fig. 4.20, we observe that the integral of the reaction rate at $t = 30$ is lower for $Le = 0.3$, $\gamma = 0.05$ than for $Le = 1$, $\gamma = 0$. In both cases, heat losses reduce the reaction rate. However, in the case where heat loss is mainly due to radiation, the pre-heat zone does not absorb this energy. As a consequence, for large values of γ, the flame extinguishes. Thus, even if the splitting of the flame front is a consequence of the thermodiffusive instability, which depends on Le, higher radiative heat losses involves a splitting into more parts, the extreme case being the extinction.

Concerning the numerical method, we remark that, in all the cases, the grid adapts well to the evolution of the solution. The highest level is reached in the reaction zone, around the flame front. The performances in term of required CPU time and memory compared to the same computation using the finite volume method on the finest grid are given in Table 4.4.

In this table, we notice that the compression rate, both for CPU time and memory, strongly depends on the test-case. For large values of γ, the flame ball extinguishes and,

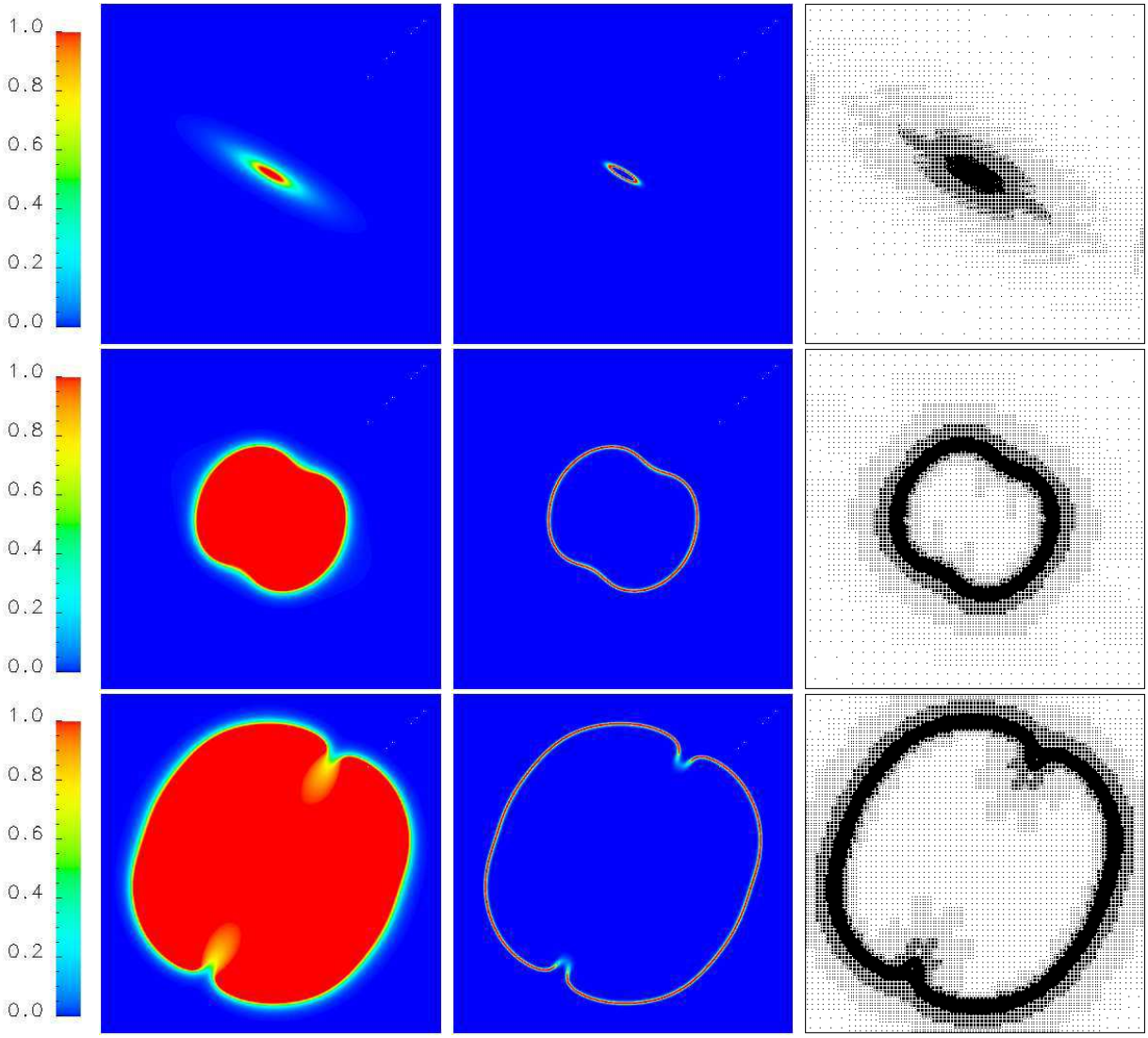

Figure 4.17: Temperature (*left*), reaction rate (*center*) and corresponding mesh (*right*) at $t = 0$ (*top*), $t = 15$ (*middle*), and $t = 30$ (*bottom*) for a 2D flame ball, $Le = 0.3$, $Ze = 10$, $\alpha = 0.64$, $\gamma = 0$.

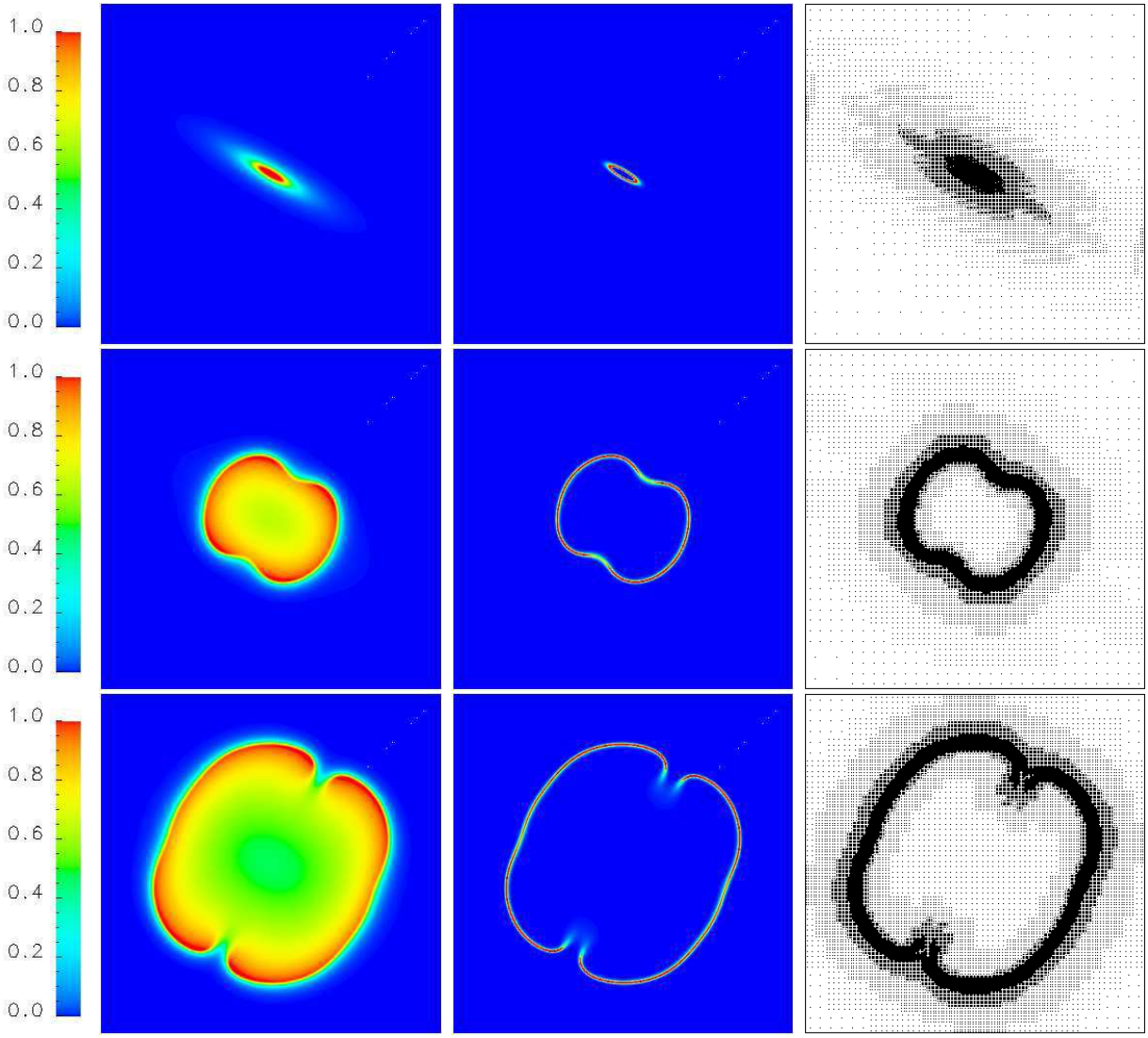

Figure 4.18: Temperature (*left*), reaction rate (*center*) and corresponding mesh (*right*) at $t = 0$ (*top*), $t = 15$ (*middle*), and $t = 30$ (*bottom*) for a 2D flame ball, $Le = 0.3$, $Ze = 10$, $\alpha = 0.64$, $\gamma = 0.01$.

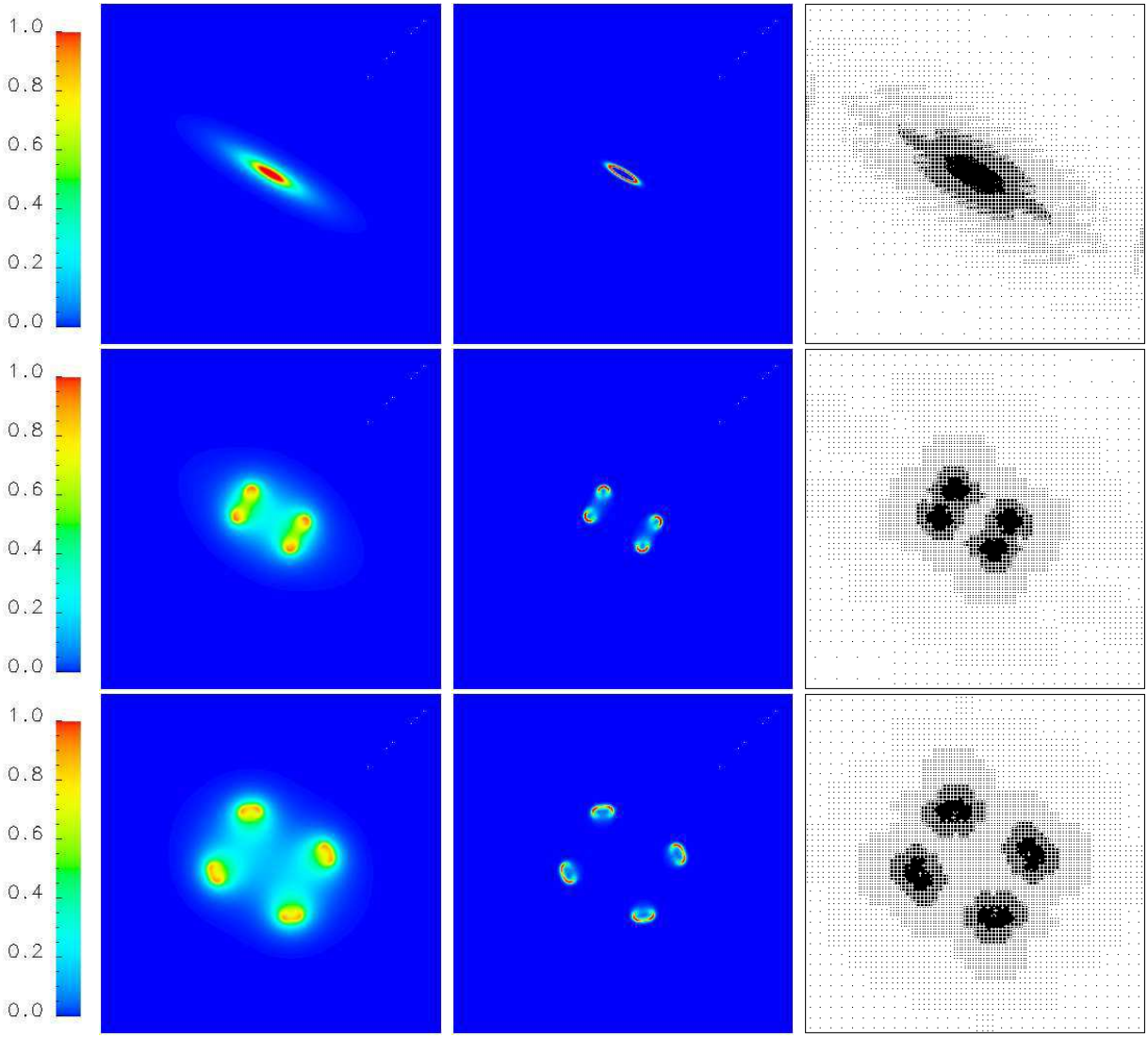

Figure 4.19: Temperature (*left*), reaction rate (*center*) and corresponding mesh (*right*) at $t = 0$ (*top*), $t = 15$ (*middle*), and $t = 30$ (*bottom*) for a 2D flame ball, $Le = 0.3$, $Ze = 10$, $\alpha = 0.64$, $\gamma = 0.05$.

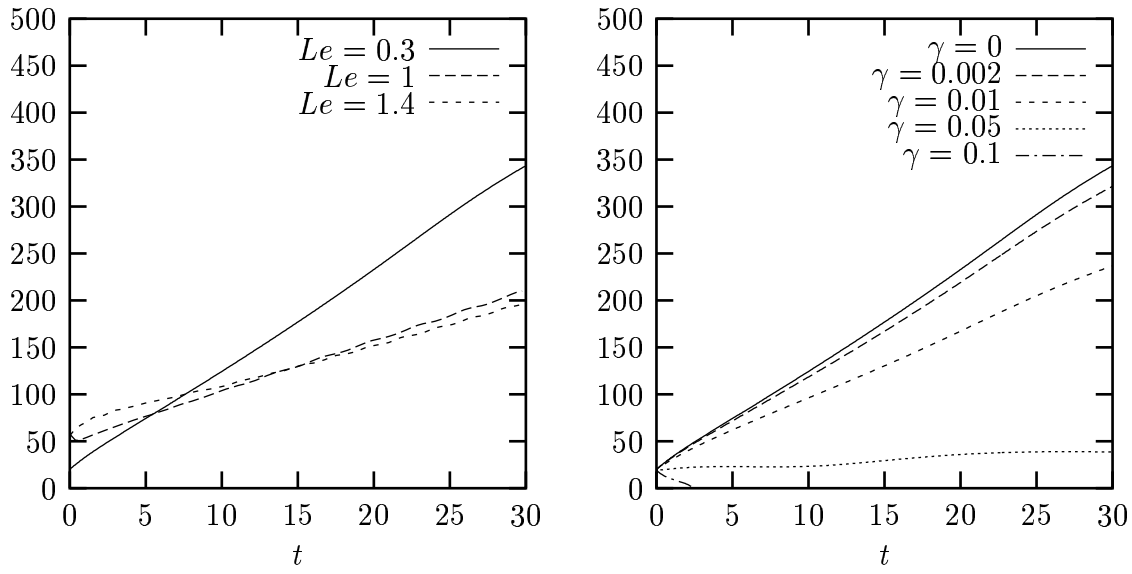

Figure 4.20: Integral of the reaction rate $\mathcal{R}$ for a 2D flame ball, $Ze = 10$, $\alpha = 0.64$. Left: Influence of the Lewis number, $\gamma = 0$. Right: Influence of the radiation at $Le = 0.3$.

Le	γ	L	ϵ	% CPU	% Mem
1.4	0	8	0.05	37.60%	19.80%
1	0	8	0.05	36.31%	18.65%
0.3	0	9	$5 \cdot 10^{-3}$	33.67%	15.97%
0.3	$2 \cdot 10^{-3}$	9	$5 \cdot 10^{-3}$	32.08%	15.65%
0.3	0.01	9	$5 \cdot 10^{-3}$	30.22%	14.43%
0.3	0.05	9	$5 \cdot 10^{-3}$	14.25%	7.03%
0.3	0.1	9	$5 \cdot 10^{-3}$	4.53%	2.39%

Table 4.4: Average CPU time and memory compressions for the 2D flame ball initially stretched, $Ze = 10$, $\alpha = 0.64$, $\Omega = [-50, 50]^2$.

consequently, the number of coefficient is successively reducing and tending towards 0 when $t \to \infty$.

4.4.2 Three-dimensional flame ball

We now perform three dimensional computations of flame balls initially stretched in one direction to check for 3D instabilities. The aim is to show if the behaviors of 2D flame balls - spherical growth, splitting, extinction - are also observed in 3D. For the numerical simulation of a 3D stable flame balls, i.e when $Le = 1$, radiation effects are neglected, as in the 2D case. The spherical initial condition is stretched in one direction and a rotation on two axes is applied. Hence, we have

$$r = \sqrt{\frac{X^2}{a^2} + \frac{Y^2}{b^2} + \frac{Z^2}{c^2}}$$

where

$$\left\{ \begin{array}{rcl} X & = & x\cos\theta - y\sin\theta \\ Y & = & (x\sin\theta + y\cos\theta)\ \cos\varphi - z\sin\varphi \\ Z & = & (x\sin\theta + y\cos\theta)\ \sin\varphi + z\cos\varphi \end{array} \right.$$

The parameters of the ellipsoid are $a = b = 1.5$, $c = 3$, and the rotation angles are $\theta = \frac{\pi}{3}$ and $\varphi = \frac{\pi}{4}$. The initial radius is $r_0 = 1$. The Zeldovich number and the temperature ratio are $Ze = 10$ and $\alpha = 0.8$. The elapsed time is $t = 10$. For the multiresolution computation, we use a maximum of $L = 7$ scales, and the tolerance is set to $\epsilon = 8.10^{-2}$. Since the computation is much longer than in 2D, we have reduced the physical time. This also enables us to choose a smaller domain, and consequently less scales to get the same smallest space step. Two isosurfaces of temperature ($T = 0.5$ and $T = 0.1$) at $t = 0$, 5, 10 and the corresponding meshes are plotted in Fig. 4.21.

We observe, as in the 2D case, a relaxation of the ellipsoidal flame towards a spherically symmetric structure which is then growing in space. This shows that the flame ball is stable, since the initial perturbation is not amplified. The scenario of evolution of the flame ball is in this case a spherical growth.

Now we simulate the evolution of a 3D flame ball with $Le = 0.3$, i.e. fast diffusing reactants. The temperature ratio is $\alpha = 0.64$. We consider also radiation effects. This test-case was proposed in [13, 46] and solved using a Fourier pseudo-spectral method. To evaluate the influence of the radiation, we perform simulations with two different values of γ: $\gamma = 0.1$ and $\gamma = 0.5$. We use a maximum of $L = 8$ levels and a tolerance $\epsilon = 0.05$.

In Fig. 4.22, we observe, as in the 2D case, the ellipsoid splitting along its two shortest axes and growing in space. After the first splitting, the new cells also split and one gets more and more cells. We therefore have *cellular flame structures*, as described in Chapter 1. This result agrees well with both theory [89] and former simulations [13, 46] using Fourier pseudo-spectral methods.

In Fig. 4.23, we report the integral of the reaction rate $\mathcal{R}$, defined as

$$\mathcal{R} = \int_\Omega \omega \; dx \; dy \; dz.$$

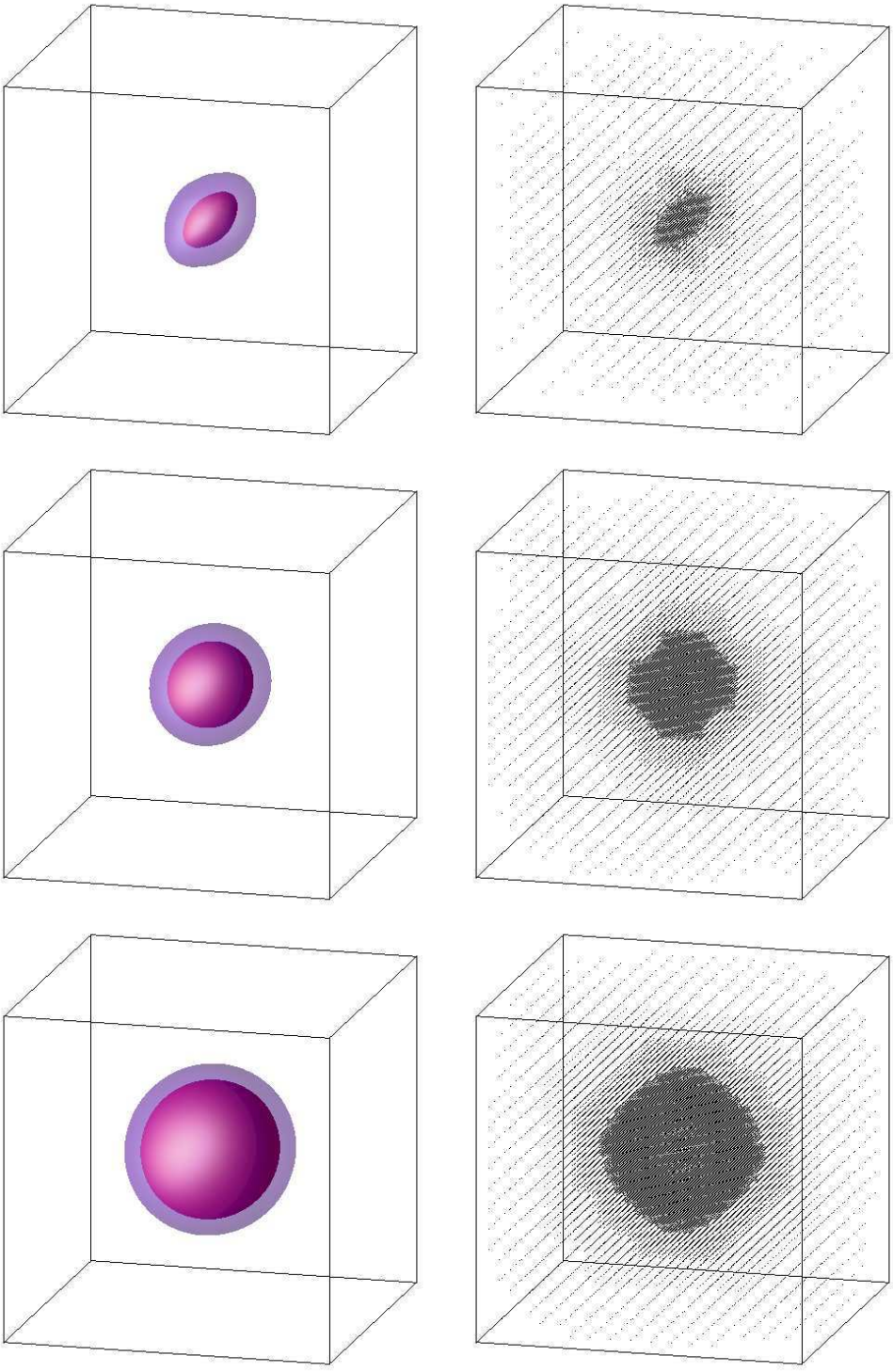

Figure 4.21: Isosurfaces $T = 0.5$ (red) and $T = 0.1$ (purple), and corresponding mesh at $t = 0$ (*top*), $t = 6$ (*middle*), and $t = 12$ (*bottom*) for the 3D flame ball, $Le = 1$, $Ze = 10$, $\alpha = 0.8$.

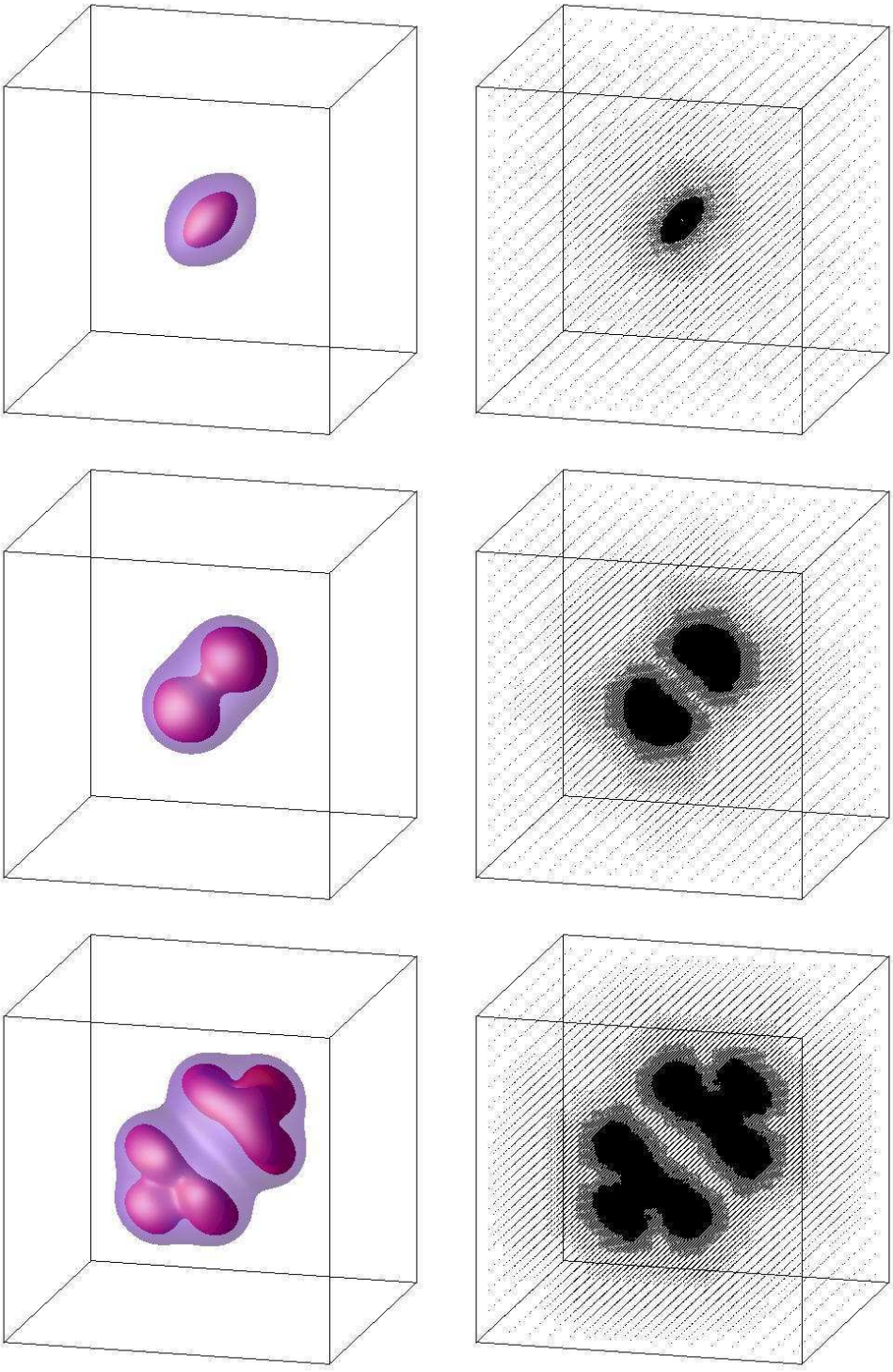

Figure 4.22: Isosurfaces $T = 0.5$ (red) and $T = 0.1$ (purple), and corresponding mesh at $t = 0$ (*top*), $t = 5$ (*middle*), and $t = 10$ (*bottom*) for the 3D flame ball, $Le = 0.3$, $Ze = 10$, $\alpha = 0.64$, $\gamma = 0.1$.

for the three different cases studied here.

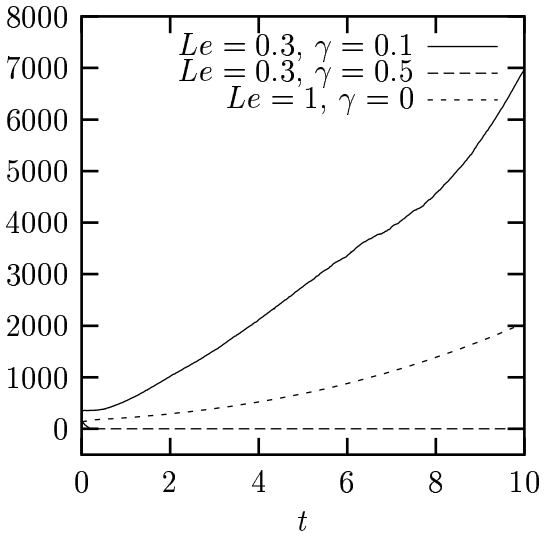

Figure 4.23: Time evolution of the integral of the reaction rate $\mathcal{R}$ for different scenarios: spherical growth ($Le = 1$, $\gamma = 0$), splitting ($Le = 0.3$, $\gamma = 0.1$), and extinction ($Le = 0.3$, $\gamma = 0.5$).

We observe the three different scenarios of evolution for a flame ball initially perturbated. For $Le = 1$, $\gamma = 0$, the perturbation is not amplified and the flame ball growths spherically. For $Le = 0.3$, $\gamma = 0.1$, the perturbation is amplified and the flame ball splits into more and more parts. The first splitting is here visible at $t \approx 6$. Finally, for $Le = 0.3$, $\gamma = 0.5$, the heat loss due to radiation is too high and the flame ball extinguishes. A last case has also been observed experimentally and numerically: the *steady* flame ball [47]. It has not been treated in this thesis.

The performances in terms of CPU time and memory are given in table 4.5. We remark that, compared to 2D computations, the compression is increased in 3D for well-localized problems, as already noticed in the previous chapter for a linear convection-diffusion equation.

Le	γ	L	ϵ	% CPU	% Mem
1	0	7	0.08	12.98%	4.38%
0.3	0.1	8	0.05	5.10%	1.72%
0.3	0.5	8	0.05	1.04%	0.32%

Table 4.5: Average CPU time and memory compressions for the 3D flame ball initially stretched, $Ze = 10$, $\Omega = [-20, 20]^3$.

4.5 Interaction of a flame ball with an adiabatic wall

In the previous section, premixed flames were studied far enough from the walls of the combustion chamber so that the influence of the boundaries is negligible. However, in laboratory experiments, the combustion chamber is of finite size and it may happen that a flame encounters a wall. Moreover, the quantity of available fresh mixture is finite.

In [35], the simulation of a premixed flame front in a channel has been performed. The thermodiffusive approximation has been chosen, without radiation, and the premixed gas flow followed a Poiseuille law. The authors showed two modes of extinction of the flame depending on the channel width: total flame extinction in narrow channels by excessive heat loss, and partial flame extinction near the wall of wider channels.

The present study aims at evaluating the influence of the Lewis number Le on a flame ball interacting with an adiabatic wall. In the following computations, the radiation is always neglected and the following parameters are set: $Ze = 10$ and $\alpha = 0.64$.

4.5.1 Flame front-wall interaction: the 1D case

In this part, we consider a planar flame interacting with an adiabatic wall. The physical problem is now one-dimensional and the set of equations modelling this phenomenon is the one of the propagating planar flame, i.e. (4.5). The computational domain is $\Omega = [x_0, x_M] = [0, 30]$. At $x = x_M$, we have a Neuman boundary condition. The boundary at $x = x_0$ has no influence on the computation. For reasons of simplicity, we decided to set the same condition on this border. Thus we have

$$\frac{\partial T}{\partial x}(x_0, t) = \frac{\partial T}{\partial x}(x_M, t) = 0 \tag{4.14}$$

$$\frac{\partial Y}{\partial x}(x_0, t) = \frac{\partial Y}{\partial x}(x_M, t) = 0 \tag{4.15}$$

We choose an initial condition similar to the one of the propagating planar flame, but this time the flame is initially located at $x = X$, $X \in \Omega$, i.e.

$$T(x, 0) = \begin{cases} 1 & \text{if} \quad x \leq X; \\ \exp(X - x) & \text{if} \quad x > X. \end{cases} \tag{4.16}$$

$$Y(x, 0) = \begin{cases} 0 & \text{if} \quad x \leq X; \\ 1 - \exp[Le(X - x)] & \text{if} \quad x > X. \end{cases} \tag{4.17}$$

The position of the flame front at $t = 0$ is $X = 22$, so that no long computation is required before the flame reaches the wall, i.e around 8 time units since $v_f \approx 1$. The time evolution of the temperature and the reaction rate are plotted in Fig. 4.24 for three different values of the Lewis number: 0.3, 1, and 1.4. For $Le = 0.3$, the intermediate state corresponds to $t_m = 4$ and the final one to $t_f = 20$. For $Le = 1$, we have $t_m = 4$ and $t_f = 7$. Finally, for $Le = 1.4$, we have set $t_m = 5$ and $t_f = 6$.

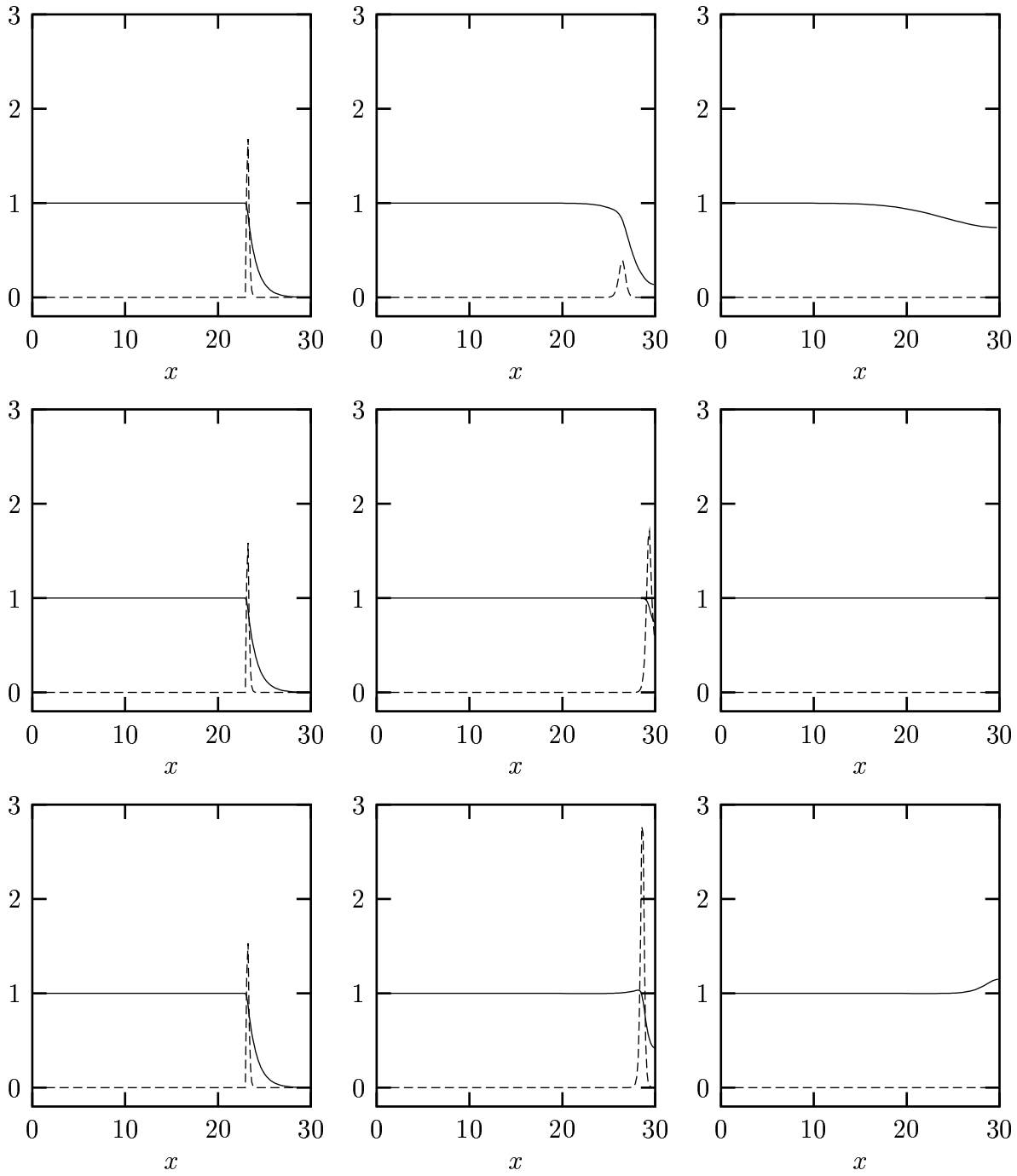

Figure 4.24: Interaction of a flame front with an adiabatic wall for $Le = 0.3$ (*top*), $Le = 1$ (*middle*), and $Le = 1.4$ (*bottom*). Profiles of T (*plain*) and ω (*dashed*) at $t = 0$ (*left*), $t = t_m$ (*center*), and $t = t_f$ (*right*).

In these plots, we observe the influence of the Lewis number on the flame when interacting with an adiabatic wall. For $Le = 0.3$, the reaction rate is gradually decreased, and the flame almost extinguishes at the contact with the wall. For $Le = 1$, ω is almost constant, slightly increased. For $Le = 1.4$, ω significantly increases. We also remark, at $t = t_f$, that $T < 1$ for $Le = 0.3$, whereas $T > 1$ for $Le = 1.4$. Therefore the total energy, which is only thermal, differs in the three cases. This is due to the fact that the partial mass at $t = 0$ depends on Le. In fact, since the total energy is conserved, the same difference of energy at $t = 0$ is observed at $t = t_f$.

In Fig. 4.25, we plot the time evolution of the flame velocity v_f for different values of the Lewis number. The limit between the two behaviors at the boundary - reaction rate increasing or decreasing - is not close to $Le = 1$. The phenomenon can be explained this way: for $Le < 1$, there is more ingoing reactant flux than outgoing heat flux in the reaction zone. Consequently, when the flame front is close to the wall, since less and less reactant is available, the reaction rate is decreased. However, the drop is gradual, because only little heat leaves the reaction zone. Moreover, since the maximum of the reaction rate is decreased, the flame velocity also diminishes. Therefore the decrease lasts a long time (Fig. 4.25, left side). On the other side, when $Le > 1$, the heat release involves an accelerated ignition of the reactant at the interphase between preheat and reaction zone, as discussed in Subsection 1.7.4. Here we observe a strong increase in the reaction rate and, therefore, for the flame velocity. However, as soon as the flame hits the wall, all the reactant is burnt, and the flame instantaneously extinguishes (Fig. 4.25, right side).

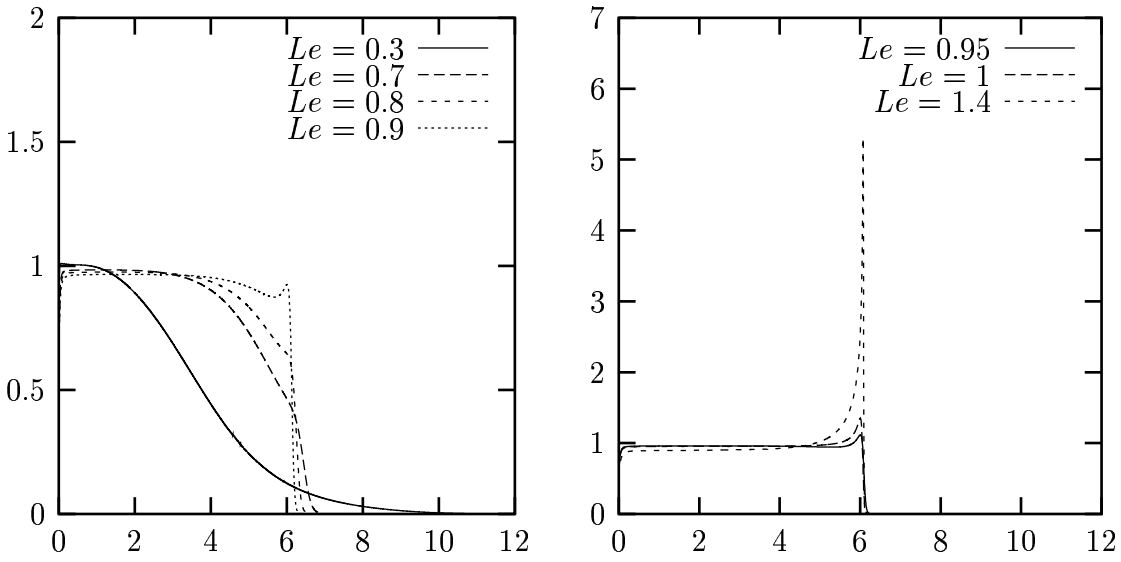

Figure 4.25: Interaction of a flame front with an adiabatic wall for $Le < 0.95$ (*left*) and $Le \geq 0.95$ (*right*). Time evolution of the flame velocity v_f.

To summarize, the Lewis number determines the behavior of a planar flame encoun-

tering an adiabatic wall. When $Le < 1$, the reaction rate is decreased, and the flame gradually extinguishes. When $Le > 1$, the reaction rate is increased, the flame accelerates, then quickly extinguishes when all the reactant is burnt.

4.5.2 Flame ball-wall interaction in 2D

In this part, we investigate the curvature effects in the interaction flame-adiabatic wall. Therefore we choose a flame front being initially circular. The system of modelling equations is the one of the 2D flame ball, i.e. (4.9). The walls is adiabatic, hence the boundary conditions are given by

$$\left.\frac{\partial T}{\partial n}\right|_{\partial\Omega} = \left.\frac{\partial Y}{\partial n}\right|_{\partial\Omega} = 0. \tag{4.18}$$

For the initial condition, we apply a translation to (4.11-4.12) in the x-direction, so that, at $t = 0$, the temperature at the intersection between the x-axis and the wall is equal to 1% of the initial temperature in the burnt gas zone.

Denoting by X the x-coordinate of the center of the flame ball, T on the x-axis at $t = 0$ is given by

$$T(x,0) = \begin{cases} 1 & \text{if} \quad x \leq X + r_0; \\ \exp\left(1 - \frac{x-X}{r_0}\right) & \text{if} \quad x > X + r_0. \end{cases}$$

where the x-coordinate of the center of the flame ball is

$$X = (L - r_0) + r_0 \ln 0.01 \ .$$

In Figs. 4.26-4.28, the time evolution of a flame ball encountering an adiabatic wall is plotted for three different values of the Lewis numbers and the same initial radius $r_0 = 2$. First, we observe an effect similar to the one described in the 1D case, i.e. for $Le < 1$, the reaction rate is gradually decreased when the flame reaches the wall, whereas its almost constant for $Le = 1$ and increased for $Le > 1$. This is confirmed by the cuts at $y = 0$, further described (Fig. 4.29). Then, we also observe a modification of the front curvature, due to tangential diffusion, when the flame front reaches the wall.

This phenomenon presents similarities with *capillarity* effects in fluid mechanics. When a fluid droplet encounters a wall, the angle between the surface of the droplet and the wall at the intersection can be smaller or bigger than $\frac{\pi}{2}$ depending on the superficial tension between both materials. For more details on this phenomenon, we refer e.g. to [49]. Here, we may interpret that the Lewis number characterizes this kind of capillarity. The flame ball contracts when $Le = 0.3$, whereas it spreads out when $Le = 1.4$. For $Le = 1$, the angle between the flame ball and the wall is close to $\frac{\pi}{2}$.

One can explain the phenomenon this way. On one side, when $Le < 1$, the ingoing reactant flux is strong everywhere *except in the region where the reactant is deficient.* Therefore, close to the wall, the reaction rate is decreased and the flame front slows down whereas, everywhere else, the reaction rate remains high. This phenomenon has already been observed in the 1D case. When the flame has extinguished on the wall, the diffusion

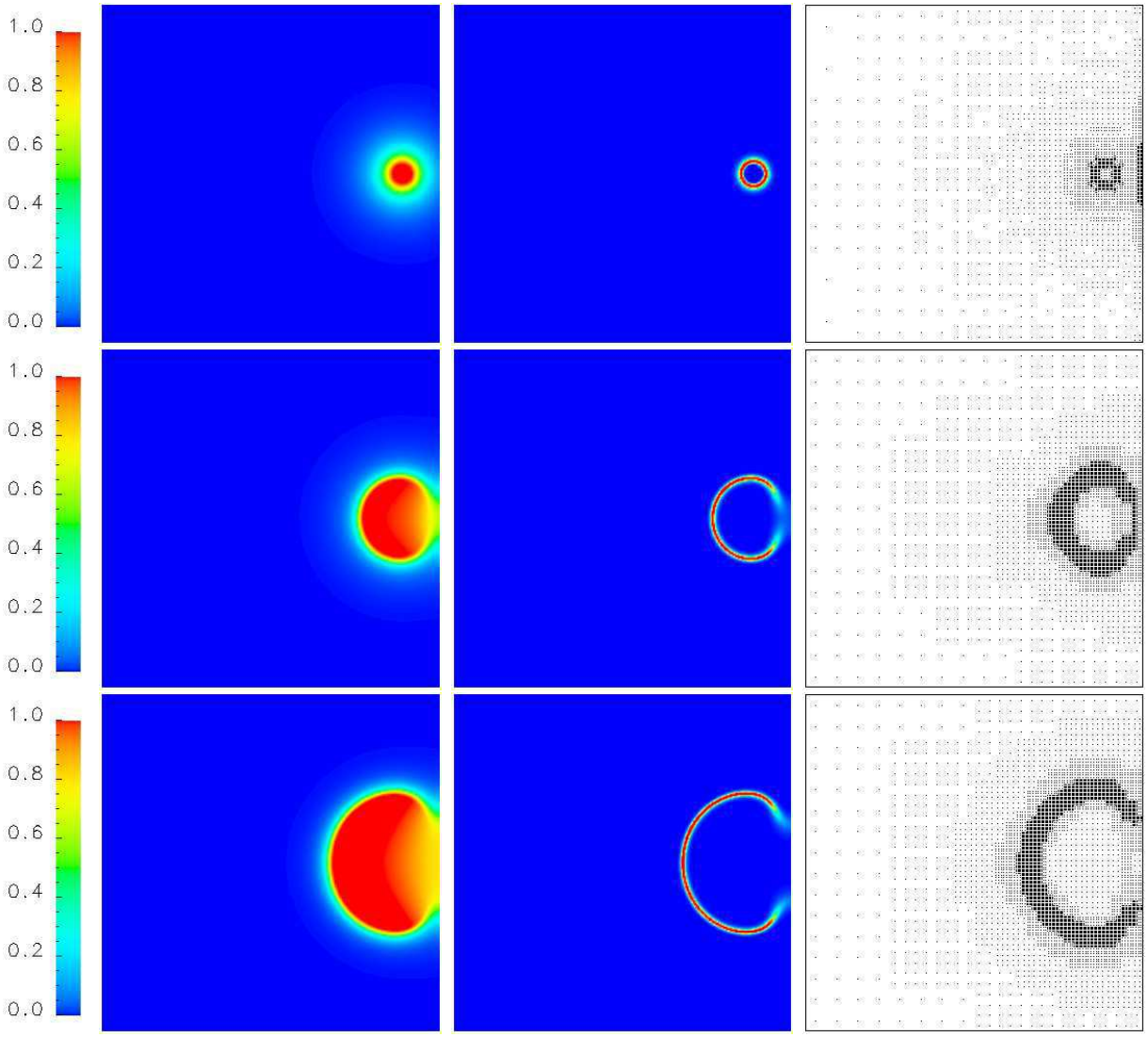

Figure 4.26: Left: Temperature T at $t = 0$ (*top*), $t = 5$ (*middle*), and $t = 10$ (*bottom*) for the interaction of a flame ball with an adiabatic wall, $Le = 0.3$. Center: Corresponding reaction rate ω. Right: corresponding meshes.

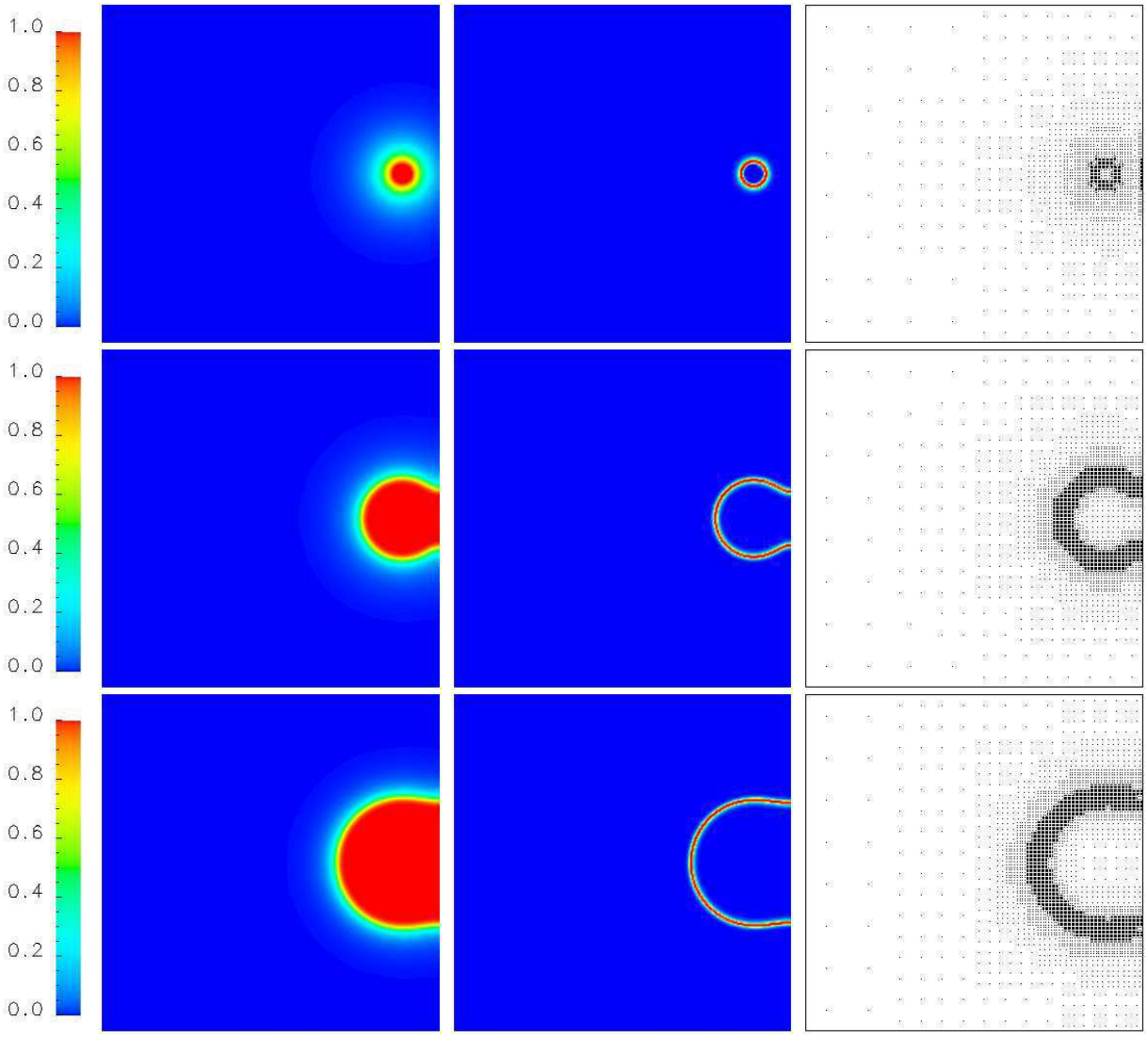

Figure 4.27: Left: Temperature T at $t = 0$ (*top*), $t = 5$ (*middle*), and $t = 10$ (*bottom*) for the interaction of a flame ball with an adiabatic wall, $Le = 1$. Center: Corresponding reaction rate ω. Right: corresponding meshes.

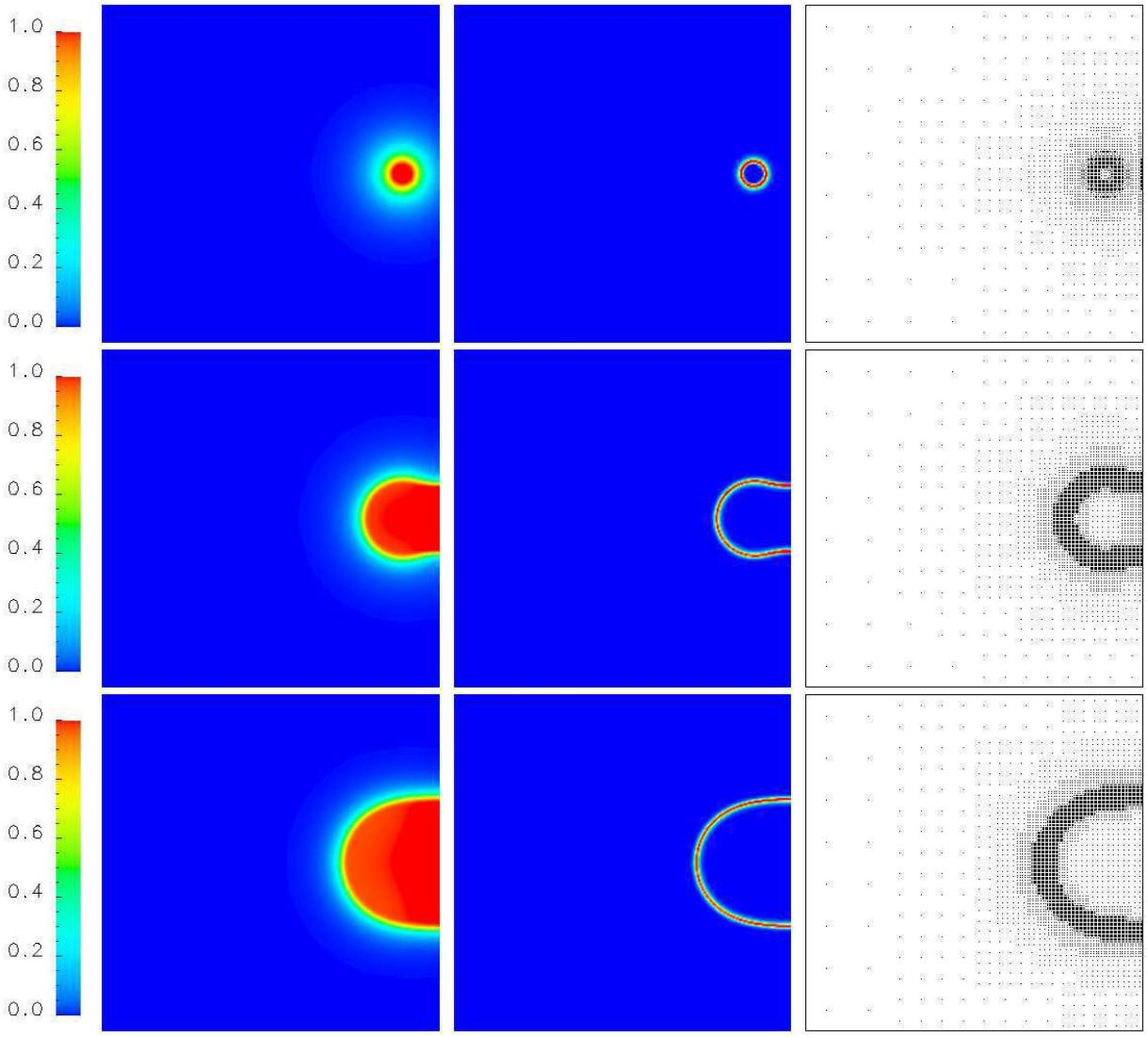

Figure 4.28: Left: Temperature T at $t = 0$ (*top*), $t = 5$ (*middle*), and $t = 10$ (*bottom*) for the interaction of a flame ball with an adiabatic wall, $Le = 1.4$. Center: Corresponding reaction rate ω. Right: corresponding meshes.

regulates the temperature, and thus the temperature is lower on the wall than inside the flame ball. On the other side, when $Le > 1$, the ignition is accelerated in the region close to the wall. When the flame has touched the wall, the acceleration is visible at the intersections between the wall, the fresh gas mixture and the burnt gas mixture. The reaction rate in these regions is stronger than in the rest of the flame front, which explains that the flame ball spreads out.

On the right side of the temperature cuts, the corresponding meshes are given. Here the chosen tolerance is $\epsilon = 10^{-2}$, which is sufficient for $L = 8$ scales. We observe that the mesh follows well the flame front propagation. The CPU time and memory compressions are respectively 25.5% and 14.1% for $Le = 0.3$, 21.5% and 11.1% for $Le = 1$, and 21.0% and 11.75% for $Le = 1.4$.

The cuts at $y = 0$ confirm the behavior of a flame encountering an adiabatic wall in the 1D case. For $Le = 0.3$, the reaction rate is decreased when the flame front is close to the wall, whereas it is almost stable for $Le = 1$ and increased for $Le = 1.4$.

In Fig. 4.30 (*left*), the integral of the reaction rate $\mathcal{R}$, defined in (4.13), is plotted for three different values of the Lewis number. At $t \approx 3$, the flame front reaches the wall located at $x = x_M$. This contact is characterized by a small peak on the curve of $\mathcal{R}$, but only for $Le \geq 1$. For $Le = 0.3$, as already observed in 1D, the reaction rate is gradually decreased when the flame front reaches the wall. Consequently, no peak is observed.

Then, the flame front simultaneously touches the upper and lower walls. For $Le = 0.3$, this happens at $t \approx 21$. Even if no peak is observed, $\mathcal{R}$ is strongly decreased thereafter, because the flame ball can no more expand. Moreover, the flame front reaches these same walls only at $t \approx 29$ for $Le = 1$, and $t \approx 30$ for $Le = 1.4$. This shows that the flame velocity is larger for $Le = 0.3$ than for $Le = 1$, and larger for $Le = 1$ than for $Le = 1.4$. This dependency of v_f on Le has already been observed in the previous sections. The last wall is reached at $t \approx 42$ for $Le = 0.3$, $t \approx 55$ for $Le = 1$, and $t \approx 61$ for $Le = 1.4$. Finally, when all the reactant is burnt, the chemical reaction stops.

When the flame front reaches one of the walls, we observe a strong peak for $Le = 1.4$, a moderate peak for $Le = 1$ and no peak for $Le = 0.3$. Since the flame velocity is equal to $\mathcal{R}$ in 1D, we can conclude that the qualitative behavior of the 2D flame ball touching an adiabatic wall is similar to what we observed in the 1D case.

Let us remark that, in the case $Le = 0.3$, the flame ball perturbated by the interaction with the wall does not split. This is because the flame front reaches the upper and lower walls before the splitting.

4.5.3 Flame ball-wall interaction in 3D

In this part, we extend the previous results to three space dimensions, in order to investigate the 3D effects of the interaction. As for the 2D case, the system of modelling equations is (4.9) and the boundary conditions are given by (4.18). They correspond to a closed box with adiabatic walls. The initial condition is the same as in the 2D case, with $r = \sqrt{x^2 + y^2 + z^2}$. We perform numerical simulations from $t = 0$ to $t = 10$ with $L = 7$ scales

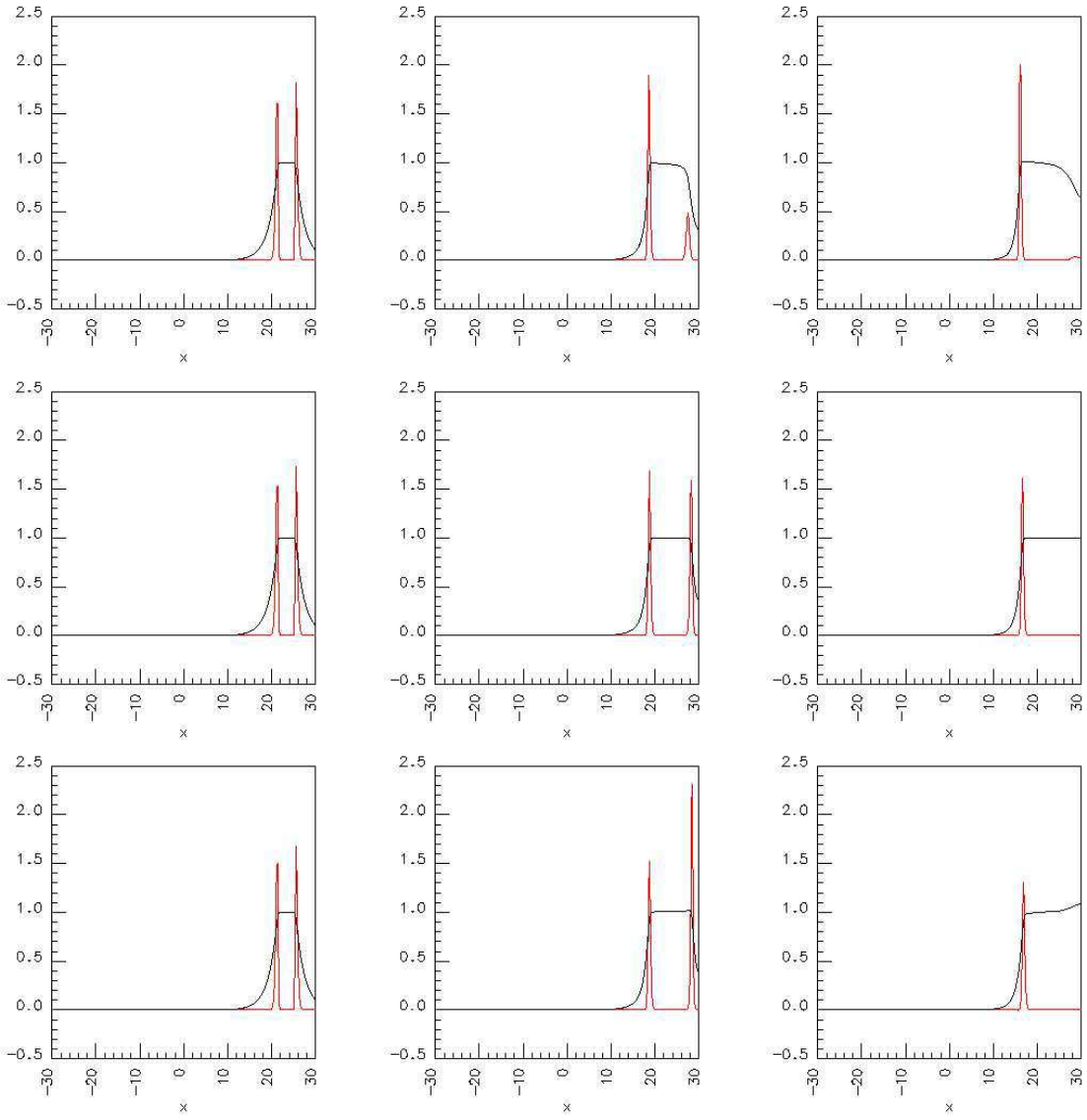

Figure 4.29: Left: Profile of T (black) and ω (red) for $y = 0$ at $t = 0$ (*left*), $t = 2.5$ (*center*), and $t = 5$ (*right*) for the interaction of a flame ball with an adiabatic wall, $Le = 0.3$ (*top*), $Le = 1$ (*middle*), $Le = 1.4$ (*bottom*).

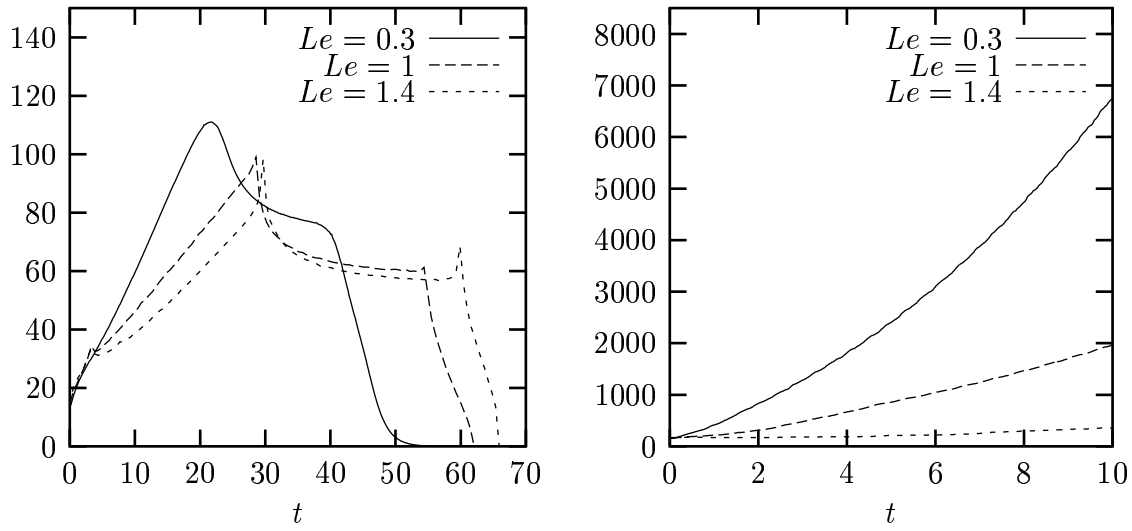

Figure 4.30: Interaction of a flame ball with an adiabatic wall. Time evolution of $\mathcal{R}$ in 2D (*left*) and 3D (*right*) for different values of Le.

and a tolerance set to $\epsilon = 10^{-2}$. The numerical solution for T and ω and the corresponding grids are plotted in Figs.4.31-4.33.

We can observe the same capillarity effect as in the 2D case. However, being given the configuration and the physical elapsed time, this effect is more difficult to detect. The isosurfaces of temperature confirm the axisymmetry of the problem. However, the time evolution of $\mathcal{R}$ is different than in the 2D case, since no peak is visible when the flame front reaches the wall for $Le = 1$ and $Le = 1.4$ (Fig. 4.30, right side). This is due to the fact the the flame extends in the two other directions. Thus, even if the chemical reaction stops close to the wall, the flame ball goes on growing in the rest of the domain. We also remark that the peak was already much sharper in 1D than in 2D, given that, in the 1D case, the reaction stops as soon as the planar flame front reaches the wall. In the 2D case, the integral of the reaction rate is significantly modified by the interaction with the wall. In the 3D case, the extinction of the part of the flame front reaching the wall has little influence on the global reaction rate. Let us finally remark that we focused on the early times. For late times, the flame ball extinguishes as soon as all the fresh mixture is burnt.

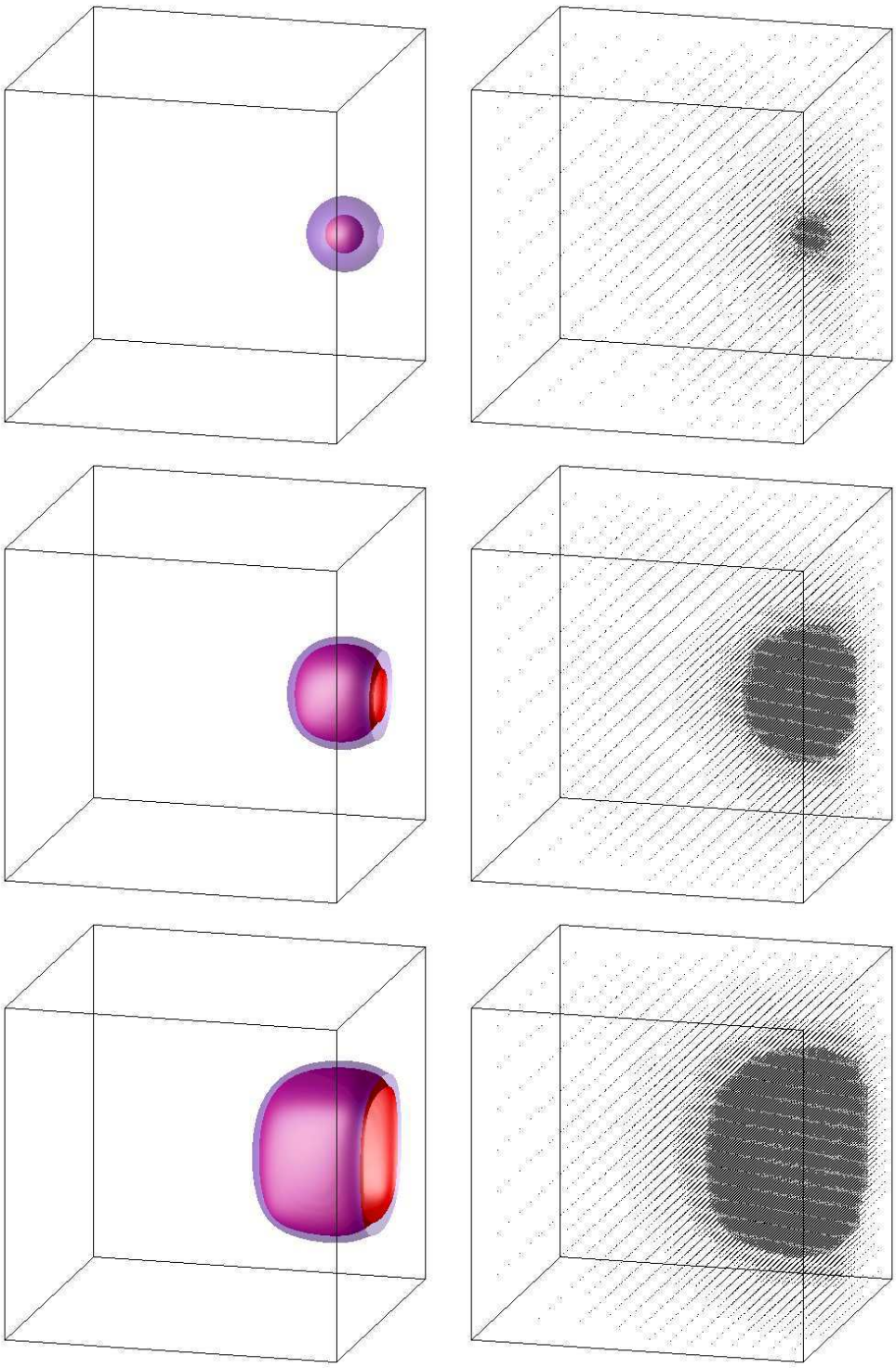

Figure 4.31: Left:Isosurfaces $T = 0.5$ (red) and $T = 0.1$ (purple) at $t = 0$ (*top*), $t = 3$ (*middle*), and $t = 5$ (*bottom*) for the interaction of a flame ball with an adiabatic wall, $Le = 0.3$. Right: corresponding meshes.

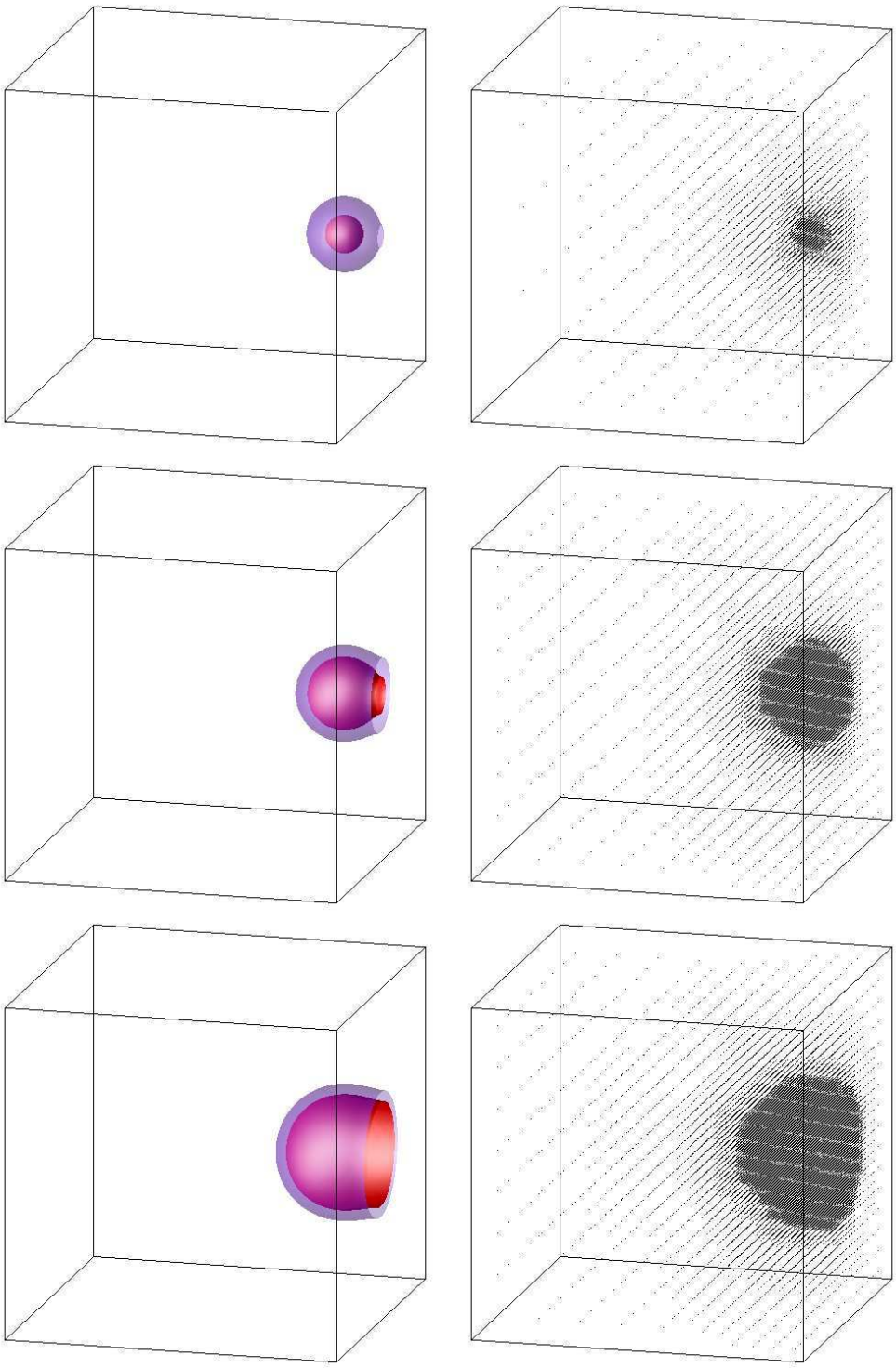

Figure 4.32: Left:Isosurfaces $T = 0.5$ (red) and $T = 0.1$ (purple) at $t = 0$ (*top*), $t = 5$ (*middle*), and $t = 10$ (*bottom*) for the interaction of a flame ball with an adiabatic wall, $Le = 1$. Right: corresponding meshes.

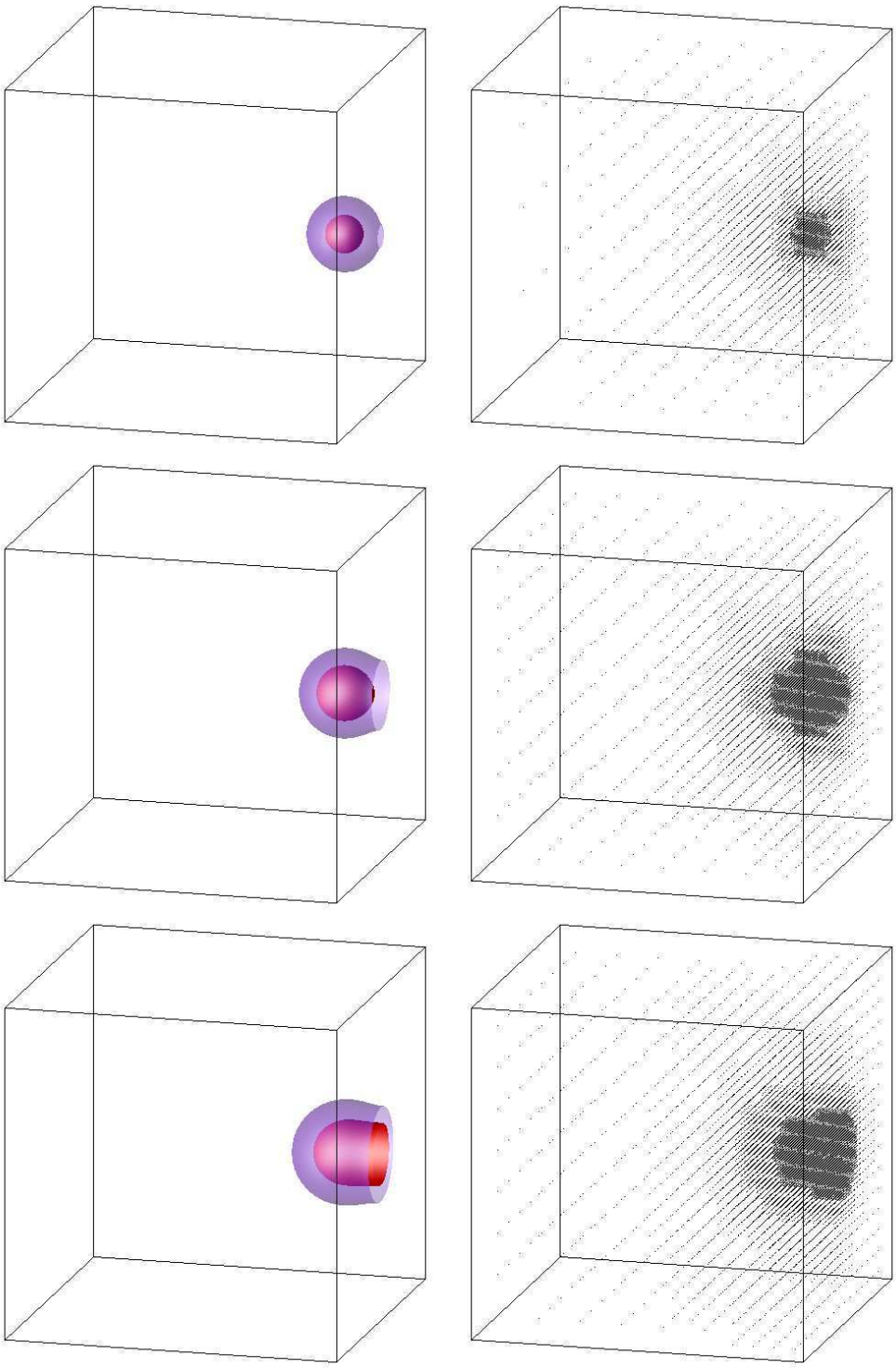

Figure 4.33: Left: Isosurfaces $T = 0.5$ (red) and $T = 0.1$ (purple) at $t = 0$ (*top*), $t = 5$ (*middle*), and $t = 10$ (*bottom*) for the interaction of a flame ball with an adiabatic wall, $Le = 1.4$. Right: corresponding meshes.

4.6 Interaction of a flame ball with a vortex

This section is an introduction for a future work concerning flame balls inside a moving fluid. Here we consider the interaction of a flame ball, i.e. a spherical flame structure, with an isolated vortex in a combustion chamber filled with premixed gas. Such a phenomenon can be observed e.g. in furnaces. The aim is to show the influence of the fluid flow on the flame propagation.

As before, we restrict ourselves to the hypothesis of constant density approximation. In this case, the reaction has no influence on the fluid flow. The velocity field of the gaseous mixture $\vec{v}(x,t)$ is solution of the incompressible Navier-Stokes equations. Following (1.9), the system of equations modelling this phenomenon is, for $(\vec{x},t) \in \Omega \times [0,+\infty)$,

$$\begin{aligned} \frac{\partial T}{\partial t} + \vec{v}\cdot\vec{\nabla}T &= \nabla^2 T + \omega - s \\ \frac{\partial Y}{\partial t} + \vec{v}\cdot\vec{\nabla}Y &= \frac{1}{Le}\nabla^2 Y - \omega \end{aligned} \tag{4.19}$$

where ω and s are defined in (4.1). The chosen initial condition is the same as when the fluid is at rest, but this time the center of the flame ball is translated in the x-direction. Thus we have

$$T(r,0) = \begin{cases} 1 & \text{if} \quad r \le R; \\ \exp\left(1-\frac{r}{R}\right) & \text{if} \quad r > R. \end{cases} \tag{4.20}$$

$$Y(r,0) = \begin{cases} 0 & \text{if} \quad r \le R; \\ 1-\exp\left[Le\left(1-\frac{r}{R}\right)\right] & \text{if} \quad r > R. \end{cases} \tag{4.21}$$

where $r = \sqrt{(x-X)^2+y^2}$. As before, we consider that the combustion chamber is a closed box with adiabatic walls. It is taken sufficiently large, so that the premixed gas close to the wall is at rest. Therefore, we have a Neuman condition on the boundary, i.e.

$$\left.\frac{\partial T}{\partial n}\right|_{\partial\Omega} = \left.\frac{\partial Y}{\partial n}\right|_{\partial\Omega} = 0. \tag{4.22}$$

Let us consider that the fluid motion is two-dimensional and axisymmetric. In this case, the vorticity $\vec{\varpi} = \vec{\nabla}\times\vec{v}$ is a pseudo-scalar ($\vec{\varpi} = \varpi\ \vec{u}_z$) and function only of time t and distance to the origin r [5]. Moreover, the incompressible Navier-Stokes equations in velocity-vorticity formulation reduce to one equation, which can be expressed in the following dimensionless form

$$\frac{\partial \varpi}{\partial t} = \frac{1}{Re}\nabla^2\varpi\ . \tag{4.23}$$

where Re denotes the Reynolds number. Thus, given the initial condition

$$\varpi(r,0) = -\Gamma\frac{Re}{4\ \pi\ \tau}e^{-Re\frac{r^2}{4\ \tau}}\ ,$$

where Γ denotes the circulation and τ a characteristic time ($\tau > 0$), we get the analytical solution in an infinite domain [5]

$$\varpi(r,t) = -\Gamma \frac{Re}{4\,\pi\,(t+\tau)} e^{-Re\frac{r^2}{4\,(t+\tau)}} \ . \tag{4.24}$$

We deduce from (4.24) the analytical solution verified by the velocity

$$\vec{v}(r,t) = -\frac{\Gamma}{2\,\pi\,r}\left(1 - e^{-Re\frac{r^2}{4\,(t+\tau)}}\right)\,\vec{u}_\theta \ . \tag{4.25}$$

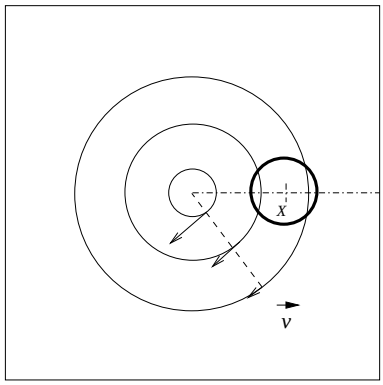

Figure 4.34: Interaction of a flame ball with a vortex. Initial condition.

The temperature ratio is $\alpha = 0.64$. The corresponding Lewis and Zeldovich numbers are $Le = 0.3$ and $Ze = 10$. The radius of the flame ball is $R = 0.5$ and the x-coordinate of the center is $X = 2.5$. Concerning the fluid motion, the Reynolds number is $Re = 100$, the circulation $\Gamma = 10$, and the characteristic time $\tau = 0.1$. For the multiresolution computation, the domain is $\Omega = [-10,\ 10]^2$. We use a maximum of $L = 9$ scales with a tolerance $\epsilon = 10^{-2}$. The advective term is discretized by a second-order centered scheme. Temperature, reaction rate and adaptive mesh for $t = 0$, $t = 0.5$ and $t = 1$ are plotted in Fig. 4.35. The profiles of T and ω on the plans $x = X$ and $y = 0$ are given in Fig. 4.36. On average we only use 5.90% out of $512^2 = 262144$ control volumes. Comparing the elapsed CPU time with the one obtained by the same finite volume scheme on the finest grid, we get a CPU compression of 8.60%.

We observe that the vortex is advecting the flame ball clockwise and around the center of the vortex. Since the velocity increases when getting closer to the center, the initially circular flame structure gets more and more distorted. Moreover, as $Le = 0.3$, the perturbation involved by the vortex is amplified. From the cuts of Fig. 4.36, we observe that the reaction rate is stronger in the part of the flame front which penetrates inside the fresh mixture.

The integral of the reaction rate $\mathcal{R}$ is plotted for the adaptive method on 9 scales and non-adaptive method on 9 and 10 scales (Fig. 4.37, left side). We find comparable results,

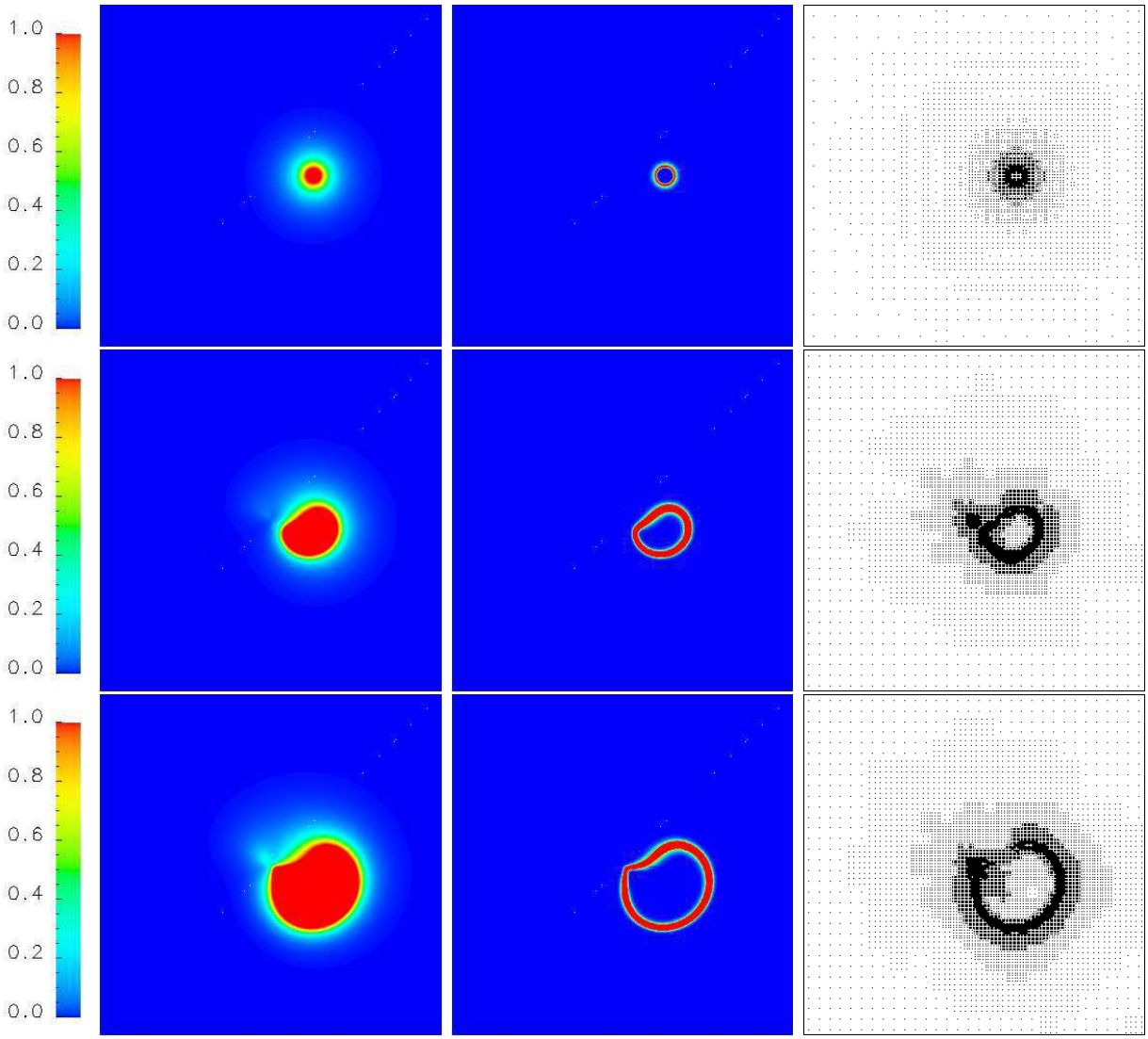

Figure 4.35: Left: Contours of T from 0 (blue) to 1 (red) at $t = 0$ (*top*), $t = 0.5$ (*middle*), and $t = 1$ (*bottom*) for the interaction of a flame ball with a vortex. Center: Corresponding contours of ω. Right: Corresponding meshes.

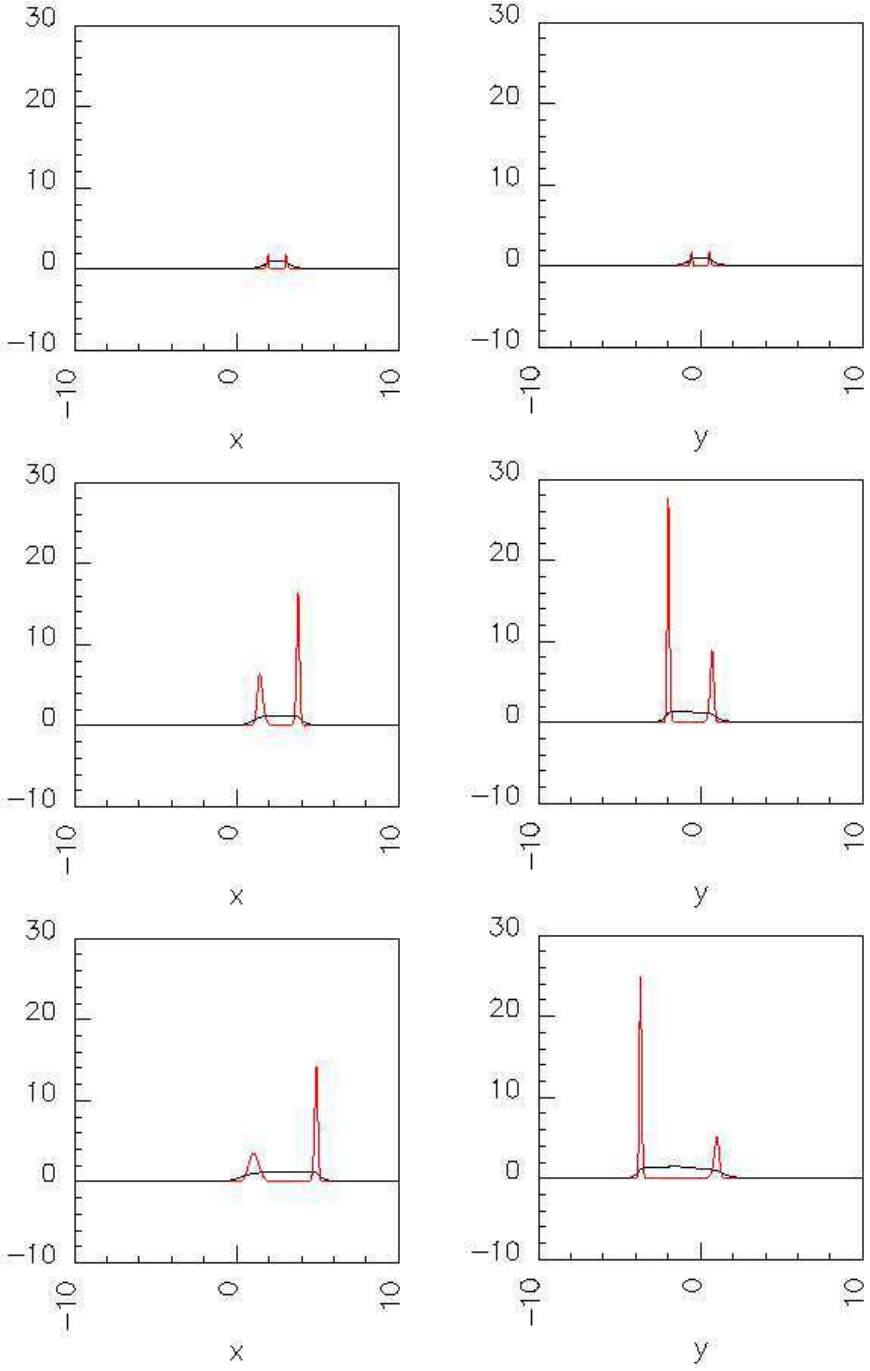

Figure 4.36: Cuts of T (black) and ω (red) at $t = 0$ (*top*), $t = 0.5$ (*middle*), and $t = 1$ (*bottom*) for the interaction of a flame ball with a vortex on the plans $y = 0$ (*left*) and $x = X$ (*right*).

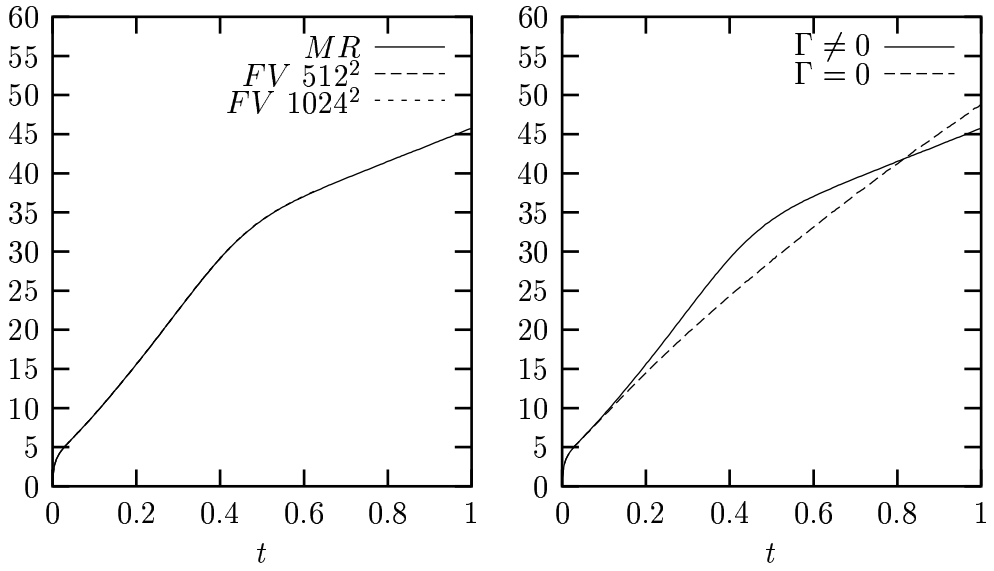

Figure 4.37: Left: Integral of the reaction rate $\mathcal{R}$ for adaptive multiresolution method (MR) on 9 scales and finite volume method (FV) on 9 and 10 scales. Right: Integral of the reaction rate $\mathcal{R}$ with vortex and without vortex.

which shows that the choice for the scale and the tolerance give a sufficiently accurate result. On Fig. 4.37 (right side), we compare with the case where no vortex exists. We observe this way the influence of the vortex. Even if it has a positive effect on the global reaction rate at the beginning, it finally penalizes the chemical reaction.

4.7 Discussion of the results

The computations of planar flame fronts have shown the efficiency and the accuracy of the adaptive multiresolution method for thermodiffusive equations in 1D, which is a stiff problem for large values of Ze. The study of pulsating planar flames, which requires more than 12 scales when $Ze > 40$, has improved the previous results obtained with a non-adaptive method [77]. For large values of Ze, the adaptive numerical simulations confirm the asymptotic theory presented in [60], which was not the case for previous non-adaptive computations. Moreover, for large values of Le and moderate values of Ze, we have shown that stable planar flames can exist and we have given a physical interpretation to this phenomenon. However, the number of required scales was estimated for a given Ze and for $Le = 1.25$. For pulsating flames, the flame velocity can strongly increase and the reaction zone can be much smaller than in the case $Le = 1.25$. As a consequence, the number of scales may not be sufficient when the reaction rate reaches its maximal value. Moreover, the computation of flames whose velocity tends towards infinity logically leads to a numerical instability, because the numerical method is explicit in time. A solution to

this problem could be to adapt the time step during the computation.

Concerning 2D and 3D simulations of flame balls, the numerical computations of flame balls initially stretched have shown that, depending on the Lewis number and the radiation coefficient, the different scenarios of evolution - spherical growth, splitting, extinction - have been well observed and confirm the previous numerical computations in 2D [14] and 3D [47]. The adaptive multiresolution method shows a much better performance than a classical finite volume method. This is particularly true for 3D computations where, as shown in the previous chapter, the performance in terms of CPU time and memory requirements is much larger than in 2D. Nevertheless, due to an explicit time integration, three-dimensional adaptive computations for stiff problems on 8 scales are cheap in terms of memory requirements, but become expensive in terms of CPU time when a lot of iterations are required. The parallelization of the algorithm, which is the subject of a work in progress, could solve this problem by dispatching the computation on several processors.

4.8 Conclusion

In this chapter, we have applied the adaptive multiresolution method to thermodiffusive flame instabilities, which require very fine grids, but only in the thin chemical reaction zone. First, we have performed 1D computations for steady and propagating planar flames and compared the results on the flame velocity for different Le and Ze with asymptotic ones. We have also studied pulsating planar flames, which appear for Lewis numbers larger than unity. Then, multidimensional adaptive simulations were performed for 2D and 3D flame balls. We have first simulated perturbated flame balls to see the influence of the Lewis number and the radiation on the stability and the evolution of flame balls. Then, we have studied the interaction of a flame ball with an adiabatic wall, first for a flame front, which leads to a 1D case, then for flame balls in 2D and 3D configurations. Finally, we have applied our adaptive multiresolution method to a flame ball interacting with a vortex.

For all the computations performed in this chapter, CPU and memory performances show that the adaptive method is always more efficient than the finite volume method on the regular finest grid. Concerning pulsating flames, the bifurcation diagram with Lewis and Zeldovich numbers as control parameters was improved using the adaptive multiresolution method. In particular, our computations confirm the asymptotic theoretical result from Joulin-Clavin [60] for $40 < Ze < 55$. Moreover, for large values of the Lewis number and moderate Zeldovich numbers, i.e. $10 < Ze < 20$, we show that stable planar flames can exist. Concerning simulations in 2D and 3D, our results concerning flame balls initially stretched and far from the walls confirm the results obtained by other methods. The different scenarios of evolution, i.e. spherical growth, splitting and extinction, are the same as the ones computed in 2D with the adaptive wavelet-vaguelette method [14] and in 3D with the Fourier pseudo-spectral method with a parallelized algorithm [47]. We have also shown that, when a flame front reaches an adiabatic wall, the reaction rate is growing when $Le > 0.9$ and diminishing when $Le < 0.9$. Moreover, 2D and 3D computations show

a phenomenon similar to capillarity when a flame ball interacts with an adiabatic wall. Finally, the adaptive computation of a flame ball interacting with a vortex shows that, for $Le = 0.3$ and when the center of the flame ball does not coincide with the one of the vortex, this latter one reduces the global chemical reaction rate. Moreover, as observed in the other computations, the grid follows well the physical phenomenon. Thus, the adaption strategy used in this thesis is not dedicated to a specific problem, like e.g. shock or flame front propagations. It aims at solving with a reduced cost every stiff problem for which the time evolution is continuous both in space and scale.

Conclusion and perspectives

In the present thesis we developed a new fully adaptive numerical scheme to speed up finite volume computations of parabolic PDEs in Cartesian geometry, in one, two and three space dimensions. We demonstrated its computational efficiency and the numerical accuracy by computing several test-cases of linear and non linear parabolic PDEs. We then applied the method to the numerical simulation of thermodiffusive flame instabilities. In particular, we studied the pulsating behavior for planar flames, the cellular behavior for flame balls initially perturbated, the interaction of a flame ball with an adiabatic wall and with a vortex.

Starting point of the method is a finite volume discretization on a regular equidistant grid, together with an explicit time integration, both of second order. Time integration is performed through an explicit Runge-Kutta scheme. Space discretization uses centered schemes for diffusive and source terms. For the advective terms, we used an ENO decentered scheme for convection-diffusion and viscous Burgers equations, a centered scheme for convection-diffusion-reaction equations. Using discrete multiresolution analysis techniques the computational grid is reduced by deleting non significant grid points while maintaining the second order accuracy of the scheme. A dynamical adaptation strategy which exploits the multiscale representation of the solution by adding neighbored coefficients in scale and space to account for translation and the creation of finer scales of the solution allows to advance the grid in time. For the evaluation of the numerical fluxes on the locally refined grid we devise a conservative scheme without increasing significantly the number of costly flux evaluations. The presented error analysis yields a theoretical relation for the choice of a level dependent threshold for convection-diffusion equations in order to guarantee the second order accuracy, which is confirmed by numerical computations. The adaptive algorithm is implemented using a graded tree data structure to represent the locally refined grid in the computer memory. A recursive procedure is used to address each element of the tree. Although this concept is slightly more complex, i.e. an $O(N \log N)$ complexity instead of $O(N)$ (where N denotes the number of active grid points), this choice enables us to avoid hash-tables, which require large arrays and therefore much memory which may be prohibitive for large scale 3D computations.

The accuracy of the algorithm has been validated by solving convection-diffusion and viscous Burgers equations. We compared the computed solutions with the exact ones and studied the error as a function of the maximal level and the prescribed tolerance. The presented theoretical relation for the level dependent tolerance to maintain the second

order accuracy has been confirmed by our computations.

To demonstrate the efficiency of the algorithm, we have compared the performance in terms of CPU time and memory requirements to a finite volume method using the same numerical schemes on the finest regular grid with a static data structure. We have shown that the relative performance increases with the number of required levels and tends towards a minimal value which depends on the test case. Furthermore the gain increases significantly with the spatial dimension of the problem.

Then we presented several applications to combustion problems in the thermodiffusive approximation. Concerning planar flames, we first presented computations of steady and propagating planar flames and found a good agreement on the value of the flame velocity with asymptotic results [73]. Then we studied the pulsating planar flames, a consequence of the thermodiffusive instability for $Le > 1$. In this thesis, we have completed the $Le - Ze$ bifurcation diagram to the domains $50 > Ze > 40$ and $10 > Le > 5$ and compared with previous results [60, 77]. Since the thickness of the chemical reaction zone is $O(Ze^{-1})$, the problem gets stiffer and stiffer when Ze grows, and the adaptive computation becomes more and more efficient compared to a computation on a regular fine grid. For $Ze > 40$, we have confirmed the theoretical results obtained using asymptotic expansions [60]. We have also shown that stable flames exist for large values of the Lewis number and moderate Zeldovich numbers.

Concerning flame balls in two- and three-dimensional configurations, we have studied the stability and the evolution of a flame ball far from the walls and initially stretched for different values of the Lewis number Le and the radiation coefficient γ. The different scenarios of evolution, i.e. spherical growth for $Le = 1$, splitting for $Le = 0.3$ and $0 < \gamma \leq 0.05$, and extinction for $Le = 0.3$ and $\gamma > 0.05$, confirm the previous numerical results obtained by an adaptive wavelet-vaguelette method in 2D [14] and a non-adaptive Fourier pseudo-spectral method in 3D [47].

Then we have studied the influence of the Lewis number for a flame interacting with an adiabatic wall. For a planar flame, the reaction rate in the chemical reaction zone increases for $Le > 0.9$ and decreases for $Le \leq 0.9$ when the flame front reaches the wall. In the multidimensional case, we have shown that a flame ball interacting with an adiabatic wall has a behavior which presents an analogy with capillarity in fluid dynamics.

The final result is a first computation of a flame ball in a moving fluid using the adaptive multiresolution method. We have simulated the interaction of a flame ball with a vortex and shown that, for the given parameters, the presence of the vortex reduces the global chemical reaction rate. In all the numerical simulations, we showed that the grid follows well the physical phenomenon and that the adaptive computation is always cheaper in terms of CPU time and memory requirements than the computation on a fine equidistant grid.

Current work is dealing with the parallel implementation of the algorithm on a PC cluster to perform large scale 3D computations for combustion problems. Actually, for more than 8 scales and for long-time problems, the required CPU time becomes prohibitive for 3D computations on a single PC, whereas the memory requirements remains affordable. To reach this goal, the data structure is organized as a "forest", i.e. an ensemble of trees,

each one working on a different processor.

Future work will focus on the extension of the developed scheme to systems of reactive Navier-Stokes equations, in order to take into account hydrodynamic effects in combustion problems. To simulate and to model turbulent reactive flows on adaptive grids, we will also use the CVS (Coherent Vortex Simulation) approach (Farge and Schneider [42]). Another perspective concerns the extension to complex geometries, which would enable us to study combustion problems in industrial configurations. The extension to structured meshes in 2D has already been done for hyperbolic problems and applied to supersonic fluid flows around airfoils [16]. Adaptive multiresolution method on unstructured triangular meshes for hyperbolic problems has also been done [27]. An important perspective is the adaptivity in time, which has already been implemented with success in adaptive mesh refinement methods for shock computations [74]. We plan to implement a time stepping which depends on the scale, in order to use larger time steps in the large scales.

Appendix

Appendix A

Wavelets and multiresolution analysis

The cell-average multiresolution representation of Harten [52, 54], which has been described in the second chapter, relies on the more general theory of wavelets. In this appendix, we present some features of this theory, i.e. the multiresolution analysis and the biorthogonal wavelets, and their link with the cell-average multiresolution representation. We restrict ourselves to the one-dimensional case. The extension to n dimensions can be made using a tensor-product construction. For an exhaustive treatment, we refer to textbooks [37, 68, 27].

A.1 Definition

The concept of *multiresolution analysis* (MRA) was firstly introduced by Mallat [67]. A multiresolution analysis in $\mathcal{L}^2(\mathbb{R})$ is a sequence of embedded subspaces V_l, $l \in \mathbb{Z}$, verifying

$$\begin{gathered} V_l \subset V_{l+1} \\ \overline{\bigcup_{l\in\mathbb{Z}} V_l} = \mathcal{L}^2(\mathbb{R}) \\ \bigcap_{l\in\mathbb{Z}} V_l = \{0\} \\ f(\cdot) \in V_l \Longleftrightarrow f(2\cdot) \in V_{l+1} \end{gathered} \tag{A.1}$$

A *scaling function* $\phi(x)$ is required to exist. The translates of ϕ, denoted $\phi_{l,i}$, generate bases of the spaces V_l. This can be written in the following form:

$$\forall l \in \mathbb{Z},\ V_l = \overline{\mathbf{span}}\{\phi_{l,i}\}_{i\in\mathbb{Z}}\ , \tag{A.2}$$

where

$$\forall l, i \in \mathbb{Z},\ \phi_{l,i}(x) = 2^{\frac{l}{2}}\ \phi(2^l x - i)\ .$$

Since $V_0 \subset V_1$, the scaling function ϕ can be expanded in terms of the basis of V_1, i.e.

$$\phi(x) = \sum_{i \in \mathbb{Z}} h_i \, \phi(2x - i) \ , \quad h_i \in \mathbb{R}. \tag{A.3}$$

This equation is called the *refinement equation*. A function that satisfies such an equation is called a *refinable function*, and the coefficients h_n are called the *refinement coefficients*.

A scaling function $\phi \in \mathcal{L}^2(\mathbb{R})$ is said to be *orthonormal* when it satisfies

$$< \phi(\cdot - i), \ \phi(\cdot - j) >_{\mathbb{R}} = \delta_{i,j} \ , \quad i, j \in \mathbb{Z}. \tag{A.4}$$

In this case, the family $\{\phi_{l,i}\}_{i \in \mathbb{Z}}$ is an orthonormal basis of V_l, $l \in \mathbb{Z}$, i.e.

$$< \phi_{l,i}, \phi_{l,j} >_{\mathbb{R}} = \delta_{i,j} \ , \quad i, j \in \mathbb{Z}.$$

Example: The "box function"

$$\phi(x) = \chi_{[0,1[} = \begin{cases} 1 & \text{if } x \in [0,1[\\ 0 & \text{elsewhere} \end{cases} \tag{A.5}$$

generates a multiresolution analysis that consists of the spaces V_l defined by

$$V_l = \{ f \in \mathcal{L}^2(\mathbb{R}) \mid f(x) = Cste \text{ for } x \in I_{l,i} \ , \ i \in \mathbb{Z} \}$$

where $I_{l,i} = [2^{-l} \ i \ , \ 2^{-l} \ (i+1)[$. It satisfies the refinement equation

$$\phi(x) = \phi(2x) + \phi(2x - 1)$$

i.e $h_0 = h_1 = 1$, $h_i = 0$ elsewhere. The basis of V_l generated by ϕ is

$$\phi_{l,i}(x) = 2^{\frac{l}{2}} \phi(2^l \ x - i) = 2^{\frac{l}{2}} \chi_{I_{l,i}}$$

In this example, the scaling function is orthonormal. Therefore, the family $\{\phi_{l,i} \mid i \in \mathbb{Z}\}$ constitutes an orthonormal basis of V_l. The box function $\phi = \phi_{0,0}$ and two of its translates and dilates are plotted in Fig. A.1.

■

The main issue of the wavelet approach is now to work with the *complement spaces* W_l defined by

$$V_{l+1} = V_l \oplus W_l. \tag{A.6}$$

Analogously to the scaling function, one can find an *analyzing function* $\psi(x)$, called *mother wavelet*, whose translates $\psi_{l,i}$ constitute bases of the spaces W_l, i.e.

$$\forall l \in \mathbb{Z}, \ W_l = \overline{\mathbf{span}}\{\psi_{l,i}\}_{i \in \mathbb{Z}} \ , \tag{A.7}$$

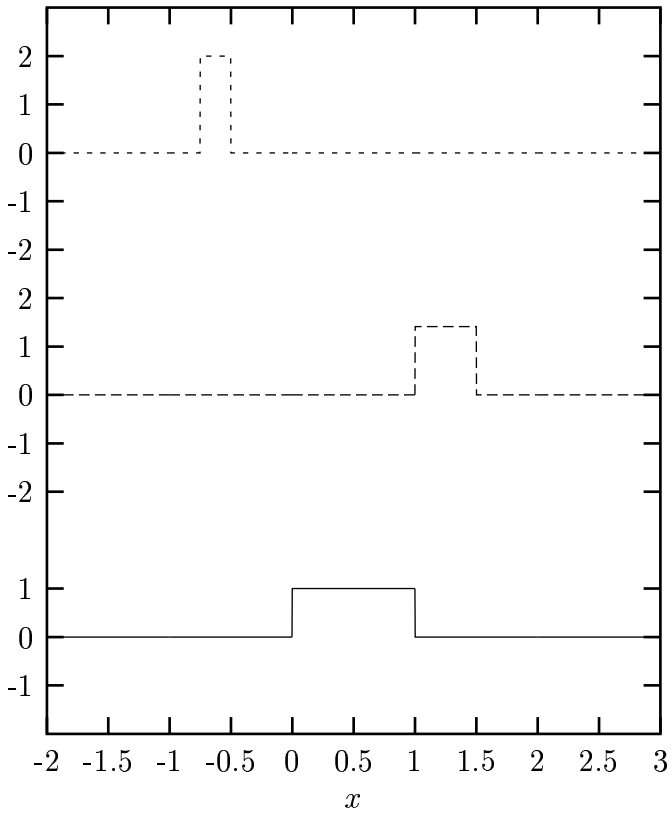

Figure A.1: Functions $\phi_{0,0} = \phi$ (*bottom*), $\phi_{1,2}$ (*middle*), and $\phi_{2,-3}$ (*top*).

where

$$\forall l, i \in \mathbb{Z},\ \psi_{l,i}(x) = 2^{\frac{l}{2}}\ \psi(2^l x - i)\ .$$

Since $W_0 \subset V_1$, the mother wavelet ψ can also be expanded in terms of the basis of V_1. Therefore ψ fulfills the following refinement equation:

$$\psi(x) = \sum_{i \in \mathbb{Z}} g_i\ \phi(2x - i)\ ,\quad g_i \in \mathbb{R}. \tag{A.8}$$

Applying (A.6) for $l-1$ and replacing it into (A.6), one gets

$$V_{l+1} = (V_{l-1} \oplus W_{l-1}) \oplus W_l,$$

and by recursion, for $l_0 < l$, we get

$$V_l = V_{l_0} \oplus \bigoplus_{n=l_0}^{l-1} W_n. \tag{A.9}$$

Therefore, given $l_0 \in \mathbb{Z}$, the family $\{\phi_{l_0,i},\ \psi_{l,i} \mid l \geq l_0,\ i \in \mathbb{Z}\}$ constitutes a basis of $\mathcal{L}^2(\mathbb{R})$, and each function $f \in \mathcal{L}^2(\mathbb{R})$ can be expressed on this basis, i.e.

$$f(x) = \sum_{i \in \mathbb{Z}} c_{l_0,i}\phi_{l_0,i}(x) + \sum_{l=l_0}^{+\infty}\sum_{i \in \mathbb{Z}} d_{l,i}\psi_{l,i}(x) \tag{A.10}$$

where $c_{l,i},\ d_{l,i} \in \mathbb{R}$, $\forall l, i \in \mathbb{Z}$. Such a basis is called a *wavelet basis*. When it is orthonormal, the coefficients $c_{l,i}$ and $d_{l,i}$ can be determined by

$$\begin{aligned} c_{l,i} &= < f\ ,\ \phi_{l,i} > \\ d_{l,i} &= < f\ ,\ \psi_{l,i} > \end{aligned}$$

where $<,>$ denotes the scalar product in $\mathcal{L}^2(\mathbb{R})$

$$\forall f, g \in \mathcal{L}^2(\mathbb{R}),\ < f, g >= \int_{\mathbb{R}} f(x)\, g(x)\, dx.$$

Example: Using the "box function" $\phi(x) = \chi_{[0,1]}$ as scaling function, the mother wavelet ψ can be defined by the following refinement equation

$$\psi(x) = \phi(2x) - \phi(2x-1) = \begin{cases} 1 & \text{if } x \in \left[0, \frac{1}{2}\right[\\ -1 & \text{if } x \in \left[\frac{1}{2}, 1\right[\\ 0 & \text{elsewhere} \end{cases}$$

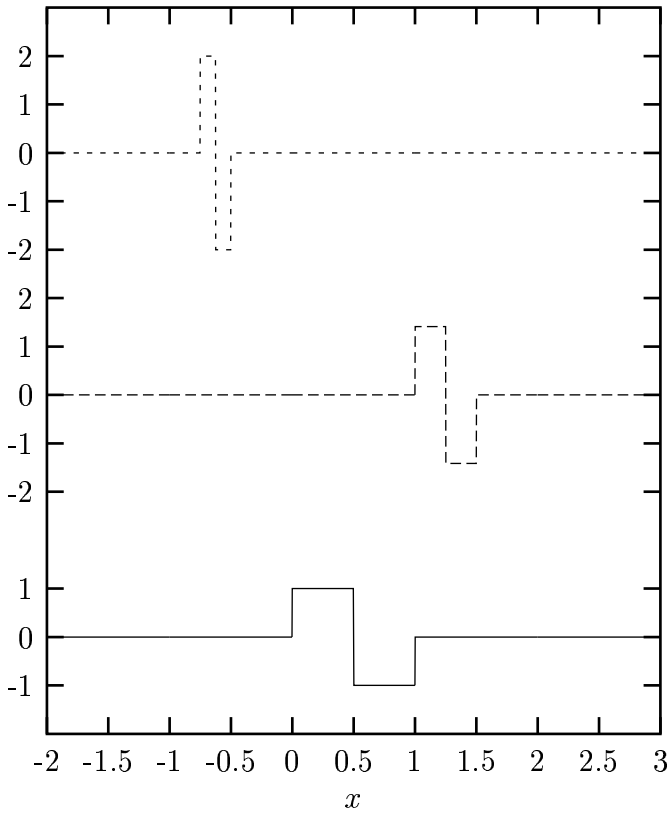

Figure A.2: Functions $\psi_{0,0} = \psi$ (*bottom*), $\psi_{1,2}$ (*middle*), and $\psi_{2,-3}$ (*top*).

Therefore we have $g_0 = 1$, $g_1 = -1$, else $g_i = 0$. The basis of W_l generated by ψ is

$$\psi_{l,i}(x) = 2^{\frac{l}{2}}\psi(2^l\, x - i) = 2^{\frac{l}{2}}(\chi_{I_{l+1,2i}} - \chi_{I_{l+1,2i+1}})$$

The function $\psi = \psi_{0,0}$ and two of its translates and dilates are plotted in Fig. A.2.

Haar [50] showed that, for a given l_0, the family $\{\phi_{l_0,i},\ \psi_{l,i} \mid l \geq l_0,\ i \in \mathbb{Z}\}$ constitutes an orthonormal basis of $\mathcal{L}^2(\mathbb{R})$. This basis is known as the *Haar basis*. When $l_0 \leq l \leq L$, one gets the piecewise constant approximation f_L of f on the intervals $I_{L,i}$, $i \in \mathbb{Z}$. This approximation uniformly converges towards f in the $\mathcal{L}^2$-norm for $L \to \infty$.

■

A.2 Biorthogonal wavelets

The property of *biorthogonality* [29, 27] offers more flexibility than orthonormality. It requires that ϕ admits a *dual* refinable function $\tilde{\phi}$ which verifies

$$\forall i, j \in \mathbb{Z},\ <\phi(x-i)\ ,\ \tilde{\phi}(x-j)>= \delta_{i,j}. \tag{A.11}$$

The refinement equation fulfilled by $\tilde{\phi}$ is

$$\tilde{\phi}(x) = \sum_{i\in\mathbb{Z}} \tilde{h}_n\ \tilde{\phi}(2x-i),\ \tilde{h}_i \in \mathbb{R}.$$

A *dual wavelet* $\tilde{\psi}$ is required to exist. It verifies the refinement equation

$$\tilde{\psi}(x) = \sum_{i\in\mathbb{Z}} \tilde{g}_n\ \tilde{\phi}(2x-i),\ \tilde{g}_i \in \mathbb{R}.$$

The above filter coefficients verify the following properties

$$g_n = (-1)^n \tilde{h}_{1-n} \text{ and } \tilde{g}_n = (-1)^n h_{1-n}. \tag{A.12}$$

The expression of a function $f \in \mathcal{L}^2(\mathbb{R})$ in the wavelet basis becomes

$$f(x) = \sum_{i\in\mathbb{Z}} c_{l_0,i}\phi_{l_0,i}(x) + \sum_{l=l_0}^{+\infty}\sum_{i\in\mathbb{Z}} d_{l,i}\psi_{l,i}(x) \tag{A.13}$$

where

$$\begin{aligned} c_{l,i} &= <f\ ,\ \tilde{\phi}_{l,i}> \\ d_{l,i} &= <f\ ,\ \tilde{\psi}_{l,i}> \end{aligned} \tag{A.14}$$

The functions $\tilde{\phi}_{l,i}$ and $\tilde{\psi}_{l,i}$ respectively denote the translates and dilates of $\tilde{\phi}$ and $\tilde{\psi}$, i.e.

$$\begin{aligned} \tilde{\phi}_{l,i}(x) &= 2^{\frac{l}{2}}\,\tilde{\phi}(2^l x - i) \\ \tilde{\psi}_{l,i}(x) &= 2^{\frac{l}{2}}\,\tilde{\psi}(2^l x - i) \end{aligned} \tag{A.15}$$

We remark that, for given ϕ, the choice of a function $\tilde{\phi}$ is not unique. Moreover, in contrast with ϕ, $\tilde{\phi}$ does not have to be in V_0. The orthonormal case can be seen as a particular case of biorthogonality where $\tilde{\phi} = \phi$ and $\tilde{\psi} = \psi$.

A.3 Wavelets and cell-average multiresolution

In this section, we show that the cell-average multiresolution approach can be embedded in the general framework of the biorthogonal wavelet approximation. This part is borrowed from [27, 31].

In the case where the prediction is made through a polynomial interpolation, we have in 1D [31]

$$\hat{u}_{l+1,2i} = \sum_{m=-s}^{s} \lambda_{i+m} \bar{u}_{l,i+m} \ , \ \lambda_{i+m} \in \mathbb{R}$$

Using the wavelet terminology, we can write that

$$\bar{u}_{l,i} = \frac{1}{|\Omega_{l,i}|} \int_{\Omega_{l,i}} u \, dx = \frac{< u, \tilde{\phi}_{l,i} >}{\sqrt{|\Omega_{l,i}|}} \tag{A.16}$$

The dual scaling function $\tilde{\phi}_{l,i}$ is given by

$$\tilde{\phi}_{l,i} = \frac{\chi_{\Omega_{l,i}}}{\sqrt{|\Omega_{l,i}|}}$$

Thus, the details $\bar{d}_{l+1,2i}$ can be defined as

$$\bar{d}_{l+1,2i} = \bar{u}_{l+1,2i} - \hat{u}_{l+1,2i} = \bar{u}_{l+1,2i} - \sum_{m=-s}^{s} \lambda_{i+m} \bar{u}_{l,i+m} = \frac{< u, \tilde{\psi}_{l,i} >}{\sqrt{|\Omega_{l,i}|}} \tag{A.17}$$

where the dual wavelet $\tilde{\psi}_{l,i}$ is given by

$$\tilde{\psi}_{l,i} = \tilde{\phi}_{l+1,2i} - \sum_{m=-s}^{s} \lambda_{i+m} \tilde{\phi}_{l,i+m}$$

The details for odd indices $\bar{d}_{l+1,2i+1}$ are redundant and verify $\bar{d}_{l+1,2i} + \bar{d}_{l+1,2i+1} = 0$.

Denoting $u|_L$ the restriction of u to the finest grid, which is by definition

$$u|_L(x) = \sum_{i=0}^{2^L-1} < u, \tilde{\phi}_{L,i} > \ \phi_{L,i}(x)$$

Harten's multiresolution transform corresponds to a representation of $u|_L$ in the biorthogonal wavelet basis $(\phi_{0,0}, \psi_{l,i})$

$$u|_L = < u, \tilde{\phi}_{0,0} > \ \phi_{0,0} + \sum_{l=0}^{L-1} \sum_{i=0}^{2^l-1} < u, \tilde{\psi}_{l,i} > \ \psi_{l,i} \tag{A.18}$$

For a cell-average multiresolution analysis on $\Omega = [0,1]$, the dual scaling function is $\tilde{\phi} = \chi_{[0,1]}$. Therefore it verifies the refinement equation $\tilde{\phi}(x) = \tilde{\phi}(2x) + \tilde{\phi}(2x-1)$, which

means that the refinement coefficients defined in (A.3-A.8) verify $\tilde{h}_0 = \tilde{h}_1 = 1$, and $\tilde{h}_n = 0$ elsewhere. We then have $g_0 = 1$, $g_1 = -1$, and $g_n = 0$ elsewhere.

For a prediction operator as the one defined in the previous section, if we choose a multiresolution accuracy $r = 3$, we have

$$h_0 = h_1 = 1,\ h_{-1} = h_2 = \frac{1}{8},\ h_{-2} = h_3 = -\frac{1}{8},\ \text{and } h_n = 0 \text{ elsewhere.}$$

from which we deduce that

$$\tilde{g}_0 = 1,\ \tilde{g}_1 = -1,\ \tilde{g}_2 = \tilde{g}_3 = \frac{1}{8},\ \tilde{g}_{-1} = \tilde{g}_{-2} = -\frac{1}{8},\ \text{ and } \tilde{g}_n = 0 \text{ elsewhere.}$$

As described in [27], we can find the approximate values $\phi(2^{-l}\, i) = c_{l,i}$ on the grid Ω_L using the following algorithm

$$\begin{aligned} c_{0,i} &= \delta_{0,i}\ ,\ i \in \mathbb{Z} \\ c_{l+1,i} &= \sum_{n \in \mathbb{Z}} h_{i-2n}\, c_{l,n}\ ,\ i \in \mathbb{Z}\ ,\ l \in \{0, \ldots, L-1\} \end{aligned} \tag{A.19}$$

From (A.12) we can also compute the approximate values $\psi(2^{-l}\, i)$, $i \in \mathbb{Z}$, $l \in \{0, \ldots, L\}$. As we have an analytic expression of $\tilde{\phi}$, we can deduce from (A.3-A.8) an analytic expression of $\tilde{\psi}$. The corresponding scaling functions and wavelets for $r = 3$ are plotted in Fig. A.3 and A.4.

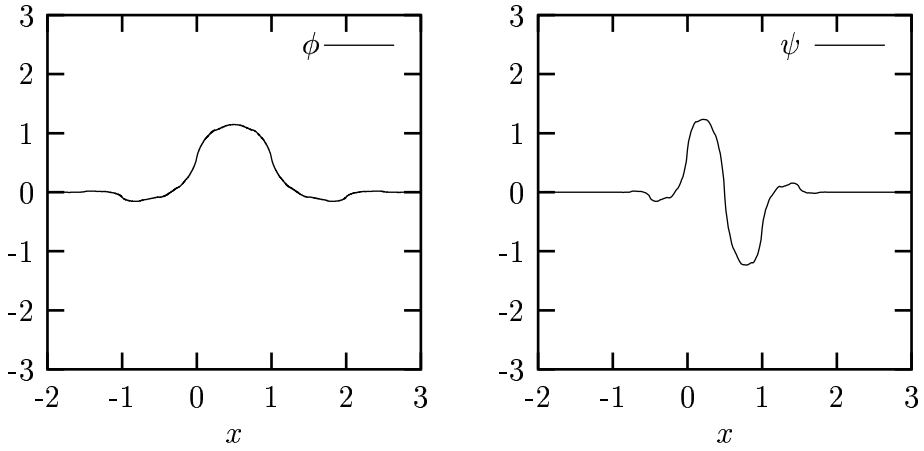

Figure A.3: Scaling function ϕ and wavelet ψ for $r = 3$.

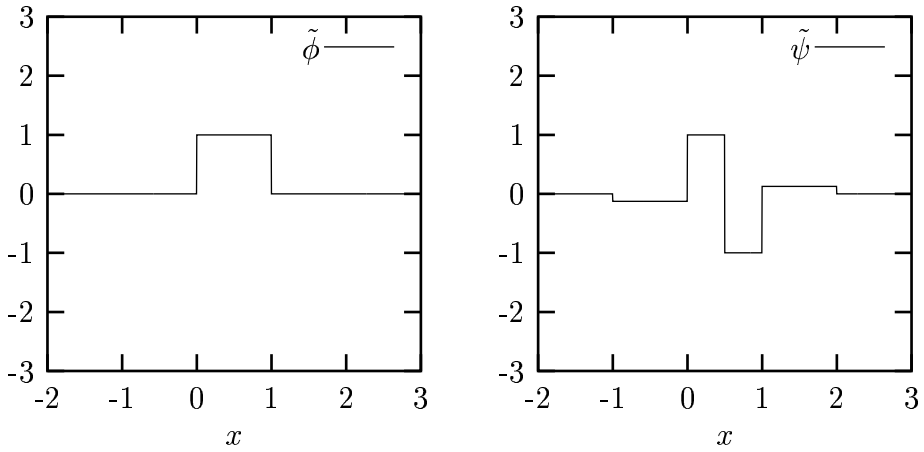

Figure A.4: Dual scaling function $\tilde{\phi}$ and dual wavelet $\tilde{\psi}$ for $r = 3$.

Appendix B

Harten's prediction operator

In this appendix we give the result of the prediction operator for the linear polynomial interpolation in the 1D, 2D and 3D cases.

B.1 One-dimensional case

For the 1D case, Harten [54] chose as prediction operator a linear polynomial interpolation on the cell-average values. Therefore, we have, for $n \in \{0, 1\}$,

$$\begin{aligned} \hat{u}_{l+1,2i+n} &= I(\bar{U}_l; l+1, 2i+n) \\ &= \bar{u}_{l,i} - (-1)^n \, Q_x^s(\bar{U}_l; i) \end{aligned} \tag{B.1}$$

$$\tag{B.2}$$

where

$$Q_x^s(\bar{U}_l; i) = \sum_{n=1}^{s} \gamma_n \left(\bar{u}_{l,i+n} - \bar{u}_{l,i-n} \right)$$

B.2 Two-dimensional case

For the 2D case, Bihari and Harten [12] obtained the following values using a tensor product approach. For $n, p \in \{0, 1\}$, we have

$$\begin{aligned} \hat{u}_{l+1,2i+n,2j+p} &= I(\bar{U}_l; l+1, 2i+n, 2j+p) \\ &= \bar{u}_{l,i,j} - (-1)^n \, Q_x^s(\bar{U}_l; i, j) - (-1)^p \, Q_y^s(\bar{U}_l; i, j) \\ &\quad + (-1)^{np} \, Q_{xy}^s(\bar{U}_l; i, j) \end{aligned} \tag{B.3}$$

where

$$Q_x^s(\bar{U}_l; i, j) = \sum_{n=1}^{s} \gamma_n \left(\bar{u}_{l,i+n,j} - \bar{u}_{l,i-n,j} \right)$$

$$Q_y^s(\bar{U}_l; i, j) = \sum_{p=1}^{s} \gamma_p \left(\bar{u}_{l,i,j+p} - \bar{u}_{l,i,j-p}\right)$$

$$Q_{xy}^s(\bar{U}_l; i, j) = \sum_{n=1}^{s} \gamma_n \sum_{p=1}^{s} \gamma_p \left(\bar{u}_{l,i+n,j+p} - \bar{u}_{l,i+n,j-p} - \bar{u}_{l,i-n,j+p} + \bar{u}_{l,i-n,j-p}\right)$$

B.3 Three-dimensional case

We apply the same method to get the prediction in the 3D case. Thus, for $n, p, q \in \{0, 1\}$, we have

$$\begin{aligned} \hat{u}_{l+1,2i+n,2j+p,2k+q} &= I(\bar{U}_l; l+1, 2i+n, 2j+p, 2k+q) \\ &= \bar{u}_{l,i,j,k} - (-1)^n Q_x^s(\bar{U}_l; i, j, k) - (-1)^p Q_y^s(\bar{U}_l; i, j, k) \\ &\quad -(-1)^q Q_z^s(\bar{U}_l; i, j, k) + (-1)^{np} Q_{xy}^s(\bar{U}_l; i, j, k) \\ &\quad +(-1)^{pq} Q_{yz}^s(\bar{U}_l; i, j, k) + (-1)^{nq} Q_{xz}^s(\bar{U}_l; i, j, k) \\ &\quad -(-1)^{npq} Q_{xyz}^s(\bar{U}_l; i, j, k) \end{aligned} \tag{B.4}$$

where

$$Q_x^s(\bar{U}_l; i, j, k) = \sum_{n=1}^{s} \gamma_n \left(\bar{u}_{l,i+n,j,k} - \bar{u}_{l,i-n,j,k}\right)$$

$$Q_y^s(\bar{U}_l; i, j, k) = \sum_{p=1}^{s} \gamma_p \left(\bar{u}_{l,i,j+p,k} - \bar{u}_{l,i,j-p,k}\right)$$

$$Q_z^s(\bar{U}_l; i, j, k) = \sum_{q=1}^{s} \gamma_q \left(\bar{u}_{l,i,j,k+q} - \bar{u}_{l,i,j,k-q}\right)$$

$$Q_{xy}^s(\bar{U}_l; i, j, k) = \sum_{n=1}^{s} \gamma_n \sum_{p=1}^{s} \gamma_p \left(\bar{u}_{l,i+n,j+p,k} - \bar{u}_{l,i+n,j-p,k} - \bar{u}_{l,i-n,j+p,k} + \bar{u}_{l,i-n,j-p,k}\right)$$

$$Q_{yz}^s(\bar{U}_l; i, j, k) = \sum_{p=1}^{s} \gamma_p \sum_{q=1}^{s} \gamma_q \left(\bar{u}_{l,i,j+p,k+q} - \bar{u}_{l,i,j+p,k-q} - \bar{u}_{l,i,j-p,k+q} + \bar{u}_{l,i,j-p,k-q}\right)$$

$$Q_{xz}^s(\bar{U}_l; i, j, k) = \sum_{n=1}^{s} \gamma_n \sum_{q=1}^{s} \gamma_q \left(\bar{u}_{l,i+n,j,k+q} - \bar{u}_{l,i+n,j,k-q} - \bar{u}_{l,i-n,j,k+q} + \bar{u}_{l,i-n,j,k-q}\right)$$

$$
\begin{aligned}
Q^s_{xyz}(\bar{U}_l; i, j, k) \;=\; & \sum_{n=1}^{s} \gamma_n \sum_{p=1}^{s} \gamma_p \sum_{q=1}^{s} \gamma_q \, (\bar{u}_{l,i+n,j+p,k+q} - \bar{u}_{l,i+n,j+p,k-q} \\
& - \bar{u}_{l,i+n,j-p,k+q} - \bar{u}_{l,i-n,j+p,k+q} + \bar{u}_{l,i+n,j-p,k-q} \\
& + \bar{u}_{l,i-n,j+p,k-q} + \bar{u}_{l,i-n,j-p,k+q} - \bar{u}_{l,i-n,j-p,k-q})
\end{aligned}
$$

Whatever the dimension, the multiresolution accuracy r is related to the number of required nearest uncles by $r = 2s + 1$. The corresponding coefficients γ_n are

$$
\begin{cases}
r = 3 \;\Rightarrow\; \gamma_1 = -\dfrac{1}{8} \\[2ex]
r = 5 \;\Rightarrow\; \gamma_1 = -\dfrac{22}{128},\ \gamma_2 = \dfrac{3}{128}
\end{cases}
$$

Bibliography

[1] R. Abgrall. Multiresolution analysis on unstructured meshes: application to CFD. In K. W. Morton and M. J. Baines, editors, *Numerical methods for fluid dynamics*, volume 5, pages 271–276. Oxford Science Publications, 1995.

[2] R. Abgrall and A. Harten. Multiresolution representation in unstructured meshes. *SIAM J. Numer. Anal.*, 35(6):2128–2146, 1998.

[3] F. Aràndiga, R. Donat, and A. Harten. Multiresolution based on weighted averages of the hat function I: Linear reconstruction techniques. *SIAM J. Numer. Anal.*, 36(1):160–203, 1998.

[4] F. Aràndiga, R. Donat, and A. Harten. Multiresolution based on weighted averages of the hat function II: Non-linear reconstruction techniques. *SIAM J. Sci. Comput.*, 20(3):1053–1093, 1999.

[5] G. K. Batchelor. *An introduction to fluid dynamics.* Cambridge University Press, 1967.

[6] A. Bayliss, G. K. Leaf, and B. J. Matkowsky. Pulsating and chaotic dynamics near the extinction limit. *Comb. Sci. Tech.*, 84:253–278, 1992.

[7] J. Bell, M. J. Berger, J. Saltzman, and M. Welcome. Three-dimensional adaptive mesh refinement for hyperbolic conservation laws. *SIAM J. Sci. Comput.*, 15:127–138, 1994.

[8] M. J. Berger and P. Colella. Local adaptive mesh refinement for shock hydrodynamics. *J. Comput. Phys.*, 82:67–84, 1989.

[9] M. J. Berger and J. Oliger. Adaptive mesh refinement for hyperbolic partial differential equations. *J. Comput. Phys.*, 53:484–512, 1984.

[10] G. Beylkin, R. Coifman, and V. Rokhlin. Fast wavelet transforms and numerical algorithms I. *Comm. Pure Appl. Math.*, 44:141–183, 1991.

[11] B. L. Bihari. Multiresolution schemes for conservation laws with viscosity. *J. Comput. Phys.*, 123:207–225, 1996.

[12] B. L. Bihari and A. Harten. Multiresolution schemes for the numerical solution of 2-D conservation laws I. *SIAM J. Sci. Comput.*, 18(2):315–354, 1997.

[13] H. Bockhorn, J. Fröhlich, W. Gerlinger, and K. Schneider. Numerical investigations on the stability of flame balls. In *Proceedings of the 4th European Computational Fluid Dynamics*, pages 990–995. John Wiley and Sons, 1998.

[14] H. Bockhorn, J. Fröhlich, and K. Schneider. An adaptive two-dimensional wavelet-vaguelette algorithm for the computation of flame balls. *Combust. Theory Modelling*, 3:1–22, 1999.

[15] M. R. Booty, S. B. Margolis, and B. J. Matkowsky. Interaction of pulsating and spinning waves in nonadiabatic flame propagation. *SIAM J. Appl. Math.*, 47(6):1241–1286, 1987.

[16] F. Bramkamp, B. Gottschlich-Müller, M. Hesse, P. Lamby, S. Müller, J. Ballmann, K. H. Brakhage, and W. Dahmen. H-adaptive multiscale schemes for compressible Navier-Stokes equations - polyhedral discretization, data compression and mesh generation. In J. Ballmann, editor, *Flow modulation and fluid-structure-interaction at airplane wings*, volume 84 of *Numerical notes on Fluid Mechanics*, pages 125–204. Springer, 2003.

[17] A. Brandt. Multi-level adaptive solutions to boundary value problems. *Math. Comp.*, 31:333–390, 1977.

[18] J. D. Buckmaster and G. S. Ludford. *Lectures on mathematical combustion.* SIAM, Philadelphia, Pennsylvania, 1983.

[19] W. B. Bush and F. E. Fendell. Asymptotic analysis of laminar flame propagation for general Lewis numbers. *Combust. Sci. Tech.*, 1:421–428, 1970.

[20] P. Charton and V. Perrier. A pseudo-wavelet scheme for the two-dimensional Navier-Stokes equations. *Matematica Aplicada y Computacional*, 15:139–160, 1996.

[21] G. Chiavassa and R. Donat. Point value multi-scale algorithms for 2D compressible flows. *SIAM J. Sci. Comput.*, 23(3):805–823, 2001.

[22] G. Chiavassa and J. Liandrat. On the effective construction of compactly supported wavelets satisfying homogeneous boundary conditions on the interval. *Appl. Comput. Harm. Anal.*, 4:62–73, 1997.

[23] G. Chiavassa and J. Liandrat. A fully adaptive wavelet algorithm for parabolic partial differential equations. *Appl. Numer. Math.*, 36:333–358, 2001.

[24] A. J. Chorin. Numerical solution of the Navier-Stokes equations. *Math. Comp.*, 22:745–762, 1968.

[25] P. Clavin. Dynamic behaviour of premixed flame fronts in laminar and turbulent flows. *Prog. Energy Combust. Sci.*, 11:1–59, 1985.

[26] P. Clavin and F. A. Williams. Effects of molecular diffusion and of thermal expansion on the structure and dynamics of premixed flames in turbulent flows of large scale and low intensity. *J. Fluid Mech.*, 116:251, 1982.

[27] A. Cohen. *Wavelet methods in numerical analysis*, volume 7 of *Handbook of Numerical Analysis*. P.G. Ciarlet and J.L. Lions, editors, Elsevier, Amsterdam, 2000.

[28] A. Cohen. Adaptive methods for PDE's - Wavelets or mesh refinement ? In *International Conference of Mathematics*, Beijing, 2002.

[29] A. Cohen, I. Daubechies, and J. C. Feauveau. Biorthogonal bases of compactly supported wavelets. *Comm. Pure Appl. Math.*, 45:485–560, 1992.

[30] A. Cohen, N. Dyn, S. M. Kaber, and M.Postel. Multiresolution finite volume schemes on triangles. *J. Comput. Phys.*, 161:264–286, 2000.

[31] A. Cohen, S. M. Kaber, S. Müller, and M. Postel. Fully adaptive multiresolution finite volume schemes for conservation laws. *Math. Comp.*, 72:183–225, 2002.

[32] W. Dahmen. Wavelet and multiscale methods for operator equations. *Acta Numerica*, 6:55–228, 1997.

[33] W. Dahmen, B. Gottschlich-Müller, and S. Müller. Multiresolution schemes for conservation laws. *Numer. Math.*, 88(3):399–443, 2001.

[34] W. Dahmen and A. Kunoth. Multilevel preconditioning. *Numer. Math.*, 63:315–344, 1992.

[35] J. Daou and M. Matalon. Influence of conductive heat-losses on the propagation of premixed flames in channels. *Combust. Flame*, 128:321–339, 2002.

[36] G. Darrieus. Propagation d'un front de flamme. communication presented at La Technique Moderne, 1938, and Sixième Congrès de Mécanique Appliquée, Paris, 1946.

[37] I. Daubechies. *Ten lectures on wavelets*. CBMS lecture notes series. SIAM, 1991.

[38] B. Denet and P. Haldenwang. Numerical study of thermal-diffusive instability of premixed flames. *Combust. Sci. Tech.*, 86:199–221, 1992.

[39] B. Denet and P. Haldenwang. A numerical study of premixed flames: Darrieus-Landau instability. *Combust. Sci. Tech.*, 104:143–167, 1995.

[40] R. DeVore. Nonlinear approximation. *Acta Numerica*, 7:51–150, 1998.

[41] D. Dutoya and B. Courbet. Développement du solveur NSH dans le cadre du projet MSDH. ONERA RT 44/3446 DSNA/Y, 1999.

[42] M. Farge and K. Schneider. Coherent Vortex Simulation (CVS), a semi-deterministic turbulence model using wavelets. *Flow, Turbulence and Combustion*, 66(4):393–426, 2001.

[43] J. Fröhlich and K. Schneider. An adaptive wavelet Galerkin algorithm for one- and two-dimensional flame computations. *Eur. J. Mech., B/Fluids*, 13(4):439–471, 1994.

[44] J. Fröhlich and K. Schneider. Numerical simulation of decaying turbulence in an adaptive wavelet basis. *Appl. Comput. Harm. Anal.*, 3:393–397, 1996.

[45] J. Fröhlich and K. Schneider. An adaptive wavelet-vaguelette algorithm for the solution of PDEs. *J. Comput. Phys.*, 130:174–190, 1997.

[46] W. Gerlinger. *Direkte numerische Simulation der Wechselwirkung von chemischen Reaktionen, Vermischungsvorgängen und Transportprozessen.* PhD thesis, Universität Karlsruhe, 2002.

[47] W. Gerlinger, K. Schneider, J. Fröhlich, and H.Bockhorn. Numerical simulations on the stability of spherical flame structures. *Combust. Flame*, 132:247–271, 2003.

[48] B. Gottschlich-Müller and S. Müller. Adaptive finite volume schemes for conservation laws based on local multiresolution techniques. In M. Fey and R. Jeltsch, editors, *Hyperbolic problems: Theory, numerics, applications*, pages 385–394. Birkhäuser, 1999.

[49] E. Guyon, J. P. Hulin, and L. Petit. *Hydrodynamique physique.* InterEditions/Editions du CNRS, 1991.

[50] A. Haar. Zur Theorie der orthogonalen Funktionensysteme. *Math. Ann.*, 69:331–371, 1910.

[51] P. Haldenwang and D. Pignol. Dynamically adapted mesh refinement for combustion front tracking. *Comp. Fluid*, 31(4-7):589–606, 2002.

[52] A. Harten. Discrete multi-resolution analysis and generalized wavelets. *J. Appl. Num. Math.*, 12:153–193, 1993.

[53] A. Harten. Adaptive multiresolution schemes for shock computations. *J. Comput. Phys.*, 115:319–338, 1994.

[54] A. Harten. Multiresolution algorithms for the numerical solution of hyperbolic conservation laws. *Comm. Pure Appl. Math.*, 48:1305–1342, 1995.

[55] A. Harten. Multiresolution representation of data: a general framework. *SIAM J. Numer. Anal.*, 33(3):1205–1256, 1996.

[56] A. Harten and S. Osher. Uniformly high order accurate nonoscillatory schemes I. *SIAM J. Numer. Anal.*, 24:279–309, 1987.

[57] C. Hirsch. *Numerical computation of internal and external flows*, volume 1. John Wiley and Sons, 1988.

[58] C. Hirsch. *Numerical computation of internal and external flows*, volume 2. John Wiley and Sons, 1990.

[59] S. Jaffard. Wavelet methods for fast resolution of elliptic problems. *SIAM J. Numer. Anal.*, 29:965–986, 1992.

[60] G. Joulin and P. Clavin. Linear stability analysis of nonadiabatic flames: diffusional-thermal model. *Combust. Flame*, 35:139–153, 1979.

[61] L. Landau. On the theory of slow combustion. *Acta Physicochim. USSR*, 19:77, 1944.

[62] B. Larrouturou, H. Berestycki, C. M. Brauner, P. Clavin, and C. Schmidt-Lainé, editors. *Modélisation de la combustion.* Images des mathématiques. CNRS, 1996.

[63] B. Lewis and G. von Elbe. *Combustion, flames and explosions of gases.* Academic Press, New York, 1961.

[64] J. Liandrat and P. Tchamitchian. Resolution of the 1D regularized Burgers equation using a spatial wavelet approximation: algorithms and numerical results. Technical Report No. 90-83, ICASE, 1990.

[65] Y. Maday, V. Perrier, and J. C. Ravel. Adaptivité dynamique sur base d'ondelettes pour l'approximation d'équations aux dérivées partielles. *C. R. Acad. Sci. Paris, Série I*, 312:405–410, 1991.

[66] Y. Maday and J. C. Ravel. Adaptivité par ondelettes: conditions aux limites et dimensions supérieures. *C. R. Acad. Sci. Paris, Série I*, 315:85–90, 1992.

[67] S. Mallat. Multiresolution approximation and wavelet orthonormal bases of $\mathcal{L}^2(\mathbb{R})$. *Trans. Amer. Math. Soc.*, 315:69–88, 1989.

[68] Y. Meyer. *Ondelettes et opérateurs I/II.* Hermann, Paris, 1990.

[69] S. Müller. Adaptive multiresolution schemes. In R. Herbin and D. Kröner, editors, *Finite Volumes for Complex Applications*, volume 3, pages 119–136. Hermes Penton Science, 2002.

[70] S. Müller. *Adaptive multiscale schemes for conservation laws*, volume 27 of *Lecture Notes in Computational Science and Engineering.* Springer-Verlag, Heidelberg, 2003.

[71] H. G. Pearlman and P. D. Ronney. Near-limit behavior of high-Lewis number premixed flames in tubes at normal and low gravity. *Phys. Fluids*, 6(12):4009–4018, 1994.

[72] H. G. Pearlman and P. D. Ronney. Self-organized spiral and circular waves in premixed gas flames. *J. Chem. Phys.*, 101(3):2632–2633, 1994.

[73] N. Peters and J. Warnatz, editors. *Numerical methods in laminar flame propagation*, volume 6 of *Notes on numerical fluid mechanics*. Vieweg, 1982.

[74] J. J. Quirk. *An adaptive grid algorithm for shock hydrodynamics*. PhD thesis, Cranfield Institute of Technology, College of Aeronautics, 1991.

[75] P. H. Renard, D. Thévenin, J. C. Rolon, and S. Candel. Dynamics of flame/vortex interactions. *Prog. Energy Combust. Sci.*, 26:225–282, 2000.

[76] P. L. Roe. Approximate Riemann solvers, parameter vectors, and difference schemes. *J. Comput. Phys.*, 43:357–372, 1981.

[77] B. Rogg. The effect of Lewis number greater than unity on an unsteady propagating flame with one-step chemistry. In N. Peters and J. Warnatz, editors, *Numerical methods in laminar flame propagation*, volume 6 of *Notes on numerical fluid mechanics*, pages 38–48. Vieweg, 1982.

[78] P. D. Ronney. Near-limit flame structures at low Lewis number. *Combust. Flame*, 82:1–14, 1990.

[79] P. D. Ronney. Premixed laminar and turbulent flames at microgravity. *Space Forum*, 4:49–98, 1998.

[80] O. Roussel, E. M. Duclairoir, K. Schneider, and H. Bockhorn. Numerical investigation of spherical flame structures interacting with an adiabatic wall using adaptive mutiresolution schemes. *in preparation.*

[81] O. Roussel and M. P. Errera. Adaptive mesh refinement : a wavelet point of view. In *Proceedings of ECCOMAS 2000 Conference*, page 1010, Barcelona, Spain, 2000.

[82] O. Roussel and K. Schneider. A fully adaptive multiresolution scheme for 3D reaction-diffusion equations. In R. Herbin and D. Kröner, editors, *Finite Volumes for Complex Applications*, volume 3, pages 833–840. Hermes Penton Science, 2002.

[83] O. Roussel and K. Schneider. An adaptive multiresolution scheme for combustion problems: application to flame ball-vortex interaction. Preprint, L3M, CNRS et Universités d'Aix-Marseille, 2003.

[84] O. Roussel, K. Schneider, A. Tsigulin, and H. Bockhorn. A conservative fully adaptive multiresolution algorithm for parabolic PDEs. *J. Comput. Phys.*, 188(2):493–523, 2003.

[85] K. Schneider. *Wavelets, turbulence and chemical reactions.* PhD thesis, Universität Kaiserslautern, 1996.

[86] K. Schneider. *Modélisation et simulation numérique en base d'ondelettes adaptative, applications en mécanique des fluides et en combustion.* Habilitation thesis, Université Louis Pasteur, Strasbourg, 2001.

[87] K. Schneider and M. Farge. Adaptive wavelet simulation of a flow around an impulsively started cylinder using penalisation. *Appl. Comput. Harm. Anal.*, 12:374–380, 2002.

[88] K. Schneider, N. K. R. Kevlahan, and M. Farge. Comparison of an adaptive wavelet method and nonlinearly filtered pseudospectral methods for two-dimensional turbulence. *Theoret. Comput. Fluid Dynamics*, 9:191–206, 1997.

[89] G. I. Sivashinsky. Diffusional-thermal theory of cellular flames. *Combust. Sci. Tech.*, 15:137–146, 1977.

[90] G. I. Sivashinsky. Nonlinear analysis of hydrodynamic instability in laminar flames - I. derivation of basic equations. *Acta Astronautica*, 4:1177–1206, 1977.

[91] K. Urban. A wavelet-Galerkin algorithm for the driven-cavity-Stokes-problem in two space dimensions. In M. Feistauer, R. Rannacher, and K. Kozel, editors, *Numerical Modelling in Continuum Mechanics*, pages 278–289. Charles-University Prague, 1995.

[92] F. A. Williams. *Combustion theory.* Benjamin Cummings, Menlo Park, 1985.

[93] Y. B. Zeldovich, G. I. Barenblatt, V. B. Librovich, and G. M. Makhviladze. *The mathematical theory of combustion and explosions.* Consultant Bureau, New York, 1985.

[94] Y. B. Zeldovich and D. A. Frank-Kamenetskii. *Acta phys.-chim. USSR IX*, 2:348, 1938.